

Multi-scale Investigation of Damage Mechanisms in SiC/SiC Ceramic Matrix Composites

by

Jared Michael Tracy

A dissertation submitted in partial fulfillment
of the requirements for the degree of
Doctor of Philosophy
(Materials Science and Engineering)
in the University of Michigan
2014

Doctoral Committee:

Assistant Professor Samantha H. Daly, Chair
Professor John W. Halloran
Professor Richard E. Robertson
Kathleen M. Sevener
Professor Anthony M. Waas

© Jared Michael Tracy 2014

All Rights Reserved

Acknowledgements

This thesis work could not have been accomplished without the support and assistance of several engineers and scientists at the University of Michigan and from the company that funded my research. First and foremost, I would like to thank my advisor, Prof Samantha Daly, and my committee for providing the support and guidance needed to shape the scope and direction of experimentation and analyses in this work. Their collective knowledge, experience and critical feedback were essential for high-temperature experimentation, statistical analysis, damage analyses and toughness evaluation. Many of the small-scale, in-situ testing techniques addressed throughout the thesis were achieved through close collaboration with a fellow lab member, Adam Kammers. High-speed and elevated temperature techniques were developed and refined through collaboration with Joshua DeBoer. Lucas Hansen was extraordinarily helpful in sanity checking mathematical and theoretical work. I would like to thank Ron Nimmer for his valuable discussions on evaluating fracture toughness. Experimentation was possible through the assistance of Dr. John Mansfield and Dr. Haiping Sun from the Electron Microbeam Analysis Laboratory at Michigan as well as Dr. Sandrine Martin, Dr. Pilar Herrera-Fierro, Greg Allion and Matthew Oonk from the Lurie Nanofabrication Facility at Michigan. Doug Carper, Greg Wilson and Dave Johnson provided valuable feedback as technical experts in ceramic composites.

TABLE OF CONTENTS

ACKNOWLEDGEMENTS	ii
LIST OF FIGURES	vi
LIST OF ABBREVIATIONS	xix
CHAPTER	
I. Introduction	1
1.1 Ceramic Matrix Composites	1
1.2 Background Motivation for Damage Characterization	3
1.3 Organization	6
II. Techniques for Generating Tracking Patterns for Digital Image Correlation at Microscopic Length Scale	9
2.1 Introduction	9
2.2 Speckle Patterns for DIC at Macroscopic Length Scales	13
2.3 Speckle Patterns for DIC at Microscopic Length Scales	15
2.3.1 Nanoparticle Deposition by Self-Assembly	16
2.3.2 Nanoparticle Deposition by Drop Casting	18
2.3.3 Electron Beam Lithography	21
2.4 Conclusion	22
III. Constituent Level Characterization of Damage in Ceramic Matrix Composites at High Temperature	25
3.1 Introduction	25
3.2 Background	25
3.2.1 Small-Scale Digital Image Correlation	26

3.3	Method	29
3.3.1	Materials Preparation and Patterning	29
3.3.2	High Temperature SEM-DIC	33
3.4	Discussion	36
3.4.1	High Temperature Full-Field Deformations	36
3.4.2	High Temperature Damage Evolution	39
3.4.3	Sources of Error in SEM-DIC	42
3.5	Conclusions	43
IV.	Experimental Assessment of Fracture Toughness in Ceramic Matrix Composites Using the J-integral with Digital Image Correlation	47
4.1	Introduction	47
4.2	Background	48
4.3	Analytical Validation: Line Integral and Area Integral	51
4.3.1	Analytical Validation – Line Integral	52
4.3.2	Analytical Validation – Area Integral	54
4.4	Application of Line and Area Integrals to Experimental DIC Data	59
4.4.1	Impact of Contour Truncation on Measurements of Toughness	59
4.4.2	Experimental Application – Line Integral	62
4.4.3	Experimental Application – Area Integral	65
4.5	Fracture Characterization: Assessment of Line and Area Integrals	66
4.5.1	Fracture Characterization in Isotropic Materials	66
4.5.1.a	Fracture Characterization: PMMA	66
4.5.1.b	Fracture Characterization: Aluminum	73
4.5.2	Fracture Characterization: SiC/SiC	75
4.5.2.a	Fracture Characterization: SiC/SiC [0/90/0/90]s at 795°C	76
4.5.2.b	Fracture Characterization: Unidirectional CMC	84
4.5.2.c	Comparison of Results from Crossply and Unidirectional Laminates	87
4.5.2.d	Experimentally Derived Bridging Zone Laws	88
4.6	Influence of Experimental Variability on the J-integral	90
4.7	Influence of Damage Mechanisms in CMCs on the J-integral	94
4.8	Conclusions	97
V.	Fractographic Observations in CMCs	102
5.1	Introduction	102
5.2	Background	103
5.3	Methods	104
5.4	Results and Discussion	105
5.4.1	Case Study: Single edge-notched [0/m/0]s Unidirectional Laminate	106
5.4.2	Modes of Failure in Ceramic Matrix Composites	112
5.4.3	Observations from Fracture Surfaces in the Vicinity of Notch Tips	

	114
5.4.4	Subsurface Behavior of Propagating Cracks	117
5.4.5	Crack Propagation in Longitudinal Lamina	120
5.4.6	Wallner Lines in Transverse Unidirectional Laminates	122
5.4.7	Influence of Fibers on Crack Propagation	123
5.5	Conclusions	125
VI.	On the Association between Microscopic and Macroscopic Damage Evolution in Ceramic Matrix Composites	127
6.1	Introduction	127
6.2	Experimental Methods	130
6.3	Evolution of Damage in CMCs at Multiple Length Scales	134
6.3.1	Damage Evolution at the Constituent Length Scale	134
6.3.2	Damage Evolution at the Lamina Length Scale	142
6.3.3	Damage Evolution at the Laminate Length Scale	145
6.3.4	Connecting Microscopic Damage to Macroscopic Damage	151
6.4	Conclusions	155
	Appendix A	160
VII.	Summary and Future Work	162
7.1	Summary	162
7.2	Future Work	165

List of Figures

Figure

- 2.1 Longitudinal strain fields captured with DIC at the tip of an edge notch CMC tensile coupon loaded vertically in the plane of the page. Strain magnitudes are color-coded; magenta indicates strains at or around zero, while red indicates strains orders of magnitude larger than the fracture stain. In (a), the strain fields have been filtered to remove noise at the expense of significantly reducing spatial resolution. In (b), the strain filter has been reduced, which results in bias that manifests as localized fluctuations in color from blue to purple. Although noisier, the higher spatial resolution of (b) provides a more accurate depiction of damage behavior in the material. 13
- 2.2 Speckle patterns for macroscopic DIC. Both patterns were created using paint and an airbrush. The black paint was dilute with water (1:1) to reduce speckle size. The FOV of (a) is smaller that of (b). For both patterns, the smallest attainable subset size was 41 x 41 pixels. 15
- 2.3 Self-assembled 40 nm Au speckle patterns applied to SiC/SiC CMC. 50 μm FOVs are shown for equivalent locations using optical microscopy and scanning electron microscopy in secondary electron mode. Arrows point to equivalent locations of an NP agglomerate. 18
- 2.4 Drop cast Au (150 nm) speckle patterns deposited on SiC substrates. The image in (a) was captured at the interior of the pattern. A low-magnification image of a drop cast pattern surrounding an edge notch is shown in (b). Both patterns were designed for 250 μm FOVs. 19
- 2.5 Coffee ring effect illustrated for Au NPs deposited on polished alumina (left) and polished SiC (right) substrates. 20

2.6	Drop cast high-temperature speckle patterns consisting of 80 nm (a) WC and (b) Ti nanopowder agglomerates. Roll milling and a pH buffer (bicine) prevented excessive agglomeration.	21
2.7	Titanium e-beam lithography pattern deposited on SiC. Pattern is of high contrast, randomly and uniformly distributed, and is reproducible.	22
3.1	Dimensions of (a) tensile coupon and (b) edge notch.	30
3.2	High-temperature DIC tracking pattern for tests at 795°C, consisting of slightly aggregated 80 nm Ti nanopowder on a SiC substrate and applied by drop casting. A greyscale pattern intensity histogram is shown in the upper left indicating good pattern quality.	31
3.3	Ti nanopowder tracking patterns for high temperature SEM-DIC experiments at a) 500 and b) 800 micron fields of view. In both images, the tip of the notch is located on the left hand side. Variations in speckle density and the presence of a small number of abnormally large agglomerates is observed in both patterns. ...	32
3.4	CMC mounted in load frame and fitted with heater (a). Double layer of tantalum heat shields with imaging aperture reduce thermal emissions (b).	33
3.5	(a) Chamber views of load frame, with heater and thermal shielding attached, in SEM at 23° C and 795° C. At 795° C (right), thermal radiation from the heater is evident in its glowing case, but is contained by the shielding. (b) SEM and heat stage at 800° C with no thermal shielding.	33
3.6	Longitudinal strain fields along crack path. Each panel represents a shift in FOV as the crack propagates from left to right. The far right panel shows final fracture. Arrows indicate loading axis.	35
3.7	Crack initiation (left) and propagation (right) in a SiC/SiC composite at 795° C for FOVs of (a) 500 and (b) 800 microns. Longitudinal strain fields on left hand side correspond to the initial manifestation of surface matrix-crack at notch tip. Although both (a) and (b) exhibit high-strain process zones ahead of the crack tip, that of (b) appears larger. Note the different strain magnitude bars for (a) and (b).	37
3.8	Longitudinal strain fields illustrating the smearing effect of strain filters. Panels sequence indicates crack growth from left to right. In (a) the strain filter is 7x the subset size whereas in (b) it is 1.5x the subset size. The smaller strain filter does not mitigate artifacts of image noise and aliasing, however, it does reveal more damage, specifically multiple matrix cracks propagating from the notch tip, than	

	the larger filter. The data filtering in (a) masks the real behavior.	38
3.9	Longitudinal strain fields depict crack deflection in the outer longitudinal lamina of the CMC (a). Fiber pullout lengths are of similar magnitude as deflection lengths (b).	39
3.10	Microstructure is segmented into fiber, fiber pullout, matrix, and crack bins. Mean strains are computed for each bin.	40
3.11	Mean strains in fibers (computed from red and orange fiber bins) are plotted alongside their mean strains (computed from orange bins) in their corresponding pullout regions at each load increment. Inset in panel “Inc 3” is a magnified view of the localized tensile strain in a longitudinal fiber at fiber fracture.	41
3.12	Evolution of fracture in fiber. Double arrows point to position in fiber prior to and after fracture. Magnitude of longitudinal strain prior to fracture, as measured by DIC, are on order of the fibers theoretical fracture strain.	43
4.1	Graphical illustration of a rectangular (a) line contour and (b) area contour overlaid on vertical displacement fields (dark blue shades indicate negative displacement). In (a), J is evaluated at each node and the line integral along the contour is evaluated numerically. In (b), J is evaluated at four Gauss points in each element and the area integral is evaluated over the outer and inner area contours using Gaussian integration.	51
4.2	Assessment of path independency and accuracy of line integral (a) and area integral (b). In (a), line integral evaluations of fracture toughness over a large contour and small contour, irrespective of position, are 1.0000. In (b), area integral evaluations of fracture toughness vary slightly with position, ranging from 0.0007% to 0.0011% error as the left hand side of the contour is shifted toward the crack tip.	54
4.3	Illustration of the confidence interval approach to truncation. In (a), truncation points are defined at the boundaries of the Gaussian-shaped region of the confidence interval plotted along the left hand leg of the contour. In (b), the equivalent points on a plot of the longitudinal strains along the left hand leg. The truncated contour is overlaid on a plot of longitudinal strains in (c). Although data nodes with poor correlations are removed from the contour, nodes with unrealistic strains remain.	60
4.4	Illustration of the strain approach to truncation. In (a), truncation points are defined at the boundaries of the Gaussian-shaped region of the longitudinal strains	

	plotted along the left hand leg of the contour. The truncated contour is overlaid on a plot of longitudinal strains in (b). Longitudinal strains at the termination points are below 1000 $\mu\epsilon$, which are reasonable values of strain near the crack flange of a CT specimen.	61
4.5	J-integral contours prior to and after crack initiation, with the contour oriented in the direction of crack propagation. Displacement and strain data collected along angled contours must be transformed into the crack coordinate system.	62
4.6	Area contours overlaid on longitudinal strain fields in (a) PMMA and (b) SiC/SiC CMC. In both cases, the contour was truncated on either side of the crack flange and extends beyond regions of plastic deformation. In (a), plastic deformation occurs at 2000 $\mu\epsilon$. Strain values have been withheld for the CMC in (b).	66
4.7	(a) Illustration of constant-K PMMA compact tension specimen and (b) R-curves as measured by line (red squares) and area (blue circles) integrals. The area integral stress intensity factors in (b) are larger the line integral values because the displacement data used in the area integral has not been filtered.	68
4.8	Line and area integrals are evaluated for the cases of: (1) assumption of straight crack propagation and (2) transformation of deformation data in the direction of local crack propagation. Transforming data had no significant impact on the stress intensity factor measurements.	69
4.9	In (a), longitudinal strain fields are plotted for less aggressive (5 node) and more aggressive (15 node) strain filtering. Truncated line integral contours are overlaid on the strain fields. In (b), R-curves generated from line integral measurements with 5 node and 15 node filtering schemes are plotted. The smaller filtering operations resulted in slightly higher stress intensity factors	70
4.10	R-curves for PMMA tapered DCB-CT sample as measured by line and area integrals after: (a) 5 node, (b) 15 node and (c) 30 node averaging filters are applied to displacement data from DIC. The area integral is more sensitive to displacement smoothing than the line integral because it contains more mathematical operations on displacements.	71
4.11	R-curves for PMMA tapered DCB-CT sample as measured by line and area integrals using (a) 5 pixel and (b) 21 pixel DIC step sizes. Stress intensity factors were lower for J-integrals evaluated using deformation data from the larger step size.	72

4.12	Stress intensity factors vary with contour size for both the (a) line integral and (b) area integral. Although the variations are small, the J-integral is path dependent. 73
4.13	Aluminum single edge notch tensile specimen loaded in uniaxial tension. 21 mm DIC field of view is overlaid on tensile specimen. Contour for line integral is plotted on longitudinal strain field. Note that the boundaries of the contour are outside of the plastic zone. 74
4.14	Plots of stress intensity factor versus crack opening displacement for the line and area integrals. In (a), increasing the step size from 5 to 21 pixels resulted in a slight drop in stress intensity factors. In (b), applying a (21 node) averaging filter to the displacement data prior to evaluating J had little to no effect on the stress intensity factors. 75
4.15	(a) CMC mounted in mini tensile stage. Attached to the bottom of the sample is a resistance heater capable of heating to 800 ⁰ C in the SEM. (b) Experimental R-curves for SiC/SiC CMC at 795 ^o C derived using a closed form analytical expression (black diamonds), line integral (red squares) and area integral (blue circles). The analytical curve represents global measures of stress intensity for a single matrix crack, whereas the J-integral solutions are a measure of local stress intensity in the vicinity of the notch. Note: all stress intensity factors are normalized to a reference value, <i>K</i> 78
4.16	Unfiltered resistance curves generated from the line integral, area integral, and closed form solution. In (a) the crack is assumed to be macroscopically straight; data is not transformed. In (b), data is transformed into the local crack-tip coordinate system. Curves from the unfiltered data of (a) and (b) behave erratically in contrast to the filtered data curves of Figure 4.15 (b). This is attributed to variability in the displacement data. Note: all stress intensity factors are normalized to a reference value, <i>K</i> 80
4.17	Effect of displacement filtering and step size on stress intensity factors. In (a), R-curves generated from unfiltered data (squares) are plotted against r-curves generated from filtered displacement data (asterisks). Increasing the step size reduced variability in the curves and stress intensity factors. In (b), an increase in step size from 2 pixels to 10 pixels did not reduce scatter in the curves for unfiltered data (squares), but did reduce the disparity between the line and area integrals for filtered data (asterisks). Note: all stress intensity factors are normalized to a reference value, <i>K</i> 81
4.18	Line integrals evaluated using large and small contours. Both (a) and (b) illustrate the path dependency of the J-integral when applied to DIC data for stiff materials.

	In (a), contours were truncated about the notch such that the contour terminated outside of the fiber bridging zone and excluded high intensity noise emanating from the notch tip. In (b), contours were truncated about the crack flange within the fiber bridging zone.	83
4.19	In (a), R-curves are plotted for two 795° C SEM tensile tests of edge-notched cross-ply CMCs. Up to 1.25 μm , the R-curves for both tests exhibit similar stress intensities. At crack opening displacements above 1.25 μm , artificially large strains and displacement in the vicinity of a region of fiber pullout merge with the deformation field in the vicinity of the notch tip, resulting in unreliable measures of J and K. This is illustrated in (b), where longitudinal strain fields are overlaid on the fracture image from Test 2 equating to a crack opening displacement greater than 1.25 μm . Note: all stress intensity factors for CMC tests are normalized to a reference value, K.	84
4.20	Line and area integral derived resistance curves for the first of two uniaxial CMC laminate tension tests. Fibers are oriented in the loading direction. Two cracks initiated simultaneously from the notch tip, with final fracture ultimately dominated by the upper crack. Plane stress fracture toughness is attained at or below the range 0.9K to 1.1K. Note: all stress intensity factors for CMC tests are normalized to a reference value, K.	85
4.21	Resistance curves derived from J-integral for longitudinal unidirectional laminate CMCs loaded in uniaxial tension. Inset are longitudinal strain fields corresponding to earliest detection of crack initiation at edge-notch. J-integral measures of fracture toughness were at or below the range 0.9K to 1.5K. Note: all stress intensity factors for CMC tests are normalized to a reference value, K. ...	87
4.22	Fiber bridging laws for a cross-ply CMC tested at 795° C in the SEM (blue circles) and unidirectional laminates tested at ambient temperature (red squares and black diamonds). Bridging tractions are normalized to the net section stress at fracture of each test coupon. Bridging tractions represent stresses exhibited by fibers that act to close the faces of the crack flange. The local traction varies along the crack with crack opening displacement.	90
4.23	Vertical displacement fields from Westergaard equations are modified to include random noise. Noise scaling increases from 0.1% to 10% taken clockwise from top left. Error in computing J substantially increases with noise.	91
4.24	Longitudinal strain profiles along RHS contours for center-crack biaxial Westergaard solution (a), biaxial Westergaard solution with added noise capped at $\pm 0.1\%$ of actual displacement (b), and biaxial Westergaard solution with noise smoothed by 15 node displacement filter (c). Errors in calculating fracture	

	toughness with J-integral are 0%, 0.17% and 0.02% for cases (a), (b) and (c) respectively.	92
4.25	Longitudinal strain profiles plotted along RHS contours for case of (a) biaxial Westergaard solution with added noise capped at $\pm 0.1\%$ of displacement values and (b) DIC data from PMMA DCB-CT specimen. The noise range in (a) spans $350 \mu\epsilon$ while that in (b) spans $2000 \mu\epsilon$. Displacement/strain filtering in experimental data is necessary to improve the accuracy of J-integral fracture toughness measurements.	93
4.26	Full-field principal strain maps from images captured in-situ in an SEM on a CMC specimen loaded in uniaxial tension. 4.26 (a) and (b) show fiber clusters within a 50 micron FOV located in the outer and inner transverse lamina, respectively. 4.26 (c) shows a single fiber within a 30 micron FOV located in the outer transverse lamina. All three FOVs are located near the center of the gage section, nearly 13 mm from the location of final fracture. Note the onset of cracking at the fiber-matrix interface in (b) at an applied stress that is half the proportional limit (PL).	95
4.27	Full-field longitudinal strain maps for CMCs loaded in-SEM under uniaxial tension. 4.27 (a) and (b) show crack initiation from a notch during a tensile test at 795°C in a $500 \mu\text{m}$ FOV. 4.27 (c) shows crack accumulation in a CMC during a tensile test at ambient temperature over a $250 \mu\text{m}$ FOV. In (a), DIC parameters were adjusted to smooth cracks emanating from the notch, giving the appearance of a continuous elastic deformation field. In (b), the unadjusted data is shown where it is clear that several cracks emanate from the notch and a contour that fully encircles all discontinuities is not attainable. In (c), a secondary crack is seen to appear within $100 \mu\text{m}$ of a matrix crack that initiated at a notch in an ambient temperature tensile test. The secondary crack would likely traverse any contour drawn around the initial matrix crack.	96
5.1	Initiation of matrix cracks from notch of longitudinal laminate tensile coupon. The bottom crack dominated at failure. Three areas of interest were probed for fractographic analysis.	106
5.2	Schematic demonstrating perspectives from which images of fracture surface were captured. In (a), a matrix crack initiates from the edge notch and propagates through the width of the coupon. SEM images are captured from the perspective shown by the eyes. SEM images of the top and bottom fracture halves in the vicinity of the notch are shown in (b). Folding the images such that squares touch squares and circles touch circles would reassemble the broken specimen.	107

5.3	Magnified image of top fracture surface. Perspective is indicated on left hand side. Several flaws, likely zipper cracks induced by grinding the notch, emanate from the fillet. Coarse hackle emanates from the zipper cracks and along the crack front in the direction of crack propagation. The orientation of the hackle indicated that the crack front varied through the thickness of CMC, favoring left hand side (unimaged side) over the right hand side (painted and imaged side). 108
5.4	Features resembling zipper cracks located beneath a machining groove that resulted from grinding. Solid black arrows depict semi-elliptical cracks that initiate from the zipper-crack like features. Coarse hackle is present all the way up to the zipper cracks. Bright white features are fracture debris. Note the presence of one of several machining grooves that result from grinding a notch with a diamond saw. 109
5.5	Image of bottom section of fracture surface in the vicinity of the notch. Features that resemble zipper cracks and the hackle that originates from these features are indicated by black arrows. 109
5.6	Stepped surface of region where crack path transitions to an orientation normal to the loading direction. Inset at the top-left is a longitudinal strain field with a black arrow indicating the transition region. Features that resemble arrest lines are depicted with black dotted arrows. Note: this micrograph depicts the surface opposite of that on which the DIC deformation field (inset) was captured; the crack propagates from right to left. 110
5.7	Semi-circular deviation in crack path is preceded by features that resemble arrest lines. Black arrow in longitudinal strain field (inset top-right) points to DIC data corresponding to deviation in crack path. Orientation of arrest lines suggests that crack temporarily arrested at deviation while crack front near painted (imaged for DIC) surface was allowed to catch up with rear surface. Twist hackle ('tails' in wake of crack path at fibers) indicate that the crack front re-oriens itself after passing the deviation. 112
5.8	SEM micrographs of crack propagation from notch and fracture surface at notch for in-SEM testing of (a) cross-ply laminate tested at ambient temperature and (b) cross-ply laminate tested at 795 °C. Fiber pullout is evident in the longitudinal laminas with pullout lengths ranging from microns to hundreds of microns. ... 113
5.9	SEM micrographs of (a) crack propagation path on surface and (b) fracture surface of a cross-ply laminate tested at 795 °C in a SEM. Fiber pullout is evident in the longitudinal laminas. Pullout lengths range from several microns to several millimeters. 114

5.10	Example of subsurface damage likely induced by machining with diamond saw. On left, jagged features emanate from fillet of edge notch in a unidirectional laminate. On right, mating surface shows semi-elliptical cracks emanating from those same jagged features. 115
5.11	Additional examples of elliptical and circular cracks at notch tip (fillet) of longitudinal unidirectional tensile coupons. 116
5.12	Semi-elliptical and circular cracks emanating from notch tips in cross-ply laminates loaded in tension in an SEM at (a) ambient temperature and (b) 795 °C. In both (a) and (b), the cracks lie beneath machining grooves induced by cutting the notch with a diamond saw blade. 117
5.13	Fractograph of final fracture in single edge notched cross-ply laminate loaded in uniaxial tension. Inset is a longitudinal strain field measured with DIC. Cracks on the front and rear surfaces of the tensile coupon propagated at opposite angles with respect to the loading axis. Fracture observations from DIC must be interpreted with caution as they do not necessarily reflect subsurface behavior. Note that the front face of the fracture slopes upward while the back face slopes downward. 118
5.14	Fractograph of crack propagation in longitudinal unidirectional laminate and corresponding longitudinal strain field measured with DIC. Direction of crack propagation below the surface deviates locally from that at the surface. Additionally, matrix cracks propagate in the loading direction. 119
5.15	Examples of crack propagation along multiple planes in longitudinal unidirectional tensile specimens. In (a), fractures propagate along planes that originate at or near the notch tip and within each of the longitudinal plies. Arrows point towards source of crack initiation as indicated by the observed hackle/mist patterns. In (b) a matrix crack propagates along a plane that originates at the notch tip as well as along another plane within a large pool of free silicon. Full-field deformation measurements at the surface cannot detect the subsurface deviations from the initial propagation path. 120
5.16	Hackle markings in the SiC matrix of a longitudinal unidirectional CMC indicate a new fracture surface originated in the longitudinal lamina. 121
5.17	Apparent crack initiation in longitudinal laminas of a cross-ply ([0/90/0/90] _s) CMC loaded in uniaxial tension at 795 °C. In (a), a hackle emanates from longitudinal fibers adjacent to a transverse lamina. In (b), hackle emanates from longitudinal fibers adjacent to matrix-rich region. 122

5.18	Micrograph of fracture surface in transverse unidirectional laminate loaded in tension in longitudinal direction. Hackle points towards potential source of crack initiation, which is flaw at matrix-coating interface. Wallner lines can be observed beyond hackle and coincide with regions of spalling in coatings of fibers that bound the matrix. 123
5.19	Nanoindent location in a cross-ply CMC matrix. In (a), the average elastic modulus measured from six indents was 330 GPa with the lowest modulus (290 GPa) at the indent nearest a fiber. In (b), moduli were measured in the matrix region along the perimeter of a fiber. The average modulus was 355 GPa with the lowest measurement (300 GPa) again located nearest the fiber. 124
5.20	Wake hackle on the fracture surface of a longitudinal unidirectional laminate that failed in tension. The orientation of the tails of several hackle markings (circled in white) mimic the undulations in the distribution of longitudinal fibers. This suggests that the arrangement of fibers may influence the orientation of the crack front during propagation. 125
6.1	Experimental set-up for in-situ testing in the SEM. In (a), a CMC tensile coupon is mounted in the grips of a miniature load frame that is attached to a door-mounted stage. The grips are rotated 90 degrees to image the edge of the test coupon. In (b), the entire load frame is enclosed in the SEM. 131
6.2	SEM micrographs of transverse fibers captured along the edge of a [0/90/0/90] _s SiC/SiC CMC loaded in tension. Gold NP agglomerates covering the fibers permit measurement of full-field deformations using DIC. A larger scale micrograph of the cross-ply CMC depicts several longitudinal (0) and transverse (90) lamina. 133
6.3	Full-field maximum principal strains overlaid on SEM images of transverse fibers at three load increments for a CMC loaded in tension. Frames (1) through (3) are below the proportional limit. Strains localize in regions of fiber coatings oriented along the loading axis, which is vertical in the plane of the page. 135
6.4	Full-field maximum principal strains overlaid on SEM images of transverse fibers at four load increments for a CMC loaded in tension. Frames (1) through (3) are below the proportional limit. Strains localize in regions of fiber coatings oriented along the loading axis. Frame (4) is captured after an unexpected drop in load that was likely due to cracking remote from the FOV. Localized strains in several adjacent fibers converge into a band of localized strain that is likely a matrix crack. The applied stress has been normalized to the PL stress. 136

6.5	Comparison of full-field strains in transverse lamina of as-received and annealed CMCs loaded in tension at 150 MPa. Both examples exhibit widespread (several fibers) strain localization in the fiber coatings. Strain localization is prominent in regions of the coatings aligned with the loading axis as well as in fibers in contact. 138
6.6	Crack openings (as measured using virtual extensometers and DIC data) across the fiber-coating-matrix interface for SiC/SiC CMC loaded to failure in tension. In (a), crack openings are larger for extensometers oriented in the loading direction (vertical in the plane of the page). In (b), crack openings are largest for extensometers bridging fibers in contact and for extensometers oriented nearest the loading direction. At their greatest, crack openings are on the order of tens of nanometers. 139
6.7	Strain maps are plotted on micrographs for two-minute tensile dwell fatigue cycles above proportional limit (PL). Above: fibers are sampled from a transverse ply; below: fibers are sampled from a longitudinal ply after (a) 10 cycles, (b) 10 cycles unloaded, (c) 20 cycles and (d) 50 cycles. After 20 cycles, there is no apparent increase in the intensity and dispersion of the strain localization. Upon unloading after 10 cycles, there was residual damage at the fiber-coating interface. 140
6.8	Full-field strains collected from various areas of interests along the edges of tensile coupons during dwell fatigue for an as-received (top) and annealed (bottom) CMC. Images captured after 40 two-minute dwell cycles at 150 MPa. Damage, as indicated by strain localizations, appears more widespread in the annealed sample than in the as-received sample; however, this may be noise in the DIC data that manifested as an artifact of charging in the SEM for the heavily-oxidized annealed coupon. 141
6.9	Load-drop during dwell cycles for as-received and annealed CMCs. Samples exhibit similar behavior: load drop approaches a minimum value of about 0.75 MPa after 30 cycles of tensile dwell fatigue. 142
6.10	Damage evolution as depicted in longitudinal strain fields sampled along the edge of a notched tensile coupon. Micrographs depict the edge opposite of the notched edge. Numbered locations in stress-strain space of (a) correspond to frames in (b). Despite an increase in global applied stress between the second and third frame, the matrix crack at the lower-left of each from relaxes as the matrix crack at the upper-right evolves. 143
6.11	Longitudinal strain fields emphasizing the significance of scale in analyses of damage evolution in CMCs. Panels sequence indicates crack growth from left to

	right. The strains in (a) have been filtered more aggressively ($> 4x$) than those in (b) at the expense of spatial resolution. As a result of the effectively smaller length scale in (b), fine cracks originating at the notch are detectable.	144
6.12	Longitudinal strain fields of matrix cracks propagating through the outer longitudinal lamina of cross-ply CMC. In (a) the matrix crack deflects along longitudinal fibers as it traverses the lamina. In (b), a second matrix cracks emerges at the surface of the longitudinal lamina. An advantage of lamina-scale experimentation is that it can detect fine matrix cracks in the early stages of their evolution.	145
6.13	Longitudinal strain fields at multiple length scales at applied stresses near the tensile strength. Loading is vertical in the plane of the page. Frames (a) and (b) depict crack accumulation at the laminate length scale in a finite width coupon (a) and an edge-notched coupon (b). The smallest resolvable crack spacing at the macroscale was 400 microns (a). The finite width coupon had a greater crack density than the notched coupon. The higher resolution deformation field of (c) shows that crack spacing can be as small as 180 microns.	146
6.14	Velocity of a matrix crack that initiates from a notch in a cross-ply CMC. Inset at upper-right is a longitudinal strain field captured just prior to final fracture. Crack speed varies during propagation. Initial propagation is slow (0.007 m/s). The crack then pauses and shifts left before continuing slow propagation (0.001 m/s). Velocity increases by several orders of magnitude at final fracture.	148
6.15	Evolution of damage in cross-ply CMC under fully reversed cycle. Sample had previously undergone 40 cycles of tensile dwell fatigue at an applied stress that near the upper bound of PL stress range. Macroscale detection of matrix cracks does not occur until well above the dwell stress.	149
6.16	Matrix cracks in smooth bar samples do not always evolve as continuous cracks that span the gage section, leaving fully bridged fibers in their wake. For example, damage evolution is shown as applied stress approaches fracture stress. Sample had previously undergone 40 cycles of tensile dwell fatigue as well as a fully reversed compression-tension cycle. Matrix cracks manifest at the surface of the coupon at three distinct locations (indicated by black arrows). The strain localizations at each arrow broaden with applied stress, ultimately forming a band of localized strain.	150
6.17	Initiation of angled cracks from notch tips of three different samples. The notches in (a) and (b) were cut perpendicular to the loading axis (which is vertical in the plane of the page). The former was shorter than the latter. The notch in (c) was cut at angle 15° clockwise from horizontal.	151

6.18	Comparison of damage evolution as-observed at microscopic and macroscopic length scales at the dwell stress. On the left is a macroscale deformation field along the edge of a cross-ply tensile. On the right are four microscale deformation fields corresponding to the positions (solid black boxes) on the macroscale field. The underlying structure of the laminate is indicated in the micrograph on the right. Macroscale measurements to do not capture damage in the microstructural constituents. 153
6.19	Macroscale view of damage progression along the edge of the annealed CMC tensile coupon. CMC previously underwent 40 cycles of dwell fatigue at σ_{dwell} . The solid black boxes correspond to locations where microscale the fields of view in Figure 6.19. From the macroscale perspective, cracks initiate in right half of the laminate and propagate towards the left half. Of the four microscale FOVs, only two reside near a macroscale crack. This implies damage in coatings detected at the microscale at low stress does not always evolve into large matrix cracks detectable at the macroscale. 155
6.A1	Crack openings (as measured using virtual extensometers and DIC data) across the fiber-coating-matrix interface for SiC/SiC CMC loaded to failure in tension. Extension is plotted as a function of applied stress for the extensometers highlighted in yellow. Extensometers oriented along the loading axis (1a and 1b) exhibit positive extensions; those oriented along or nearly along the transverse axis (1c and 1d) experience compressive extension. 160
6.A2	Crack openings (as measured using virtual extensometers and DIC data) across the fiber-coating-matrix interface for SiC/SiC CMC loaded to failure in tension. Extension is positive for extensometers oriented along or nearly along the loading axis (2b and 2c). Extension is negligible for the extensometer oriented in the transverse direction (2a). 161
6.A3	Crack openings (as measured using virtual extensometers and DIC data) across the fiber-coating-matrix interface for SiC/SiC CMC loaded to failure in tension. Extension is positive for extensometers oriented along the loading axis (3b and 3e). Extension is compressive for extensometers oriented in the transverse direction (3a, 3c, 3d and 3f). 161

List of Abbreviations

AOI Area of Interest

Au Gold

BSE Back-scatter Electron

CCD Charge-Coupled Device

CMC Ceramic Matrix Composite

COD Crack Opening Displacement

CT Compact Tension or Computed Tomography

DCB Double-cantilever Beam

DIC Digital Image Correlation

E-beam Electron Beam

FOV Field of View

IPA Isopropyl Alcohol

LHS Left Hand Side

LVDT Linear Variable Differential Transformer

NN Nearest Neighbor

NP Nanoparticle

PCA Principle Components Analysis

PL Proportional Limit

PMMA poly(methyl methacrylate)

R-curve Resistance Curve

RHS Right Hand Side

RMS Root Mean Square

SD Standard Deviation

SE Secondary Electron

SEM Scanning Electron Microscope

SiC Silicon Carbide

Ti Titanium

VIF Variance Inflation Factor

WC Tungsten Carbide

CHAPTER I

Introduction

The objective of this research was to characterize damage progression – from crack initiation to final failure – in ceramic matrix composites (CMCs) by addressing (1) when (with respect to stress-strain behavior) and where (with respect to microstructure) cracks initiate; (2) the influence of microstructural parameters on crack propagation and accumulation; and (3) the appropriate characterization of toughness in these materials. Since damage in CMCs evolves in stages spanning several length scales, a multi-scale approach was adopted. Scanning electron microscopy was used to investigate crack initiation and propagation at microscopic length scales during the early stages of damage. Macroscopic imaging was used to investigate crack accumulation at large length scales during the latter stages of crack propagation. Each length scale revealed unique information about damage evolution, demonstrating the critical need for multi-scaling in a comprehensive damage analysis.

1.1 Ceramic Matrix Composites

A ceramic matrix composite (CMC) is a combination of a ceramic material (matrix) with a reinforcing phase, which is often another ceramic. The reinforcing phase can vary by geometry: examples are short fiber, whisker, and particulate. The matrix phase can vary by microstructure: examples are fully dense or intentionally porous. Both phases may vary by chemical composition/structure; oxide ceramic, non-oxide ceramic and glass are common CMC

components. The combination of parameters utilized – geometry, microstructure, and chemical composition – is driven by the engineering application of the composite. For example, continuous fiber reinforcements are impractical for applications that require small, complex shapes. This research is concerned only with CMCs reinforced with long, continuous ceramic fibers for use in high-temperature, structural applications. The material investigated was composed of silicon carbide (SiC) fibers coated with a boron nitride (BN) based interphase and immersed in a melt-infiltrated silicon/silicon carbide matrix. For brevity, they are referred to as SiC/SiC CMCs.

Continuous fiber CMCs are desirable for high-temperature, structural applications because they possess excellent thermal properties (high-melting temperature, low thermal expansion) and respectable mechanical properties (high strength, high toughness). These properties may seem counterintuitive, as CMCs are composed of brittle monolithic ceramics with stochastic tensile strengths. A monolithic ceramic test specimen under a tensile load will fail when a sufficiently large flaw initiates a crack that unstably propagates through the gage section. Unlike monolithic ceramics, however, damage and failure in continuous fiber CMCs do not result from the propagation of a single crack. Instead, small cracks initiate throughout the matrix because shear at the fiber-matrix interface facilitates the transmission of applied load to the fibers. In the vicinity of a matrix crack, load is shed from the matrix to the fiber. Each crack grows stably until the matrix is saturated and no more matrix cracks develop. Because cracks flood the matrix prior to failure, a CMC can exhibit nominal strains that are orders of magnitude larger than its monolithic counterpart and, like a metal, it can exhibit non-linear deformation and non-catastrophic failure.

The high toughness and non-linear deformation of continuous fiber CMCs result from a weakly bonded fiber-matrix interface. The fiber coating in the SiC/SiC system has a lower elastic modulus and lower tensile strength than both the fiber and matrix. This produces a weak fiber-matrix interface that encourages cracks to propagate around fibers rather than through them, a phenomenon called crack deflection. Crack deflection allows fibers in the wake of crack to remain intact and exert fiber bridging tractions that prevent the crack from growing unstably. Above and below the fracture plane, portions of the fiber-matrix interface debond; the length

over which the interface debonds is known as the debond length. As a fiber is stretched, portions along the debond length slide against the matrix, dissipating energy as a result of frictional shear.

Thus far two mechanisms of crack resistance have been discussed – crack deflection and frictional sliding. The toughness of CMCs is attributed to these mechanisms, as well as widespread cracking. This is best illustrated using the example of a unidirectional laminate loaded in tension with fibers oriented in the loading direction. As load is applied, the composite first deforms elastically, with deformation becoming non-linear at or after matrix crack initiation. Periodically spaced matrix cracks accumulate throughout the gage length of the laminate (generally oriented normal to the loading direction) up to a point of saturation, which is characterized by uniformly spaced matrix cracks. Fibers eventually fracture with continued loading; the distance between the fiber fracture location and the nearest crack plane is called the pullout length. Frictional sliding along this length dissipates energy, allowing for graceful failure.

1.2 Background and Motivation for Damage Characterization

At the present time, CMCs are ending a decades-long period of development and entering an ambitious new phase of application in commercial gas-turbine engines. Understandably, CMC manufacturers are protective of the innovative techniques they have developed to process and characterize (chemically and mechanically) these materials. It is for this reason that quantitative information and discussions of material processing and composition cannot be presented in this dissertation. General discussions of processing of SiC/SiC CMCs can be found in [1-4]. A review of early work characterizing damage and toughness in CMCs is discussed in the chapters that follow. Here I present a brief review of recent studies of melt-infiltrated SiC/SiC ceramic matrix composites and discuss the importance of understanding damage mechanisms in these materials.

The material investigated was a melt-infiltrated (MI) SiC/SiC composite composed of SiC fibers, coated with boron nitride and embedded in a siliconized SiC matrix. In the melt-infiltration process, a fiber preform is immersed in liquefied silicon, which reacts with carbon and organic binders in the preform to create a Si-SiC matrix. There are two methods of creating melt-infiltrated SiC/SiC CMCs, referred to in literature as *prepreg* and *slurry casting*. In prepreg

CMCs, SiC fibers are coated with BN via chemical vapor deposition, then run through a matrix slurry containing SiC, carbon, binders and solvents, before being wound into unidirectional preform tapes [1]. The tapes can be stacked to form a desired laminate architecture before being densified through infiltration of molten silicon. The silicon reacts with carbon in the preform to form a Si-SiC matrix. Slurry casting, on the other hand, involves infiltration of woven fiber preforms. Fibers in contact can fail simultaneously under load, weakening the composite. The prepreg method results in a more uniform distribution of fibers and a composite that exhibits comparable tensile strength as a slurry cast composite but with much fewer fibers, making it the more desirable method [1-2]. Further information on the two processes and mechanical performance of the two types of CMCs can be found in [1].

The fiber coating, or interphase, greatly influences the strength and toughness of the composite. Not only does the BN coating permit matrix crack deflection, which activates energy dissipating mechanisms that toughen the ceramic matrix, but it protects the fiber from chemical attack both during processing and when thermomechanically loaded in hot and humid environments [2]. If combustion gases penetrate the coating through a matrix crack, the SiC fiber may form a performance-degrading silica layer that can cause the fiber to chemically bond to the matrix [5] such that it can no longer deflect matrix cracks. Similarly, fibers in close contact may bond to each other if the coating that separates them reacts with oxygen to create liquid boria, resulting in simultaneous (rather than sequential) failure of both fibers [5]. Thus, the BN coatings provide protective barriers that can delay fiber attack. Furthermore, it has been shown that debonding at the coating-matrix interface leads to higher ultimate tensile strengths, higher failure strains and longer stress-rupture times [5-6]. For these reasons, debonding of the coating-matrix interface is preferred over debonding of the fiber-coating interface. Clearly the coating serves a vital role in toughening fibrous SiC/SiC CMCs. Consequently, investigation of damage evolution in coatings is a major component of this dissertation.

In addition to energy dissipating effects along the fiber-matrix interface, fibrous CMCs exhibit tough, non-linear loading as a result of matrix crack accumulation. Understanding when and where matrix cracks initiate is critical to characterize damage evolution in an oxidizing combustion environment. Matrix cracks introduce pathways for oxygen to diffuse into the composite's interior, which cause strength degradation [7-8]. Acoustic emission techniques have

been used to identify when cracks develop with respect to the state of stress in the material [7-9]. It was found that matrix cracks initiated in transverse lamina and unreinforced matrix regions of woven MI SiC/SiC CMCs [7]. Although dependent on composite architecture, interfacial shear stress, and elastic modulus, crack initiation (as detected by acoustic events) fell within a global strain range of about 500 to 1000 $\mu\epsilon$ [7]. These findings suggest the load-bearing longitudinal fibers are protected from oxygen ingress in the early stages of loading. A similar acoustic emission study of woven MI SiC/SiC CMCs demonstrated that crack behavior varies with stress; microcracking dominates at low stresses (beginning with crack initiation in transverse plies occurring around 75 MPa) whereas through-thickness matrix cracks dominate at higher stresses (above the deviation from linearity in stress-strain curves) [8].

The SiC/SiC system is a prime candidate for gas-turbine engine applications because it is lightweight, low porosity, strong at high temperature, tough, has low thermal expansion, is a good heat conductor, and is stable at high temperatures [1-2]. Furthermore, it has good shock, creep and oxidation resistance relative to other CMCs [1]. Their effectiveness as hot-section gas-turbine engine components has been demonstrated in several studies [10-12]. It is well-established that SiC/SiC CMCs are damage tolerant and exhibit graceful failure [2]; however, more comprehensive damage characterization is necessary to ensure that the material will safely perform under rigorous design specifications. While damage analyses of continuous fiber composites have been conducted for several decades [13-20], some of these analyses have been devoted to investigations of damage at the constituent length scale [18-20], but none have comprehensively characterized damage with sub-micron spatial resolution. Acoustic emission tests [7-9] can determine when matrix cracks initiate with respect to stress-strain behavior; however, they cannot pinpoint crack location with spatial resolution fine enough to detect damage in individual constituents. Acrylic replica testing [18] can detect positions of cracks on the surface of the material, but its ability to identify fine cracks at stresses well below the proportional limit (PL) is questionable (note that the proportional limit is defined in this work as the stress at which strain deviates from linear loading by 0.005%). It also requires that loading be temporarily interrupted as the replica cures, and thus cannot capture dynamic crack behavior. To the best of our knowledge, neither acoustic emission nor acrylic replica testing has been able to identify damage in coatings at low stresses. More sophisticated techniques are necessary to

determine when and where damage initiates and how it evolves during thermomechanical loading.

Full-field deformation measurement techniques, such as digital image correlation (DIC), provide a reliable means of measuring damage at multiple length scales. DIC is length scale independent, meaning that sub-micron damage can be detected if images are captured at a sufficiently high magnification (as in scanning electron microscopy). Interrupted loading is necessary at microscopic length scales because of the raster-scan nature of electron microscopy, making it impossible to capture real-time crack advance. However, dynamic crack propagation and damage accumulation can be captured with DIC at larger length scales. This provides the capability to comprehensively characterize damage at all stages of evolution.

This thesis investigates damage evolution at multiple length scales: constituent, lamina and laminate. Scanning electron microscopy and DIC are used to characterize crack initiation and propagation at the constituent and lamina length scales. Since the SiC/SiC CMCs are intended for use in ambient and high temperature environments, damage is investigated at ambient temperature and at 795° C. Damage is also investigated at the macroscale using digital cameras and lenses, with a focus on characterizing crack accumulation at and above the proportional limit. Damage behavior observed at each length scale is compared and contrasted.

1.3 Organization

Chapter II discusses techniques used to create DIC tracking patterns that maintain fidelity under thermo-mechanical loading. Chapter III examines toughening mechanisms in notched CMCs loaded in tension at 795°C. It addresses the challenges of in-SEM testing at elevated temperatures and the special considerations that need to be taken when interpreting DIC data from CMCs. Chapter IV presents a method of numerically computing toughness in CMCs using the J-integral. Techniques for reducing the impact of data variability on measurements of J are discussed. Traction-separation laws for unidirectional and cross-ply laminates are generated from J-derived resistance curves. Chapter V combines surface DIC data with post-test fractography to gain a three-dimensional perspective of crack behavior and identify factors that promote local crack initiation and propagation. Chapter VI examines damage evolution at the microscale and macroscale. It compares and contrasts the capabilities and limitations of both length scales and

discusses the significance of multi-scale analyses in characterizing damage in CMCs. Chapter VII summarizes significant findings and suggests ways to improve multi-scale experimental damage analyses.

References

1. K. L. Luthra and G. S. Corman, “Melt Infiltrated (MI) SiC/SiC Composites for Gas Turbine Applications,” in *High Temperature Ceramic Matrix Composites*, Wiley (2001).
2. G. S. Corman and K. L. Luthra, “Silicon Melt Infiltrated Ceramic Composites (HiPerComp™),” in *Handbook of Ceramic Composites*, Kluwer Academic Publishers, Boston (2004).
3. G. S. Corman, K. L. Luthra, and M. K. Brun, “Silicon Melt Infiltrated Ceramic Composites – Processes and Properties,” in *Progress In Ceramic Gas Turbine Development, Vol. II, Ceramic Gas Turbine Component Development and Evolution, Fabrication, NDE, Testing and Life Prediction*, ASME Press, New York, (2003).
4. K. L. Luthra, R. N. Singh, and M. K. Brun, “Toughened Silcomp Composites – Process and Preliminary Properties,” *Am. Ceram. Soc. Bull.*, **72** (7) 79–85 (1993).
5. J. A. DiCarlo, H-M. Yun, G. N. Morscher and R. T. Bhatt, “SiC/SiC Composites for 1200°C and Above,” in *Handbook of Ceramic Composites*, Kluwer Academic Publishers, Boston (2004).
6. G. N. Morscher, H-M. Yun, J. A. DiCarlo, and L. Thomas-Ogbuji, “Effect of a BN Interphase that Debonds Between the Interphase and the Matrix in SiC/SiC Composites,” *J. Am. Ceram. Soc.*, **87**, 104–112 (2004).
7. G. N. Morscher, “Stress-Dependent Matrix Cracking in 2D Woven SiC-fiber Reinforced Melt-Infiltrated SiC Matrix Composites,” *Comp. Sci. Tech.*, 64 [9] 1311-1319 (2004).
8. G. N. Morscher, J. Hurst and D. Brewer, “Intermediate-Temperature Stress Rupture of a Woven Hi-Nicalon, BN-Interphase, SiC-Matrix Composite in Air,” *J. Am. Ceram. Soc.*, **83** 1441–1449 (2000).
9. G. N. Morscher, “Modal Acoustic Emission of Damage Accumulation in a Woven SiC/SiC Composite,” *Comp. Sci. Tech.*, **59** 687-697 (1999).
10. A. J. Dean, G. S. Corman, B. Bagepalli, K. L. Luthra, P. S. DiMascio and R. M. Orenstein, “ASME Paper 99-GT-235,” *Proceedings of the ASME International Gas Turbine & Aeroengine Congress & Exhibition*, 1999.

11. G. S. Corman, A. J. Dean, S. Brabetz, M. K. Brun, K. L. Luthra, L. Tognarelli, and M. Pecchioli, "ASME paper 2000-GT-0638," *Proceedings of ASME Turbo Expo 2000*, May 8-11, 2000, Munich, Germany.
12. R. M. Orenstein, M. S. Schroder, G. S. Corman, and K. L. Luthra, *Proceedings of Power-Gen International 2000*, Nov. 14-16, 2000, Orlando, FL.
13. J. Aveston, A. Cooper and A. Kelly, "Single and Multiple Fracture: The Properties of Fiber Composites," *IPC Science and Technology Press*, 15-26 (1971). [Conference Proceedings]
14. J. Aveston and A. Kelly, "Theory of Multiple Fracture of Fibrous Composites," *J. Mater. Sci.*, **8** 352-362 (1973).
15. B. Budiansky, J. Hutchinson and A. Evans, "Matrix Fracture in Fiber Reinforced Ceramics," *J. Mech. Phys. Solids*, **34** [2] 167-189 (1986).
16. J. Solti, S. Mall and D. Robertson, "Modeling Damage in Unidirectional Ceramic Matrix Composites", *Comp. Sci. Tech.*, **54** 55-56 (1995).
17. D. Beyerle, S. Spearing, F. Zok and A. Evans, "Damage and Failure in Unidirectional Ceramic-Matrix Composites," *J. Am. Ceram. Soc.*, **75** [10] 19-25 (1992).
18. B. Sorenson and R. Evans, "Analysis of Damage in a Ceramic Matrix Composite," *Int. Journ. Dam. Mech.*, **2**, 246-271 (1993).
19. M. Walter and G. Ravichandran, "An Experimental Investigation of Damage Evolution in a Ceramic Matrix Composite," *J. Engin. Mater. Technol.*, **117**, 101-108 (1995).
20. J. Daniel and G. Anastassopoulos, "Failure Mechanisms and Damage Evolution in Crossply Ceramic Matrix Composites," *Int. J. Solids Structures*, **32** [3] 341-355 (1995).

Chapter II

Techniques for Generating Tracking Patterns for Digital Image Correlation at Microscopic Length Scale

2.1 Introduction

Work in this dissertation relied heavily on the use of digital image correlation for measuring full-field deformation in thermo-mechanically loaded ceramic matrix composites. Under large applied loads, elastic deformation in the stiff ceramic constituents was very small (failure strains in SiC can be below 1000 $\mu\epsilon$), so maximizing the spatial resolution of deformation measurements was a necessity. Since DIC is independent of length scale, nano-scale deformations could be measured so long as the speckles of the tracking pattern were sufficiently small; nanoparticle (NP) tracking patterns were developed for sub-micron measurements.

In addition to microscopic experimentation, macroscopic experimentation investigated widespread crack accumulation in CMCs. Nanoparticle speckles were unresolvable at macroscopic (> 1 mm) fields of view (FOV), so patterns were created with paint. The sections that follow discuss techniques for applying quality tracking patterns to mechanical test specimens at macroscopic length scales and microscopic length scales. Subsequent chapters address digital image correlation patterns; all were generated using the techniques described in Sections 2 and 3 of this chapter.

Digital image correlation is a non-contact method of measuring deformation fields (displacement, rotation and strain) on the surface of a material. It accomplishes this by tracking

deformation in fiducial markers applied to a region of interest on the material. This requires that images are captured before and after mechanically loading the material. If a single imaging sensor is used, only in-plane deformation can be measured. If two imaging sensors are used, out-of-plane deformation can be measured as well. A comprehensive review of the technique is provided in [1]. A brief discussion of DIC fundamentals is presented here to familiarize the reader with its capabilities and limitations.

DIC discretizes a digital image of a reference surface (captured prior to mechanical loading) into an array of square sub-images (or subsets), then uses an iterative algorithm to identify the equivalent sub-images in digital images captured during or after deformation. The subsets need to be unique, such that any given subset in the reference image corresponds to only one subset in the deformed image. This often requires a tracking (or speckle) pattern to be applied to the surface that is imaged. The speckle pattern must be isotropic (no preferred spatial orientation) and non-periodic to prevent erroneous image registration [1]. Furthermore, the dimensions of each subset must be large enough that it samples several unique speckles, and each speckle must be large enough that it samples enough image pixels to be distinguishable from other speckles [1, 2]. Speckles that contain too few pixels can introduce aliasing, which manifests as noise in the deformation fields that resembles Moiré patterns [2]. It has been shown that speckle patterns that produce the most accurate correlations generally require that each speckle encompasses three by three pixels of a pixelated image [3].

The image matching algorithm works by determining the rigid body displacements, rotations, and deformation gradients that minimize a normalized cross-correlation function [1]

$$\chi^2 = 1 - \frac{\Sigma FG}{\sqrt{F^2 G^2}} \quad (1)$$

where χ^2 is the cost function, F represents grey-scale intensities of the reference image and G represents grey-scale intensities of the deformed image. Under complex deformation, a subset in the deformed image can take on a significantly different shape than its equivalent subset in the reference image; hence, polynomial shape functions are used to characterize the grey-scale intensity patterns of each subset [1]. The shape functions are essentially low-pass filters of the underlying displacement fields; thus, spatial resolution is constrained by the size of the subset [1]. Speckle patterns that permit small subsets are necessary to maximize spatial resolution of the

deformation fields. In many cases, changes in lighting and environmental effects may alter the grey-scale intensities in the deformed images. Scanning electron microscope images, for example, may brighten from one image to another as a result of specimen charging or darken as volatilized organic contaminants deposit on the surface. In these cases, the zero-mean normalized sum of squared differences (ZNSSD) is used in lieu of the normalized cross-correlation function as it is insensitive to scaling or shifts in grey-scale values [1]:

$$\chi_{ZNSSD}^2 = 1 - \sum \left(\left(\frac{\sum \bar{F}_i \bar{G}_i}{\sum \bar{G}_i^2} G_i - \bar{G} \frac{\sum \bar{F}_i \bar{G}_i}{\sum \bar{G}_i^2} \right) - (F_i - \bar{F}) \right)^2 \quad (2)$$

The power of DIC is that it can resolve displacements with spatial resolution as low as 0.01 pixels [1]. To achieve sub-pixel accuracy, the cost function is evaluated at non-pixel locations, which requires interpolating grey-scale values between pixels [1]. Interpolation can introduce error in the form of bias [1, 4]. It has been found, however, that this error is small (as small as 1/200th of a pixel) for high-coefficient interpolation filters [1]. Gaussian noise in digital images also generates measurement bias; the magnitude of the error is dependent on the intensity of the noise [1, 2]. There exists a tradeoff between spatial resolution and accuracy; this tradeoff is regulated through optimization of DIC processing parameters (subset size, step size (i.e. the amount of subset overlap) and strain filters). Studies have shown that smaller subset sizes offer better spatial resolution but introduce more error while smaller step sizes also improve resolution but generate noise [3, 5]. Taking derivatives of noisy displacement data to obtain strain results in large strain errors. It has been shown that applying a strain filter 150% of the subset size offers an optimum value of spatial resolution and accuracy [3].

SEM images introduce additional sources of error, namely spatial and temporal distortion. Calibration techniques have been developed to identify and remove distortion associated with pixel drift from SEM raster scans and spatial distortion from the magnetic lenses [6-9]. The process of conducting DIC with SEM images has been termed SEM-DIC. With the exception of images collected at elevated temperatures (time at temperature did not permit collection of calibration images), distortion was removed using code developed in-house [9] or DIC software (VIC-2D) in the work presented throughout the dissertation.

A major challenge of using DIC to measure strain fields in stiff materials like SiC is distinguishing bias (Gaussian noise, interpolation bias and aliasing) from real deformation. For

DIC measurements on the stiff materials tested in this work, strain errors often fell within the range of $\pm 1000 \mu\epsilon$. Failure strains in monolithic ceramics like SiC fall within this noise window. At discontinuities in the material, DIC mistakenly reports unrealistically large strain magnitudes. For the case of cracks in stiff ceramics, DIC-measured strain in the vicinity of a crack faces may be orders of magnitude larger than the actual strain. The intensity of this strain error increases as the crack opening increases. The algorithm loses correlation in the vicinity of the crack faces if the crack opening grows too large. An example of a strain field in a CMC is provided in Figure 2.1. Strain magnitudes are color-coded; magenta indicates strain values around zero while red indicates strain values much larger than the fracture strain of monolithic SiC. In Figure 2.1 (a), the strain fields have been filtered to remove noise. In Figure 2.1 (b), a smaller strain filter is applied, increasing spatial resolution but introducing bias. The sections that follow discuss techniques to generate DIC speckle patterns that produce high spatial resolution measurements that minimize bias.

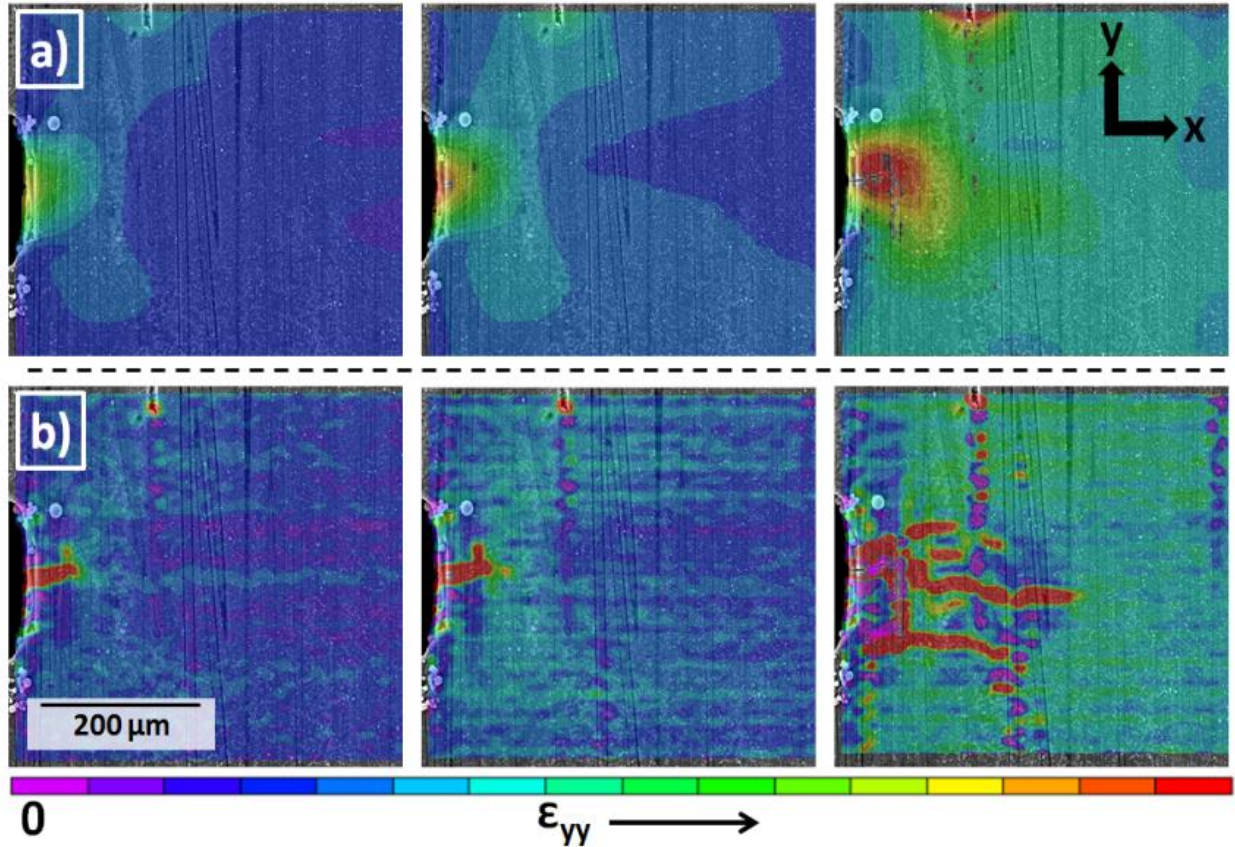


Figure 2.1 Longitudinal strain fields captured with DIC at the tip of an edge notch CMC tensile coupon loaded vertically in the plane of the page. Strain magnitudes are color-coded; magenta indicates strains at or around zero, while red indicates strains orders of magnitude larger than the fracture strain. In (a), the strain fields have been filtered to remove noise at the expense of significantly reducing spatial resolution. In (b), the strain filter has been reduced, which results in bias that manifests as localized fluctuations in color from blue to purple. Although noisier, the higher spatial resolution of (b) provides a more accurate depiction of damage behavior in the material.

2.2 Speckle Patterns for DIC at Macroscopic Length Scales

The macroscopic length scale was characterized as having a field of view larger than 1 mm. At this scale, quality tracking patterns were obtained with an airbrush and paint. To ensure accurate measurement and avoid systematic errors that can occur in DIC (e.g. aliasing [2]), patterns were used only when they met several constraints, many of which are well established in DIC literature [1-3]:

1. speckles diameters at least three image pixels in diameter (image resolution governed speckle size in physical space)

2. high contrast between speckles and background
3. random but uniform distribution of speckles
4. number of speckles per unit was high enough to use small DIC subsets, but low enough to provide high contrast under incandescent light

Regarding the fourth constraint, larger speckles generally required a larger subset size, which reduced spatial resolution of the deformation measurements. A major challenge of patterning was to obtain a pattern that provided the greatest spatial resolution (this was true irrespective of length scale) and still provided sufficient contrast while meeting the three-pixel rule.

Macoscopic speckle patterns were composed of black paint droplets (Golden Artist Colors, carbon black) on a white paint backdrop (Golden Artist Colors, titanium white). To ensure the speckles met the three-pixel criteria, they were measured using an optical microscope (Olympus BX51M) with an attached digital camera (Olympus UC50). *Note that the image resolution of the imaging device used for evaluating pattern quality must be the same as that used for experimentation.* Paint droplets often overlapped, producing larger paint agglomerates. This was desirable for DIC, as the imperfect shapes formed by overlapping droplets made subset recognition easier.

An Iwata Custom Micron-b airbrush was used to apply macroscopic patterns. For the smallest fields of view (1 mm), the black paint was diluted with a 1:1 ratio of distilled water and black paint; this was necessary to obtain small paint droplets (in physical space, droplets were between 10 and 50 μm in diameter). The paint brush was positioned perpendicular to the surface of the sample, 8 to 12 inches away. Air pressure was set to 60 psi and the flow rate was set to the lowest level (the flow rate knob was position half way between 0 and 1 on the Iwata Custom Micron-b). Figure 2.2 (a) shows an example pattern for an FOV slightly larger than 1 mm.

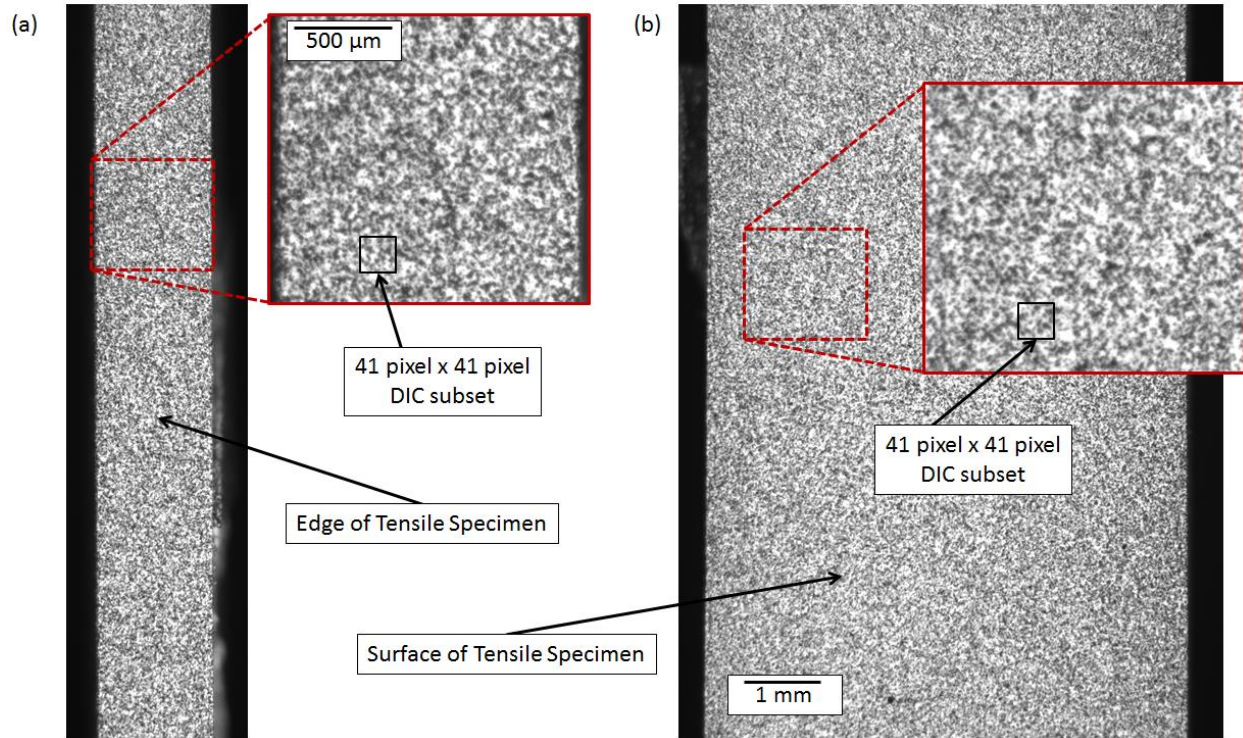


Figure 2.1 Speckle patterns for macroscopic DIC. Both patterns were created using paint and an airbrush. The black paint was dilute with water (1:1) to reduce speckle size. The FOV of (a) is smaller that of (b). For both patterns, the smallest attainable subset size was 41 x 41 pixels.

The paint did not require dilution for FOVs larger than 1 mm. The flow rate was increased (level 3 on the Iwata Custom Micron-b) and air pressure reduced (30 psi) to account for higher viscosity. Figure 2.2 (b) shows a pattern for an FOV several millimeters wide.

2.3 Speckle Patterns for DIC at Microscopic Length Scales

Patterns at microscopic length scales were designed exclusively for use in scanning electron microscope imagery; this encompassed fields of view below a millimeter. Digital Image Correlation, in conjunction with high-magnification images of CMCs loaded *in-situ* in an SEM, provided a means of measuring full-field strains and displacements in CMCs at spatial resolutions on order of their microstructure. High contrast, randomly dispersed, and isotropic tracking patterns were developed using three methods: (1) nanoparticle self-assembly, (2) nanoparticle (NP) drop casting, and (3) electron beam (e-beam) lithography. NP self-assembly was used for FOVs below 100 μm and when control of the pattern's location on the tensile

coupon was not a priority. NP drop casting was used for FOVs greater than 100 μm and when control of pattern location was a high priority (such as the tip of a notch).

Although a procedure for generating e-beam lithography patterns for FOVs below 100 μm was developed, e-beam patterns were not used in any mechanical tests because they were more costly and time consuming than NP patterning. However, the procedure is discussed because e-beam lithography may be the only possible way of developing very fine (FOVs less than 100 μm) patterns that maintain fidelity at high-temperature. Tungsten carbide nanopowder, for example, has a small thermal expansion coefficient and does not react with SiC carbide at temperatures above 800°C, making it excellent for high-temperature speckle patterns. However, it agglomerates too severely for small FOV patterns using the techniques discussed in this dissertation. E-beam lithography, which can create patterns with a wide range of high-temperature metals and ceramics, would then be necessary.

Surface finish greatly influenced the quality of the speckle patterns. NPs tended to agglomerate in scratches and other large defects, reducing the overall speckle density and introducing regions of sparse particle distribution as well as regions of severe agglomeration. E-beam patterns were particularly sensitive to surface topography; significant variations in topography resulted in incomplete or excessively dense patterns. Before patterning, the CMC surfaces were polished to sub-micron finishes. The specimens were first lapped with a 10 μm metal-bonded diamond disc (purchased from 3M) to remove large grooves. Then they were polished with 9, 3 and 1 μm diamond polishing pastes (Buehler MetaDi) on firm polishing cloths (Buehler TexMet) until a sub-micron finish was attained. Lapping pressures and times were in accordance with Buehler's polishing guide for CMCs [10].

2.3.1 Nanoparticle Deposition by Self-Assembly

NP self-assembly was the preferred deposition technique when uniform coverage of the entire gage section of a tensile coupon was required. Self-assembled patterns covered every surface of the coupon; however, the dispersion of particles was patchy – some patches were densely populated with particles, some were sparsely populated. This method guaranteed that a good pattern could be located somewhere on the coupon, but there was no guarantee that a good

pattern would assemble in a pre-determined location. If control of the pattern location is mandatory, drop casting is the better technique.

Silane patterning was conducted using a technique reported by Kammers [11]. After polishing, samples to be patterned were placed in an ultrasonic cleaner for 30 minutes to remove polishing residue; this was followed by rinses in methanol and deionized water. The samples were then immersed in a vial containing one part silane (3-mercaptopropyl)methyl)dimethoxysilane) and four parts methanol for 24 hours. Upon removal, they were rinsed in a bath of methanol that was agitated with a magnetic stir rod for 60 minutes (the bath was replaced with fresh methanol after 30 min) to remove excess silane. This was followed by an identical rinse using deionized water. The samples were then placed in a vial of nanoparticles (NP size depended on FOV; 40 nm Au colloid was used for 50 μm FOV). Functional groups in the silane attach to Au NPs, promoting self-assembly [12, 13]. After 24 hours, the samples were removed from the vial, rinsed with deionized water, and gently dried with low pressure air. The pattern density was inspected with an optical microscope. If the NP dispersion was sparse, the entire patterning process was repeated (minus ultrasonic cleaning) to increase the density of the pattern.

Figure 2.3 shows an example of a self-assembled NP pattern on a SiC/SiC CMC imaged under an optical and scanning electron microscopes. 40 nm Au nanoparticles were used to construct the 50 μm FOV pattern.

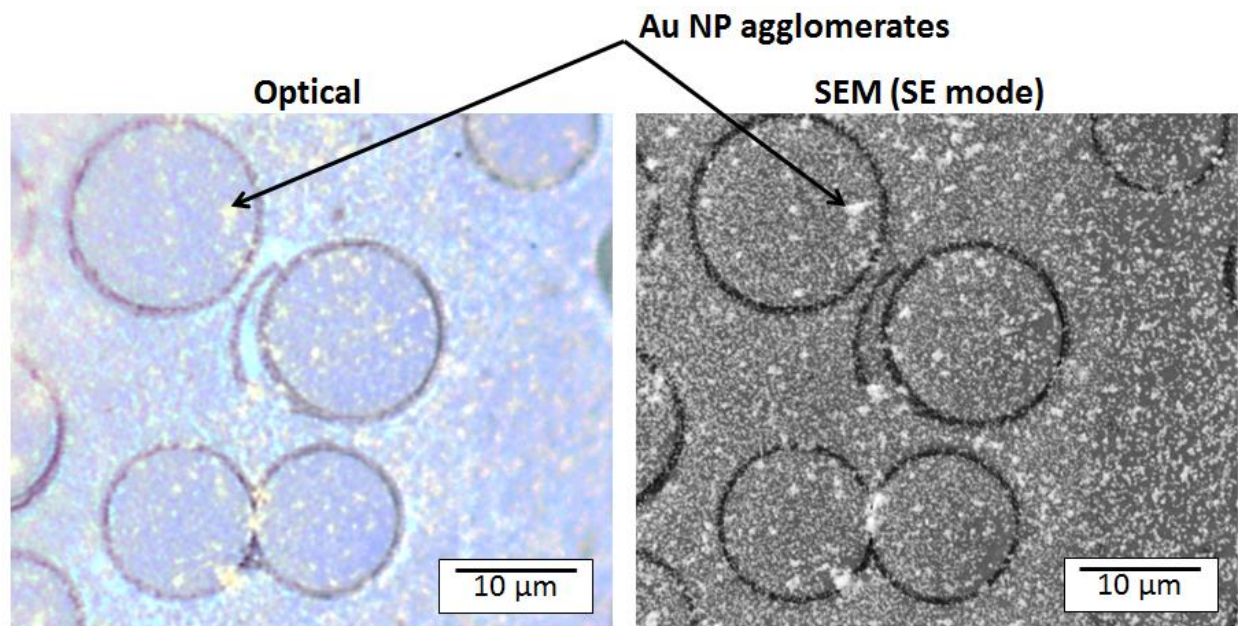


Figure 2.3 Self-assembled 40 nm Au speckle patterns applied to SiC/SiC CMC. 50 μm FOVs are shown for equivalent locations using optical microscopy and scanning electron microscopy in secondary electron mode. Arrows point to equivalent locations of an NP agglomerate.

2.3.2 Nanoparticle Deposition by Drop Casting

Drop casting was used when control of the location of the pattern was required, such as at the tips of edge-notches. The technique was adopted from work done by Kammers [14]. Drop cast patterns were generated by depositing small ($\sim 1\text{mm}$) beads of colloidal nanoparticles on the surface of a substrate using a micropipette (pipette sizes ranged from $0.5\ \mu\text{L}$ to $25\ \mu\text{L}$ depending on required surface coverage). This method was used for FOVs ranging from 250 to 500 μm and required larger NP colloids (100 to 150 nm). Figure 2.4 shows examples of Au NP drop cast patterns at high and low magnifications. Figure 2.4(a) was captured from the center of a drop cast pattern deposited on a SiC substrate. Figure 2.4(b) is a low magnification image of a pattern that was drop cast on the edge-notch of a SiC/SiC tensile coupon; it was designed for a 250 μm FOV.

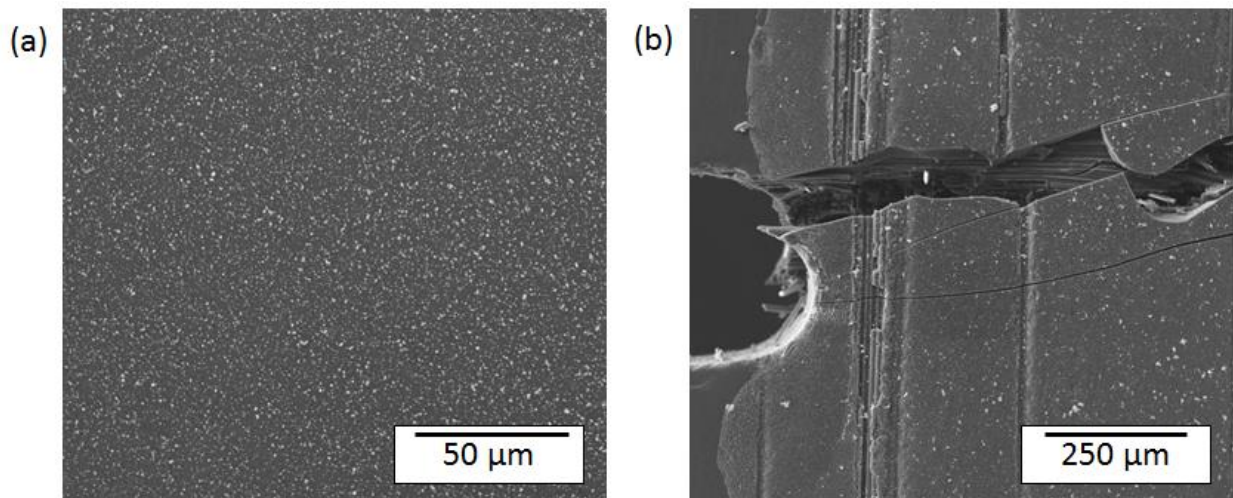


Figure 2.2 Drop cast Au (150 nm) speckle patterns deposited on SiC substrates. The image in (a) was captured at the interior of the pattern. A low-magnification image of a drop cast pattern surrounding an edge notch is shown in (b). Both patterns were designed for 250 μm FOVs.

The speckle patterns of Figure 2.4 have sufficient contrast, randomness, and uniformity for DIC. To get this uniformity, a dispersant was added to the NP suspension prior to drop casting. In the absence of a dispersant, the nanoparticles tend to migrate to the outer edge of the droplet (also known as the contact line), leaving a thick ring of nanoparticles at the boundary and a sparser distribution of particles in the interior. This phenomenon is known as the “coffee ring effect”, and has been attributed to capillary flows inside the droplet that are active during evaporation [15]. Agglomeration at the contact line was reduced by adding isopropyl alcohol (IPA) to the Au NP colloids (1:1 ratio of colloid and IPA). Two mechanisms were likely responsible for reducing the coffee ring effect: (1) IPA enhanced Marangoni flow in the evaporating droplet, which reduced capillary flow from the center of the droplet to the perimeter [15-19] and (2) the alcohol attached to NPs, acting as an intermediary to mitigate Coulombic interactions between adjacent particles [20]. Figure 2.5, shows two examples of agglomeration of Au NPs at the contact line of an evaporated droplet. The pattern densities in the center were reduced as a result of the coffee ring phenomenon.

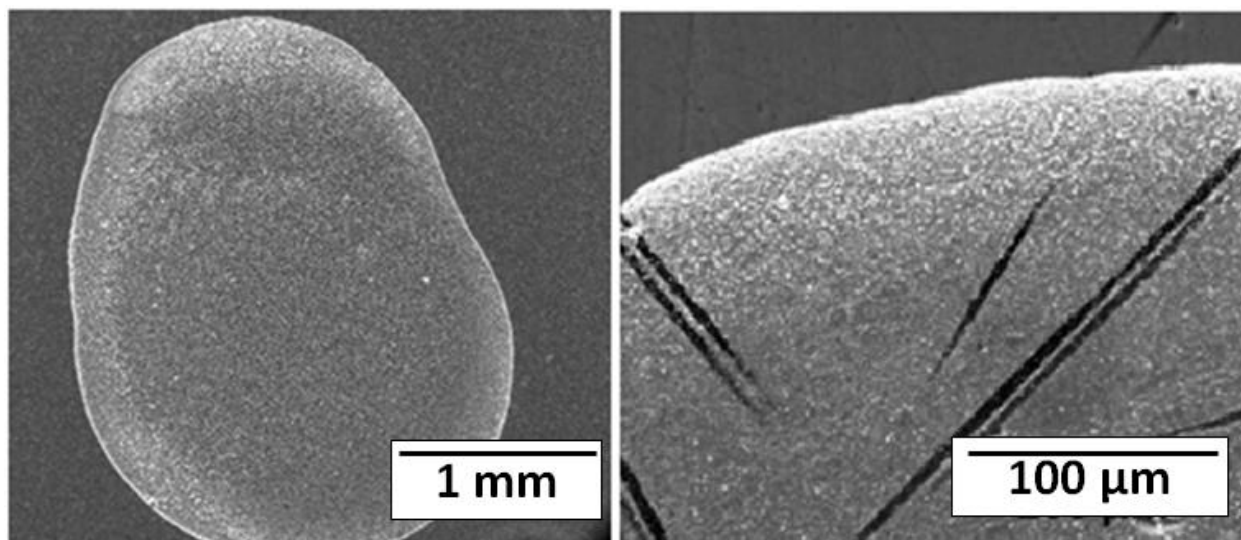


Figure 2.3 Coffee ring effect illustrated for Au NPs deposited on polished alumina (left) and polished SiC (right) substrates.

The Au NP patterning methods discussed up to this point were only practical for ambient temperature experiments. Experiments conducted at elevated temperatures required patterns that would maintain their fidelity up to 800°C; for these experiments, titanium and tungsten carbide (WC) speckle patterns were developed. Colloidal suspensions were created by mixing the 80 nm nanopowders in water. Because they were received as dry powder, the particles agglomerated severely when suspended in water. To reduce agglomeration, bicine (a pH buffer) was dissolved in the suspensions (22 mg of bicine and 3 mg of nanopowder in 1 ml of distilled water). The suspensions were then roll-milled for 24 hours at an intermediate speed. Patterns were drop cast immediately after milling using a 0.5 μL pipette. After the droplet evaporated (several minutes), the solidified bicine was burnt off by placing the substrate on a 300°C hot plate for several minutes. Figure 2.6 shows examples of high-temperature Ti and WC speckle patterns.

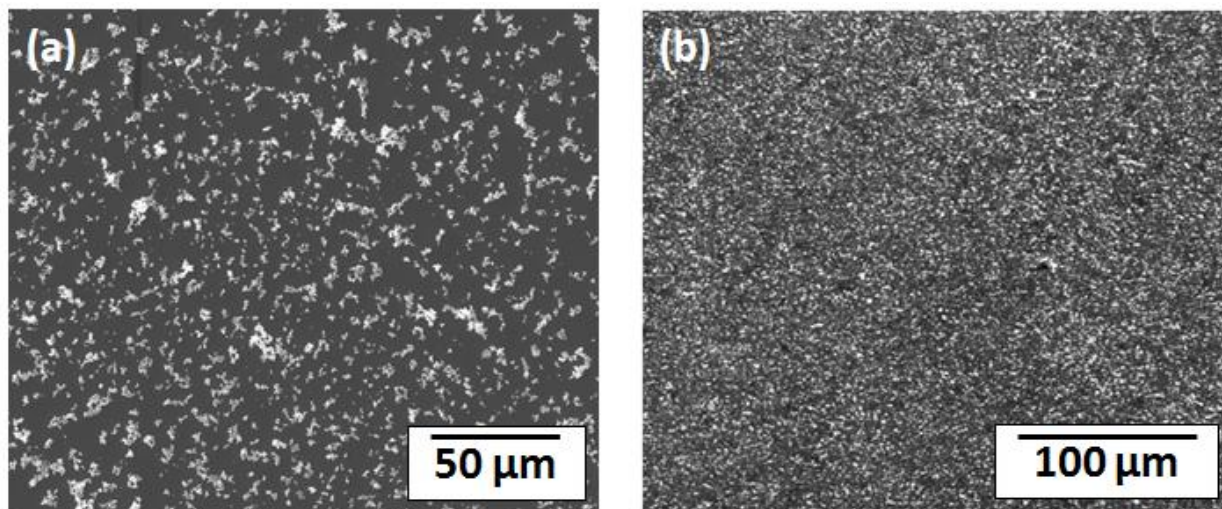


Figure 2.4 Drop cast high-temperature speckle patterns consisting of 80 nm (a) WC and (b) Ti nanopowder agglomerates. Roll milling and a pH buffer (bicine) prevented excessive agglomeration.

2.3.3 *Electron Beam Lithography*

The primary advantage of e-beam lithography over nanoparticle deposition is that it allows for total control of speckle size and distribution and can be scaled to accommodate various small-scale fields of view. Additionally, a large variety of materials (to include high-temperature metals and ceramics) can be used for patterning. FOVs beyond 100 μm , however, are both expensive and time consuming, making NP deposition a more practical alternative.

Electron beam lithography patterns were constructed with a Raith-150 e-beam system. A random speckle pattern was generated in MATLAB then imported into the e-beam computer. The lithography process involved exposing an image of the speckle pattern into a thin layer of poly(methyl methacrylate), or PMMA, which was spin coated on the surface of the substrate to be patterned. During the exposure process, speckle locations are bombarded with a flux of electrons that destroys chemical bonds in the PMMA. These areas preferentially dissolve when immersed in a chemical developer. The speckle pattern is essentially etched into the PMMA, leaving behind bare substrate upon which another material (e.g. Au, Ti, various ceramics) can be evaporated. The remaining unexposed PMMA was then dissolved in a solvent, leaving behind the speckle pattern. Figure 2.7 shows a magnified titanium e-beam pattern designed for a 50 μm FOV.

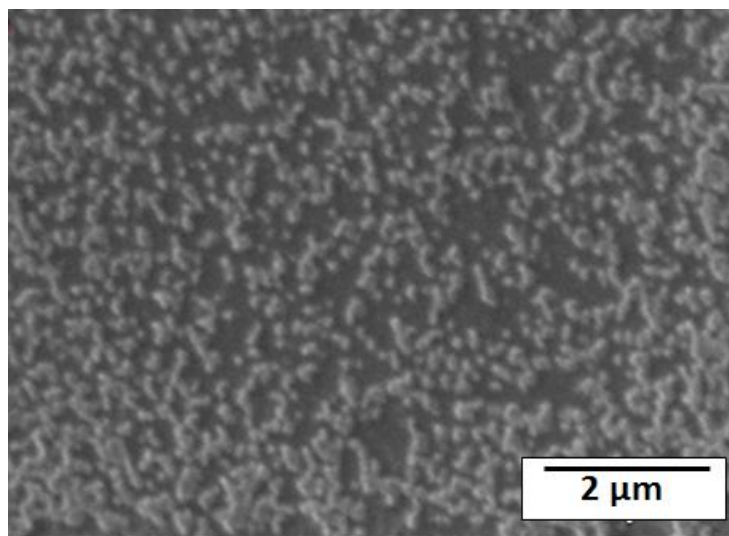


Figure 2.7 Titanium e-beam lithography pattern deposited on SiC. Pattern is of high contrast, randomly and uniformly distributed, and is reproducible.

2.4 Conclusion

Tracking patterns for digital image correlation were developed at multiple length scales. They contained speckles that were randomly and uniformly distributed and were of high contrast with the background. Patterns for fields of view larger than 1 mm were generated with paint and an airbrush. Paint viscosity, air pressure, and flow rate were varied to produce speckles for small and large macroscopic FOVs. Patterns for SEM imaging were generated using two nanoparticle deposition techniques: self-assembly and drop casting. NP self-assembly was used when very small FOVs ($<100\ \mu\text{m}$) were needed and when location of the pattern on the test coupon was not a concern. Drop casting was used for larger microscopic FOVs ($>100\ \mu\text{m}$) and when location of the pattern was a concern (e.g. patterning notch tips). Au nanoparticles were used for patterns intended for ambient temperature. Ti was used for high-temperature (800°C) patterning. Although they were not used in testing, WC patterns were designed for temperatures above 800°C . Due to uncontrollable agglomeration, the use of Ti and WC patterns was constrained to FOVs hundreds of microns wide. E-beam lithography was investigated as a method to produce very small FOV (below $100\ \mu\text{m}$) higher temperature speckle patterns. The patterns were nearly perfect in quality and were repeatable. Although lithography was capable of producing ambient temperature patterns as well, the cost and time to generate the patterns in comparison to the relative simplicity and low-cost of NP drop casting and NP self-assembly rendered it impractical.

References

1. M. Sutton, J. Orteu and H. Schreier, *Image Correlation for Shape, Motion and Deformation Measurements: Basic Concepts, Theory and Applications*, Springer, New York, NY, 2009.
2. Correlated Solutions, Advanced Bias, 2011; <http://correlatedsolutions.com/support/>
3. V. Rajan, M. Rossol, and F. Zok, "Optimization of Digital Image Correlation for High-resolution Strain Mapping of Ceramic Composites," *Exp. Mech.*, **52** 1407-1421 (2012).
4. X. Ke, H. Schreier, M. Sutton and Y. Wang, "Error Assessment in Stereo-based Deformation Measurements," *Exp. Mech.*, **51** 423-441 (2011).
5. H. Haddadi and S. Belhabib "Use of rigid-body motion for the investigation and estimation of the measurement errors related to digital image correlation technique," *Opt. Laser Eng.*, **46** 185-196 (2008).
6. M. A. Sutton, N. Li, D. Garcia, N. Cornille, J. Orteu, S. R. McNeill, H. W. Schreier, and X. Li, "Metrology in a Scanning Electron Microscope: Theoretical Developments and Experimental Validation," *Meas. Sci. Technol.*, **17** 2613-2622 (2006).
7. M. A. Sutton, N. Li, D. C. Joy, A. P. Reynolds, and X. Li, "Scanning Electron Microscopy for Quantitative Large Deformation Measurements Part I: SEM Imaging at Magnifications from 200 to 10,000," *Exp. Mech.*, **47** 775-787 (2007).
8. M. A. Sutton, N. Li, D. Garcia, N. Cornille, J. J. Orteu, S. R. McNeill, H. W. Schreier, A. P. Reynolds, and X. Li, "Scanning Electron Microscopy for Quantitative Large Deformation Measurements Part II: Experimental Validation for Magnifications from 200 to 10,000," *Exp. Mech.*, **47** 789-804 (2007).
9. A. D. Kammers and S. Daly, "Digital image correlation under scanning electron microscopy: Experimental methodology and validation," *Exp. Mech.*, **53** 1743-1761 (2013).
10. Buehler, Buehler Sum-Met – The Science Behind Materials Preparation, 2004; <https://shop.buehler.com/sites/default/files/resources/>
11. A. Kammers and S. Daly, "Self-Assembled Nanoparticle Surface Patterning for Improved Digital Image Correlation in a Scanning Electron Microscope," *Exp. Mech.*, **53** 1333-1341 (2013).
12. R. Freeman, et. al., "Self-assembled Metal Colloid Monolayers: An Approach to SERS Substrates," *Science*, **267** 1629–1632 (1995).

13. K. Grabar, R. Freeman, M. Hommer, and M. Natan, 1995, "Preparation and Characterization of Au Colloid Monolayers," *Anal. Chem.*, **67** 735–743 (1995).
14. A. Kammers and S. Daly, "Small-scale Patterning Methods for Digital Image Correlation Under Scanning Electron Microscopy," *Meas. Sci. Technol.*, **22** 125501 (2011).
15. R. Deegan, O. Bakajin, T. Dupont, G. Huber, S. Nagel and T. Witten, "Capillary flow as the cause of ring stains from dried liquid drops," *Nature*, **389** 827-829 (1997).
16. H. Hu and R. Larson, "Marangoni Effect Reverses Coffee-Ring Depositions," *Phys. Chem. B*, **110** 7090-7094 (2006).
17. B. Weon and J. Je, "Capillary force repels coffee-ring effect," *Phys. Rev. E*, **82** 1-4 (2010).
18. V. Nguyen and K. Stebe, "Patterning of Small Particles by a Surfactant-Enhanced Marangoni-Bénard Instability," *Phys. Rev. Lett.*, **88** [16] 1-4 (2002).
19. M. Maillard, L. Motte, A. Ngo and M. P. Pileni, "Rings and Hexagons Made of Nanocrystals: A Marangoni Effect," *J. Phys. Chem. B*, **104** 11871-11877 (2000).
20. O. Nayfeh, D. Antoniadis, K. Mantey, and M. Nayfeh, "Uniform Delivery of Silicon Nanoparticles on Device Quality Substrates Using Spin Coating from Isopropyl Alcohol Colloids," *Appl. Phys. Lett.*, **94** 1-3 (2009).

Chapter III

Constituent Level Characterization of Damage in Ceramic Matrix Composites at High Temperature

3.1 Introduction

The next generation of high-temperature ceramic composite materials for use in aerospace applications will experience more rigorous thermo-mechanical loading than their superalloy counterparts currently in service. Ceramic matrix composites (CMCs) are lighter than superalloys while maintaining their structural integrity at higher temperatures, qualities that are desirable for improving aircraft engine efficiency. The SiC/SiC materials system is relatively new; although there exist analytical and numerical models to predict its mechanical behavior at elevated temperature, experimental information is needed to validate these models. Unfortunately, grossly averaged macroscopic empirical data such as stress-strain curves alone do not fully explain the evolution of damage in composites. Advanced experimental techniques are needed for vigorous validation of current models and to better understand the mechanisms of damage and toughening. This chapter describes a novel approach to probe damage progression in CMCs at high temperatures and to lay a foundation for quantifying toughening mechanisms at the constituent scale for incorporation into damage models and product design.

3.2 Background

Several researchers have investigated the micromechanics of deformation and fracture in ceramic matrix composites. Marshall, Cox and Evans [1] attributed toughening in CMCs to regularly spaced matrix cracks bridged by uniaxially aligned fibers. They suggest that toughening during fracture is caused by debonding of the fiber-matrix interface followed by frictional sliding of the matrix over the debonded fiber during pullout. As a result, fiber bridging tractions act to reduce the displacement between the crack faces and thus stresses at the crack tip. They proposed strain energy and stress intensity based analytical models suggesting that the steady state cracking stress depends on the composite microstructure. Budiansky, Hutchinson and Evans [2] likewise proposed an analytical model for weakly bonded fiber-matrix interfaces that predicts a critical stress for cracking based on the debond lengths of fibers that have been subjected to matrix cracks; here, toughening is attributed to frictional resistance at the debonded interface. Zok [3] also suggested that toughening in CMCs can be attributed to fiber bridging tractions and fiber pullout, however, the degree of toughening is dependent on a characteristic bridging zone length behind the tip of a propagating crack. When the bridging fibers located furthest from the crack tip fracture, the degree of toughening has reached a maximum. From a micromechanics perspective, fracture resistance depends on frictional sliding resistance at the fiber-matrix interface as well as the length of the intact fiber [3]. Although severable reputable analytical models exist to explain toughening in CMCs, little is known about crack nucleation and propagation. Full-field deformation measurements at the constituent scale will elucidate composite behavior for a better quantitative understanding of damage onset in CMCs.

3.2.1 *Small-Scale Digital Image Correlation*

Recall from Chapter II that digital image correlation is a non-contact method of measuring full-field deformations on the surface of a material. This experimental approach measures the relative displacements between features in a tracking pattern applied to the surface of a test specimen. During thermo-mechanical loading, images of the tracking pattern are captured sequentially and deformation fields are then generated from these images using a subset-matching algorithm. Early work in DIC focused on optimizing its accuracy by removing the spatial distortions inherent in optical imaging equipment such as cameras [4-5]. Recently,

the development of methods for removing both spatial and temporal image distortions, coupled with advances in small-scale patterning, have expanded this approach to high magnification SEM imaging. For brevity, we refer the interested reader to [6-15] for details. The combination of SEM and DIC (termed here as SEM-DIC), with custom-developed patterning and distortion correction procedures, was used to investigate the small-scale mechanical behavior of a CMC.

SEM-DIC measurement accuracy strongly depends on the tracking pattern quality. Several studies have addressed methods of generating high-contrast, isotropic and randomly distributed patterns on the surface of various materials at microscopic and macroscopic length scales [4-5, 16-17]. A successful means for small-scale patterning utilizes the self-assembly of gold and silver nanoparticles [11, 15, 18-20]. However, these metals are not suitable patterning mediums at elevated temperatures because of their relatively low melting temperatures. Alternatively, electron beam lithography can produce adequate patterns using a variety of temperature resistant metals and ceramics [12]. However, e-beam patterning requires a perfectly flat surface and tends to produce repetitive or pseudo-repetitive patterns that are detrimental to correlation accuracy. Additionally, for fracture investigations, uncertainty in the crack propagation path requires that the tracking pattern cover a generous portion of the tensile coupon. Patterning large areas by electron beam lithography is time consuming and expensive, rendering this approach infeasible for fracture studies.

For high temperature studies, a good alternative to the aforementioned patterning techniques is nanopowder (NP) deposition. Materials such as titanium (Ti) and tungsten carbide (WC) have higher melting temperatures than gold and silver, making them preferable high-temperature patterning mediums. However, nanopowders naturally tend to aggregate both in powder form and in suspension. While a limited amount of short-range aggregation can be beneficial for patterning, to prevent excessive agglomeration the particles must be stabilized in a colloidal dispersion. Identifying dispersants, surfactants or stabilizers that minimize aggregation is critical. WC has been shown to form a stable colloid in water alone [21], but incorporation of dispersants or buffers can further reduce aggregation [22-25]. Mechanical milling (roll-milling and sonication) enhances the effectiveness of dispersants by breaking down large clumps and agglomerates.

The combination of scanning electron microscopy and digital image correlation, referred to here as SEM-DIC, was used to quantitatively characterize CMC deformation at the constituent length scale. SEM-DIC has limitations: currently it is constrained to 2-D deformation mapping and its fastest frame rates are orders of magnitude slower than optical instruments. Working within these limitations, it is a unique and powerful approach for investigating heterogeneous deformations in multi-phase material at the constituent length scale. This approach, introduced in 2007 [6-7], was recently used by researchers to probe microscale mechanical behavior in fiber-reinforced composites [10, 26]. In 2012, Canal et al. found that larger DIC subsets (~36% of fiber diameter) did not accurately capture the sharp displacement gradients that exist at the fiber-matrix interface as compared to smaller subsets (~18% of fiber diameter). At magnifications high enough that the subset size was below 20 percent of the fiber diameter, interface smoothing was sufficiently reduced such that the average strains computed in each constituent were qualitatively equivalent to what numerical models predicted; i.e., the average strains were smaller in transversely loaded fibers than in the matrix. However, the error between the finite element and DIC predictions was large (5700 $\mu\epsilon$ and 23700 $\mu\epsilon$ for the fiber and matrix respectively) [10]. For both large and small magnifications, average strains in the composite matched what the researchers expected (to within 300 $\mu\epsilon$) based on the applied stress and known elastic constants.

To date, DIC-characterization of CMCs has focused on either ambient temperature studies or studies conducted at elevated temperatures but at macroscopic fields of view [16-17]. In conducting a review of DIC measurement error on CMCs at macroscopic length scales, Rajan et al. [16] identified optimized subset sizes and strain-filter lengths for minimizing displacement and strain error. Utilizing SEM-DIC on ceramic composites in order to characterize deformations at the constituent length scale presents new and complex challenges. These stem from the fact that as the field of view decreases, it encompasses a lower density of matrix cracks. Portions of the field of view (FOV) that fall outside of the process zone of a crack contain only elastic deformations. The elastic strains in ceramics are low enough that noise and bias induced error can mask the strain measurements. However, as long as caution is used to minimize potential sources of error, SEM-DIC is a remarkably useful tool for assessing deformation and damage in CMCs.

SEM-DIC has several advantages for the characterization of high temperature composites. First, thermal turbulence (heat haze) is a non-issue in the SEM vacuum environment. Novak [17] macroscopically characterized C-SiC CMCs at 1450° C in air, noting that a major challenge was minimizing heat haze and its detrimental effect on image distortion. Although spatial and temporal image distortions resulting from electron beam rastering should be considered when using SEM-DIC, these can be successfully accounted for [7-9, 11]. The SEM must also be appropriately shielded to contain thermal radiation; the importance of this is discussed in *Section 3.3*.

3.3 Method

3.3.1 Materials Preparation and Patterning

Two 8-ply [0/90/0/90]_s SiC/SiC composite laminates were machined into single edge-notch tensile coupons with the dimensions shown in Figure 3.1(a). The composites were composed of SiC fibers immersed in a SiC matrix of similar modulus. The fibers were coated with boron nitride to provide a weak interface with the matrix. The individual lamina were approximately 200 microns thick, stacked on top of each other with a thin matrix layer (on the order of tens of microns) between plies. The outer longitudinal plies were partially lapped, resulting in variable ply thicknesses ranging between 100 and 200 microns. Notches were cut with a Mager diamond wafering blade as shown in Figure 3.1(b). Specimens were polished using 9, 3 and 1 micron diamond lapping films (Buehler) to prevent nanopowders from aggregating in rough surface features and to create a uniformly flat surface as currently required by SEM-DIC. To ensure uniform removal of material during lapping and polishing, the tensile coupons were encased in an acrylic sacrificial mold. Upon completion of polishing, coupons were separated from the mold and agitated in a sonicator, in both water and ethanol, in preparation for patterning.

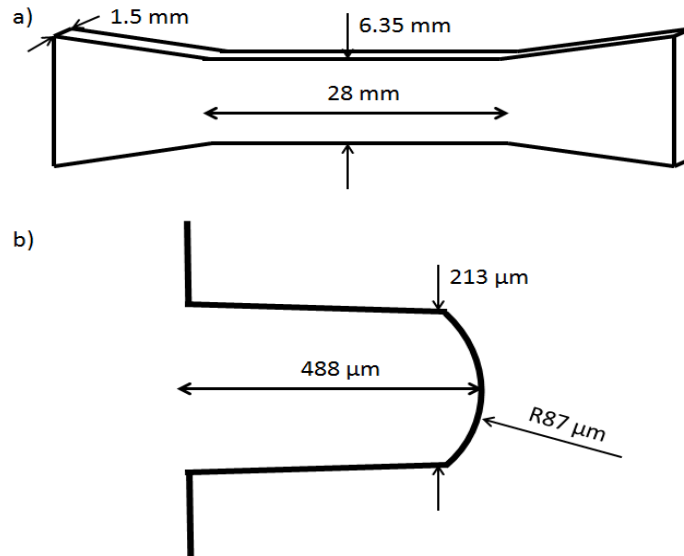


Figure 3.1 Dimensions of (a) tensile coupon and (b) edge notch.

WC is an ideal material for patterning SiC at or above 1000°C because it does not react with the underlying substrate, although Ti forms well-dispersed patterns more readily. All tests were conducted at 795° C due to a stage heater limitation of 800° C. At this temperature, Ti can be used because it does not yet react with the underlying SiC to form a silicide, which degrades the pattern and can degrade the mechanical properties of the composite. The Ti NP suspension contained water and bicine; the bicine served as a pH buffer to stabilize the colloid. Figure 3.2 shows a SiC substrate coated with the Ti colloidal suspension. The combination of roll milling and pH buffering broke up the heavily aggregated nanopowder.

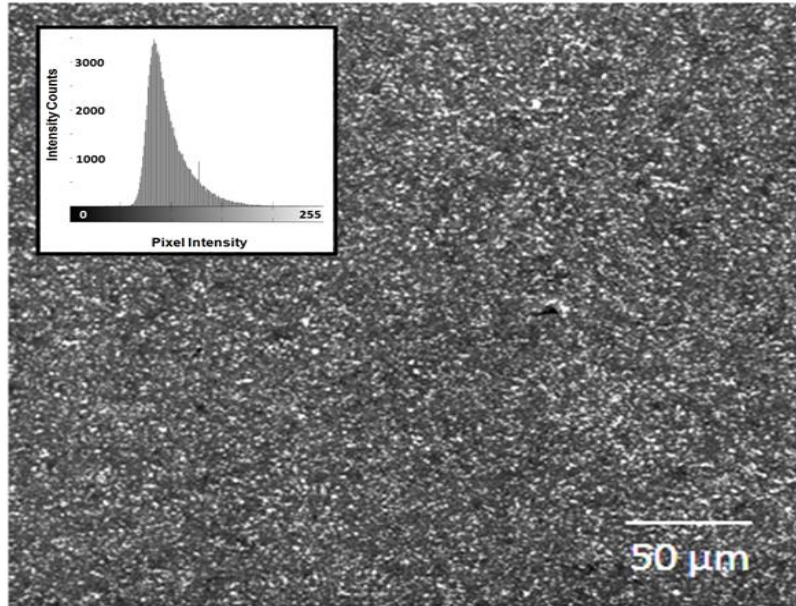


Figure 3.2 High-temperature DIC tracking pattern for tests at 795° C, consisting of slightly aggregated 80 nm Ti nanopowder on a SiC substrate and applied by drop casting. A greyscale pattern intensity histogram is shown in the upper left indicating good pattern quality.

Tracking patterns were applied by drop casting approximately 0.5 microliter droplets of Ti nanopowder colloid onto the surface of the tensile specimen. The colloidal suspension contained 22 mg of bicine and 3 mg of 80 nm titanium powder in 1 ml of distilled water. The suspension was roll milled for 24 hours prior to drop casting to break up agglomerates. Deposition droplets were applied at the notch and throughout the width of the sample. Upon evaporation, the sample was heated to 300° C on a hot plate to burn off the bicine. The resulting tracking patterns for the two test coupons are shown in Figure 3.3.

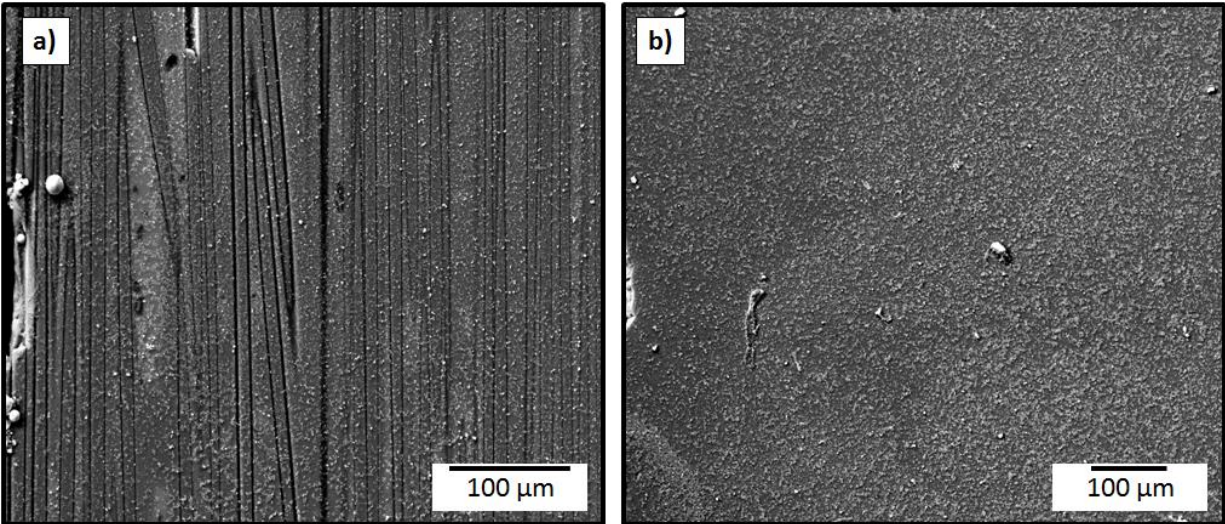


Figure 3.3 Ti nanopowder tracking patterns for high temperature SEM-DIC experiments at a) 500 and b) 800 micron fields of view. In both images, the tip of the notch is located on the left hand side. Variations in speckle density and the presence of a small number of abnormally large agglomerates is observed in both patterns.

To confirm that the patterns were suitable for SEM-DIC, static image pair and rigid body translation images were captured in the SEM and post-processed to remove spatial and temporal image distortions with a combination of laboratory-developed code and commercial code (VIC-2D digital image correlation software [27]). For details on SEM-DIC distortion corrections, please see [7, 8, and 9]. After distortion correction, high frequency noise and spatial warping was significantly reduced but not eliminated. During testing (particularly in early loading in which grip ends of the coupon slip into and deform the compliant grips), rigid body motion generates displacement error in addition to that from noise and bias.

Although CMC testing was conducted at high temperature, pattern suitability was tested at ambient temperature. This was acceptable as independent experiments determined that pattern quality did not degrade at high temperature. Pattern quality is a critical factor in the accuracy of DIC-calculated displacement fields. Poor patterns can result in incomplete correlations and introduce irremovable variability in the deformation data. In addition to error that can arise from poor-quality tracking patterns, there is inherent Gaussian noise in SEM images arising from multiple sources: mechanical vibrations, out-gassing and volatilization of foreign matter, and the statistical nature of electron interactions with the surface may all manifest as noise in DIC data.

3.3.2 High Temperature SEM-DIC

High temperature testing was conducted in an FEI Quanta 3D scanning electron microscope using an *in-situ* tensile stage and heater (Figure 3.4a) purchased from Kammrath & Weiss. In order to prevent thermal emissions from flooding the SEM scintillator, a double layer of tantalum heat shields with small apertures for beam access were fitted above the sample as in Figure 3.4b. The importance of reducing thermal noise is illustrated in Figure 3.5. CCD images of the load frame inside the SEM captured during testing at ambient temperature and 795° C show a dramatic reduction in radiation with heat shielding.

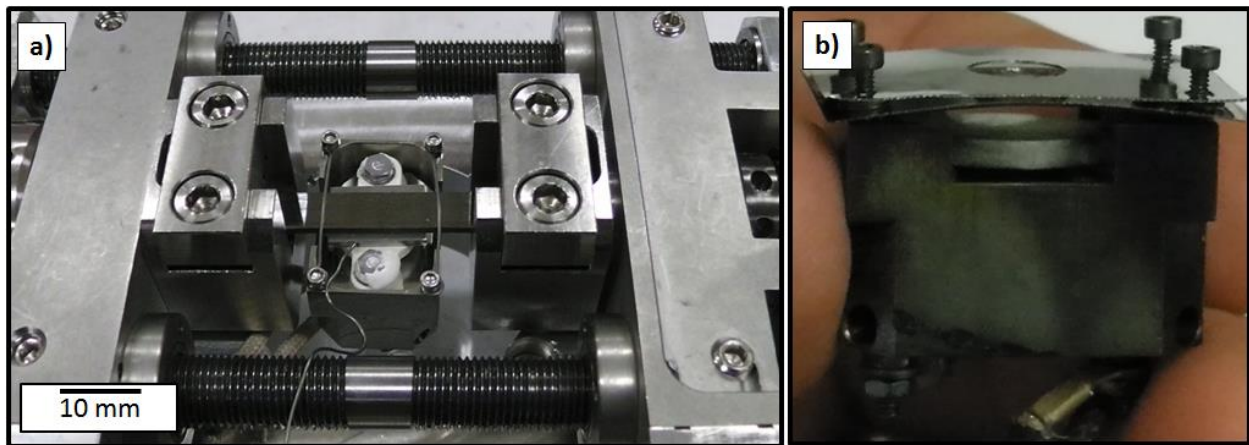


Figure 3.4 CMC mounted in load frame and fitted with heater (a). Double layer of tantalum heat shields with imaging aperture reduce thermal emissions (b).

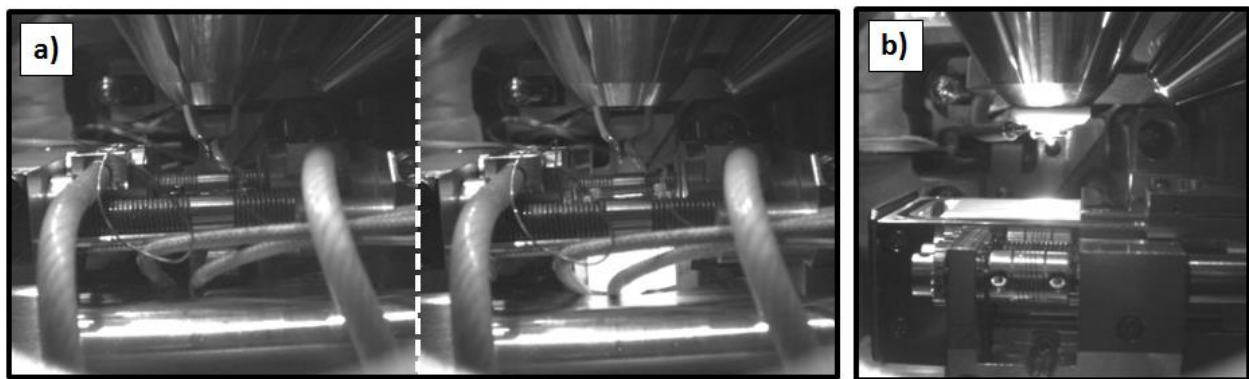


Figure 3.5 (a) Chamber views of load frame, with heater and thermal shielding attached, in SEM at 23° C and 795° C. At 795° C (right), thermal radiation from the heater is evident in its glowing case, but is contained by the shielding. (b) SEM and heat stage at 800° C with no thermal shielding.

In order to monitor the effect of stage heating and prevent damage to the SEM, four type-K thermocouples were placed on the load cell, SEM stage, near the pole piece and near the EDAX detector. The heater was comprised of a heating element encased in alumina upon which a steel thermocouple platen sat. To improve the efficiency of heat transfer from the steel to the SiC tensile coupon under vacuum, a piece of compliant graphite foil was sandwiched between the two surfaces.

A preliminary test, referred to here as “HT-1”, was conducted using a 500 μm FOV. For a second test on a different tensile coupon, referred to as “HT-2”, an 800 μm FOV was used to ensure a sufficient amount of data for a J-integral calculation. Each micrograph was 2048 x 1768 pixels. Images were captured in secondary electron mode using a 30 kV accelerating voltage and 2.6 nAmp beam current at a frame rate of 36.3 sec/frame, integrated four times. These parameters provided images with the highest contrast and lowest noise at the fastest imaging speed. A summary of test parameters is provided in Table 3.1.

	FOV (μm)	Image Size (pixels)	Image Resolution (nm/pix)	DIC Subset (pixels)	Displacement Rate ($\mu\text{m/s}$)	Temperature ($^{\circ}\text{C}$)	Duration of Test
HT-1	500	2048 x 1768	244	51	2	795	>1000 μm crack
HT-2	800	2048 x 1768	391	51	2	795	Final fracture

The samples were heated to 795 $^{\circ}$ C and then mechanically loaded while held at 795 \pm 0.2 $^{\circ}$ C. The temperature was set five degrees underneath the built-in 800 $^{\circ}$ C limit of the heater in order to buffer against any thermal fluctuations. Prior to heating, the samples were preloaded to 100 N and then relaxed to 0 N to remove slack and prevent slippage during the initial loading phase of testing. The unloaded samples were heated to just under 800 $^{\circ}$ C in temperature increments of 100 $^{\circ}$ C. During each temperature increment, the load was continuously adjusted to maintain 0 N as the sample and grips expanded. At 500 $^{\circ}$ C and every 100 $^{\circ}$ C increment thereafter, contrast, brightness and focus were adjusted to maintain a high quality image. After the sample stabilized at 795 $^{\circ}$ C, the LVDT was zeroed so that subsequent loading would start at zero displacement. To protect the proprietary nature of the test material, stress and strain values have been non-dimensionalized.

Although the tensile stage was operated in displacement control at $2 \mu\text{m/s}$, loading was started and stopped at 50 N load increments so that the notch could be inspected frequently for crack initiation. At each loading increment, the reading on the load cell was allowed time (one to two minutes depending on the applied load and state of cracking in the material) to stabilize prior to capturing an image. During the early stages of loading, the notch was imaged at higher magnifications at each loading increment in order to identify crack initiation. Upon crack initiation, load increments were increased slightly to allow a small amount of crack propagation through the FOV. Once the crack cleared the FOV, the stage was shifted to the next speckle pattern ahead of the advancing crack. The sample was unloaded and a reference image was captured at a load of 0 N. The sample was then reloaded and the process of capturing images of the advancing crack continued until final fracture. The load-hold-unload process is non-reversible. Consequently, the reference image in the new FOV reflects a damaged state even though it is captured under no applied load. The deformation fields measured upon re-loading may not accurately reflect fracture behavior in a CMC loaded monotonically. Of the two tests, one (HT-2) was carried out to final fracture. Figure 3.6 shows the sequence of crack propagation across the tensile specimen and the corresponding longitudinal strain fields of test HT-2. The undulating variations in color (magnitude of longitudinal strain) are attributed to Gaussian salt-and-pepper noise and aliasing. The DIC parameters chosen (51 pixel subset and 71 pixel strain filter) presented the best displacement resolution the pattern would permit without flooding the corresponding strain field overlay with noise. The subset size was near that of the fiber diameter.

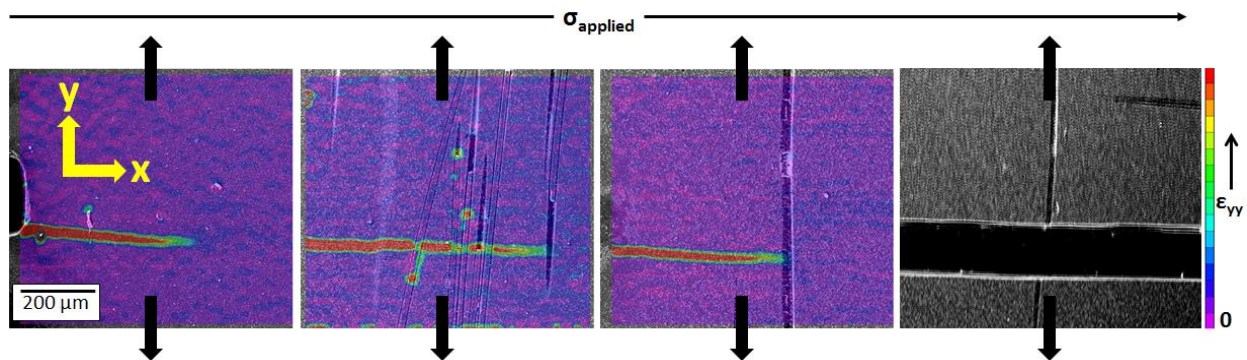


Figure 3.6 Longitudinal strain fields during crack propagation in HT-2. Each panel represents a shift in FOV as the crack propagates from left to right. The far right panel shows final fracture. Arrows indicate loading axis.

3.4. Results and Discussion

3.4.1 High Temperature Full-Field Deformations

Figures 3.6 and 3.7 illustrate high-temperature, in-SEM, full-field quantitative maps of damage progression as a crack initiates at a notch and propagates through a CMC. Figure 3.7 compares longitudinal strain fields measured at fracture initiation from the notches for both high temperature tests: (3.7a) uniaxial tension at 795° C in SEM at 500 μm FOV (test HT-1) and (3.7b) uniaxial tension at 795° C in SEM at 800 μm FOV (test HT-2). Both test specimens are cross-ply layups with partially lapped outer longitudinal lamina. HT-1 contained exposed longitudinal fibers in the vicinity of the notch tip whereas HT-2 had a thin layer of matrix material. Although not presented for proprietary concerns, the load-displacement curves for the samples were similar. Fracture behavior at the notch tips, however, was quite different. Upon crack initiation in HT-2 (3.7b), a small region of elevated longitudinal strain (as indicated by forked blue lobes) in the process zone is observed immediately ahead of the crack tip. In HT-1 (3.7a) a much shorter crack appears upon initiation, and emanating from the crack tip are two forked lobes of strain in a larger process zone than of HT-2. Note that the strain values are scaled differently in Figure 3.7; the upper limit of (3.7b) is two times larger than the reference strain value, ϵ_{yy} , in (3.7a). This scaling scheme mitigates noise effects in the strain fields of (3.7b), but consequently reduces the spatial resolution of the strain field, which attenuates the strain signal at the forked strain lobes.

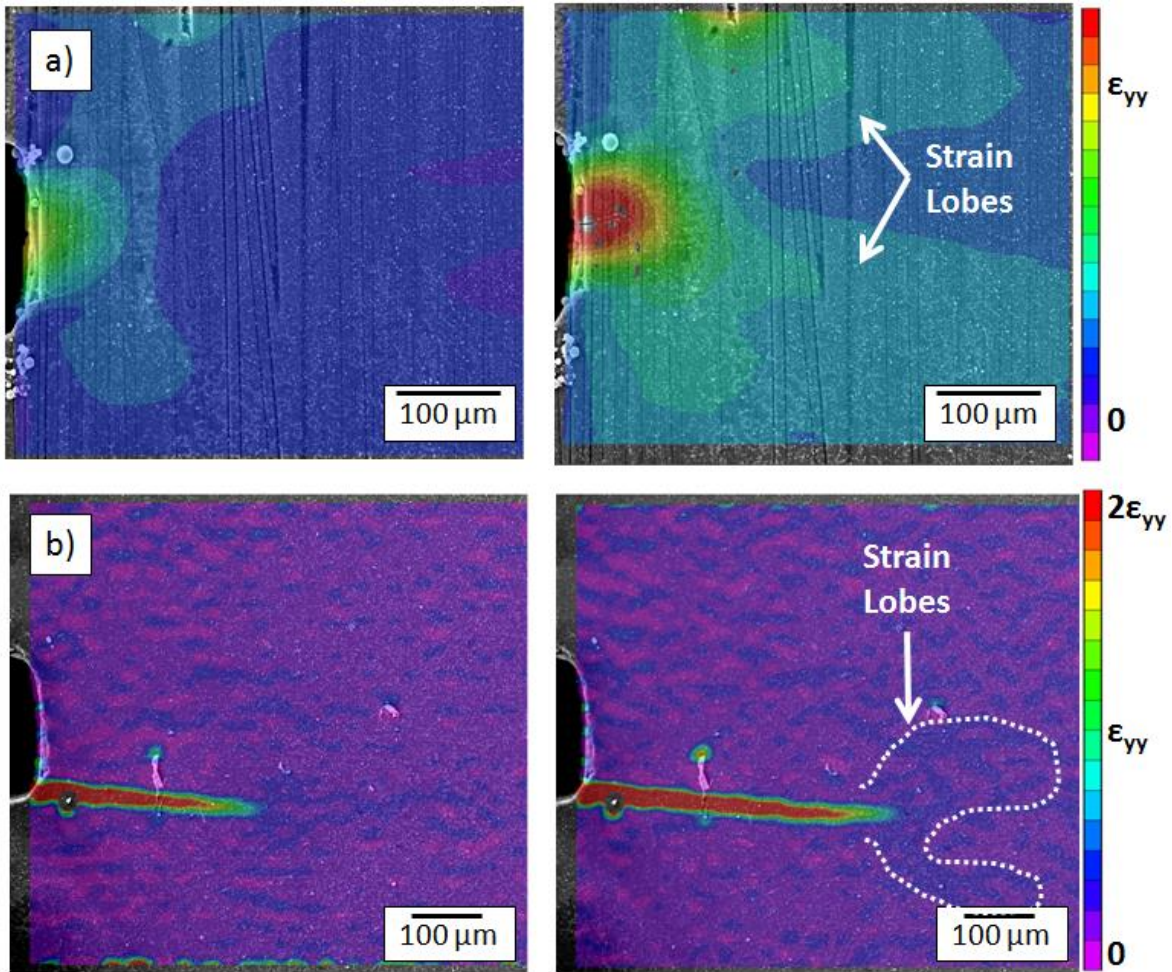


Figure 3.7 Illustration of different fracture behavior in HT-1 and HT-2. Cracks initiate (left) and propagate (right) in SiC/SiC composites at 795° C for FOVs of (a) 500 and (b) 800 microns. Longitudinal strain fields on left hand side correspond to the initial manifestation of surface matrix-crack at notch tip. Although both (a) and (b) exhibit high-strain process zones ahead of the crack tip, that of (b) appears larger. Note the different strain magnitude bars for (a) and (b).

DIC parameter selection greatly influences the extent of the damage detected. Modifying DIC parameters for HT-1 (51 pixel subset and 375 pixel strain filter) as in (3.7a) effectively smoothed over smaller, discrete regions of high strain that revealed the presence of additional matrix cracks. To illustrate this difference, Figure 3.8 shows the evolution of longitudinal strain with load for test HT-1 for two distinctly different DIC parameter sets: Figure (3.8a) uses a subset of 51 pixels and strain filter of 375 pixels whereas Figure (3.8b) uses a subset of 51 pixels and a strain filter of 75 pixels. Although the strain fields of (3.8b) are substantially noisier than those in (3.8a), they reveal four distinct matrix cracks (indicated by red contours) evolving from the notch tip. The larger strain filter of Figure (3.8a) averages these values and makes it appear

that two well-defined strain lobes emanate from the notch. These lobes are likely process zones of distinct matrix cracks and not a continuous region of high elastic and plastic strain in the silicon carbide. Further manipulation of the strain filter size (the subset size lower bound was constrained by the speckle size and distribution of the tracking pattern) applied to test HT-2 did not reveal additional matrix cracks. The displacement resolution of HT-1 was inherently less than that of HT-2 because, all other parameters equal, it was obtained for a larger field of view.

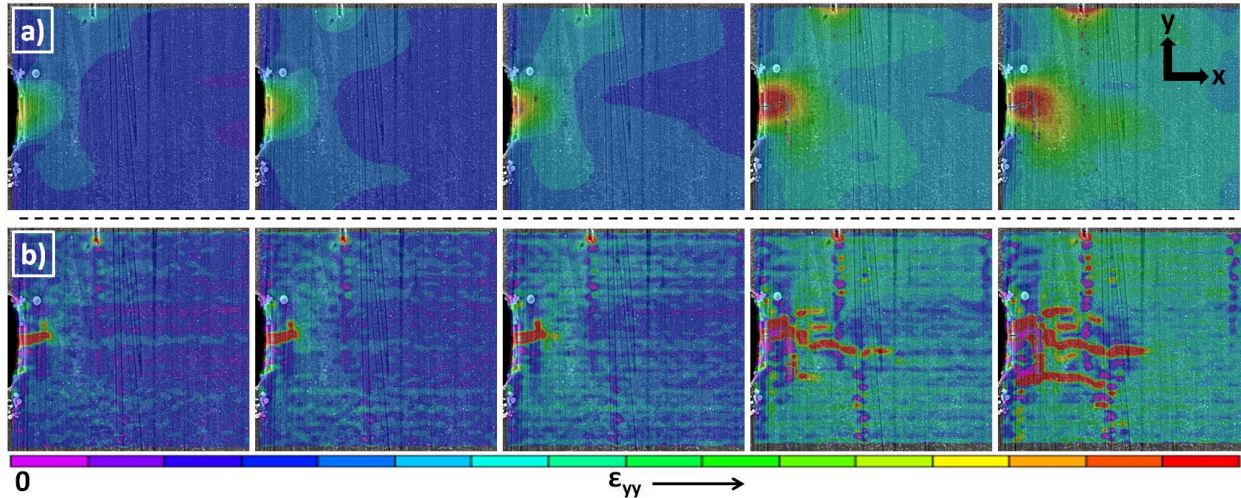


Figure 3.8 Longitudinal strain fields illustrating the smearing effect of strain filters. Panels sequence indicates crack growth from left to right. In (a) the strain filter is 7x the subset size whereas in (b) it is 1.5x the subset size. The smaller strain filter does not mitigate artifacts of image noise and aliasing, however, it does reveal more damage, specifically multiple matrix cracks propagating from the notch tip, than the larger filter. The data filtering in (a) masks the real behavior of (b).

It is beneficial to conduct analyses covering several tiers of noise filtering. In conducting both qualitative and quantitative analyses of damage in CMCs at small length scales, there appears to be no single combination of DIC parameters that yield optimal deformation field data. Over smoothing data can mask damage that would otherwise provide valuable insight into the mechanical behavior. On the contrary, in the absence of sufficient filtering, high noise levels can mask real behavior, as was shown in Figure 3.8.

Microscopically, the fracture behavior of HT-1 and HT-2 are quite different. Whereas a single crack originates from the notch in HT-2, two cracks emanate from the notch in HT-1, one of which branches into two additional matrix cracks. Small variations in microstructure and loading conditions between the two samples may strongly influence when, where and how many

cracks initiate at the notch as well as how they propagate after initiation. A study of the probabilistic nature of this behavior warrants further investigation.

3.4.2 High Temperature Damage Evolution

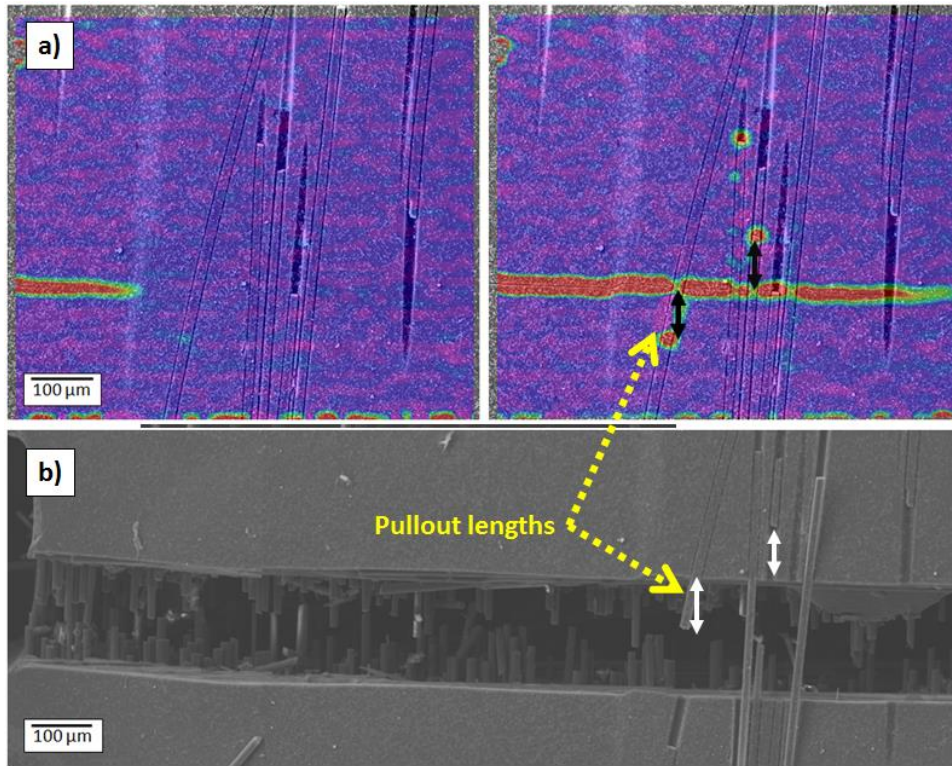


Figure 3.9 Longitudinal strain fields depict debonding at the fiber-matrix interface in the outer longitudinal lamina of the CMC (a). Fiber pullout lengths are of similar magnitude as debond lengths (b).

Accurate characterization of debond lengths in fibrous composites can be used to determine crack bridging tractions, which in turn can be incorporated into cohesive zone laws for damage modeling. In Figure 3.9 (a), debonding of the matrix crack along the length of longitudinal fibers is shown in two instances during test HT-2 (delineated with double arrows), both with debond lengths of approximately 90 μm. Note that the exposed fibers were partially lapped and polished in order to prepare the specimen for testing; it is possible that the partial removal of fiber volume and damage to the exposed fibers may have influenced this debond length. Post-fracture analysis of fiber pullout in the inner longitudinal ply nearest the coupon surface (Figure 3.9 (b)) revealed average pullout lengths of 72.7 ± 29.4 μm. Although the 90 μm debond lengths of (Figure 3.9 (a)) fall within this size distribution, a single ply-level distribution

alone may not be reflective of the full distribution of pullout lengths through the thickness of the laminate. Pullout data obtained from DIC may be most useful when applied to the assessment of local toughening behavior at the CMC surface.

Fiber bridging tractions in the wake of a matrix crack strongly influence toughness [29]. As ceramic fiber strengths are stochastic, both intact fibers that straddle the crack and ultimately fracture at the crack plane, as well as pullout fibers that break some distance away from the crack plane, contribute to toughening. In an effort to characterize the toughening contribution of surface fibers that fracture away from the crack plane, full-field strain data from HT-2 was segmented into individual bins comprised of microstructural features as illustrated in Figure 3.10.

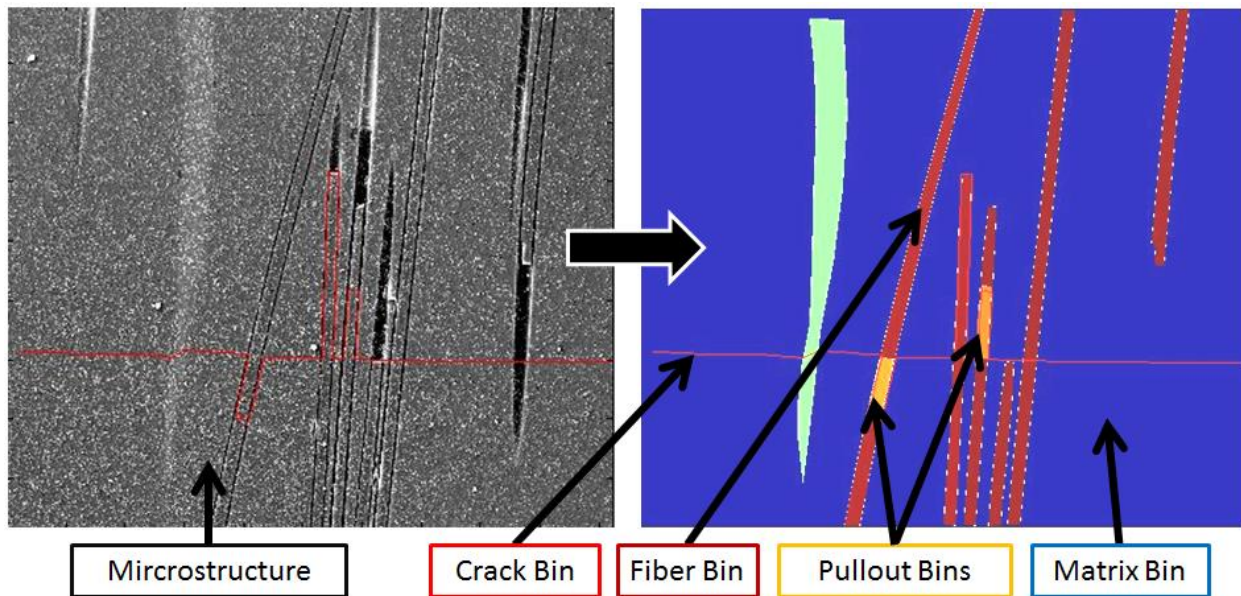


Figure 3.10 Microstructure is segmented into fiber, fiber pullout, matrix, and crack bins. Mean strains are computed for each bin.

Mean fiber and mean fiber-pullout strains at each increment of crack propagation are plotted in Figure 3.11. Initial fiber breakage occurs in Fiber 1 (nearest the crack tip) at the third load increment, corresponding to a dip in the mean fiber strain and maximum in mean fiber pullout strain. After the crack is introduced into the fiber, subsequent mean strains in both the fiber and fiber pullout bins increase as a result of the exaggerated strains computed near the crack. These exaggerated strains are an artifact of DIC measurements across a discontinuity. The minimum values in the mean fiber strain may be due to relaxation in the fibers after fiber

fracture. In reality, average strain should plateau or decrease. However, the exaggerated DIC measurements at the newly formed discontinuity result in large average strains that increase as the fiber cracks open. Up until this point, the mean strains in both the fiber and the pullout region are approximately half the theoretical failure strain of the fiber ($\epsilon_{f,u}$). Although the strain data is highly variable, the mean strain levels are within the expected strain range for this type of fiber.

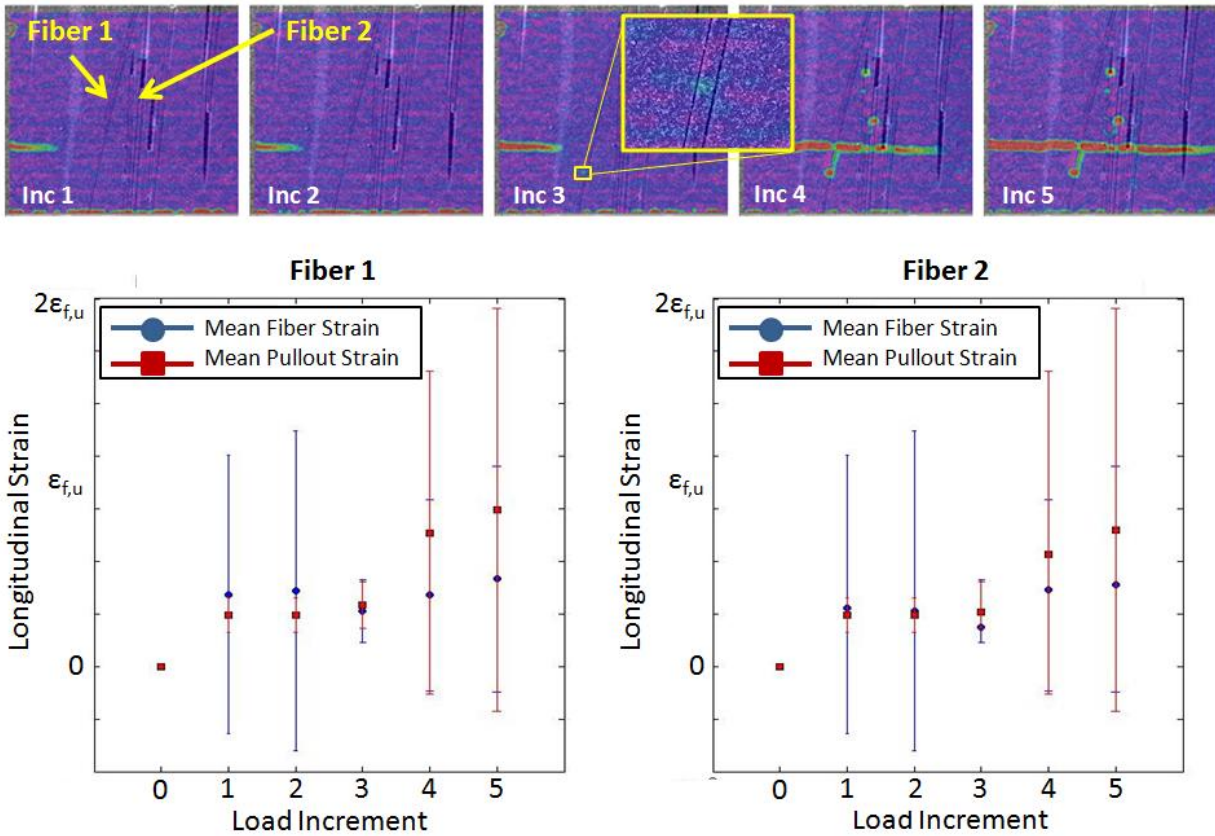


Figure 3.11 Mean strains in fibers (computed from red and orange fiber bins) are plotted alongside their mean strains (computed from orange bins) in their corresponding pullout regions at each load increment. Inset in panel “Inc 3” is a magnified view of the localized tensile strain in a longitudinal fiber at fiber fracture.

The exaggerated strains that accompany fracture prevent using this strain data for a quantitative assessment fiber traction toughening. However, both fibers indicate a sharp transition in mean strain at the point of fiber fracture. At that point, the error bars are at a minimum. Although further investigation is needed, sharp transitions in mean strains computed from DIC data may be indicative of ceramic fracture. Note that the negative ranges of standard deviation are indicative of noise in the DIC data.

Full-field strain analyses imply the following at the onset of fiber fracture:

- (1) mean strains in the fiber increase during initial loading and then decrease to a minimum at fracture;
- (2) although the standard deviation ranges are generally broad, they approach a minimum at fracture.

Although strain errors were large, mean strain measurements in the fibers fell within the realm of their failure expected strain. Strain error must be acknowledged when conducting any deformation field analysis so that erroneous conclusions are not drawn from trends in the data set.

3.4.3 Sources of Error in SEM-DIC

Aberrations in the full-field displacement data exist that inevitably introduce error into its quantitative analysis. These may be attributed to several sources of noise and bias as defined in [30]. Noise in the DIC data is likely due to Gaussian noise inherent in the SEM images. Sources of bias may be due to debris and large aggregates on the speckle pattern, degradation in SEM image contrast with time, and aliasing [30]. Gaussian noise was mitigated by utilizing 4x image integration for each SEM image capture. Image integration was used at the expense of individual pixel dwell time (reduced from 100 μ sec to 10 μ sec as a result of integration), which reduced image sharpness. Biasing effects were reduced using an optimized 8-tap interpolation filter in the correlation software [27]. Deformation data in the vicinity of debris and large aggregates was not used for quantitative analysis. Aliasing may exist in portions of the pattern with speckles that encompass only a few pixels as the corresponding subsets have lower fill factors. Aliasing effects were mitigated using a low-pass filter [27].

Due to the aforementioned error associated with noise and biasing, it is necessary to conduct quantitative analyses of DIC-SEM data with great care and discretion. Differentiating displacements to get strain magnifies pre-existing fluctuations, resulting in strain errors that can have values equal to or larger than the material failure strain. When a crack forms, it introduces an erroneously large displacement gradient that straddles both of its flanges. Consequently, the strain fields on either side of the crack may be several orders of magnitude larger than the actual

physical values. The strain error may mask the real tensile strain in the material. In Figure 3.12, double arrows point to the location of fiber fracture just before and after fiber breakage. The DIC-measured strain values prior to fracture are near the known fracture strain value for the SiC fibers used in this material, indicating that DIC can resolve tensile strain in the ceramic up to fracture. The same cannot be said with regard to the matrix; the significantly lower fracture strain of the matrix results in noise that can mask the tensile strain. After the fiber fractures, the DIC-measured longitudinal strain increases by several orders of magnitude. Although this can be helpful in identifying cracks that can otherwise go undetected, care must be taken not to use these strain measures for quantitative analysis.

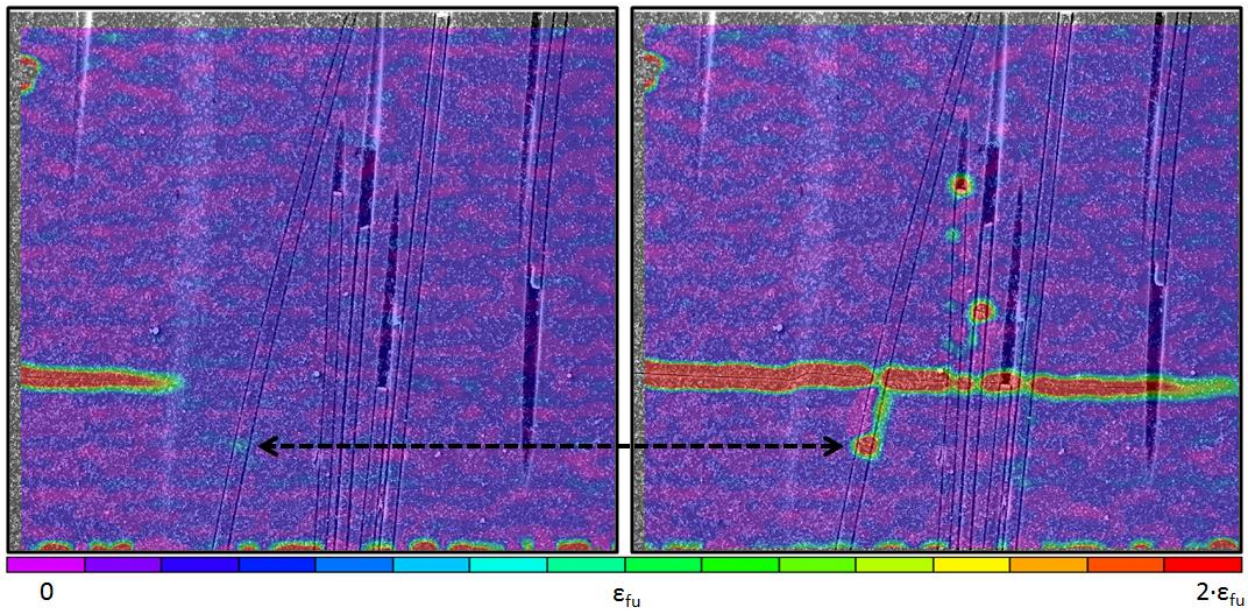


Figure 3.12 Evolution of fracture in fiber. Double arrows point to position in fiber prior to and after fracture. Magnitude of longitudinal strain prior to fracture, as measured by DIC, are on order of the fibers theoretical fracture strain.

3.5 Conclusions

A new experimental approach to investigate damage initiation and accumulation at the constituent length scale in ceramic matrix composites under high temperature and mechanical loading was evaluated. Two SiC/SiC single edge-notch tensile coupons were loaded to final fracture at 795° C in a scanning electron microscope with proper shielding of sensitive SEM components. SEM-DIC tests were conducted at two horizontal fields of view (500 and 800 μm) for deformation and fracture analyses. A colloidal system containing mechanically milled

titanium nanopowder, bicine and water was developed for use as a DIC tracking pattern that is stable at 795° C. The smaller FOV revealed a fluted process zone ahead of the tip of an initiating crack. Reducing the strain filter showed that this process zone consists of several distinct matrix cracks emanating from the notch at different angles. The larger FOV captured deflection of a matrix crack propagating through longitudinal fibers. Although the finer resolution FOV revealed more matrix cracks at the notch tip, the larger resolution FOV captured full propagation up through final failure.

In order to characterize the toughening contribution of fibers that fracture away from the crack plane, the full-field strain data was segmented into fibers and fiber pullout bins, and averaged strains were evaluated at each load increment. Plots of strain versus load increment revealed noteworthy behavior at the onset of fiber fracture: (1) mean strains in the fiber increase during initial loading then decrease to a minimum at fracture; (2) although the standard deviation ranges are generally broad, they approach a minimum at fiber fracture. Despite having large strain errors, mean strain measurements in the fibers were on par (at several thousand microstrain) with expected values based on the material's Young's modulus and failure strain. Strain error was attributed to Gaussian noise in the SEM images, as well as several types of pattern and noise induced error and systemic biasing. Strain error must be acknowledged when conducting any deformation field analysis so that erroneous conclusions are not drawn from trends in the data set.

References

1. D. Marshall, B. Cox, and A. Evans, "The Mechanics of Matrix Cracking in Brittle-matrix Fiber Composites," *Acta Metall.*, **33** 2013-2021 (1985).
2. B. Budiansky, J. Hutchinson, and A. Evans, "Matrix Fracture in Fiber-reinforced Ceramics," *J. Mech. Phys. Sol.*, **34** [2] 167-189 (1986).
3. F. Zok and C. Hom, "Large Scale Bridging in Brittle Matrix Composites," *Acta Metall. Mater.*, **38** [10] 1895-1904 (1990).
4. M. Sutton, J. Orteu and H. Schreier, *Image Correlation for Shape, Motion and Deformation Measurements: Basic Concepts, Theory and Applications*, Springer, New York, NY, 2009.
5. M. Sutton, M. Cheng, W. Peters, Y. Chao, J. Orteu, and S. McNeill, "Application of an Optimized Digital Correlation Method to Planar Deformation Analysis," *Image Vision Comput.*,

- 4 [3] 143-153 (1986).
6. M. Sutton, N. Li, D. Garcia, N. Cornille, J. Orteu, S. McNeill, W. Schreier, and X. Li, "Metrology in a Scanning Electron Microscope: Theoretical Developments and Experimental Validation," *Meas. Sci. Technol.*, **17** 2613-2622 (2006)
 7. M. Sutton, N. Li, D. Joy, A. Reynolds, and X. Li, "Scanning Electron Microscopy for Quantitative Large Deformation Measurements Part I: SEM Imaging at Magnifications from 200 to 10,000," *Exp. Mech.*, **47** 775-787 (2007).
 8. M. Sutton, N. Li, D. Garcia, N. Cornille, J. Orteu, S. McNeill, H. Schreier, A. Reynolds, and X. Li, "Scanning Electron Microscopy for Quantitative Large Deformation Measurements Part II: Experimental Validation for Magnifications from 200 to 10,000," *Exp. Mech.*, **47** 789-804 (2007).
 9. A. Kammers and S. Daly, "Digital image correlation under scanning electron microscopy: Experimental methodology and validation," *Exp. Mech.*, **53** 1743-1761 (2013).
 10. L. Canal, C. Gonzalez, J. Molina-Aldareguia, J. Segurado, and J. Llorca, "Application of Digital Image Correlation at the Microscale in Fiber-reinforced Composites," *Compos. Part A (Appl. S.)*, **43** [10] 1630-1638 (2012).
 11. A. Kammers and S. Daly, "Small-scale Patterning Methods for Digital Image Correlation Under Scanning Electron Microscopy," *Meas. Sci. Technol.*, **22** 125501 (2011).
 12. W. Scrivens, Y. Luo, M. Sutton, S. Collete, M. Myrick, P. Miney, P. Colavira, A. Reynolds, and X. Li, "Development of Patterns for Digital Image Correlation Measurements at Reduced Length Scales," *Exp. Mech.*, **47** 63-77 (2007).
 13. S. Collete, M. Sutton, P. Miney, A. Reynolds, X. Li, P. Colavita, W. Scrivens, Y. Luo, T. Sudarshan, P. Muzykov, and M. Myrick, 2004, "Development of Patterns for Nanoscale Strain Measurements: I. Fabrication of Imprinted Au Webs for Polymeric Materials," *Nanotechnology*, **15** 1812-1817 (2004).
 14. N. Thaulow and W. White, "General Method for Dispersing and Disaggregating Particulate Samples for Quantitative SEM and Optical Microscopic Studies," *Powder Technol.*, **5** 377-379 (1971).
 15. A. Kammers and S. Daly, "Self-Assembled Nanoparticle Surface Patterning for Improved Digital Image Correlation in a Scanning Electron Microscope," *Exp. Mech.*, **53** 1333-1341 (2013).

16. V. Rajan, M. Rossol, and F. Zok, "Optimization of Digital Image Correlation for High-resolution Strain Mapping of Ceramic Composites," *Exp. Mech.*, **52** 1407-1421 (2012).
17. M. Novak and F. Zok, "High-temperature Materials Testing with Full-field Strain Measurement: Experimental Design and Practice," *Rev. Sci. Instr.*, **82** 115101 (2011).
18. R. Freeman, et. al., "Self-assembled Metal Colloid Monolayers: An Approach to SERS Substrates," *Science*, **267** 1629–1632 (1995).
19. K. Grabar, R. Freeman, M. Hommer, and M. Natan, 1995, "Preparation and Characterization of Au Colloid Monolayers," *Anal. Chem.*, **67** 735–743 (1995).
20. K. Grabar, et. al., "Two-dimensional Arrays of Colloidal Gold Particles: A Flexible Approach to Macroscopic Metal Surfaces," *Langmuir*, **12** [10] 2353–2361 (1996).
21. M. Hudson, J. Peckett, and P. Harris, "Low-Temperature Sol–Gel Preparation of Ordered Nanoparticles of Tungsten Carbide/Oxide," *Ind. Eng. Chem. Res.*, **44** [15] 5575–5578 (2005).
22. O. Nayfeh, D. Antoniadis, K. Mantey, and M. Nayfeh, "Uniform Delivery of Silicon Nanoparticles on Device Quality Substrates Using Spin Coating from Isopropyl Alcohol Colloids," *Appl. Phys. Lett.*, **v 94** 1-3 (2009).
23. C. Giordano, W. Yang, A. Lindemann, R. Crombez, and J. Texter, "Waterborne WC Nanodispersions," *Colloid Surface A*, **374** 84-87 (2011).
24. E. Laarz and L. Bergstrom, "Dispersing WC-Co Powders in Aqueous Media with Polyethylenimine," *Int. J. Refract. Met. H*, **18** [6] 281-286 (2011).
25. M. Elbadawy, T. Luxton, R. Silva, T. Schekl, S. Suidan, and T. Tolymat, "Impact of Environmental Conditions (pH, Ionic Strength, and Electrolyte Type) on the Surface Charge and Aggregation of Silver Nanoparticles Suspensions," *Environ. Sci. Technol.*, **44** 1260–1266 (2010).
26. A. Godara and D. Raabe, "Microstrain Localization Measurement in Epoxy FRCs During Plastic Deformation Using a Digital Image Correlation Technique Coupled with Scanning Electron Microscopy," *Nondestruct. Test Eva.*, **23** [3] 229-240 (2008).
27. Correlated Solutions, VIC-2d [Software], Columbia, SC, 2009.
28. CoorsTek, Reaction-Bonded Silicon Carbide SC-RB Material Properties, 2013; http://www.coorstek.com/materials/ceramics/carbides_sc-rb.php
29. M. Thouless and A. Evans, "Effects of Pull-out on the Mechanical Properties of Ceramic-Matrix Composites," *Acta Metall.*, **36** [3] 517-522 (1988).
30. Correlated Solutions, Advanced Bias, 2011; <http://correlatedsolutions.com/support/>

Chapter IV

Experimental Assessment of Fracture Toughness in Ceramic Matrix Composites using the J-integral with Digital Image Correlation

4.1. Introduction

Toughness in fiber-reinforced CMCs is dependent on the complex interactions between the fibers, coatings and matrix. Constituent properties, residual stresses, interfacial sliding, bridging tractions and microcrack shielding all influence composite toughness, but quantifying the contribution of each mechanism is difficult and does not always account for their mutual influences. A rigorous means to characterize composite toughness is to use an approach capable of capturing the contribution of individual toughening mechanisms and their interactions. One such approach is through measuring the energy release rate, and subsequently stress intensity factors, by application of the J-integral. Given full-field measurements of displacement, J can be numerically evaluated along a contour that encircles the crack.

This chapter discusses two methods for evaluating J from full-field Digital Image Correlation (DIC) deformation data on materials that exhibit small elastic failure strains: (1) numerical integration over a line contour; and (2) Gaussian integration over an area contour. It is shown that both methods are sound under specific material and loading constraints, but are extremely sensitive to displacement data variability. For multiphase materials like CMCs, data smoothing is required to mitigate this variability and results in unrealistic data at and around phase interfaces and discontinuities. Additionally, the need for contour truncation near the crack

flange results in data loss and the introduction of measurement error. Furthermore, determining the exact onset of crack initiation with DIC data can be inaccurate. Consequently, defining fracture toughness from J-integral measurements derived from DIC data is somewhat arbitrary. While it has been suggested that the J-integral can be a valid means of measuring toughness in a matrix crack in a composite that exhibits large scale fiber bridging [1], the micro-scale investigations of damage in continuous fiber CMCs presented here suggest that microcracking is dispersed so widely throughout a CMC that it is not practical to calculate J over a single matrix crack in a CMC. This is because the integration paths would intersect discontinuities, rendering it fundamentally invalid. However, DIC smears deformation data across microcracks, which essentially transforms a surface full of very fine discontinuities (microcracks) into a surface of continuous elastic deformation. While the J-integral can be used for gross estimates of toughness, a more practical application is developing qualitative resistance curves that characterize toughening behavior in continuous fiber CMCs.

Although the J-integral is too sensitive to data variability to quantify fracture toughness in a CMC with certainty, it is suitable for establishing an upper bound for fracture toughness and for assessing toughening behavior. For example, resistance curves generated via the J-integral may not provide stress intensity factors with well-defined error bounds, but they can be used to determine stresses and crack opening displacements near the critical fracture toughness. Additionally, the shapes of the resistance curves indicate how toughness evolves as the composites accumulate damage. The gradient of resistance curves can in turn be used to develop fiber-bridging laws, which may aid in damage models.

4.2. Background

In this work, the J-integral was evaluated from full-field DIC deformation data for three materials: (1) a PMMA compact tension (CT) specimen loaded at ambient temperature and imaged at the macroscale; (2) an 6061 aluminum alloy single edge notch tensile coupon imaged at the macroscale; and (3) cross-ply SiC/SiC composites loaded at 800° C and imaged at the constituent level using scanning electron microscopy (SEM) as well as unidirectional SiC/SiC CMCs loaded at ambient temperature and imaged at the macroscale. The focus of this effort was to characterize fracture in SiC/SiC composites; however, validation of the approach with well-characterized materials (PMMA and aluminum) was first required.

Recent studies have investigated using full-field deformation data from *macroscopic* DIC to characterize fracture in materials [2-8], but none attempt to characterize fracture at the constituent level under thermo-mechanical loading conditions similar to those encountered in service. An advantage of using the J-integral to evaluate toughness in composites is that it can be used when the application of linear elastic fracture mechanics is not permitted [1, 9-10]; for example, it is considered a valid measure of quantifying fracture toughness when there exists large scale fiber bridging behind the tip of a growing crack [1]. Furthermore, it does not require exact knowledge of the crack tip position as long as a contour can be drawn around the general tip location and beyond the plastic zone (the plastic zone size can readily be detected in full-field strain data). This is particularly beneficial for CMCs as the position of the crack tip at the surface of the material may not coincide with position of the tip sub-surface. Some studies fit experimentally-measured full-field displacements to an analytical closed-form expression of the stress intensity factor [5-8], while others incorporated deformation measurements directly into a numerical evaluation of the J-integral [2-4].

The J-integral is a measure of the strain energy release rate in a cracked material and is expressed, in the form of a line integral, as [9]:

$$J = \int_{\Gamma} \left(W dy - \mathbf{T} \cdot \frac{du}{dx} ds \right) \quad (1)$$

where W is strain energy density, \mathbf{T} is a stress traction vector defined with respect to the outward normal along the contour (Γ), u is displacement in the crack direction, x and y are spatial positions in the crack growth direction and normal direction, respectively, and ds is a unit element along the contour. The left hand term represents the strain energy density contribution and the right hand term represents traction and displacement contributions to the energy balance along a contour that encompasses the crack tip. When coupled with full-field displacements obtained from DIC, the J-integral presents a method of generating resistance curves from in-situ testing of a single specimen [9-10]. Crack lengths can be evaluated post-test by examining image data, nullifying the need to stop a test and inspect the sample for crack progression or to test multiple identical samples to varying extents of crack propagation. As the method is theoretically path independent, a simple rectangular contour can be defined around a crack tip and the J-integral calculated using the DIC data that falls along that contour [2-3, 9-10]. The primary

disadvantage of this method is that it is not valid if the contour falls within a zone of plastic deformation or fiber bridging; thus, it is necessary to identify the size and location of the plastic zone ahead of the crack tip and ensure that the field of view (FOV) in which the J-integral is being evaluated is large enough to accommodate the contour.

In theory, the J-integral can be a unique and valuable tool to characterize composite fracture at the constituent length scale because it indirectly captures the contribution of fiber-bridging tractions. However, it must be used with caution, as it is only valid if the composite exhibits large scale bridging and if a contour can be drawn around the crack tip in such a way that it terminates beyond the fiber bridging zone and completely encircles the plastic zone around the tip. Presuming an accurate measurement of J can be determined, it can be used to establish a fiber-bridging law [1]:

$$\sigma(\delta) = \frac{dJ}{d\delta} \quad (2)$$

where σ represents the crack closing tractions exhibited by bridging longitudinal fibers. This calculation requires accurate computation of J at measured intervals of crack opening displacement, δ .

In this paper, strain energy release rates (J) and stress intensity factors (K) are calculated for a crack growing in a thermo-mechanically loaded SiC/SiC composite by incorporating full-field deformation data into a numerical computation of J. Two methods to compute J – using a line integral and an area integral - are investigated, each with its own unique benefits and disadvantages. The line integral is computationally simpler, which is useful for large sets of deformation data. In principal, the line integral is more sensitive to deformation data variability than the area integral because it samples less data points over a smaller region. Line integral and area integral algorithms based on work from Catalanotti and Becker [2-3], respectively, were applied to five categories of crack deformation data: (i) data analytically derived using Westergaard solutions for a center crack in an infinite plate of acrylic (PMMA) with a critical plane stress fracture toughness of $1 \text{ MPa}\sqrt{m}$; macroscopic DIC data for (ii) a crack in a PMMA tapered, double cantilever beam compact tension (DCB-CT) specimen (the specimen geometry results in a zone in which stress intensity factors should remain constant as the crack extends) (iii) an aluminum single edge notch tensile coupon; microscopic SEM-DIC data for (iv) cracks in

single edge notch cross-ply SiC/SiC CMC tensile coupons at 795° C and macroscopic DIC data for (v) SiC/SiC CMCs comprised of a single lamina of longitudinal fibers at ambient temperature. The following section discusses the analytical deformation fields in case (i) used to validate the algorithms, and the subsequent implementation of this analysis on experimental data.

4.3 Analytical Validation: Line Integral and Area Integral

In order to quantify the computational error in J and K before analyzing experimental data, the line and area integral methods were applied to analytical stress and displacement solutions near a crack tip. Graphical illustrations of the line and area contours, overlaid on vertical Westergaard displacement fields, are shown in Figure 4.1; note that the FOV contains only the right half of a center-cracked acrylic plate. Dark shades of blue correspond to negative displacements (down in the plane of the page), light shades of blue to positive displacements. The procedures used to validate the two methods are detailed in *Sections 4.3.1* and *4.3.2*, and the application of both methods to experimental data is described in *Section 4.4*. An assessment of the influence of variability in deformation data on the algorithm is presented in *Section 4.6*.

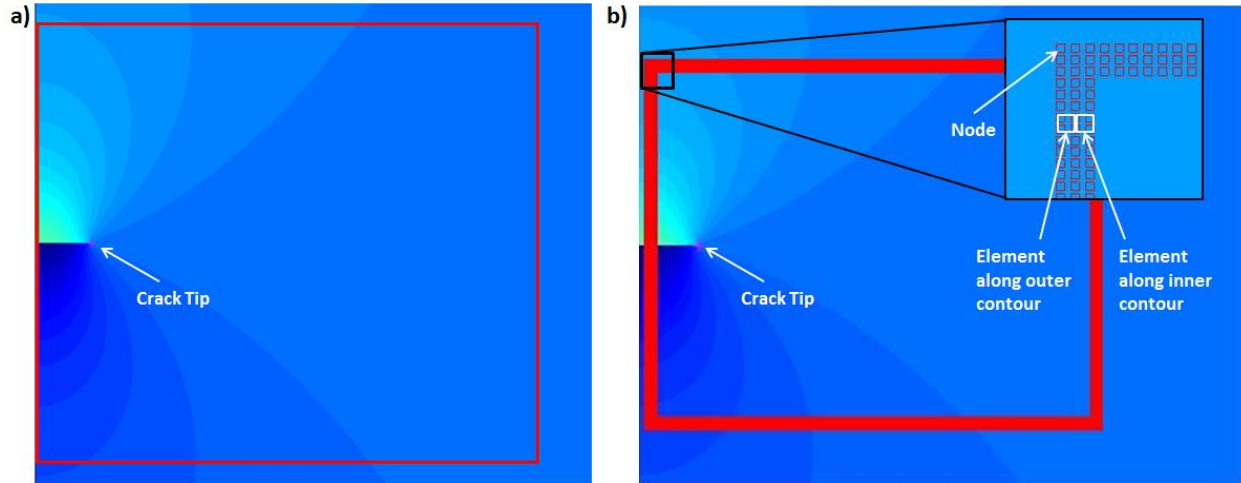


Figure 4.1 Graphical illustration of a rectangular (a) line contour and (b) area contour overlaid on vertical displacement fields (dark blue shades indicate negative displacement). In (a), J is evaluated at each node and the line integral along the contour is evaluated numerically. In (b), J is evaluated at four Gauss points in each element and the area integral is evaluated over the outer and inner area contours using Gaussian integration.

4.3.1 Analytical Validation – Line Integral

The calculation of J using the line integral applied to full-field (analytical) deformation data was path independent and accurate to less than 0.001% error. In this work, the line integral algorithm was validated using analytical expressions of the far-field Westergaard displacement/stress fields [10] generated for a center-cracked isotropic acrylic plate under equal biaxial tension. Full-field displacements (u) were calculated as:

$$\begin{aligned} 2\mu u_1 &= \frac{\kappa-1}{2} \text{Re}\varphi - x_2 \text{Im}\varphi' \\ 2\mu u_2 &= \frac{\kappa+1}{2} \text{Im}\varphi - x_2 \text{Re}\varphi' \end{aligned} \quad (3)$$

where 1 and 2 indicate the principle axes. Functions φ and φ' are the stress function and stress function derivative, respectively, for a center crack of length $2a$ in an infinite plate oriented in the 2 direction and subject to Mode-I loading:

$$\varphi = \sigma_\infty \sqrt{z^2 - a^2} + \text{constant} \quad (4)$$

$$\varphi' = \frac{\sigma_\infty z}{\sqrt{z^2 - a^2}} \quad (5)$$

where $z^2 = x^2 + y^2$. The constant of integration in φ was disregarded as it represents rigid body motion. The constant $\kappa = \frac{3-\nu}{1+\nu}$ is used for the case of plane stress, ν is Poisson's ratio, and μ is the shear modulus. The equations used to generate stress and strain fields were:

$$\begin{aligned} \sigma_{11} &= \left[\text{Re} \left(\frac{\sigma_\infty z}{\sqrt{z^2 - a^2}} \right) - x_2 \sigma_\infty \text{Im} \left(\frac{1}{\sqrt{z^2 - a^2}} - \frac{z^2}{(z^2 - a^2)^{3/2}} \right) \right] \\ \sigma_{22} &= \left[\text{Re} \left(\frac{\sigma_\infty z}{\sqrt{z^2 - a^2}} \right) + x_2 \sigma_\infty \text{Im} \left(\frac{1}{\sqrt{z^2 - a^2}} - \frac{z^2}{(z^2 - a^2)^{3/2}} \right) \right] \\ \sigma_{12} &= -\sigma_\infty x_2 \text{Re} \left(\frac{1}{\sqrt{z^2 - a^2}} - \frac{z^2}{(z^2 - a^2)^{3/2}} \right) \end{aligned} \quad (6a)$$

$$\begin{aligned} \varepsilon_{11} &= \frac{1}{E} (\sigma_{11} - \nu \sigma_{22}) \\ \varepsilon_{22} &= \frac{1}{E} (\sigma_{22} - \nu \sigma_{11}) \\ \gamma_{12} &= \frac{\sigma_{12}}{G} \end{aligned} \quad (6b)$$

where σ_∞ is the applied load ($\sigma_\infty = \frac{K_c}{\sqrt{\pi a}}$) that produces a chosen fracture toughness (K_c) of 1 MPa \sqrt{m} consistent with that of a brittle material; E and G are isotropic elastic and shear moduli.

The J-integral was calculated using the analytically derived deformation data with a rectangular contour that enclosed the right half of the center crack. Fracture toughness values were computed point-by-point along each leg of the contour in a counter-clockwise fashion using a right handed coordinate system. At each point, deformation data was incorporated into an expression adopted from [2]:

$$J = \frac{1}{2} \int_{\Gamma_0} \left[\{\sigma\} \{\varepsilon\}^T n_1 - 2 \left\{ \frac{\partial u}{\partial x_1} \right\}^T [\sigma] \{n\} \right] dS \quad (7)$$

where $\{\sigma\}$ represents the Westergaard-derived stresses, $\{\varepsilon\}$ are the strains as given in (6b), n is the contour normal, n_1 is the contour normal in the crack direction, and $\left\{ \frac{\partial u}{\partial x_1} \right\}$ are the horizontal and vertical displacement gradients with respect to the direction of crack propagation calculated using the finite difference method. J was then converted to K as follows,

$$J = \frac{K^2}{E} \quad (8)$$

where E is the Young's modulus. Note that this relationship holds true only for isotropic materials; a conversion for anisotropic materials will be discussed in *Section 4.4.2*.

Contour size and contour position were varied to confirm path independence and to determine how accurately the algorithm predicted fracture toughness. As illustrated in Figure 4.2 below, the line integral was path independent and correctly measured J ($J = 322.6$ N/m) and K ($K = 1$ MPa \sqrt{m}). Three contour dimensions were analyzed: a large contour comprised of 1800 x 1800 nodes, a smaller contour comprised of 900 x 900 nodes, and a 900 x 900 node contour shifted toward the crack tip by 50% of the half-crack length. For each, the measured value of fracture toughness was 1.0000 MPa \sqrt{m} . The contour was truncated by one pixel either side of the crack flange; although this step is unnecessary for Westergaard data, it is required for experimental data as discussed in *Section 4.4.1*. Error associated with truncation and integration was less than 0.001%.

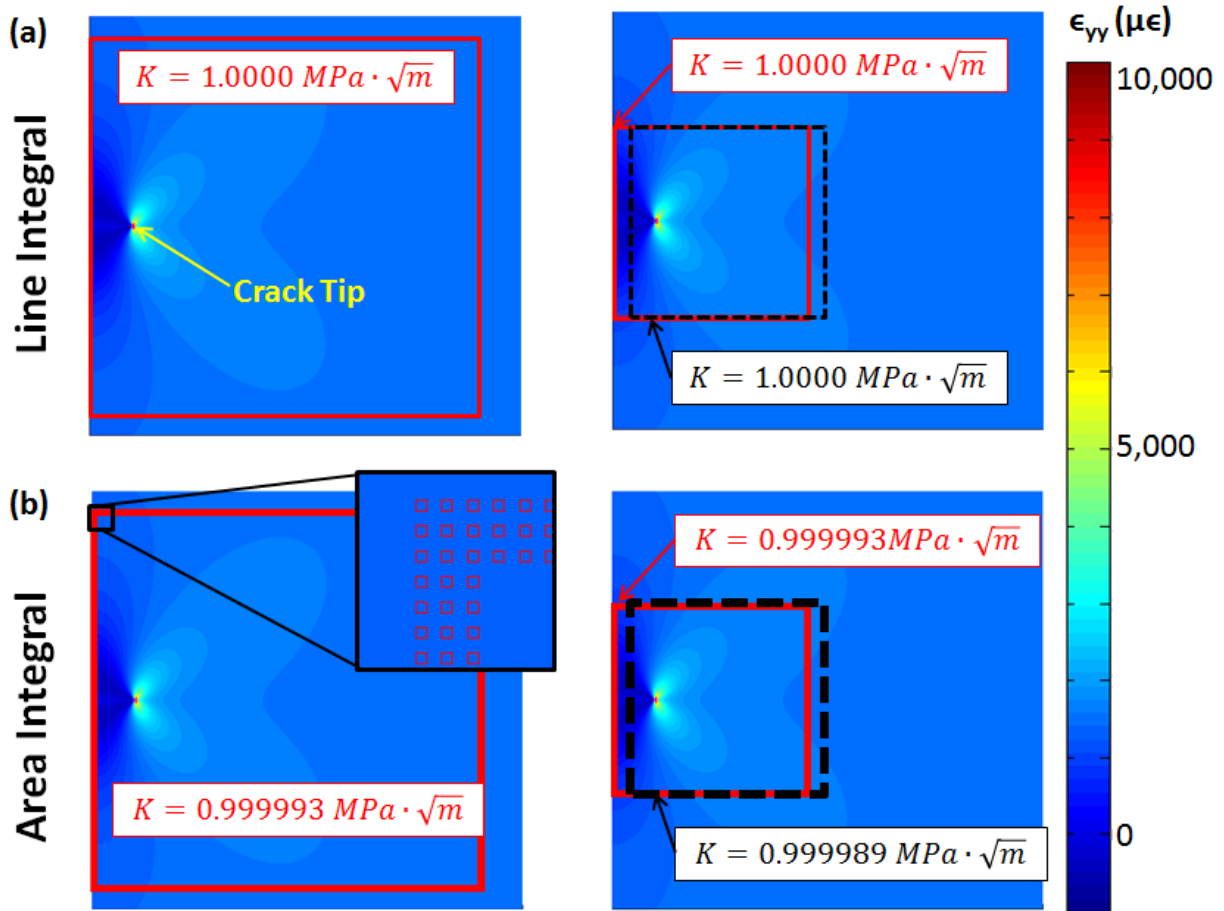


Figure 4.2 Assessment of path independency and accuracy of line integral (a) and area integral (b). In (a), line integral evaluations of fracture toughness over a large contour and small contour, irrespective of position, are 1.0000. In (b), area integral evaluations of fracture toughness vary slightly with position, ranging from 0.0007% to 0.0011% error as the left hand side of the contour is shifted toward the crack tip.

4.3.2 Analytical Validation – Area Integral

The area integral was path independent and accurate to within 0.0011% error. Error magnitude varied slightly with position and increased as the left hand side of the contour was translated toward the crack tip. However, the error was always within 0.0011% as depicted in Figure 4.2. It is attributed to contour truncation about the crack flange and is deemed negligible for assessing the validity of the area integral. As with the line integral, the Westergaard displacement solutions for equal biaxial tension were used as full-field deformation data to validate the algorithm.

From the Westergaard displacements (eqn 3), J was measured using the area integral approach of Li [11]. In this approach, two concentric (inner and outer) contours encircled the crack tip. Each contour was discretized into individual 4-node quadrilateral elements, where each node represented a data point from the displacement field. Each quadrilateral element was 3x3 nodes in size with its central node lying along the contour path. When applied to DIC data, the separation between each node equaled the DIC step size (in units of image pixels). J was evaluated at each of four gauss points within each element and then summed. This process was applied to each element along the inner and outer contours.

The area integral expression is given as:

$$J = \int_A \left[\sigma_{ij} \frac{\partial u_i}{\partial x_1} - W \delta_{1j} \right] \frac{\partial q_1}{\partial x_j} dA \quad (9)$$

For Gaussian integration, this can be expressed as:

$$J = \sum_{All\ elements} \sum_{GP=1}^4 \left[\left(\sigma_{ij} \frac{\partial u_i}{\partial x_1} - W \delta_{1j} \right) \frac{\partial q_1}{\partial x_j} \det \left(\frac{\partial x_k}{\partial \eta_k} \right) \right]_{GP} w_{GP} \quad (10)$$

The locations and displacements of points within each element are expressed in terms of nodal positions and displacements: $x_i = \sum_{K=1}^4 N_K \mathbf{X}_{iK}$ and $u_i = \sum_{K=1}^4 N_K \mathbf{u}_{iK}$ where $i = 1, 2$, with $i = 1$ being the crack propagation direction and direction 2 is orthogonal to 1. N_K are Lagrangian shape functions. \mathbf{X}_i and \mathbf{u}_i are the nodal positions and Westergaard displacements respectively. Values of q at each Gauss point (GP) can fall within the range 0 to 1 and are incorporated into an expression of virtual crack extension as proposed by Li [11]:

$$q_l = \sum_{l=1}^4 N_l \mathbf{q}_{1l} \text{ and } \frac{\partial q_1}{\partial x_j} = \sum_{l=1}^4 \sum_{J=1}^2 \frac{\partial N_l}{\partial \eta_j} \frac{\partial \eta_j}{\partial x_j} \mathbf{q}_{1l} \quad (11)$$

The innermost nodes of the inner contour were set to one ($\mathbf{q} = 1$) while the outermost nodes on the outer contour were set to zero ($\mathbf{q} = 0$). Values of interior nodes were interpolated linearly between 0 and 1. The strain energy, W , was computed as $\frac{1}{2} ([\bar{\mathbf{Q}}]\{\boldsymbol{\varepsilon}\})\{\boldsymbol{\varepsilon}\}$ where $[\bar{\mathbf{Q}}]$ is either the plane stress stiffness matrix for isotropic materials or the transformed laminate stiffness matrix for composite materials and $\{\boldsymbol{\varepsilon}\}$ is the engineering strain, whose components are expressed as a vector. Stress, $\{\boldsymbol{\sigma}\}$, was computed from strain via the stiffness matrix. The weight functions used for Gaussian integration (eqn 10) are denoted w_{GP} . In matrix and vector notation:

$$J_{GP} = \sum_{All\ Elements} \sum_{GP} \left\{ [q_{1,1} \quad q_{1,2}] (det([H])) \begin{bmatrix} \sigma_{11} & \sigma_{12} \\ \sigma_{12} & \sigma_{22} \end{bmatrix} \begin{bmatrix} \frac{\partial u_1}{\partial x_1} \\ \frac{\partial u_2}{\partial x_1} \end{bmatrix} - \frac{1}{2} [\sigma_{11} \quad \sigma_{22} \quad \sigma_{12}] \begin{bmatrix} \varepsilon_{11} \\ \varepsilon_{22} \\ \varepsilon_{12} \end{bmatrix} q_{1,1} (det([H])) \right\} w_{GP}$$

(12)

where:

$$[X] = \begin{bmatrix} X_{11} & X_{21} \\ X_{12} & X_{22} \\ X_{13} & X_{23} \\ X_{14} & X_{24} \end{bmatrix}$$

(13)

are nodal coordinates transformed into the crack coordinate system in physical space and

$$\{u\} = \begin{Bmatrix} u_{11} \\ u_{21} \\ u_{12} \\ u_{22} \\ u_{13} \\ u_{23} \\ u_{14} \\ u_{24} \end{Bmatrix}$$

(14)

are nodal displacements (either analytically derived or measured by DIC) transformed into the crack coordinate system in physical space. The Jacobian matrix $[H]$ used to transform between physical space and isoparametric space is

$$[H] = \frac{1}{4} \begin{bmatrix} -(1-\xi) & 1-\xi & 1+\xi & -(1+\xi) \\ -(1-\eta) & -(1+\eta) & 1+\eta & 1-\eta \end{bmatrix} [X]$$

(15)

The stress vector and strain vectors are denoted as follows, where $[\bar{Q}]$ is the transformed stiffness matrix for the material:

$$[G] = \frac{1}{4} \begin{bmatrix} -(1-\xi) & 0 & 1-\xi & 0 & 1+\xi & 0 & -(1+\xi) & 0 \\ -(1-\eta) & 0 & -(1+\eta) & 0 & 1+\eta & 0 & 1-\eta & 0 \\ 0 & -(1-\xi) & 0 & 1-\xi & 0 & 1+\xi & 0 & -(1+\xi) \\ 0 & -(1-\eta) & 0 & -(1+\eta) & 0 & 1+\eta & 0 & 1-\eta \end{bmatrix}$$

(16)

$$[A] = (1/det(H)) \begin{bmatrix} H(2,2) & -H(1,2) & \mathbf{0} & \mathbf{0} \\ \mathbf{0} & \mathbf{0} & -H(2,1) & H(1,1) \\ -H(2,1) & H(1,1) & H(2,2) & -H(1,2) \end{bmatrix}$$

(17)

$$[B] = [A][G]$$

(18)

$$\{\sigma\} = [\bar{Q}][B][u] \text{ and } \{\varepsilon\} = [B]\{u\} \quad (19)$$

And $\frac{\partial u_1}{\partial x_1}, \frac{\partial u_2}{\partial x_1}$ were then calculated as:

$$\begin{bmatrix} \frac{\partial u_1}{\partial x_1} \\ \frac{\partial u_2}{\partial x_1} \end{bmatrix} = (1/\det(H)) \begin{bmatrix} H(2,2) & -H(1,2) & 0 & 0 \\ 0 & 0 & H(2,2) & -H(1,2) \end{bmatrix} [G]\{u\} \quad (20)$$

For validation purposes, the area integral was applied to two sets of analytically derived displacement data: (1) uniform longitudinal strains in an infinite sheet of PMMA under plane stress; and (2) a center-cracked infinite sheet of PMMA under plane stress longitudinal loading. The purpose of evaluating J in case (1) one was to demonstrate the effect of contour truncation on measurements of J, while the purpose of case (2) was to determine how accurately the J-integral measured fracture toughness

Small systematic error arose from the application of the area integral to the analytical displacement data in both cases, which is due to contour truncation. Findings from the application of the area integral to displacement fields generated by analytically imposing a uniform longitudinal strain on an infinite plate of PMMA (case 1) include:

- Contour truncation introduces error due to the definition of the analytical mesh. For an illustrative example, consider a contour that is 101 nodes wide by 101 nodes tall with a crack that bifurcates the leftmost leg at the 51st node. This leg of the contour must be truncated such that the (non-existent) crack data at the 51st node is not sampled. As the contour is actually comprised of two concentric contours (see Fig 4.1 (b)), this effectively removes two nodes, and consequently two elements, from the leftmost leg but not from the rightmost leg. For the case of a uniform strain field, $J = -0.2567 \text{ J/m}^2$ at each element along the left leg while $J = 0.2567 \text{ J/m}^2$ for each element along the right leg. The loss of two elements from the leftmost leg results in a net value for $J = 0.5134 \text{ J/m}^2$, equating to a net $K = 0.0398 \text{ MPa}\sqrt{m}$. Note that along the bottom and top contours, element values were nominally zero (average values ranged from a minimum of $-7.4 \times 10^{-18} \pm 4.4 \times 10^{-15} \text{ J/m}^2$ on the bottom inner contour to a maximum of $2.4 \times 10^{-13} \pm 4.23 \times 10^{-15} \text{ J/m}^2$ on the top outer contour). Thus, while the area integral algorithm does generate

rounding errors (J along the top and bottom contours should be exactly zero), they are negligible; error is predominately attributed to contour truncation.

Findings from the application of the area integral to Westergaard displacement fields from applying a longitudinal stress on a center-cracked, infinite plate of PMMA large enough to initiate crack growth (i.e. $J_c = 322.5806 \text{ J/m}^2$ and $K_c = 1 \text{ MPa}\sqrt{m}$) include:

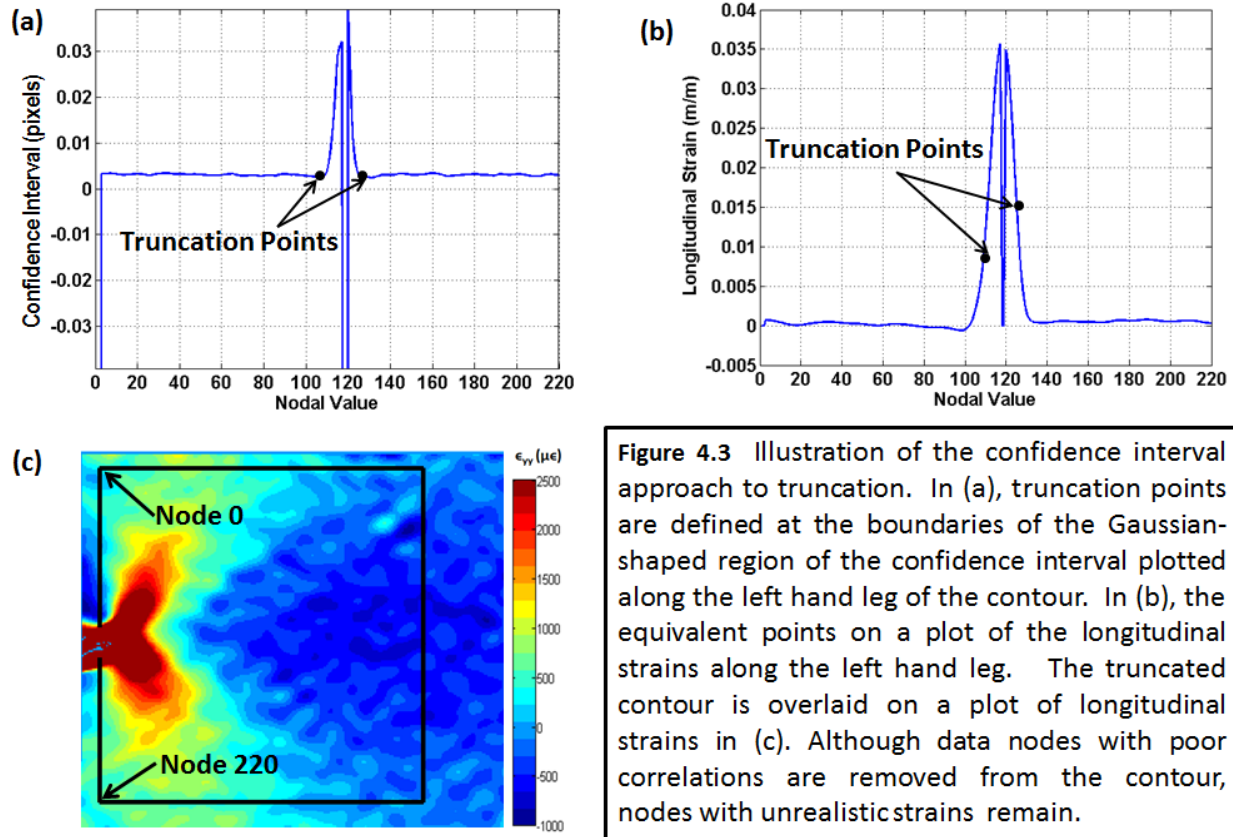
- For contour sizes similar to that which could be reasonably expected for experimental data, error in computing the plane stress fracture toughness was $\sim 0.0007\%$. For a 900 x 900 node contour with its LHS located near the center of the edge crack ($1/8^{\text{th}}$ of the half-crack length right of center), the area integral measured $J = 322.576 \text{ J/m}^2$ ($K = 0.999993 \text{ MPa}\sqrt{m}$). This corresponded to a 0.001% error in J and a 0.0007% error in K. The same values of J and K were attained for a 1800 x 1800 node contour.
- Error increased – slightly – as the contour boundary was shifted towards the crack tip. For example, when the area integral was computed along the 900 x 900 node contour shifted from the center of the crack toward the crack tip such that the left leg was situated halfway between the crack center and the crack tip, $J=322.574 \text{ J/m}^2$ and $K=0.999989 \text{ MPa}\sqrt{m}$, corresponding to underestimates of 0.002% and 0.0011% respectively.
- The primary source of error was contour truncation at the crack flange, which was small enough to neglect as only a few nodes of data were removed the contour. This is the case only for analytical deformation fields. Experimental deformation fields require more aggressive truncation and have noise, which is an additional source of error. Unlike in the case of a uniform displacement field, the contour truncation error was not constant for a non-uniform displacement field. This is because longitudinal and horizontal displacements abruptly changed along the length of the crack flange. Consequently, measured values of J and K in neighboring elements along the crack flange differed. As the position of the contour shifted along the crack flange, the magnitude of truncation error changed as J values in the elements that were removed changed. In experimental applications, it is always necessary to truncate the contour by removing elements in this manner to avoid the evaluation of J in an element containing displacement data at the crack.

4.4 Application of Line and Area Integrals to Experimental DIC Data

4.4.1 Impact of Contour Truncation on Measurements of Toughness

As discussed in *Section 4.3*, with experimental data, contour nodes in the vicinity of the crack flange contain unavoidable erroneous displacement/strain data. For the J-integral to remain valid as the crack grows, the contour must originate and terminate at the upper and lower crack flanges, and at a distance behind the crack tip that falls beyond the fiber bridging zone. Terminating the contour along the flanges of the notch ensures this criterion is met. In experimental deformation fields, however, the crack flanges fall within a region of unrealistically large strains. Thus, the contour was truncated above and below this region following an approach similar to that of Becker [3]. Longitudinal strain fields (ϵ_{yy}) were overlaid on each image to allow for the selection of a rectangular contour surrounding the crack tip that completely encircled the process zone. Two approaches were assessed to determine a proper amount of truncation: plotting, along the leg of the contour that crosses the crack flange, the (1) confidence interval and (2) longitudinal strain or vertical displacements. For case (2), if the strain filter applied to the raw DIC data was larger than the displacement, then longitudinal strains were plotted, and vice versa. A comparison of the two approaches is shown in Figures 4.3 and 4.4. Using strains/displacement for truncation is the only way to ensure that unrealistic deformation data is removed from the J-integral computation and is the recommended method for experimental data.

Plotting the confidence interval is illustrated in Figure 4.3. A contour encompassing a crack tip in a PMMA CT specimen was truncated by removing nodes with large uncertainty in DIC displacement measurements that fall within the Gaussian-shaped region of the curve. In 4.3 (a), truncation points are defined from confidence values plotted along the left leg of the contour; all nodes that fall within the boundaries of these two points are removed from the original contour. The equivalent points are then shown for longitudinal strains (plotted along the left leg) in 4.3 (b). The truncated contour is overlaid on a plot of the longitudinal strain field in 4.3 (c). As shown in 4.3 (b) and (c), even though nodes with high confidence values were removed, the terminal ends of the truncated contour still reside within a region of unrealistically large strain. The strains at the upper and lower truncation points, 8000 and 15000 $\mu\epsilon$ respectively, are well beyond the regime of plastic deformation.



The second approach of truncation using longitudinal strains plotted along the left leg of the original contour is shown in Figure 4.4. In 4.4 (a), nodes with strains that reside within the Gaussian-shaped region of the contour are removed. The corresponding contour plot is overlaid on a longitudinal strain field in 4.4 (b). The truncation points each terminate at regions in which the longitudinal strains are less than $1000 \mu\epsilon$, which are more reasonable values of strain near a crack flange.

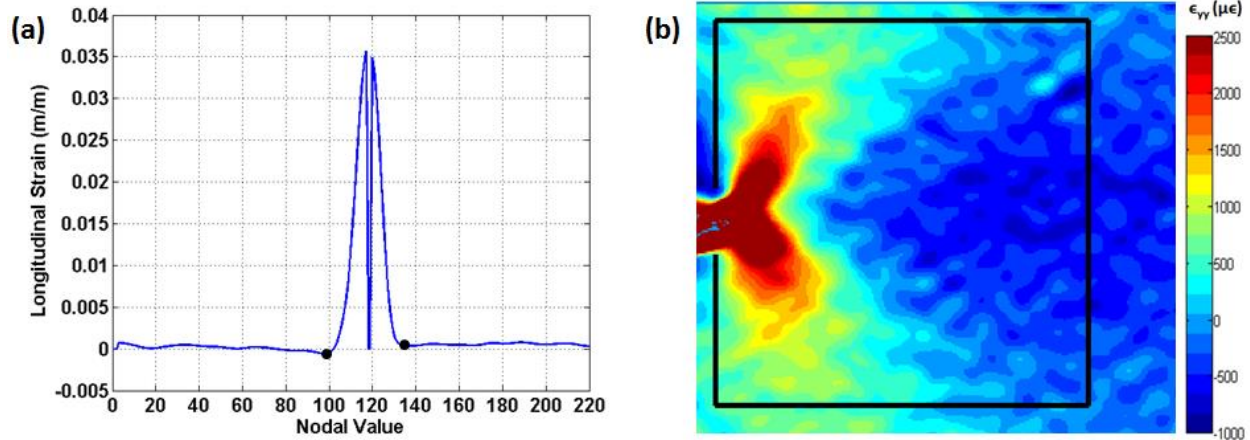


Figure 4.4 Illustration of the strain approach to truncation. In (a), truncation points are defined at the boundaries of the Gaussian-shaped region of the longitudinal strains plotted along the left hand leg of the contour. The truncated contour is overlaid on a plot of longitudinal strains in (b). Longitudinal strains at the termination points are below $1000 \mu\epsilon$, which are reasonable values of strain near the crack flange of a CT specimen.

The effect of truncation can be significant, particularly for materials with low fracture toughness. When evaluated with the J-integral, the contour in Figure 4.3 results in measured fracture toughness of $0.42 \text{ MPa}\sqrt{m}$ whereas that of Figure 4.4 is $0.56 \text{ MPa}\sqrt{m}$ (a comprehensive discussion of experimental evaluations of fracture toughness in PMMA is provided in *Section 4.5.1*). Truncation by confidence interval incorporates strains that are not real into the fracture toughness calculation and is not used in further analyses of fracture toughness. Truncating by longitudinal strain resulted in predictions closer to the range of published values. Note that truncation by longitudinal strain, however, has its own shortcomings. Real mechanical behavior exists within the Gaussian-shaped region. For materials such as CMCs that do not have well defined mechanical properties, establishing a cut-off (such as failure strain) to aid in the selection of truncation points is not possible. Consequently, truncating by removing excessive strain in along the contour introduces some additional error in the measurement. However, truncating the contour using longitudinal strain appears to be a reasonable approach that results in fracture toughness within the range of published values for PMMA, and was adopted in this work.

4.4.2 Experimental Application - Line Integral

The line integral was evaluated using a custom-coded MATLAB routine that utilized the DIC-calculated displacement and strain fields for each image of the advancing crack. For the tested CMCs, the average stress was calculated using experimentally-measured strains and the transformed laminate stiffness matrix ($[\bar{Q}]$), as described by Herakovic [12]. Integration was conducted numerically using the trapezoid rule over the contour Γ^0 . Ply-level elastic moduli were computed using the concentric cylinder model [13-14].

For all tests, when the crack deviated from its travel in a direction perpendicular to the loading axis, the image was rotated to orient the crack horizontally in its own coordinate system. A rectangular contour was then drawn around the crack in the rotated image and its transformed coordinates were recorded so that all J-integral calculations would be computed with respect to the crack coordinate system. The position of each data point, as well as the strain and displacement data at each point, were transformed into this new crack coordinate system as illustrated in Figure 4.5.

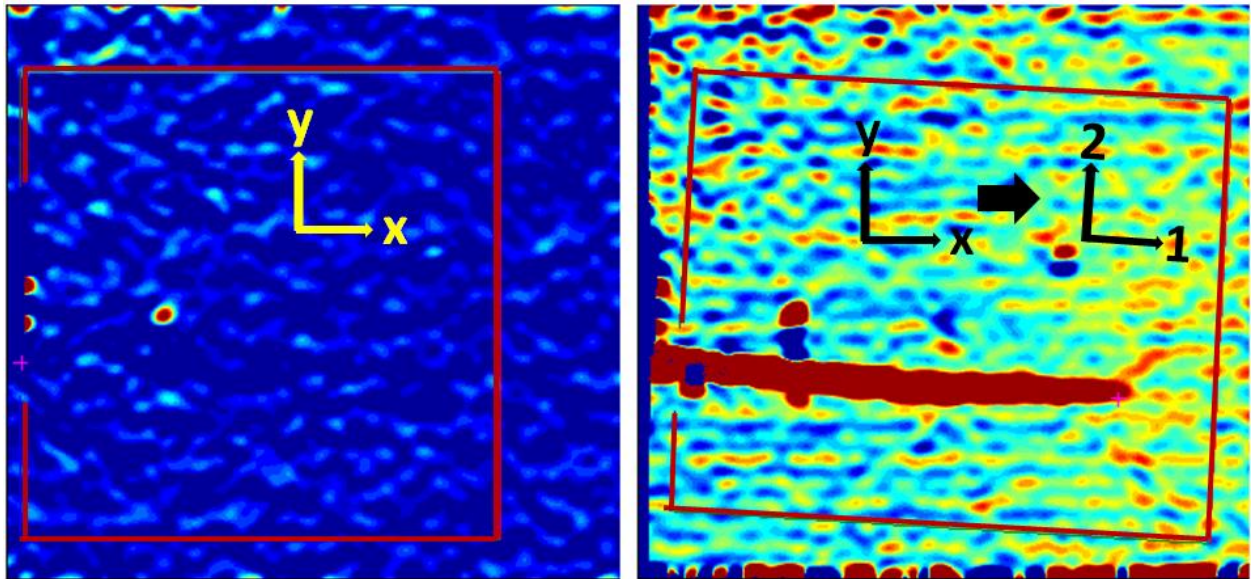


Figure 4.5. J-integral contours prior to and after crack initiation, with the contour oriented in the direction of crack propagation. Displacement and strain data collected along angled contours must be transformed into the crack coordinate system.

For the CMC test shown in Figure 4.5, the J-derived fracture toughness was evaluated in two ways (following eqn 7): (1) by transforming deformation data into the crack coordinate system

as the crack path deviated from perpendicular to the loading axis; and (2) by assuming the crack path deviation was small enough to neglect Mode II contributions (i.e. no transformations were conducted). In addition to the J-integral measurements, stress intensity factors were also calculated using the following closed-form analytical expressions for single edge notch tensile specimens per [15]:

$$K = \sigma\sqrt{\pi a} \cdot f\left(\frac{a}{W}\right) \quad (21)$$

$$f\left(\frac{a}{W}\right) = \frac{\sqrt{\frac{2W}{\pi a} \tan \frac{\pi a}{2W}}}{\cos \frac{\pi a}{2W}} \left[0.752 + 2.02\left(\frac{a}{W}\right) + 0.37\left(1 - \sin \frac{\pi a}{2W}\right)^3 \right] \quad (22)$$

where a is the total crack length, W is the width of the tensile coupon, B is the thickness of the coupon and P is the applied axial load. To account for composite orthotropy, equation (21) was multiplied by the following correction factor [16]:

$$Y(\rho) = 1 + 0.01(\rho - 1) - 0.016(\rho - 1)^2 - 0.002(\rho - 1)^3 \quad (23)$$

Where c is the notch half-width of the notches minor axis, b is the notch length; and ρ and λ are material parameters defined as:

$$\lambda = \frac{E_y}{E_x} \quad (24)$$

$$\rho = \frac{(E_x E_y)^{1/2}}{2G_{xy}} - (v_{xy} v_{yx})^{1/2} \quad (25)$$

E_y , E_x , G_{xy} , v_{xy} , and v_{yx} are the longitudinal and transverse tensile moduli, shear moduli, and Poisson's ratios of the composite laminate respectively. The accuracy of equation (23) is $\leq 2\%$ and is valid for the range of ρ within $0 \leq \rho \leq 4$.

Laminate properties were derived from the reduced transformed stiffness matrix for a symmetric cross-ply laminate [12]. The stiffness ($[\bar{Q}^\theta]$) in each lamina oriented an angle (θ) counterclockwise from the transverse direction in the material coordinate system is given by:

$$[Q^\theta] = \begin{bmatrix} \frac{E_1}{1-\nu_{12}\nu_{21}} & \frac{\nu_{12}E_2}{1-\nu_{12}\nu_{21}} & 0 \\ \frac{\nu_{12}E_2}{1-\nu_{12}\nu_{21}} & \frac{E_2}{1-\nu_{12}\nu_{21}} & 0 \\ 0 & 0 & G_{12} \end{bmatrix} \quad (26)$$

$$[T_1^\theta] = \begin{bmatrix} \cos^2 & \sin^2 & 2 \cdot \cos \cdot \sin \\ \sin^2 & \cos^2 & -2 \cdot \cos \cdot \sin \\ -\cos \cdot \sin & \cos \cdot \sin & m^2 - n^2 \end{bmatrix} \quad (27)$$

$$[T_2^\theta] = \begin{bmatrix} \cos^2 & \sin^2 & \cos \cdot \sin \\ \sin^2 & \cos^2 & -\cos \cdot \sin \\ -2 \cdot \cos \cdot \sin & 2 \cdot \cos \cdot \sin & m^2 - n^2 \end{bmatrix} \quad (28)$$

$$[\bar{Q}^\theta] = [T_1]^{-1}[Q][T_2] \quad (29)$$

The lamina engineering properties were derived via the concentric cylinder model [13] using known properties of the composite's monolithic constituents.

The stiffness of the symmetric laminate was computed as:

$$[\bar{Q}] = \frac{1}{2}([\bar{Q}^0] + [\bar{Q}^{90}]) \quad (30)$$

The laminate compliance was then:

$$[q^*] = [\bar{Q}]^{-1} \quad (31)$$

such that the laminate engineering constants in (24) and (25) become:

$$\begin{aligned} E_y &= \frac{1}{q_{11}^*} & \nu_{xy} &= -\frac{q_{12}^*}{q_{22}^*} \\ E_x &= \frac{1}{q_{22}^*} & \nu_{yx} &= -\frac{q_{12}^*}{q_{11}^*} \\ G_{xy} &= \frac{1}{q_{66}^*} \end{aligned} \quad (32)$$

J was evaluated along the contour length for each image and converted to the plane-stress stress intensity factor, K , using the expressions [17]:

$$K^2 = \frac{J\sqrt{E_x E_y}}{\sqrt{(\alpha+\beta)/2}} \quad (33)$$

$$\alpha = \sqrt{\frac{E_x}{E_y}} \quad , \quad \beta = \frac{E_x}{2G_{xy}} - \nu_{xy} \quad (34)$$

where x and y correspond to principle directions (1 and 2), the elastic constants are laminate constants, and K is Mode-I. Plane stress was assumed because deformation data was collected from the surface of a thin specimen. The plane stress critical stress intensity factor (K_{Ic}) was computed from the image in which the crack initiated at the notch. For cases where the crack propagated at an angle other than perpendicular to the loading axis, the loading was mixed mode and thus J was a mixed-mode measure of toughness.

4.4.3 Experimental Application - Area Integral

The area integral was applied to experimental data in a similar manner to the line integral except that only displacement data was used in the computation (the line integral used both experimental displacements and their associated Lagrangian strains). Since it only required displacement data, the algorithm avoided incorporating the exacerbated noise common in experimental strain data. Stresses and strains were computed from DIC-obtained displacement data using the procedure described in section 4.3.2. Area contours truncated around the notch/crack flange are shown overlaid on longitudinal strain fields in Figure 4.6. The variability apparent in both strain fields is attributed to image noise and bias related to digital image correlation at these small length scales.

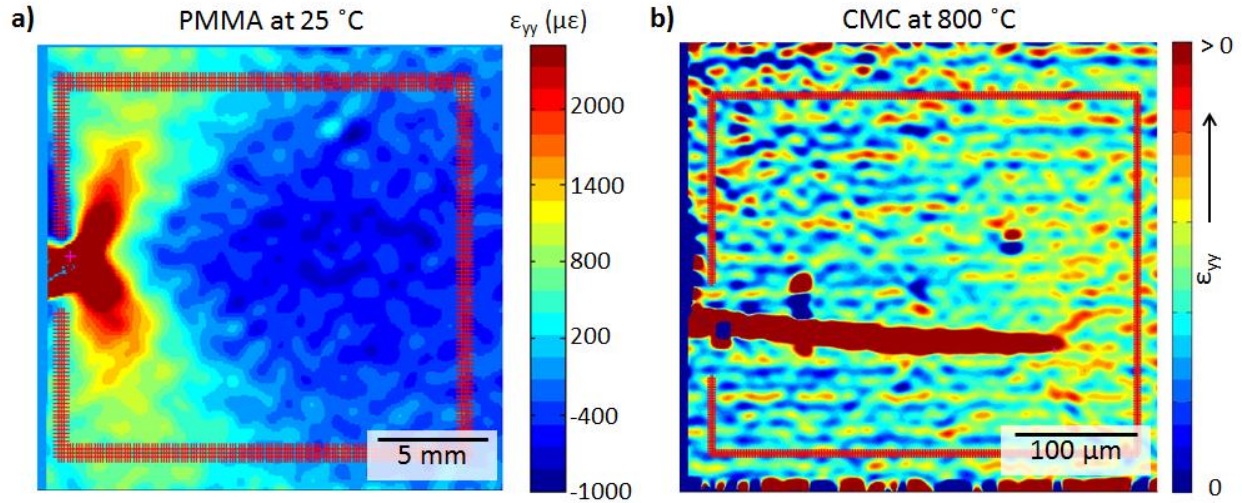


Figure 4.6 Area contours overlaid on longitudinal strain fields in (a) PMMA and (b) SiC/SiC CMC. In both cases, the contour was truncated on either side of the crack flange and extends beyond regions of plastic deformation. In (a), plastic deformation occurs at 2000 $\mu\epsilon$. Strain values have been withheld for the CMC in (b).

4.5 Fracture Characterization: Assessment of Line and Area Integrals

Characterization of toughness for PMMA, Aluminum and SiC/SiC was attempted using the line and area integrals. For all materials, the line and area integrals exhibited a degree of path dependency attributed to contour truncation and DIC data variability. This path dependency was more pronounced in the brittle PMMA and SiC/SiC samples than in the 6061 Aluminum sample. Stress intensity factors measured for PMMA and Aluminum fell within or near the range of published values, however, the area integral measurements were slightly larger than the line integral measurements. R-curves generated for SiC/SiC using the J-integral approach followed a similar trend as those derived for SiC/SiC analytically using a closed form solution but were up to three times larger in magnitude.

4.5.1 Fracture Characterization in Isotropic Materials

4.5.1.a Fracture Characterization: PMMA

To assess algorithm accuracy when applied to experimental data, the line and area integrals were computed from DIC data collected for a tapered double-cantilever PMMA compact tension coupon and a single edge notched 6061 aluminum tensile specimen. In *Section*

4.4.1, it was shown that the J-integral measurement of fracture toughness is sensitive to contour truncation. This section demonstrates that the J-integral (both line and area) is path dependent when applied to experimental data, resulting in toughness measurements that vary in accuracy for contours of different dimensions and positions. However, while path dependency was attributed to contour truncation in the analytical analysis, path dependency is attributed to both contour truncation and data variability in experimental analyses. It is also shown that J-integral measurements of toughness and stress intensity factors change when filtering operations are applied to the input data.

The tapered geometry of the PMMA CT specimen is intended to induce a 30 mm long region of constant stress intensity factors as the crack propagates [18]. As shown in Figure 4.7, both the line and area integrals generate nearly flat R-curves, indicating that both algorithms are capturing the constant-K behavior that is expected. The averaged area integral measurements were nearly twice as large as the averaged line integral: $K = 0.54 \pm 0.01 \text{ MPa}\sqrt{m}$ for the line integral and $0.96 \pm 0.02 \text{ MPa}\sqrt{m}$ for the area integral. Both these measurements were within the range of published measurements of the critical stress intensity factor (0.6 to 2.2 $\text{MPa}\sqrt{m}$ in plain strain or 0.56 to 2.07 $\text{MPa}\sqrt{m}$ in plane stress) [19] for PMMA. The line integral computation in Figure 4.7 incorporated unfiltered displacement data and filtered strain data while the area integral incorporated only unfiltered displacement data; this may explain the difference in magnitude between the two computations.

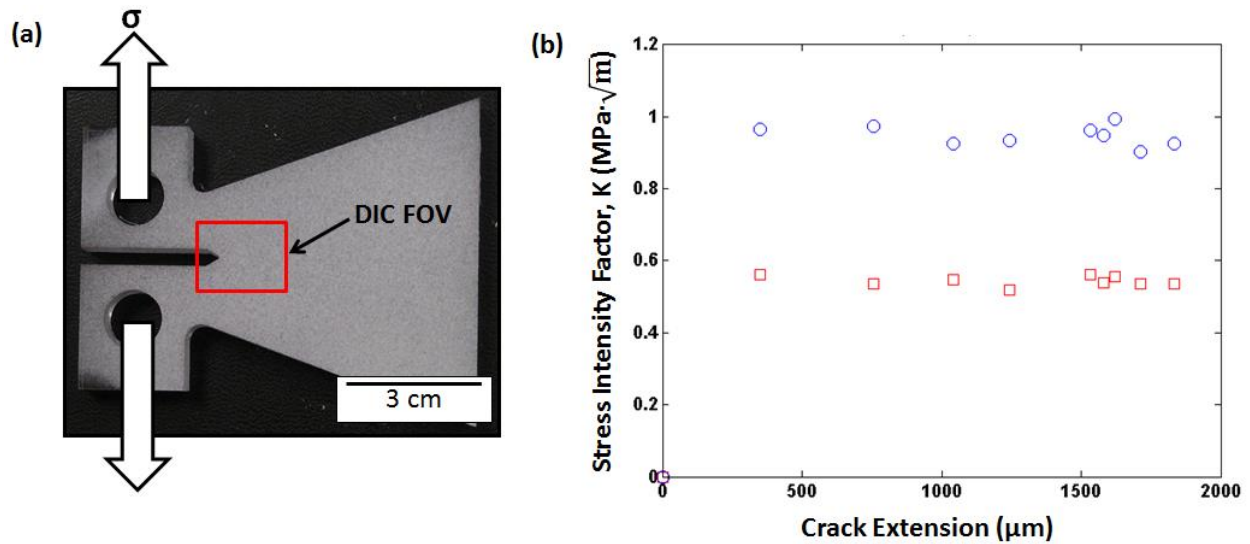


Figure 4.7. (a) Illustration of constant-K PMMA compact tension specimen and (b) R-curves as measured by line (red squares) and area (blue circles) integrals. The area integral stress intensity factors in (b) are larger than the line integral values because the displacement data used in the area integral has not been filtered.

Since variability in the DIC data, which takes the form of random noise and bias, had a significant impact on J-integral measurements (Figure 4.7), a parameter study was conducted to investigate the effect of noise reducing parameters (data filtering and DIC step size manipulation) on stress intensity measurements. The crack was assumed to be macroscopically straight for the parameter study, so data transformations were not conducted. This decision was justified since transforming data in the direction of local crack propagation at the crack tip did not significantly influence the J-integral measurements. This is shown in Figure 4.8, where line and area integrals were evaluated for the case of straight crack propagation (no data transformation was conducted) and for the case of local crack deviations (data was transformed in the direction of local crack propagation).

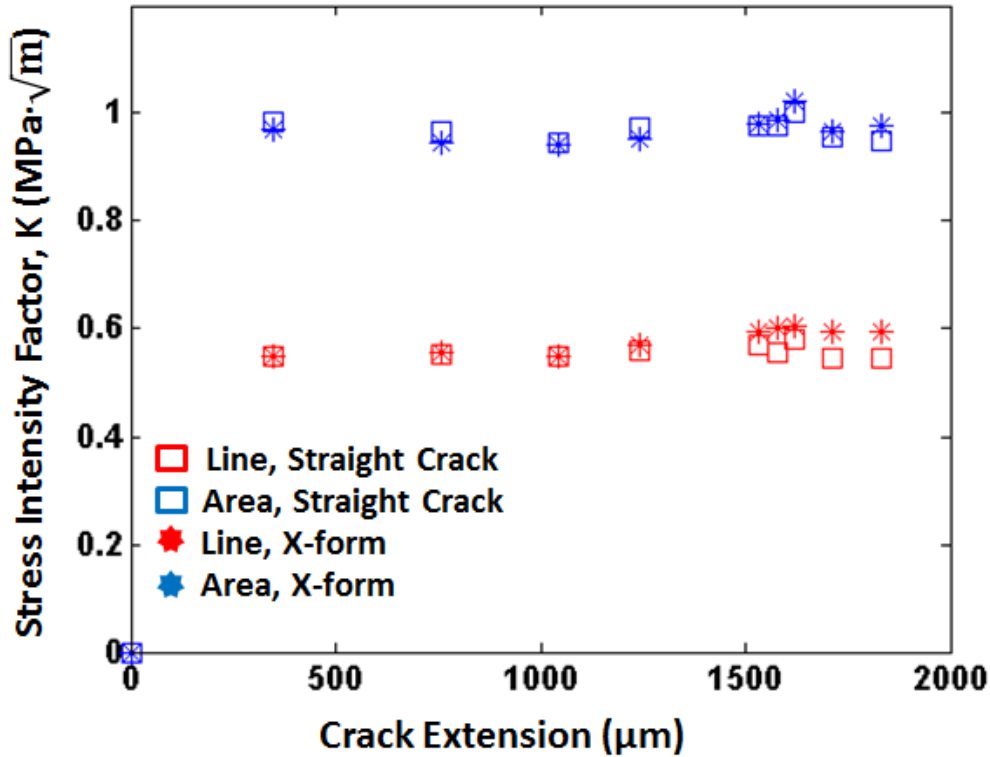


Figure 4.8 Line and area integrals are evaluated for the cases of: (1) assumption of straight crack propagation and (2) transformation of deformation data in the direction of local crack propagation. Transforming data had no significant impact on the stress intensity factor measurements.

Since the line integral algorithm incorporates the DIC-computed Lagrangian strains (unlike the area integral algorithm, which only incorporates displacements), the influence of strain smoothing on the line integral was first investigated. As shown in Figure 4.9(b), the examined filter sizes had little effect on stress intensity measurements in the line integral. However, note that while filtering operations do reduce noise (Figure 4.9 (a)), they come at the expense of reducing spatial resolution. As shown in Figure 4.9, strain data was smoothed by applying 5 and 15 node decay filters prior to evaluating the line integral. As the DIC subset size used to generate the deformation field data was 41 pixels and the DIC step size was 5 pixels, the two filtering operations smoothed the strain data over regions 61% and 180% of the subset size. In addition to the strain filters, 5 node and 15 node averaging filters were also applied to the displacement data. The filtered longitudinal strain fields are shown in Figure 4.9 (a) and the resulting stress intensity factors shown in Figure 4.9 (b).

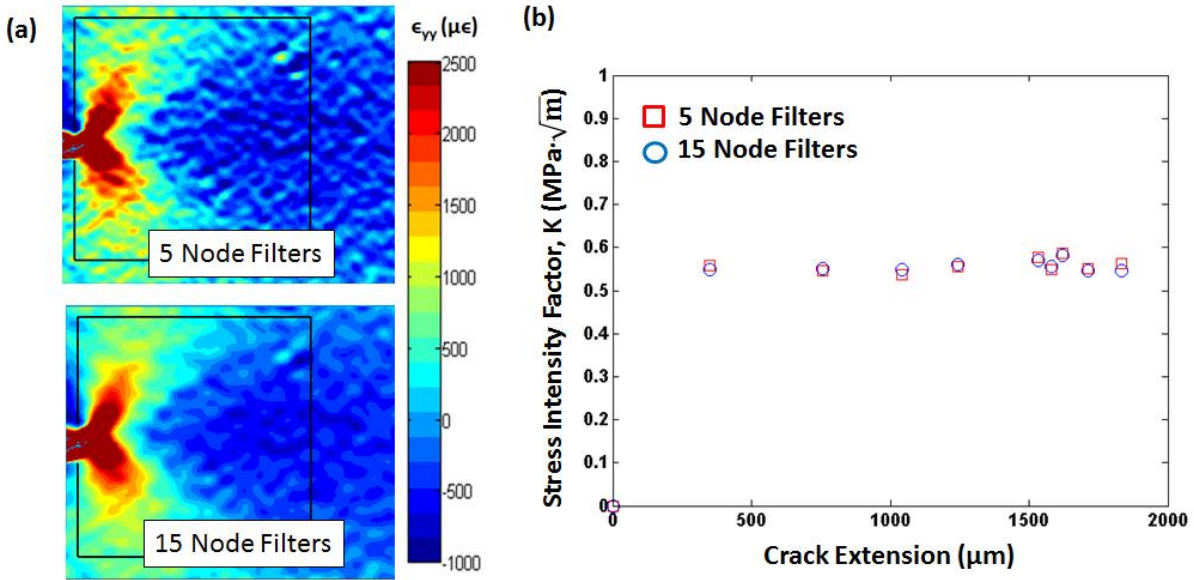


Figure 4.9 In (a), longitudinal strain fields are plotted for less aggressive (5 node) and more aggressive (15 node) strain filtering. Truncated line integral contours are overlaid on the strain fields. In (b), R-curves generated from line integral measurements with 5 node and 15 node filtering schemes are plotted. The smaller filtering operations resulted in slightly higher stress intensity factors.

Next, the sensitivity of both the line and area integrals to filtering displacement data was examined. Although toughness and stress intensity measurements for both the line and area integrals generally decreased as the amount of filtering increased, the area integral was more sensitive than the line integral. Also, increasing the filter size did not lead to convergence of the area and line integral R-curves. For this analysis, strain filtering (line integral only) was held constant at 15 nodes. The DIC subset size was 41 pixels and the step size was 5 pixels. Figure 4.10 (a) through (c) show R-curves for 5, 15 and 30 node averaging filters applied to the displacement data. As the filter size increased from 15 to 30 nodes, the average stress intensity factor for the area integral dropped from $0.96 \pm 0.02 \text{ MPa}\sqrt{m}$ to $0.7 \pm 0.04 \text{ MPa}\sqrt{m}$ but only dropped from $0.55 \pm 0.01 \text{ MPa}\sqrt{m}$ to $0.52 \pm 0.02 \text{ MPa}\sqrt{m}$ for the line integral. When the displacement filter size was increased to 40 nodes, the average stress intensity as computed by the area integral dropped drastically to $0.24 \pm 0.09 \text{ MPa}\sqrt{m}$. The area integral is more sensitive to displacement filtering because its sole source of data input is displacements, whereas filtered strains serve as input data for the majority of the mathematical operations involved in computing the line integral.

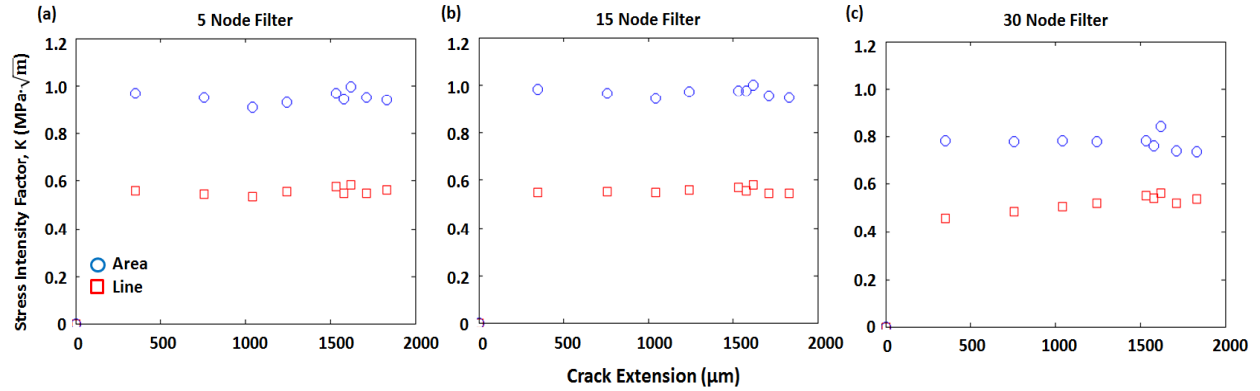


Figure 4.10. R-curves for PMMA tapered DCB-CT sample as measured by line and area integrals after: (a) 5 node, (b) 15 node and (c) 30 node averaging filters are applied to displacement data from DIC. The area integral is more sensitive to displacement smoothing than the line integral because it contains more mathematical operations on displacements.

Noise can be reduced by increasing the DIC step size, because displacement data over the entire field of view is then interpolated between data points that are spaced further apart. A comparison of R-curves collected at two different step sizes is shown in Figure 4.11. In 4.11 (a), the step size over which DIC data was collected was 5 image pixels, or $1/8^{\text{th}}$ of the 41-pixel subset size. In 4.11 (b), the step size was 21 pixels, or $1/2$ of the subset size. In (a) and (b), a 5 node (25 pixel) averaging filter was applied to the displacement data. The larger step size resulted in lower measurements of toughness and stress intensity factor for both algorithms. The resistance curves in 4.11 (b) exhibited a slight positive slope whereas those of 4.11 (a) were flat. This may be an artifact of the larger step size. A shortcoming of sampling fewer data points is that material deformation that occurs between data nodes goes undetected. If the DIC data mesh is too sparse, sharp changes in displacement at regions of the material that exhibit large deformation gradients will not be factored into the J computation. This, in turn, will affect the magnitude of J and K measurements and shape of resistance curves.

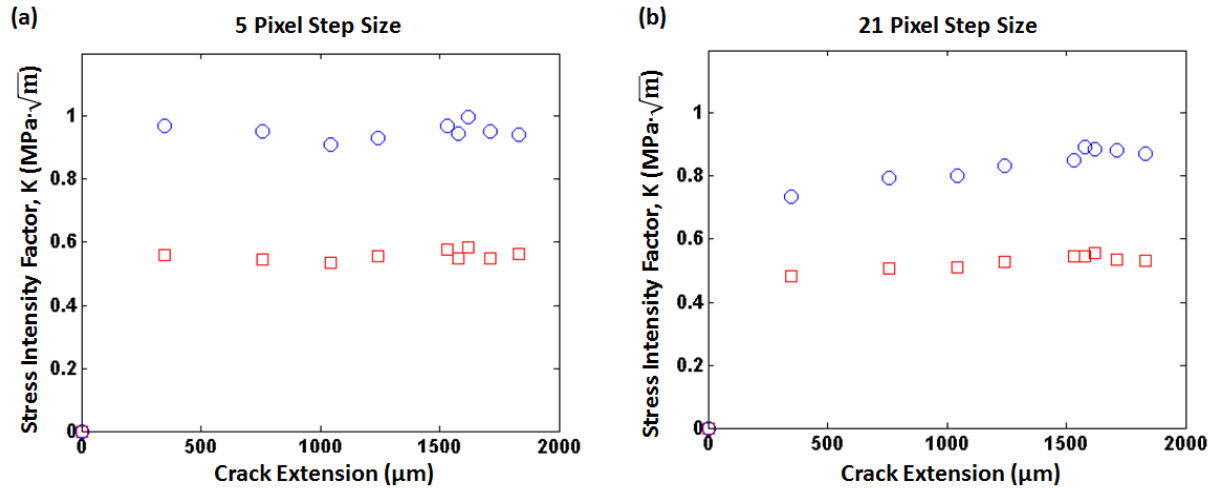


Figure 4.11. R-curves for PMMA tapered DCB-CT sample as measured by line and area integrals using (a) 5 pixel and (b) 21 pixel DIC step sizes. Stress intensity factors were lower for J-integrals evaluated using deformation data from the larger step size.

The line and area integrals were both path dependent; as the size of the contour increased, the stress intensity factor decreased. The significance of this is that, even with relatively low-noise DIC data, the supposedly path independent J-integral was in fact highly path dependent. This is attributed to a strong susceptibility of the J-integral to variability in the DIC data. To illustrate, Figure 4.12 depicts two different sized contours overlaid on a longitudinal strain field generated from DIC using a 41 pixel subset and 5 pixel step size. Line integral (4.12 (a)) and area integral (4.12 (b)) measurements were conducted using 15 node displacement (both integrals) and 15 node strain (line integral only) filtering operations. The smaller contour is 100x100 pixels and the larger contour is 200x200 pixels. In 4.12 (a), increasing the line integral contour decreases the stress intensity factor by 11%. In 4.12 (b), increasing the area integral contour decreases the stress intensity factor by 7%. The smaller path lies closer to the plastic zone, which may account for the larger stress intensity. However, when the large contour was shifted right by just 5 nodes, stress intensity factor again dropped to $0.52682 \text{ MPa} \sqrt{m}$ (-5.3%) in the line integral and $0.90371 \text{ MPa} \sqrt{m}$ (-2.8%) in the area integral. The line and area integral both predicted critical stress intensity factors within the range of published values (0.56 to 2.07 $\text{MPa} \sqrt{m}$ in plane stress), but the area integral was nearly double the line integral. It fell in the middle of this range and is expected to be a more accurate measure as it samples more data

points, making it less susceptible to variability than the line integral. A detailed analysis of variability and its impact on the J-integral is presented in *Section 4.6*.

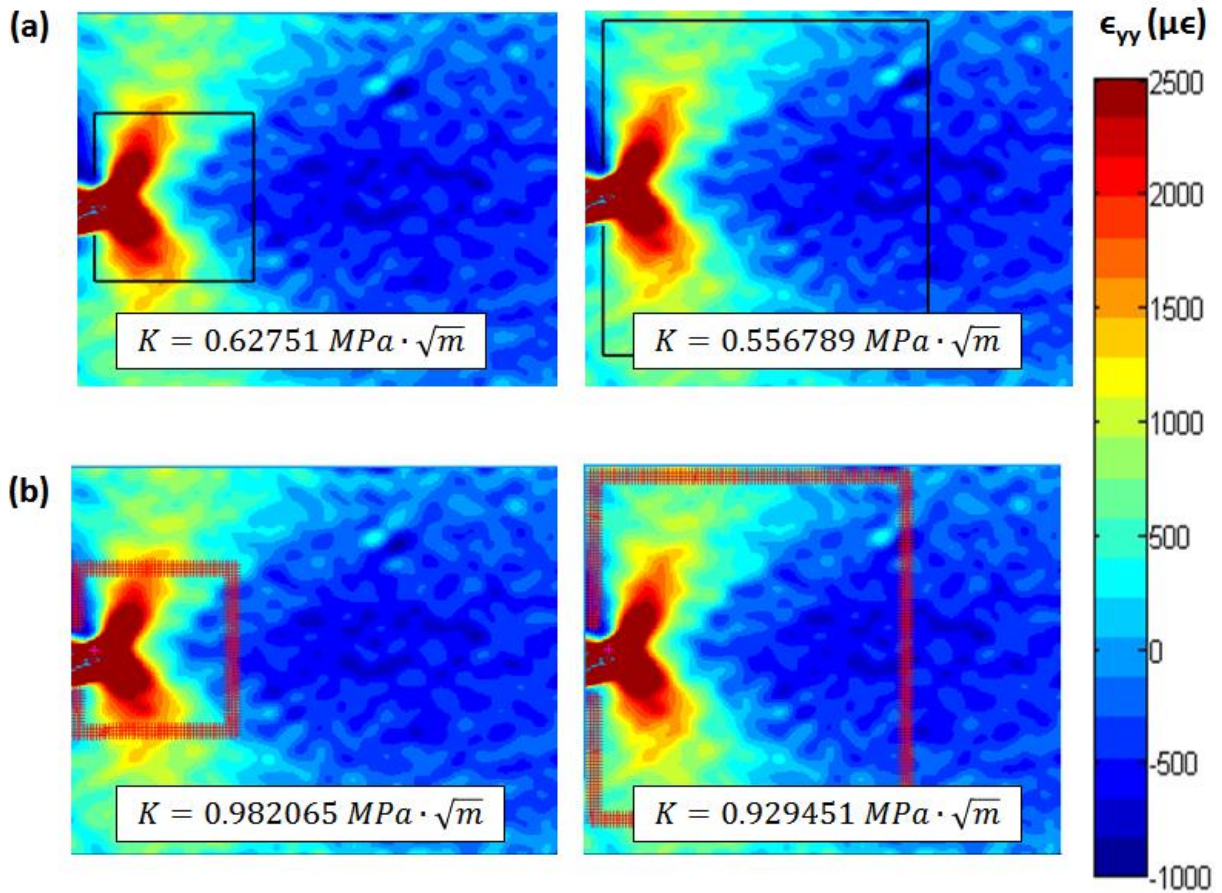


Figure 4.12. Stress intensity factors vary with contour size for both the (a) line integral and (b) area integral. Although the variations are small, the J-integral is path dependent.

4.5.1.b Fracture Characterization: Aluminum

Toughness and stress intensity factors were evaluated for a single edge-notched 6061 Aluminum tensile coupon. For all analyses, a DIC subset size of 55 pixels was used. The field of view was 21 mm (1600 image pixels). Figure 4.13 depicts the tensile specimen and DIC field of view. Given a Young's modulus of 68.9 GPa and yield strength of 276 MPa [20], the strain at yield is about 4000 $\mu\epsilon$. Thus, contours were drawn in regions outside of 4000 $\mu\epsilon$. The published plane strain fracture toughness is 34 $MPa\sqrt{m}$ [21], or 32 $MPa\sqrt{m}$ for plane stress. As DIC measurements were taken on the surface, J-integral measurements of fracture toughness were plane stress. The J-integral was evaluated until the point where plastic zone size exceeded the

size of the largest contour that could be drawn. Because this occurred before a crack initiated from the notch tip, stress intensity factors were plotted with respect to crack opening displacement.

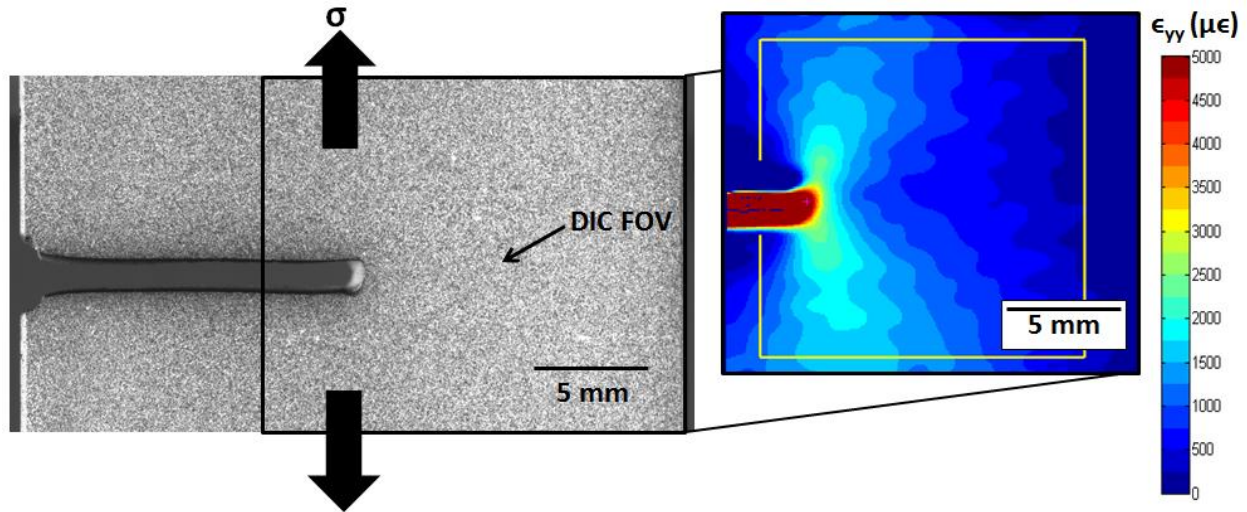


Figure 4.13 Aluminum single edge notch tensile specimen loaded in uniaxial tension. 21 mm DIC field of view is overlaid on tensile specimen. Contour for line integral is plotted on longitudinal strain field. Note that the boundaries of the contour are outside of the plastic zone.

Figure 4.14 shows plots of stress intensity factor versus crack opening displacement as derived from both the line and area integrals. Increasing the step size resulted in a slight drop in measured stress intensity factors (Figure 4.14(a)) while filtering the displacements had no significant impact on the stress intensity factors (Figure 4.14(b)). In 4.14 (a), the J-integral was measured from DIC data at step sizes of 5 pixels and 21 pixels (9% and 38% of the subset size, respectively). For the line integral only, strain filters of 21 and 5 nodes were applied to the smaller and larger step-sizes, respectively. No displacement filtering was conducted. In 4.14 (b), 21 node displacement filters were applied to the 5 pixel step-size data (with 21 node strain filtering for the line integral). The lower sensitivity of J measurements to filtering in the aluminum than in PMMA is attributed to the more ductile aluminum having less noise than the relatively brittle PMMA.

In 4.14 (a) and (b), the area integral measurements grow increasingly larger than the line integral measurements as the crack opening increases. The area integral output is more sensitive to the magnitude of the displacement data that is input, even when the displacements are filtered.

Of the data that could be sampled, all occurred before a well-defined crack emanated from the notch. Thus, the curves in Figure 4.14 terminate at or prior to reaching fracture toughness.

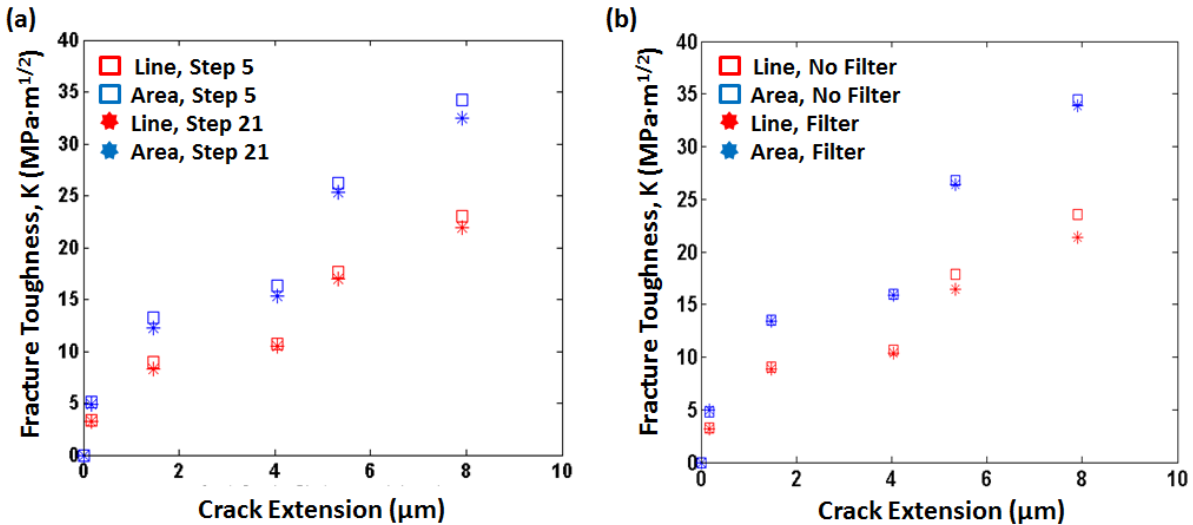


Figure 4.14 Plots of stress intensity factor versus crack opening displacement for the line and area integrals. In (a), increasing the step size from 5 to 21 pixels resulted in a slight drop in stress intensity factors. In (b), applying a (21 node) averaging filter to the displacement data prior to evaluating J had little to no effect on the stress intensity factors.

4.5.2 Fracture Characterization: SiC/SiC

Line and area integrals were used to evaluate fracture toughness for four SiC/SiC edge-notched tensile coupons: (1) [0/90/0/90]_s tensile coupons loaded in uniaxial tension at 800° C in SEM vacuum and (2) two ply unidirectional laminates loaded in uniaxial tension in the fiber direction at ambient temperature. Details of (1) and (2) are discussed in *Sections 4.5.2.a* and *4.5.2.b*, respectively. For all CMC tests, resistance (R) curves were plotted as stress intensity factor versus crack opening displacement. It is acceptable to replace J with K for the R -curves as fracture in ceramic materials exhibit local small scale yielding, which permits a direct correlation between J and K [22]. Crack opening displacements were plotted rather than crack extension. Crack extension cannot be accurately characterized in a CMC because the crack tip position varies through the thickness of the material. In fact, deducing the position of the crack tip on the surface of the material from DIC data is a circumspect technique. To reduce noise, DIC data is filtered over several nodes of deformation data. This reduces spatial resolution and consequently increases uncertainty in the crack tip position. Reducing the filter sizes raises the noise signal,

which makes accurately distinguishing the crack tip from noise difficult. It is also for this reason that no attempt is made in this work to define a single value of fracture toughness for the CMC. Determining the critical stress intensity to initiate fracture requires an accurate means of determining crack initiation, which in turn requires accurate identification of the crack tip. For this reason, no attempt was made to define a single value of fracture toughness for the CMC; instead ranges of fracture toughness (plane stress) were established.

4.5.2.a Fracture Characterization: SiC/SiC [0/90/0/90]s at 795° C

Line and area integrals were used to evaluate fracture toughness and crack resistance for two edge-notch cross-ply SiC/SiC CMCs loaded in uniaxial tension at 795° C in a SEM. In addition to the J-integral calculations, stress intensity factors were computed using a closed form solution for orthotropic materials that incorporated experimentally measured loads and crack lengths. For all three methods – line, area, and closed form - fracture toughness was measured as a function of crack length and plotted as resistance curves. The closed-form solution represents a global measure of stress intensity assuming only a single crack exists in the material. On the other hand, the numerical (J-integral) methods represent localized, constituent-level measures of fracture toughness taken in the vicinity of a single crack. The numerical (J-integral) approach was conducted in two ways: (1) deviations of the crack path in any direction other than perpendicular to the loading axis were assumed to occur over a small enough length that the crack, as a whole, was treated as if it was a straight crack perpendicular to the loading axis; (2) deviations of the crack path were large enough that all position and deformation data was transformed into a crack coordinate system that was aligned with the local direction of crack propagation. The latter case was expected to account for directional dependence on toughness in the anisotropic composites. Ultimately, transforming data into the crack coordinate system had no significant impact on toughness and stress intensity measurements.

A schematic of the loading fixture and a plot of resistance curves derived from the closed form and J-integral methods for one of the first of two tensile tests are shown in Figure 4.15. In 4.15 (a), the CMC is shown mounted in the in-situ load/heating fixture prior to being placed in the SEM. Attached to the CMC was a miniature tungsten resistance heater capable of heating to 800° C. To reduce noise from thermal emissions, tantalum heat shields with 6 mm apertures were placed above the sample. In 4.15 (b), resistance curves from the 795° C tensile test are

plotted alongside a closed form solution for stress intensity factors. The line integral and area integral curves show good shape agreement with the closed-form curve, but the magnitudes of the stress intensities are larger. It is not surprising that the closed form solution under predicts stress intensity in the CMC. By the time a single matrix crack has begun propagating, the composite contains several matrix cracks. The closed form computation only incorporates the length of one of many cracks. If the closed form K were converted to J , the resultant toughness would not accurately reflect the actual potential energy released in the material. On average, the line integral was 2.0 ± 1.2 times greater and the area integral was 3.7 ± 1.7 times greater than the closed form solution. The largest discrepancy occurred at the first two loading increments, where the noise to signal ratios were highest. The area integral measurements are expected to be more accurate than the line integral since more data is sampled, making it less susceptible to variability.

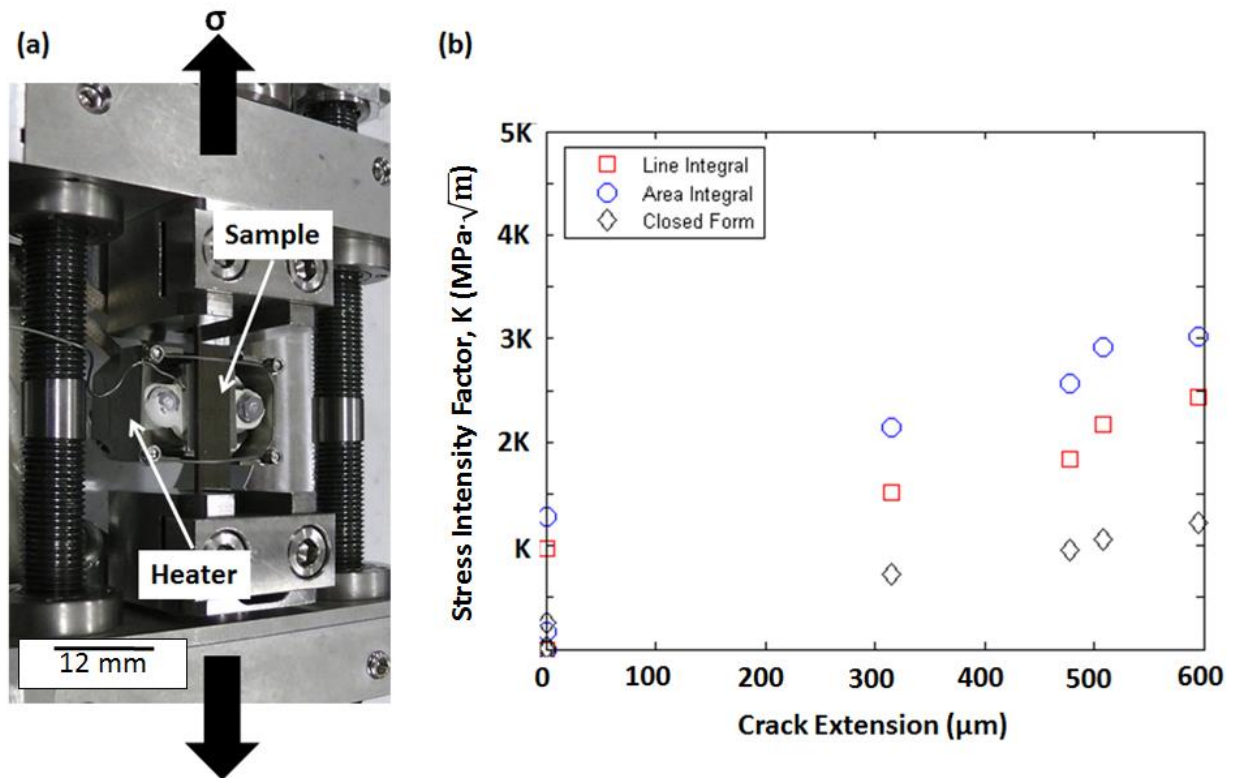


Figure 4.15 (a) CMC mounted in mini tensile stage. Attached to the bottom of the sample is a resistance heater capable of heating to 800^o C in the SEM. (b) Experimental R-curves for SiC/SiC CMC at 795^o C derived using a closed form analytical expression (black diamonds), line integral (red squares) and area integral (blue circles). The analytical curve represents global measures of stress intensity for a single matrix crack, whereas the J-integral solutions are a measure of local stress intensity in the vicinity of the notch. Note: all stress intensity factors are normalized to a reference value, K .

It is not certain whether the variation in magnitude between the J-integral resistance curves and the closed form resistance curve is a consequence of the closed form solution underpredicting stress intensities or is an artifact of the localized nature of the J-integral measurement. Unlike the closed form solution, the J-integral measurements of toughness are derived from deformation data in the vicinity of a single matrix crack. While the J-integral provides a measure of toughness in a single matrix crack, it too is not reflective of toughness in the overall composite. In the composite, potential energy released in the material results from the propagation of multiple cracks, not just a single crack. However, because neighboring cracks mutually influence each other (e.g. load relaxation), the J-integral measurements of toughness capture the local effects of fiber-fiber interactions whereas the closed form solution does not.

Regarding accuracy of J-integral measurements, there are several sources of error that should be considered:

- Contour truncation removed physical deformation data from the J-integral calculations. However, the nodes of data that were removed were in the vicinity of the crack flange; the actual deformation at those locations was likely too small to have a significant impact on the toughness measurements.
- When data was transformed into the crack coordinate system, the contour was rotated into the crack growth direction. To prevent the lower left leg of the contour from rotating out of the original FOV, the entire left leg had to be shifted toward the crack tip. Consequently, the LHS of the contour had to be truncated about the crack flange rather than the notch flange in order for the entire contour to remain within the FOV. This caused the truncation points to fall within a potential fiber-bridging zone, which would raise the toughness and stress intensity measurements. Whereas the notch flange is traction free, the crack flange (in the early stages of crack propagation) experiences closing tractions. However, at the truncation points on the contour remote from the flange faces, the deformation values in a contour that crosses the crack flange are probably close enough to the values in a contour that crosses the notch flange that the error introduced is small.
- The crack length used to compute the analytical curve was measured directly from scanning electron micrographs, and did not take into account the effective length that could result from the presence of fine microcracking ahead of the crack tip. If the effective length was larger, the values of K would also be slightly larger.
- The SEM-DIC and DIC data contained unavoidable noise and bias error. Filtering the deformation data considerably reduced this variability. For the J-integral curves in Figure 4.15 (b), the deformation data was generated with a 41 pixel subset size, 2 pixel step size, 35 node strain filter (line integral only) and 35 node displacement filter (line and area integrals). Additionally, the data was transformed into the crack coordinate system. This combination of parameters produced curves that best replicated the trend in the closed form solution. However, as is discussed in detail in *Section 4.7*, filtering

deformation data in CMCs may mask underlying damage and should be used with caution.

The low-scatter line and area integral curves presented in 4.15 (b) reflect J-integral measurements after optimal data smoothing. Adjustments to the DIC step size and filtering schemes significantly impact the J-integral measurements. In Figure 4.16, resistance curves for the line and area integrals using the same DIC parameters as 4.15 (b) are plotted with the closed form curve, this time with unfiltered displacement data. In 4.16 (a) it is assumed that the crack is generally straight. In 4.16 (b), data is transformed in the direction of the crack tip. In both plots, the stress intensity factors generally increases with crack extension. As opposed to the curves of the filtered data in 4.15 (b), the stress intensity measurements in 4.16 (b) are erratic, sometimes increasing and other times decreasing with crack extension. Measurements from the transformed data are lower than those of the straight crack data. This may be due to the curves in 4.16 (a) incorporating both Mode I and Mode II fracture toughness contributions; the crack deviated at a 4° angle shortly after initiating from the notch.

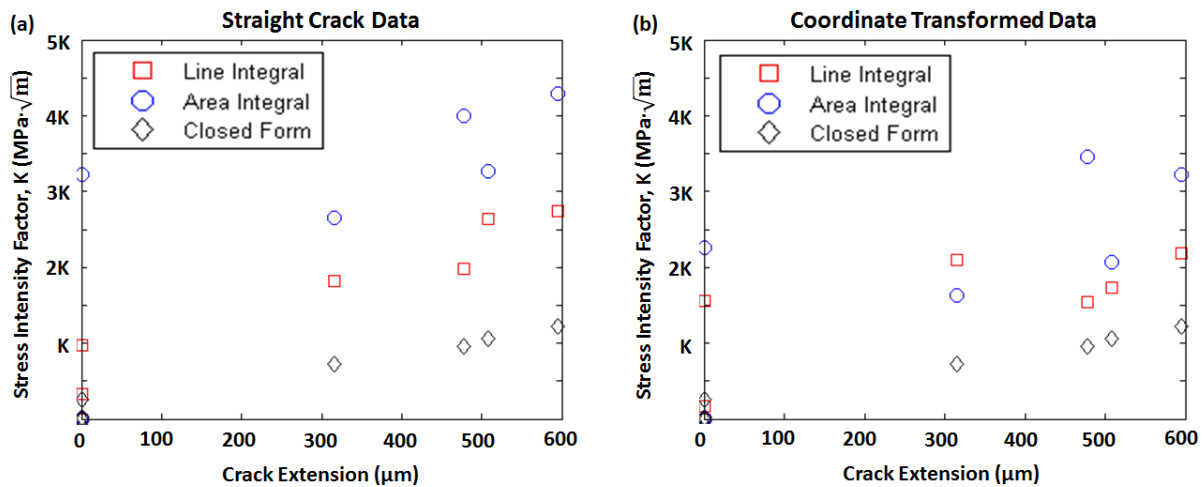


Figure 4.16 Unfiltered resistance curves generated from the line integral, area integral, and closed form solution. In (a) the crack is assumed to be macroscopically straight; data is not transformed. In (b), data is transformed into the local crack-tip coordinate system. Curves from the unfiltered data of (a) and (b) behave erratically in contrast to the filtered data curves of Figure 4.15 (b). This is attributed to variability in the displacement data. Note: all stress intensity factors are normalized to a reference value, K .

Displacement filtering and changes in the DIC step size impacted the shape and magnitude of the resistance curves. Increasing the filter size reduced noise and bias, resulting in

reduced variability in the resistance curves and lower stress intensities. This is illustrated in Figure 4.17 (a), where R-curves generated from unfiltered displacement data with a 2 pixel step size are plotted against R-curves for displacement data that has been smoothed with a 35 node (70 pixel) averaging filter. In Figure 4.17 (b), the step size was increased from 2 pixels to 10 pixels. For unfiltered data, increasing the step size did not reduce scatter in the curves. However, applying a 5 node (50 pixel) averaging filter smoothed the R-curves such that they took the form of those in 4.15 (b). Note that Becker [3] measured J values close to analytical measurements using a modest filtering scheme (a step size 25% of the subset size) for 316 stainless steel. Becker did note that using too aggressive of a filtering scheme (e.g. a step size equal to the subset size) resulted in greater error because of the reduced spatial resolution that comes from filtering, but the error associated with DIC data variability was not addressed.

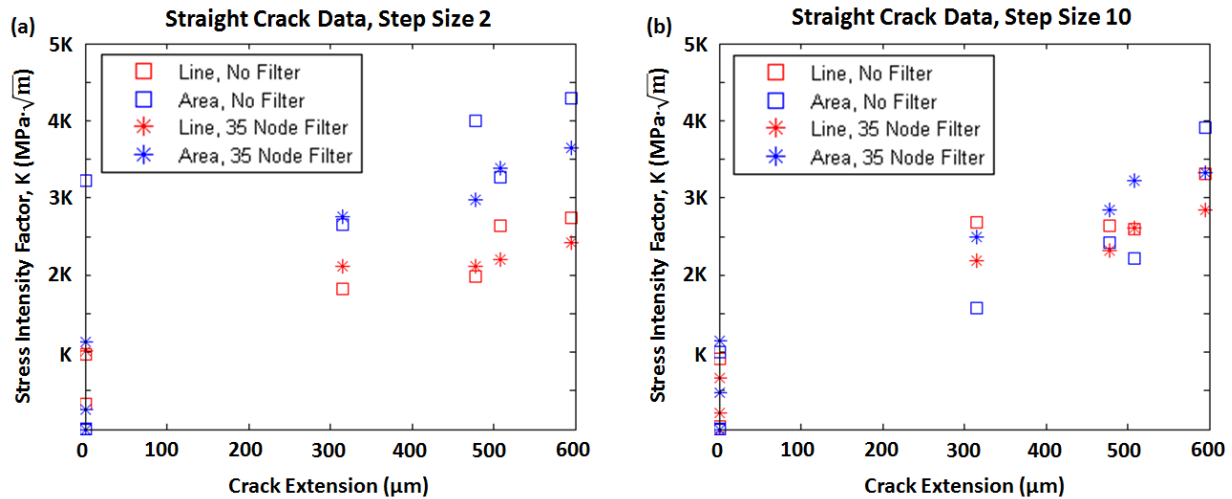


Figure 4.17 Effect of displacement filtering and step size on stress intensity factors. In (a), R-curves generated from unfiltered data (squares) are plotted against r-curves generated from filtered displacement data (asterisks). Increasing the step size reduced variability in the curves and stress intensity factors. In (b), an increase in step size from 2 pixels to 10 pixels did not reduce scatter in the curves for unfiltered data (squares), but did reduce the disparity between the line and area integrals for filtered data (asterisks). Note: all stress intensity factors are normalized to a reference value, K .

To summarize, noise and bias in DIC data, contour size and position, and the amount of truncation are all factors that impact J-integral measurements in CMC DIC data. It has been shown that filtering deformation data (strain and displacement data for the line integral, displacement data only for the area integral) reduced fluctuations and scatter in the resistance

curves computed by the J-integral algorithms. A limitation of the J-integral that remains unresolved is the dependency of toughness measurements on the contour path, which is particularly problematic for materials with low failure strains. As an illustrative example, line integrals of various sizes were evaluated on data corresponding to a crack extension at 315 μm in Figure 4.18, using the same DIC parameters and filtering scheme as in Figure 4.15 (b). In 4.18 (a), the line contours were truncated about the notch tip to remove high intensity noise emanating from the notch from the J computation. In 4.18 (b), the contour was truncated about the crack flange just ahead of the notch tip, which removed less data but resulted in contour termination within the fiber bridging zone. In both 4.18 (a) and (b), the stress intensity factors increased as the contour size decreased and shifting the contour resulted in stress intensity fluctuations. It is not possible to definitively identify which of these predictions is most accurate since variability in the data is not uniform throughout the FOV.

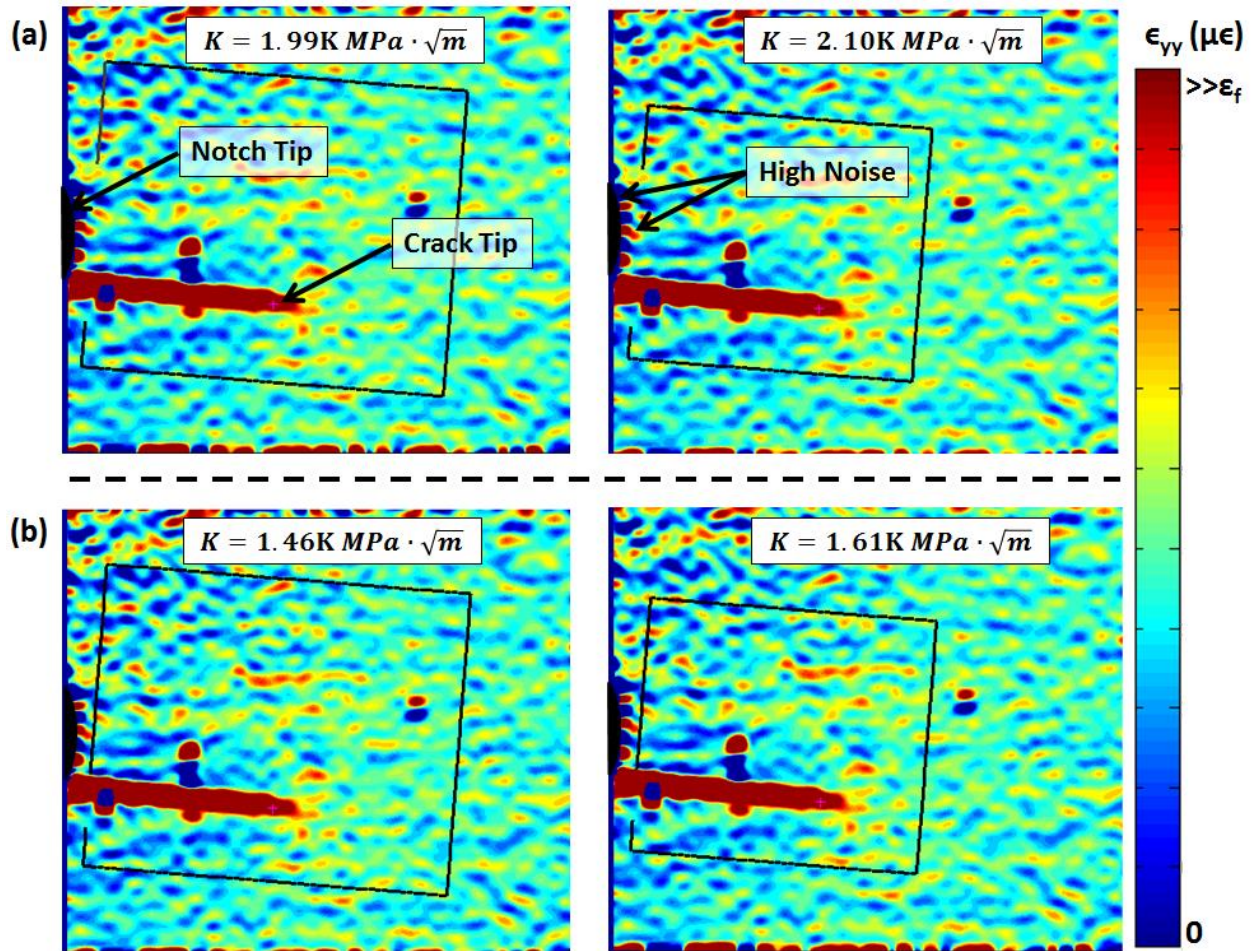


Figure 4.18 Line integrals evaluated using large and small contours. Both (a) and (b) illustrate the path dependency of the J-integral when applied to DIC data for stiff materials. In (a), contours were truncated about the notch such that the contour terminated outside of the fiber bridging zone and excluded high intensity noise emanating from the notch tip. In (b), contours were truncated about the crack flange within the fiber bridging zone.

The J-integral was applied to a set of DIC data for a second edge-notched cross-ply CMC tested at 795°C in the SEM. Whereas the first test was imaged over a $783 \mu\text{m}$ FOV, the second test was imaged over a $500 \mu\text{m}$ FOV which contained partially exposed fibers. For DIC, a 51 pixel subset, 5 pixel step size and 75 node strain filter were utilized. Prior to running the J-integral algorithms, a 75 node averaging filter was applied to the displacement data. R-curves for both tests are plotted against crack opening displacement for both tests in Figure 4.19 (a). At the largest crack opening displacements, the J and K measurements for the second test exhibited greater scatter because the process zone surrounding the notch began to merge with a region of artificially high strain surrounding a broken surface fiber that began to pullout along the fiber-

coating interface. These two regions are depicted in Figure 4.19 (b). Up to this point, the R-curves for both tests are in fairly good agreement, indicating that the J-integral measurements are consistent from one test to another. In the first test, the first crack observable from DIC data occurred at 1 μm of crack opening displacement, corresponding to stress intensity factor ranging from 1.8K (line integral) to 2.1K (area integral), implying that the plane stress fracture toughness in the CMC was at or below this range. In the second test, cracking was detected at 0.5 μm crack opening displacement, corresponding to a plane stress fracture toughness at or below 0.45K (area integral). Because of the proximity of a surface fiber experiencing pullout in the second test as well as the presence of several exposed fibers within the FOV, the fracture toughness range as measured by the J-integral here is questionable.

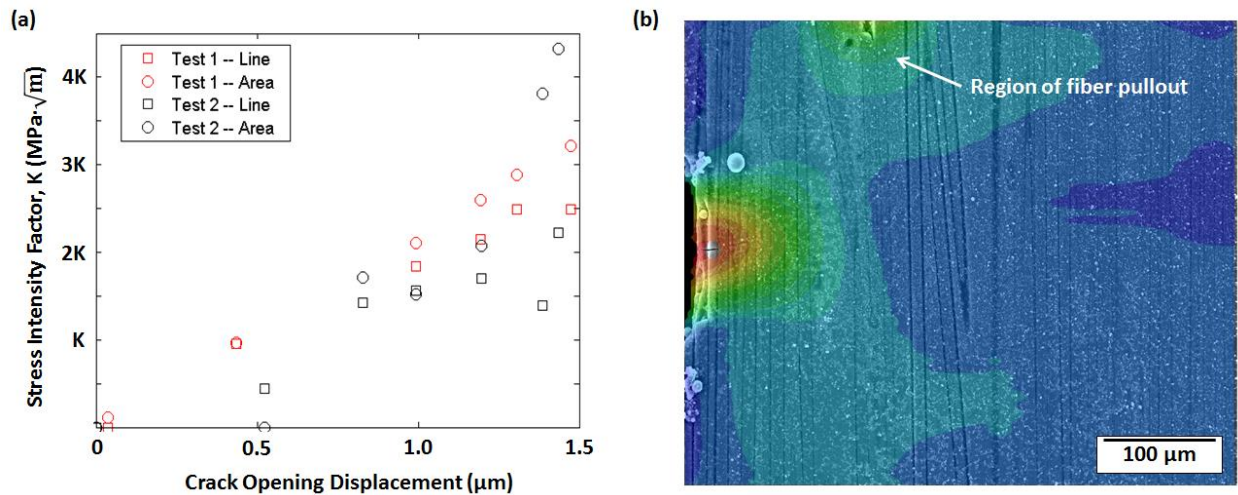


Figure 4.19 In (a), R-curves are plotted for two 795° C SEM tensile tests of edge-notched cross-ply CMCs. Up to 1.25 μm , the R-curves for both tests exhibit similar stress intensities. At crack opening displacements above 1.25 μm , artificially large strains and displacement in the vicinity of a region of fiber pullout merge with the deformation field in the vicinity of the notch tip, resulting in unreliable measures of J and K. This is illustrated in (b), where longitudinal strain fields are overlaid on the fracture image from Test 2 equating to a crack opening displacement greater than 1.25 μm . Note: all stress intensity factors for CMC tests are normalized to a reference value, K.

4.5.2.b Fracture Characterization: Unidirectional CMC

Using the line and area integrals, resistance curves were computed for two unidirectional SiC/SiC CMCs loaded in uniaxial tension under ambient environment. The edge-notched tensile coupons each consisted of a double layer of longitudinally oriented fibers. DIC data was

collected using a Grasshopper 5 megapixel CCD camera fitted with a 75 mm Tamron CCTV lens over a 6.5 mm (2048 pixel) FOV. For both data sets a DIC step size of 2 pixels was used. Smoothing was conducted using 35 node strain filters (line integral only), and 35 node displacement filters. A 45 pixel subset was used for DIC on the first data set and a 41 pixel data set for the second. During both tests, two cracks initiated and propagated from the notch. Consequently, stress intensities were plotted against crack opening displacement rather than crack extension and data was not transformed into a crack coordinate system. Resistance curves for the first data set are shown in Figure 4.20; inset in the figure are longitudinal strain fields corresponding to various lengths of crack opening displacement. The first cracks that can be detected by DIC occur at a crack opening displacement of 0.4 μm . At this COD, the stress intensity factors range between 0.9K (line integral) and 1.1K (area integral). The plane stress fracture toughness of the composite is estimated to be at or below this range of stress intensities.

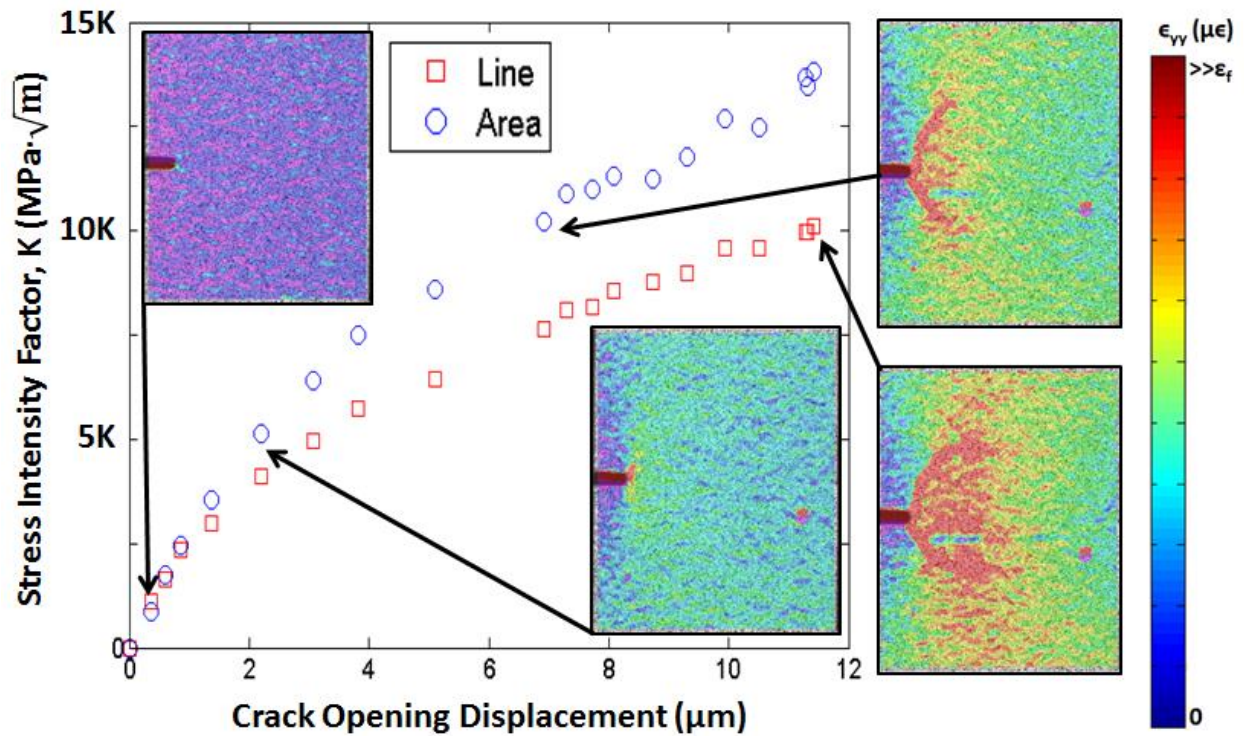


Figure 4.20. Line and area integral derived resistance curves for the first of two uniaxial CMC laminate tension tests. Fibers are oriented in the loading direction. Two cracks initiated simultaneously from the notch tip, with final fracture ultimately dominated by the upper crack. Plane stress fracture toughness is attained at or below the range 0.9K to 1.1K. Note: all stress intensity factors for CMC tests are normalized to a reference value, K.

Up to about 2 μm of crack opening displacement, the area and line integrals measured similar stress intensities. The area integral measurements were higher than line integral for all loading thereafter. This was also observed in the cross ply tests, and is attributed to the difference in filtering for the two integration methods. Although both displacements and strains are filtered in the line integral, a majority of the J computation incorporates filtered strain data. Filtering strains is preferable to filtering displacements, but this is not possible for the area integral; strains are computed at each Gauss point individually, then J immediately thereafter.

Resistance curves for both tensile tests are plotted in Figure 4.21. Inset in Figure 4.21 are longitudinal strain fields for both test which correspond to a point at which cracks have initiated from the notch tips. Stress intensities for the first test were generally less than those of the first tests. Both tests exhibited toughening behavior; the rate of increase in stress intensities decreased as crack opening displacement increased. As expected, area integral measurements were larger than line integral measurements. In the second test, crack initiation was detectable in DIC data at a crack opening displacement of 0.55 μm . This corresponds to a plane stress fracture toughness value at or below the range 1.3K (line integral) to 1.5K (area integral). Combining the results from both tests, estimates of plane stress fracture toughness as computed by the J-integral fall within or below the range 0.9K to 1.5K.

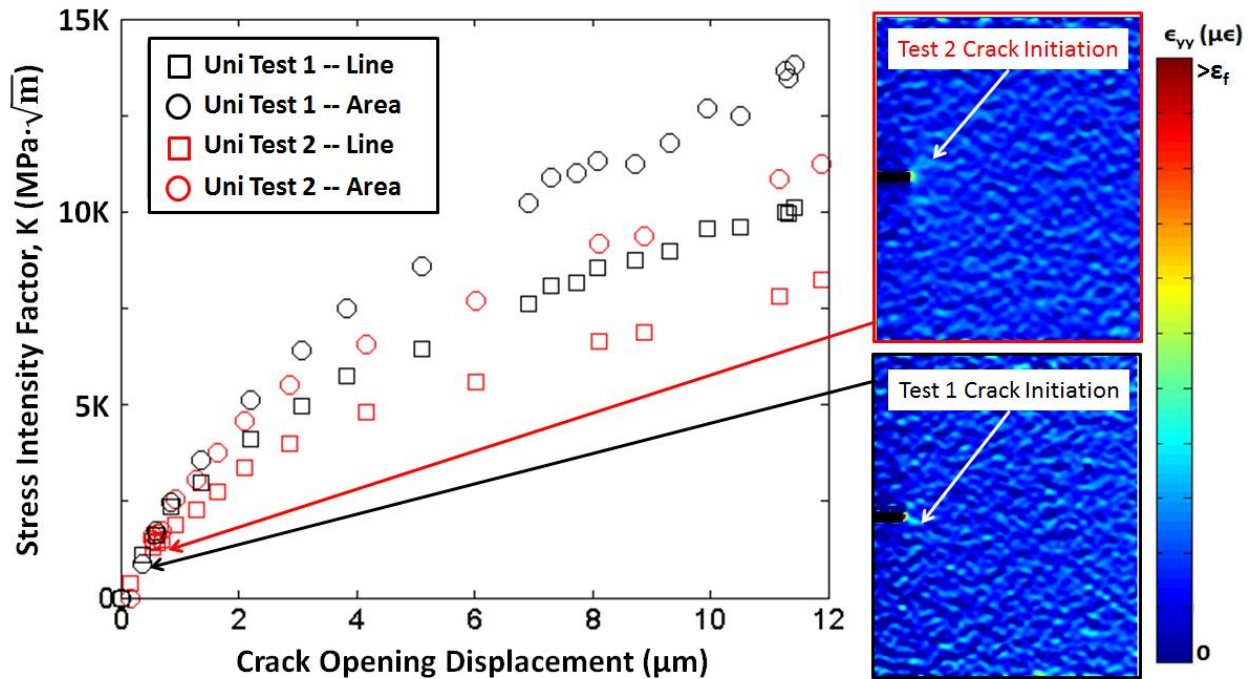


Figure 4.21 Resistance curves derived from J-integral for longitudinal unidirectional laminate CMCs loaded in uniaxial tension. Inset are longitudinal strain fields corresponding to earliest detection of crack initiation at edge-notch. J-integral measures of fracture toughness were at or below the range 0.9K to 1.5K. Note: all stress intensity factors for CMC tests are normalized to a reference value, K.

4.5.2.c Comparison of Results from Cross Ply and Unidirectional Laminates

For both the high temperature cross-ply and ambient temperature unidirectional CMC tests, the range of critical stress intensity factors measured by the J-integral were close to published values of fracture toughness for monolithic reaction bonded silicon carbide. Again, fracture toughness estimates for the composite were defined as being at or below the J-derived stress intensity factor corresponding to the first crack initiation at the notch, as detected from DIC strain fields. However, fracture toughness may not be an appropriate metric for characterizing fracture behavior in the CMCs that were tested. Cracks initiated in the matrix at low stress intensities because the matrix is inherently stiff and brittle. The existence of these cracks, however, did not result in a change in slope in the stress-strain curves of the test coupons. Unlike their monolithic counterparts, the CMC cracks did not grow unstably under sustained loading after crack initiation. As evidenced in the R-curves in Figures 4.19 and 4.21, the stress

intensities grew larger as the cracks propagated, but the rate of growth decreased with crack propagation. This is attributed to fiber bridging in the crack wake. Fibers bridging the crack apply a traction that closes the crack faces. The applied stress intensity must increase to overcome these tractions [22]. Although the estimated range of fracture toughness in the composites was near that of the monolithic matrix, the cracks that initiated grew stably under continued loading. The SIF magnitudes were larger in the unidirectional resistance curves than in the cross-ply curves. This is because the unidirectional layups contained only longitudinal fibers, which are oriented in a more favorable direction for toughening than the transverse fibers in the cross-ply.

The J-integral approach was adopted to characterize fracture toughness at the constituent level and is therefore not expected to generate results that are equivalent to a macroscale closed form solution of the stress intensity factor. One of the challenges of this new approach towards constituent level characterization of fracture toughness is the lack of a baseline to determine how much the constituent scale measurement should deviate from the macroscale. It is expected that the macroscale measurement will be incorrect, as it assumes a single crack in a material that ultimately fails through the formation of multiple widespread matrix cracks. However, the J-integral measurements at the constituent scale, while a promising new approach that provide more realistic depictions of the local fracture toughness, currently incorporate a significant amount of error. While displacement and strain error measurements (such as root mean square (RMS) and standard deviation) can be assigned to an area of interest over which DIC data has been collected [23], it cannot be assigned to each node of data individually. For example, displacement and strain errors for a set of test data can be determined by measuring the RMS error in DIC measurements generated for a static image pair. However, adding the RMS error bounds to each data point then using this modified data to evaluate J has no effect; the added error is uniform across the FOV and equates to nothing more than a rigid body translation.

4.5.2.d Experimentally Derived Bridging Zone Laws

The J-integral can be used to generate a bridging law that measures the fiber bridging tractions, which collectively exert a closing stress on the faces of the crack flange, within the bridging zone [1, 24]. The fiber bridging stresses vary along the length of the crack flange, increasing with crack opening displacement. Fiber bridging laws were generated from line

integral measurements of the energy release rate, J , for the cross-ply Test 1 data as well as both unidirectional tests. For each data set, crack opening displacement was measured at the end of the fiber bridging zone (i.e. at the notch tip). Using least squares regressions, power law curves were fitted to plots of crack opening displacement versus J for each data set. The derivative of each curve yields the fiber bridging stress as a function of crack opening displacement and constitutes a bridging law.

Bridging laws for all three data sets are plotted in Figure 4.22. In each curve, the fibers have been normalized to the net section fracture stress of the test coupon. The bridging stresses in the cross-ply sample are larger, which is attributed to half of the laminates containing fibers oriented transverse to the loading axis; the cross-ply samples have a lower volume fraction of longitudinal fibers. Although transverse fibers contribute to bridging, that contribution is expected to be much less. The magnitude of the bridging tractions in the cross-ply exceeds the far-field fracture strength because the cumulative cross-sectional area of the longitudinal bridging fibers is much smaller than that of the laminate.

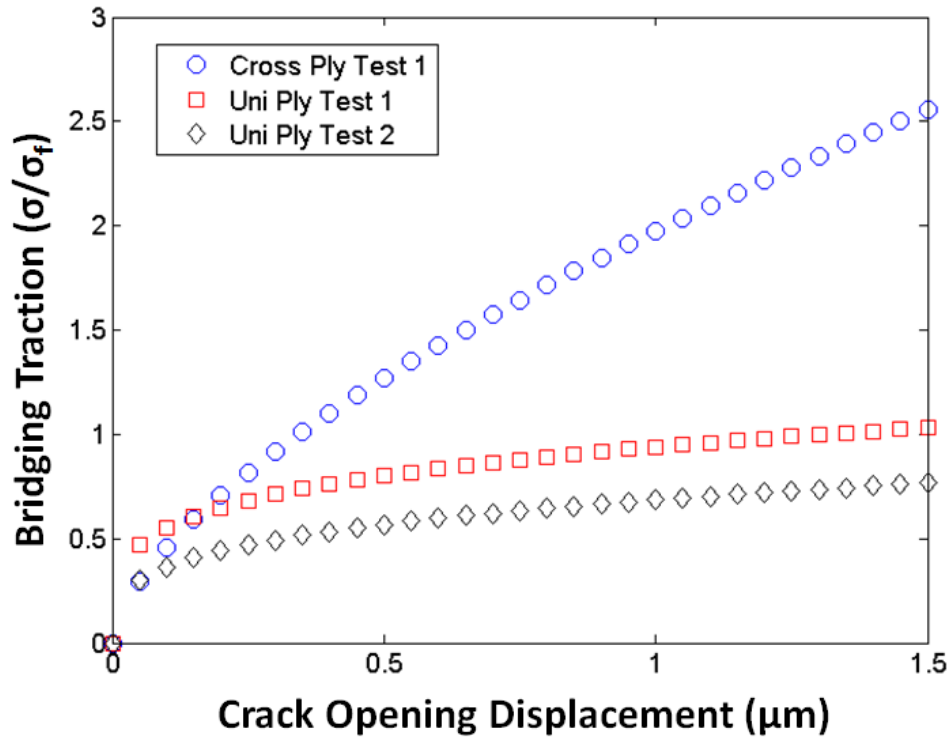


Figure 4.22 Fiber bridging laws for a cross-ply CMC tested at 795° C in the SEM (blue circles) and unidirectional laminates tested at ambient temperature (red squares and black diamonds). Bridging tractions are normalized to the net section stress at fracture of each test coupon. Bridging tractions represent stresses exhibited by fibers that act to close the faces of the crack flange. The local traction varies along the crack with crack opening displacement.

4.6 Influence of Experimental Variability on the J-integral

Variability in experimentally-obtained DIC deformation data strongly influences the J-integral calculation. This section examines the effect of variability on J through the addition of random noise to analytical Westergaard displacement data. At each data point of the vertical and horizontal displacement fields, a random number was generated and added to the displacement value at that point, thus creating artificially added noise. Upper and lower limits of the added noise varied between 0.1 and 10% of the analytical displacement value at a given location. For example, consider a node where the displacement value is 10 pixels and the noise range is chosen to be 10%. At that node, a random value ranging from -1 pixel to 1 pixel (-10% to 10% of 10 pixels) is added as noise. Figure 4.23 shows full-field vertical displacements (V) plotted for 0.1%, 1% and 10% added noise. The error in measuring toughness (J) increased as the magnitude of artificial noise increased. In this case, the errors resulted in under predictions. Recall from the

experimental analyses, noise in DIC data resulted in over predictions which were reduced through filtering. For the 0.1% noise level in Figure 4.23 (a), error is less than 1%. However, with each order-of-magnitude increase in noise level (4.23 (b) through (c)) the error becomes larger.

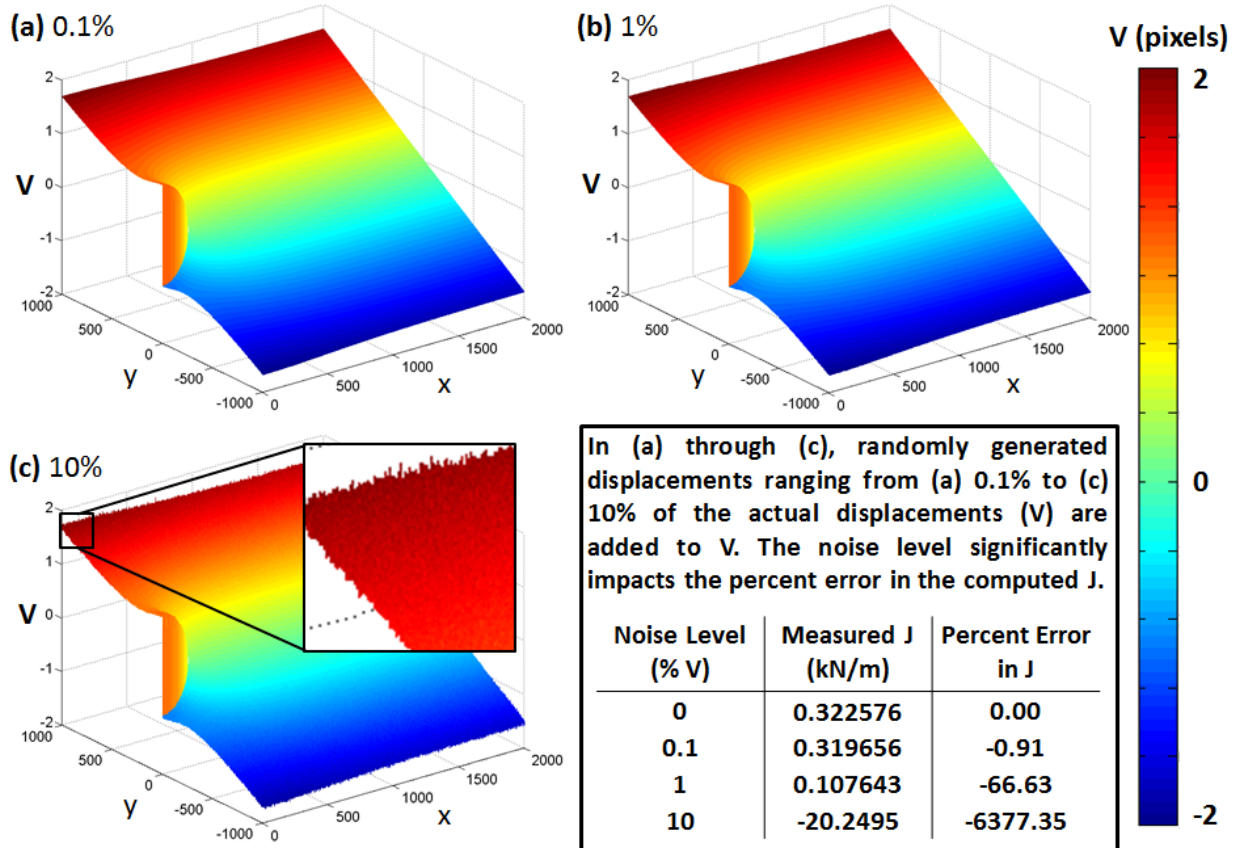


Figure 4.23 Vertical displacement fields from Westergaard equations are modified to include random noise. Noise scaling increases from 0.1% to 10% taken clockwise from top left. Error in computing J substantially increases with noise.

To better understand the high noise sensitivity of the J -integral, the manner in which noise from displacement data is amplified when that data is used to compute strain was first examined. Figure 4.24 shows longitudinal strain profiles collected from the RHS contour leg in a set of analytical deformation data with varying levels of noise: (1) biaxial Westergaard solution with no noise, (2) biaxial Westergaard solution with added noise capped at $\pm 0.1\%$ of the actual displacement values, and (3) biaxial Westergaard solution with added noise that has then been filtered with a 15 node displacement filter. The RHS contour was chosen because it provides a

considerable contribution to the J-integral; both the traction and strain energy terms are non-zero. The error in computing fracture toughness with the J-integral (in this case the area integral) for data sets (1), (2) and (3) is 0%, 0.17% and 0.02% respectively. Data filtering reduced noise by an order of magnitude.

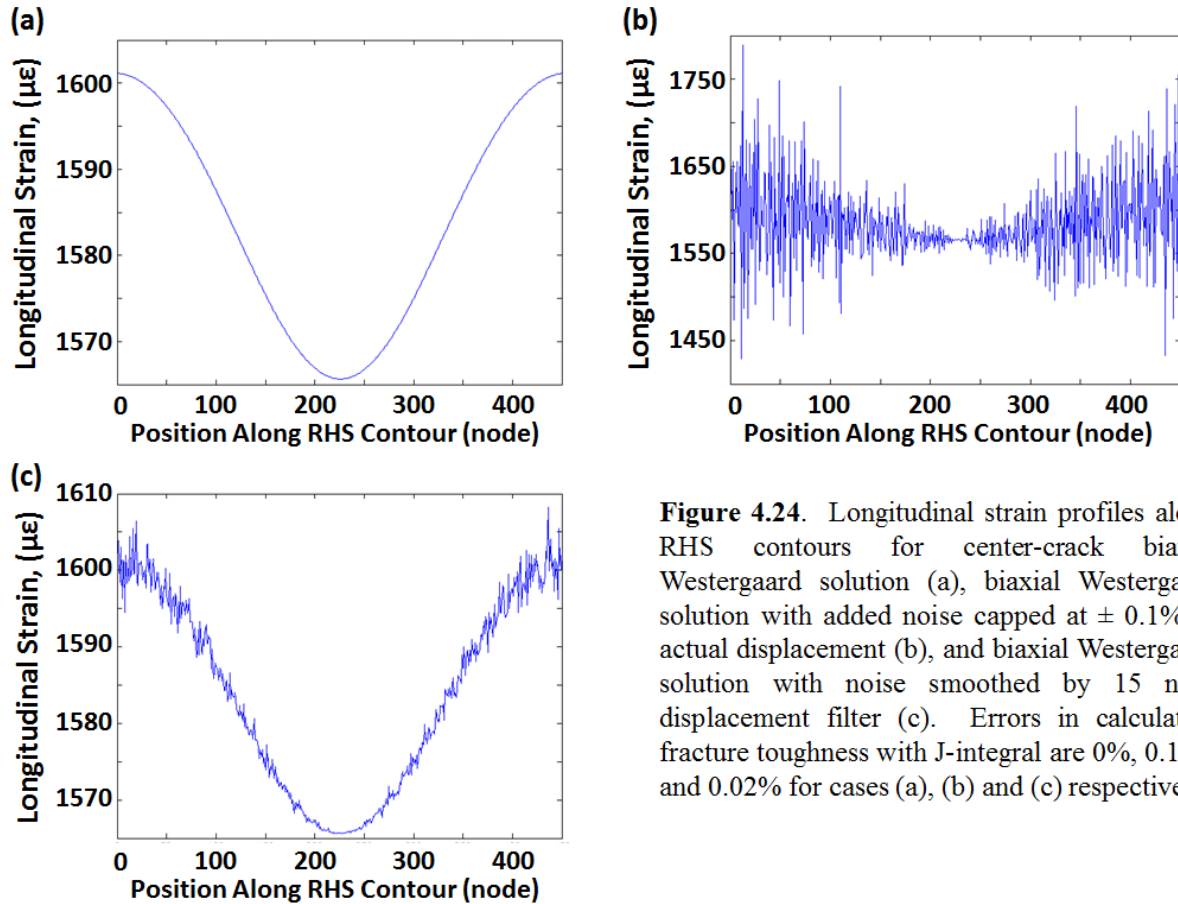


Figure 4.24. Longitudinal strain profiles along RHS contours for center-crack biaxial Westergaard solution (a), biaxial Westergaard solution with added noise capped at $\pm 0.1\%$ of actual displacement (b), and biaxial Westergaard solution with noise smoothed by 15 node displacement filter (c). Errors in calculating fracture toughness with J-integral are 0%, 0.17% and 0.02% for cases (a), (b) and (c) respectively.

Displacement filtering is necessary to improve the accuracy of J-integral calculations from experimental data. For low noise levels such as the 0.1% of data set (2), the resultant error in fracture toughness was relatively small, as a 0.1% noise only produced a strain variability of 1450 to 1800 $\mu\epsilon$ along the right hand contour. Figure 4.25 compares simulated noise in the biaxial Westergaard solution with actual DIC data from the PMMA DCB-CT specimen of *Section 4.5.1a* to illustrate the difference between noise in DIC data and the random noise added to the analytical data. Longitudinal strain profiles are plotted along the RHS contour for (a) biaxial Westergaard solution with added noise capped at $\pm 0.1\%$ and (b) DIC data with a step size of 5 pixels. The RHS contour of 4.25 (b) is 100 nodes long but spans 500 pixels because of

the 5 pixel step-size. Since the 5 pixel step size reduces the number of nodes sampled over a given range by a factor of 5, 4.25 (b) exhibits lower frequency noise than 4.25 (a). However, the noise in 4.25 (b) spans a range of 2000 $\mu\epsilon$ versus 350 $\mu\epsilon$. Since the noise amplitudes in the experimentally-obtained DIC displacement data were larger than the artificially induced noise amplitudes in the Westergaard displacements, their impact on measuring fracture toughness with the J-integral was greater.

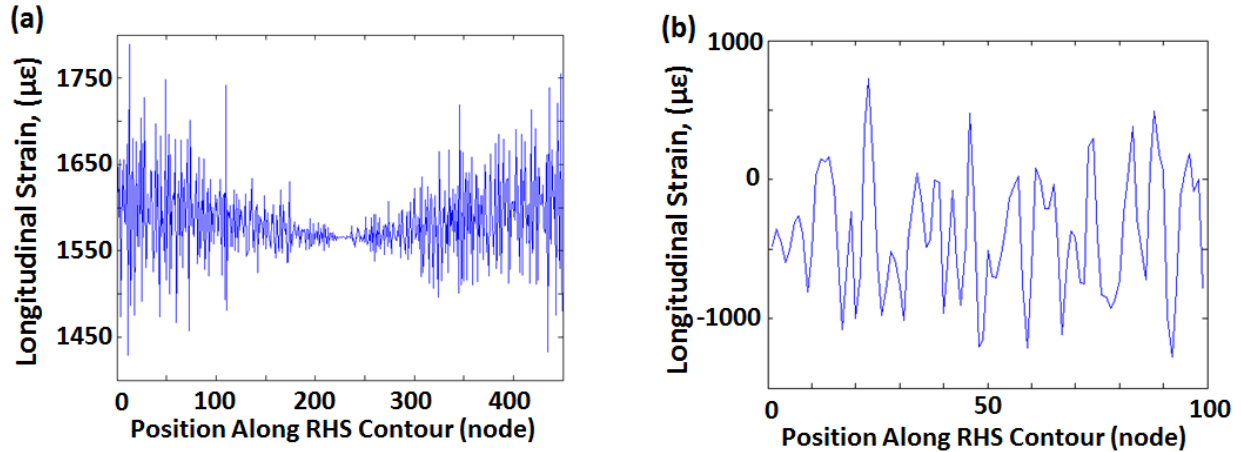


Figure 4.25 Longitudinal strain profiles plotted along RHS contours for case of (a) biaxial Westergaard solution with added noise capped at $\pm 0.1\%$ of displacement values and (b) DIC data from PMMA DCB-CT specimen. The noise range in (a) spans 350 $\mu\epsilon$ while that in (b) spans 2000 $\mu\epsilon$. Displacement/strain filtering in experimental data is necessary to improve the accuracy of J-integral fracture toughness measurements.

Recall that in Figure 4.11, larger DIC step sizes smoothed the displacement data and reduced the influence of variability on the J-integral. Doubling the step size from $\frac{1}{4}$ to $\frac{1}{2}$ of the subset size reduced the magnitude of fracture toughness values by as much as 2%. In Becker [3], a step size 25% of the subset size was used, presumably to filter displacement data and reduce noise. In Figure 4.17, combining a larger step size with a moderate filtering scheme lowered the stress intensity factors and reduced scatter in the resistance curves (increasing step size alone did not improve scatter).

For isotropic materials, manipulating the step size and filtering data appear to be valid techniques for improving the accuracy of the J-integral. For characterizing fracture in a CMC, however, this approach is not practical. The failure strains in ceramics are quite small, on the order of several hundred microstrain, which is often less than or equal to the magnitude of noise

and bias related error in DIC data. If this noise is smoothed using large filters, the data points used in computing J are not indicative of material behavior. Furthermore, CMCs fail by the accrual of fine matrix cracks. Applying data smoothing operations to CMCs that fail by microcrack accumulation may introduce error into J-integral evaluations of fracture toughness and is discussed further in *Section 4.7*.

4.7 Influence of Damage Mechanisms in CMCs on the J-integral

Certain aspects of damage accumulation in CMCs render the line and area integral methods impractical, specifically: (1) the low fracture strain of the ceramic matrix and (2) the presence of widespread matrix cracking upon loading.

In this work, the DIC data used in calculating J was collected over a continuous layer of matrix (with the exception of the lapped surface of Test 2 in *Section 4.5.2.a*), which presumably has a fracture strain that is nearly an order of magnitude smaller than the fiber fracture strain and is within the noise range of the DIC data. To minimize noise effects, the data must be heavily smoothed, greatly reducing the spatial resolution of the displacement measurements. The displacement resolution in an 800 μm FOV is not sufficient to accurately measure elastic strains in the ceramic matrix. This presents a conundrum because using a FOV small enough to measure elastic strains would not permit defining a contour that extends beyond the crack tip process zone.

Experimental evidence suggests that -- upon mechanical loading and prior to forming a well-defined matrix crack through the thickness of the laminate -- CMCs exhibit widespread microcracking, particularly in the vicinity of fiber-matrix interfaces. Figure 4.26 illustrates crack accumulation in a CMC tensile coupon loaded in uniaxial tension in a SEM. Images were captured in the inner and outer transverse plies of a $[0/90/0/90]_s$ SiC/SiC CMC at ambient temperature during interrupted loading. Even at applied stresses below the proportional limit of the material (and before initiation of a through thickness matrix crack), microcrack formation is observed to occur.

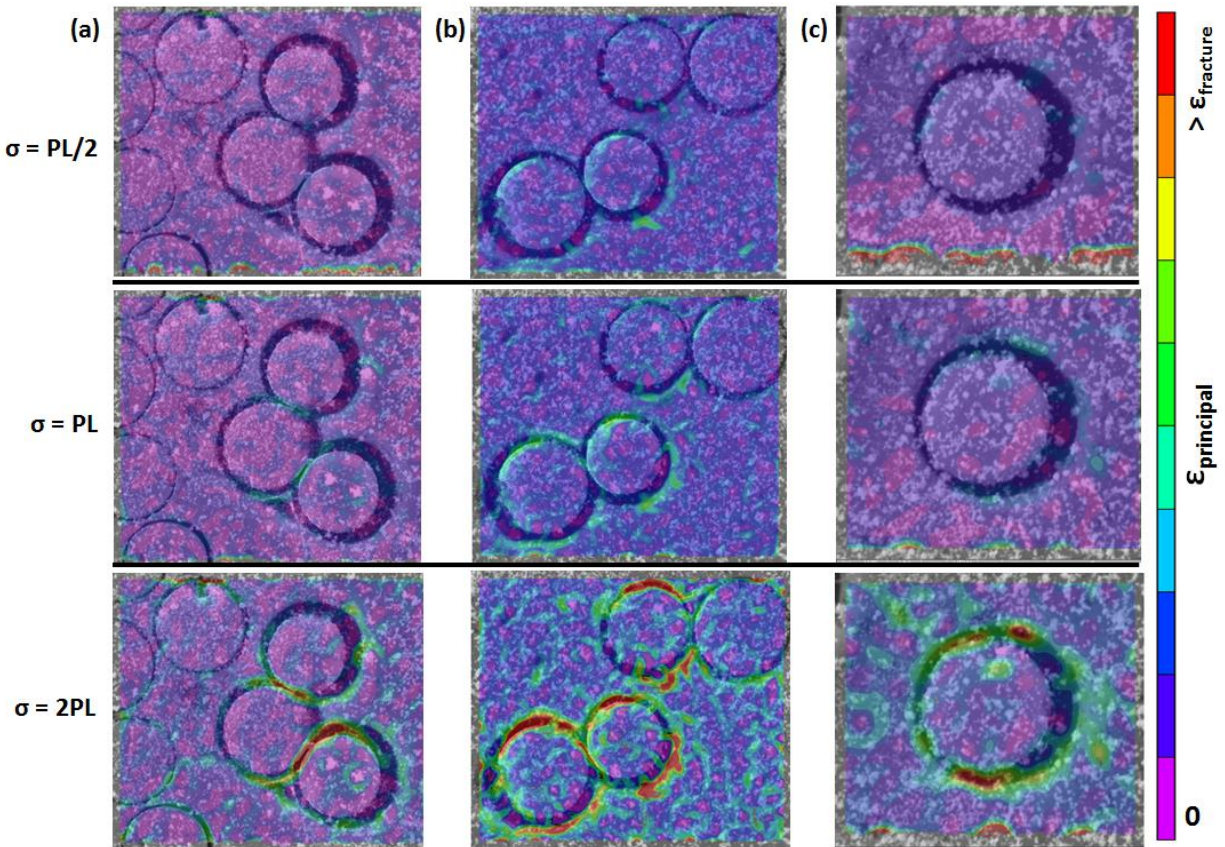


Figure 4.26 Full-field principle strain maps from images captured in-situ in an SEM on a CMC specimen loaded in uniaxial tension. 4.26 (a) and (b) show fiber clusters within a 50 micron FOV located in the outer and inner transverse lamina, respectively. 4.26 (c) shows a single fiber within a 30 micron FOV located in the outer transverse lamina. All three FOVs are located near the center of the gage section, nearly 13 mm from the location of final fracture. Note the onset of cracking at the fiber-matrix interface in (b) at an applied stress that is half the proportional limit (PL).

At FOVs of several hundred microns, a J-integral contour very likely contains through-thickness matrix crack(s) as well as artifacts of microcracking in the displacement data. At the 30 to 50 μm FOVs shown in Figure 4.26, fine microcracks are resolved with DIC. However, at the larger FOV needed to apply the J-integral (recall that the contour must fully encircle the plastic zone and begin and terminate at a notch or crack flange that is free of fiber-bridging tractions), individual microcracks cannot be readily resolved. These microcracks represent discontinuities that may traverse the contour boundaries. The contour is no longer closed and plastic zones traverse its boundary, render the J-integral fundamentally invalid.

As the applied stress increases, multiple matrix cracks evolve. As more matrix cracks form, the distance between cracks decreases until saturation crack spacing is reached. Crack spacing can be as small as hundreds of microns, as was the case for the experiments illustrated in Figure 4.27. If a contour encompasses multiple cracks, it cannot start and terminate at a single crack flange, again invalidating the J-integral. The presence of multiple matrix cracks may preclude the measurement of toughness, under the constraints established by Rice, for CMCs; there may inevitably be a point during loading when a matrix crack traverses the boundary of the contour.

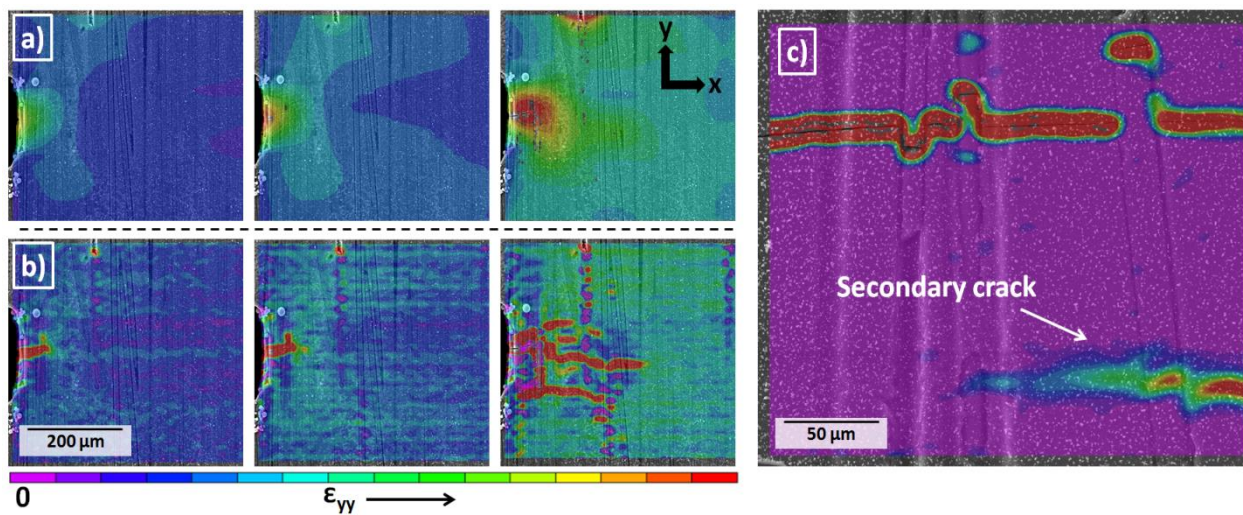


Figure 4.27 Full-field longitudinal strain maps for CMCs loaded in-SEM under uniaxial tension. 4.27 (a) and (b) show crack initiation from a notch during a tensile test at 795° C in a 500 μm FOV. 4.27 (c) shows crack accumulation in a CMC during a tensile test at ambient temperature over a 250 μm FOV. In (a), DIC parameters were adjusted to smooth cracks emanating from the notch, giving the appearance of a continuous elastic deformation field. In (b), the unadjusted data is shown where it is clear that several cracks emanate from the notch and a contour that fully encircles all discontinuities is not attainable. In (c), a secondary crack is seen to appear within 100 μm of a matrix crack that initiated at a notch in an ambient temperature tensile test. The secondary crack would likely traverse any contour drawn around the initial matrix crack.

Additionally, it should be noted that the SEM is a 2-D imaging sensor; thus crack propagation is only observed on the surface of the laminate and local toughness is characterized using only surface measurements. CMCs are not homogeneous through their thickness, and local toughness computed from surface measurements likely does not reflect the local values of toughness at the same positions sub-surface.

4.8 Conclusions

Two methods of characterizing crack resistance and fracture toughness in CMCs using the J-integral were investigated: (1) numerical integration of a line contour and (2) Gaussian integration of an area contour. The two methods were first validated by their application to analytically-derived deformation data in the form of uniform strain fields in an infinite plate and biaxial Westergaard displacement fields in a center-cracked plate. Both methods were path independent and accurate. However, small systematic error that varied with contour size and position (up to 0.0011% error) was introduced when the contour was truncated about the crack flange. Error was attributed exclusively to contour truncation.

After analytical validation, both methods were applied to deformation fields measured by DIC for PMMA and Aluminum tensile specimens to ensure the algorithms remained valid for experimental data. Experimental data introduced a new source of error, namely variability in the forms of noise and bias. Variability was reduced through displacement filtering, strain filtering (line integral only), and DIC step size manipulation. Data filtering was more effective than step size manipulation in improving the accuracy of J and K measurements. Both the line and area integrals measured fracture toughness in PMMA to within the range of published values for each material. Although a well-defined crack did not initiate at the notch before the plastic zone became too large to apply the J-integral, stress intensity factor measurements did approach plane strain fracture toughness values for aluminum. Strain energy release rate and stress intensity measurements were greater for the area integral than for the line integral. This is attributed to the way data is filtered. In the line integral, strains and displacements are filtered. For filters of equivalent size, strain filtering removes more noise than displacement filtering. Filtering strains was not possible in the area integral, however, as strain is evaluated point-by-point.

After analytical and experimental validation, the J-integral algorithms were used to estimate fracture toughness and generate resistance curves in SiC/SiC CMCs for two types of layup: (1) cross-ply single edge notched tensile coupons loaded in uniaxial tension under vacuum in an SEM at 795° C and (2) single edge notched unidirectional (i.e. fibers oriented along the loading axis) tensile coupons loaded in tension outside of the SEM at ambient temperature and pressure. Two tensile tests were conducted for each type of layup and resistance curves were generated using the J-integral algorithms. For the cross-ply laminates, J derived stress intensity

factors were plotted against a closed form expression for the stress intensity factor in an edge-notch tensile coupon in an orthotropic material. J-integral derived stress intensity factors were larger than their closed form counterparts. The closed form expression assumes a single crack in the material, which has been shown to not be the case for CMCs. Stress intensity factors computed by the J-integrals characterized the local stress intensity in the vicinity of the notch and were reflected the influence that dynamic, wide-spread cracking in CMCs imparts locally on a crack. Resistance curves for both the cross ply and unidirectional laminates revealed toughening behavior. As crack opening displacement increased, K increased but the rate of increase grew smaller, indicating stable crack growth.

Single-value assessments of fracture toughness could not be made for the CMCs. DIC data was used for assessing crack initiation from the edge notches; however, the resolution needed to detect cracks with confidence fell within the noise level of the DIC data. However, upper bounds (excluding error, which could not be quantified) for fracture toughness were established: for cross-ply coupons tested at 795⁰ C in the SEM, fracture toughness was with or below the range 0.9K to 1.1K where K is an arbitrarily chosen reference value which is similar in magnitude to that of reaction bonded SiC. For the unidirectional laminates tested at 25 ⁰C outside of the SEM, fracture toughness was within or below the range 0.9 to 1.5K. As fracture toughness was based on the detection of matrix crack initiation, it is not unreasonable that the ranges were near that of a monolithic ceramic. They are not reflective of the composites performance after crack initiation. Unlike in monolithic ceramics, cracks in the composites grew stably under increased loading.

Bridging laws were established for the cross ply and unidirectional laminates by fitting J and crack opening displacement data with power law curves. The derivative of each curve yielded fiber bridging tractions as a function of crack opening displacement, where crack opening displacement increased from the tip of the crack toward the end of the fiber bridging zone. The bridging tractions were large for a given COD in the cross ply layup than in the unidirectional layup.

The reason two coupons were tested for each layup was to assess the consistency of the J and K measurements for a given material/layup. Although the measurements were consistent, consistency was not necessarily indicative of accuracy. Variability in DIC data results from noise

in image sensors and bias inherent in the correlation. For isotropic materials, the influence of noise and bias can be reduced by using step sizes that are large with respect to the subset size at the expense of spatial resolution. In multiphase materials such as CMCs, this method of data smoothing is impractical because it averages data across cracks and constituent interfaces. Furthermore, CMCs exhibit fracture strains on order of the strain error in DIC data. While smoothing data can mitigate noise, it may unintentionally eliminate actual fracture data. Microcracking in CMCs is widespread even at applied stresses below the proportional limit. If these cracks or artifacts of these cracks in DIC data reside on the integration path, then the J-integral is no longer valid. Variability and widespread cracking thus render the J-integral as an impractical means of accurately measuring fracture toughness in CMCs. Gross estimates of toughness and stress intensity factors can be made only under the assumption that the limitations in the spatial resolution of the DIC data essentially transforms regions with fine microracking along the contour as a continuous regions of elastic deformation. However, the resistance curves do provide qualitative insight into toughening behavior in CMCs, specifically stresses and crack opening displacements at which critical fracture toughness is achieved and at which resistance curves begin to plateau. If used with care and discretion, the J-integral is an effective method of characterizing fracture behavior in CMCs.

References

1. B. Sorenson, "A Note on the Use of the J-integral in Fracture Mechanics," (Technical University of Denmark, Roskilde, February 2008).
2. G. Catalanotti, P. Camanho, J. Xavier, C. Davila and A. Marques, "Measurement of Resistance Curves in the Longitudinal Failure of Composites Using Digital Image Correlation," *Compos. Sci. Technol.*, **70** [10] 1986-1993 (2010).
3. T. Becker, M. Mostafavi, R. Tait and T. Marrow, "An Approach to Calculate the J-integral by Digital Image Correlation Displacement Field Feasurement," *Fatigue Fract. Eng. M.*, **35** 971-984 (2012).
4. S. Hedan, V. Valle and M. Cottron, "Experimental and Numerical In-plane Displacement Fields for Determining the J-integral on PMMA Cracked Specimen," *EPJ E Web of Conferences*, **6** [42003] 1-7 (2010).

5. Y. Du, F. Diaz, R. Burguete and E. Patterson, "Evaluation Using Digital Image Correlation of Stress Intensity Factors in an Aerospace Panel," *Exp. Mech.*, **51** 45-47 (2010).
6. S. McNeill, W. Peters and S. Sutton, 1987, "Estimation of Stress Intensity Factor by Digital Image Correlation," *Eng. Fract. Mech.*, **28** [1] 101-112 (1987).
7. G. Mogadpalli and V. Parameswaran, "Determination of Stress Intensity Factor for Cracks in Orthotropic Composite Materials using Digital Image Correlation," *Strain*, **44** 446-452 (2008).
8. S. Yoneyama, Y. Morimoto and M. Takashi, "Automatic Evaluation of Mixed-mode Stress Intensity Factors Utilizing Digital Image Correlation," *Strain*, **42** 21-29 (2006).
9. J. Rice, "A Path Independent Integral and the Approximate Analysis of Strain Concentrations by Notches and Cracks," *J. Appl. Mech.*, **35** 379-386 (1968).
10. A. Zehnder, *Fracture Mechanics*, Lecture Notes in Applied and Computational Mechanics, Vol. 62, Springer, 2012.
11. F. Li, C. Shih and A. Needleman, "A Comparison of Methods for Calculating Energy Release Rates," *Eng. Fract. Mech.*, **21** 405-421 (1985).
12. C. Herakovich, *Mechanics of Fibrous Composites*. Wiley, New York, 1997.
13. R. Christensen and F. Waals, "Effective Stiffness of Randomly Oriented Fibre Composites," *J. Compos. Mater.*, **6** 518-535 (1972).
14. A. Mortenson, *Concise Encyclopedia of Composite Materials*; pp. 257. Elsevier, Oxford, 2007.
15. H. Tada, P. Paris and G. Irwin, *The Stress Analysis of Cracks Handbook*. Del Research, St. Louis, MO, 1985.
16. G. Bao, S. Ho, Z. Suo and B. Fan, "The Role of Material Orthotropy in Fracture Specimens for Composites," *Int. J. Solids Struct.*, **29** [2] 1105-1116 (1992).
17. S. Lin, Z. Feng and R. Rowlands, "Thermoelastic Determination of Stress Intensity Factors in Orthotropic Composites Using the J-integral," *Eng. Fract. Mech.*, **56** [4] 579-592 (1997).

18. W. Beres, A. Koul and R. Thamburaj, "A Tapered Double-Cantilever-Beam Specimen Designed for Constant-K Testing at Elevated Temperature," *J. Test. Eval.*, **25** [6] 536-542 (1997).
19. J. Ritter, M. Lin and T. Lardner, "Application of the Crack-bridging Model for Fracture Resistance (R-curve Behavior) to PMMA," *J. Mater. Sci.*, **24**, 339-342 (1989).
20. Properties of Wrought Aluminum and Aluminum Alloys, *Properties and Selection: Nonferrous Alloys and Special-Purpose Materials*, **2**, ASM Handbook, ASM International, pp. 62–122, 1990.
21. M. Meyers and K. Chawla, *Mechanical Behavior of Materials*, Cambridge University Press, Cambridge, 2008.
22. F. Pfeiffer and P. Wriggers, *Lecture Notes in Applied and Computational Fracture Mechanics*, Springer, New York, 2012.
23. V. Rajan, M. Rossol, and F. Zok, "Optimization of Digital Image Correlation for High-resolution Strain Mapping of Ceramic Composites," *Exp. Mech.*, **52** 1407-1421 (2012).
24. B. Sorenson and T. Jacobsen, "Large-scale Bridging in Composites: R-curves and Bridging Laws," *Compos. Part A-Appl. S.*, **29** 1443-1451 (1998).

Chapter V

Fractographic Observations in CMCs

5.1 Introduction

Fiber reinforced ceramic matrix composites (CMCs) are often designed to fail in a distinctly different manner than their monolithic counterparts, where crack nucleation and propagation is widespread with many cracks evolving throughout the composite. When a ceramic material is loaded to failure, it usually breaks into several pieces, each with a newly formed fracture surface. In a single-constituent material, the fracture surface provides a comprehensive history of the events that led to final fracture which includes: the source or sources of crack nucleation, the speed at which it propagated, and the ultimate mode of failure. This is not necessarily the case for CMCs, because the fracture surface represents just one of numerous cracks that formed within the material. The surface in its entirety may not be the result of a single crack that nucleated, but a junction where several cracks converge.

The propagation of individual cracks is influenced by the local stress state in the material, which can depend on several factors, including residual stresses from processing, flaws or inclusions in the matrix, the presence and distribution of matrix fibers, morphology and properties of fiber coatings, and the test environment. CMC failure is often too complex for a single fracture surface to provide a comprehensive history of failure; however, the fracture surface can provide insight into the paths of crack propagation through the microstructure. To some extent, fracture surfaces may also indicate features or events that triggered crack initiation or altered crack propagation.

There is merit beyond academic curiosity to understanding how damage (i.e. cracks) evolves at the constituent level in CMCs. Fractographic analysis can assist in process control and

in identifying areas for material improvement. It may also aid in validating the predicted crack behavior in numerical damage models. This chapter applied principles of ceramic fractography to CMC fracture surfaces with the goal of understanding how cracks evolve in and navigate through the composite's structure.

5.2 Background

Interpreting the complex fracture surfaces of CMCs requires an understanding of how the stress state and microstructure mutually influence crack initiation and propagation. Sometimes a fracture surface provides clues as to how a crack developed or the direction it traveled, but these clues are often embedded in a convoluted landscape of uninterpretable damage. Several publications provide a comprehensive guide for conducting fractography in ceramics [1-3], but little consideration is devoted to ceramic composites. This section discusses the basic principles of ceramic fractography that were extended to analyses of CMC fracture surfaces.

Flaws and irregularities in ceramic materials can act as stress risers that initiate cracks or disrupt the local stress state enough to influence how and where cracks propagate. Examples of flaws and irregularities include voids, pores, irregular or large grains, inclusions, lakes or veins of free silicon, or defects at constituent interfaces (for composite materials) [1,3]. Machining, grinding and polishing induce small cracks that originate at the machined surface, can be several microns deep, and can be oriented parallel to or orthogonal to the machining direction [1,3].

Fracture surfaces in ceramics often contain features that reveal the history of failure. Fine grained ceramics contain three distinct topographical features at sources of crack initiation: (1) a smooth, often circular, mirror region surrounded by (2) a rougher mist region which itself is surrounded by (3) a very rough hackle region [3]. Although mirror and mist regions clearly delineate originations of fracture, they were difficult to identify in the SiC/SiC CMCs because the SiC/Si matrix grains were too coarse. On the other hand, analyses of readily visible hackle patterns indicated multiple sources of cracking along the fracture surface. This rendered pinpointing a single source of catastrophic failure through fractography infeasible; however, remnants of broken fibers did provide information regarding the mode of failure. Long sections of fibers emanating from the fracture surface indicated failure was by tensile pullout and fiber rupture. Flat surfaces with little pullout (observed on tensile coupons loaded at elevated

temperature) indicated fast fracture throughout the composite and suggested that, among other causes, the fibers were susceptible to an oxidative environment prior to failure.

There are different types of hackle, which can be identified as parallel but non-coplanar lines that may originate from a source of fracture and run in the local direction of crack propagation [3]. Velocity hackle lines indicate the point at which a propagating crack reached terminal velocity and the local direction of crack propagation [3]. Wake hackle appears as tails that extend in the local direction of crack propagation around singularities in the microstructure (such as fibers, inclusions or pores) that intercept the crack front [3]. Both velocity and wake hackle provide insight into the influence of local variations in the composite microstructure on crack propagation. Twist hackle, often referred to as river marks, manifest when a local variation in principal stress causes a propagating crack to split into several cracks on different planes oriented in the principal direction [3]. These can be traced back to local sources of fracture along the numerous crack planes that constitute a CMC's fracture surface. Grinding hackle appears near cracks induced by machining and often contains serrations resembling shark's teeth [3]. Their influence on crack initiation is prevalent at the tips of edge-notches, where the local stress is much larger than the far-field stress.

Like hackle, Wallner lines can be used to determine the local direction of crack propagation. Wallner lines resemble ribs, and are formed by the interaction between a propagating crack and the elastic pulse that results from the crack front intercepting a singularity in the microstructure [3]. Cracks propagate in the direction of the bow of a Wallner line and might suggest how microstructure influences the local direction of crack propagation. Arrest lines appear as sharp lines on the fracture surface that indicate a point where a crack temporarily stopped before resuming propagation (possibly at a different orientation) [3]. They indicate a snapshot profile of the crack at that point in time [3]. When compared with deformation fields at equivalent locations on the surface, arrest lines tell us how a crack front transitions from one spatial orientation to another.

5.3 Methods

All fracture specimens evaluated were SiC/SiC CMCs. The SiC fibers were encased in boron nitride (BN). The matrix was melt infiltrated SiC that often contained unreacted carbon and veins/pools of free silicon. Three layups were investigated: $[0/90/0/90]_s$ cross-ply,

[0/matrix/0] longitudinal unidirectional and [90/m/90] transverse unidirectional. All coupons were tested in tension; several contained single edge-notches machined with a diamond saw blade. Refer to Sections (High-temp, J-integral, Damage) for specifics regarding dimensions of coupons and procedures for thermo-mechanical testing.

Fracture surfaces were imaged optically and with a scanning electron microscope (SEM). Optical imaging was conducted with an Olympus BX51-M. SEM imaging was conducted with an FEI Quanta 3d dual beam microscope fitted with an EDAX energy dispersive spectroscopy system. EDAX was used to detect elemental composition of features of interest. Both secondary electron (SE) and backscatter electron (BSE) detection modes were utilized for SEM imaging, the latter when it was necessary to distinguish between individual phases.

Surfaces were first investigated as-fractured. Fracture debris often littered the surface. If it was severe enough to mask characteristic features like hackle, the surface was ultrasonically cleaned and re-imaged. SiC was sufficiently conductive that charging was negligible at field widths on the order of hundreds of microns. Higher magnifications, however, required sputter coating with a thin layer of gold prior to SEM imaging.

A combination of full-field deformation data from the specimen surface with fractography on the interior fracture surfaces was used to assess processes that occurred within the sample during loading. In most cases, images of the specimen surfaces were captured during loading for post-test digital image correlation (DIC). The cross-ply coupons were loaded and imaged in-situ in the SEM while the unidirectional coupons were loaded and imaged outside of the SEM with a CCD (Point Grey GRAS model).

5.4 Results and Discussion

The objective of this work was to identify features of fracture surfaces in CMCs relevant to characterizing crack propagation over the entire thickness of the material. These observations can potentially be used to validate crack propagation behavior in 3D simulations. During fracture in CMCs, the stress state and microstructure in the proximity of an advancing crack are so complex that the resulting fracture surfaces are extremely difficult to interpret, particularly for composites with several laminas. In the following sections, fracture features consistently observed in several test samples are presented and, when feasible, theories are proposed as to the nature of the crack(s) at that feature. A simple case study for a unidirectional laminate loaded to

failure in tension is presented in *Section 5.4.1* to introduce the reader to the fractography methods adopted for this study. In *Section 5.4.2*, modes of failure in the CMCs are discussed. The remaining sections are devoted to presenting characteristic features of fracture surfaces in CMCs and their relevance to crack initiation, crack propagation and modes of fracture.

5.4.1 Case Study: Single edge-notched [0/m/0]_s Unidirectional Laminate

This case study examines a longitudinal coupon loaded monotonically to failure. Full-field longitudinal strains measured from DIC indicate that at least two matrix cracks initiated from the notch and propagated in opposite directions. Ultimately, the upper crack arrested and the lower crack continued to propagate, as shown in Figure 5.1.

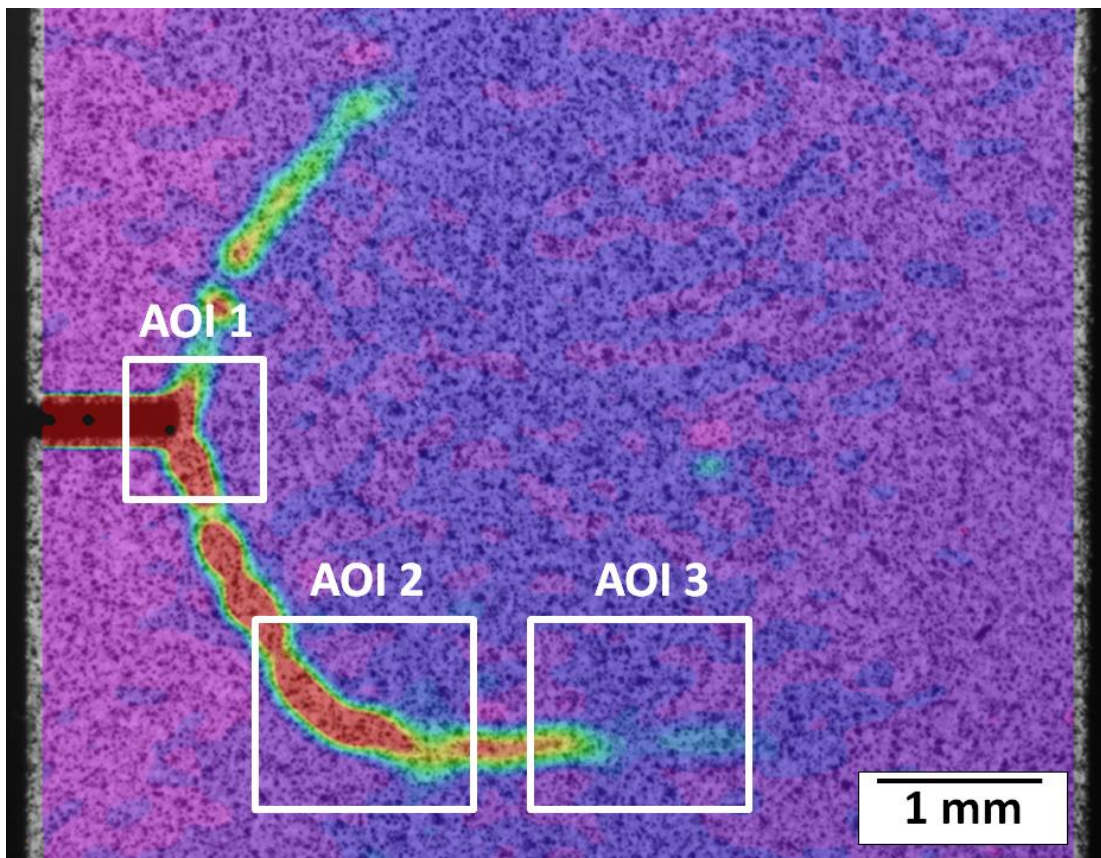
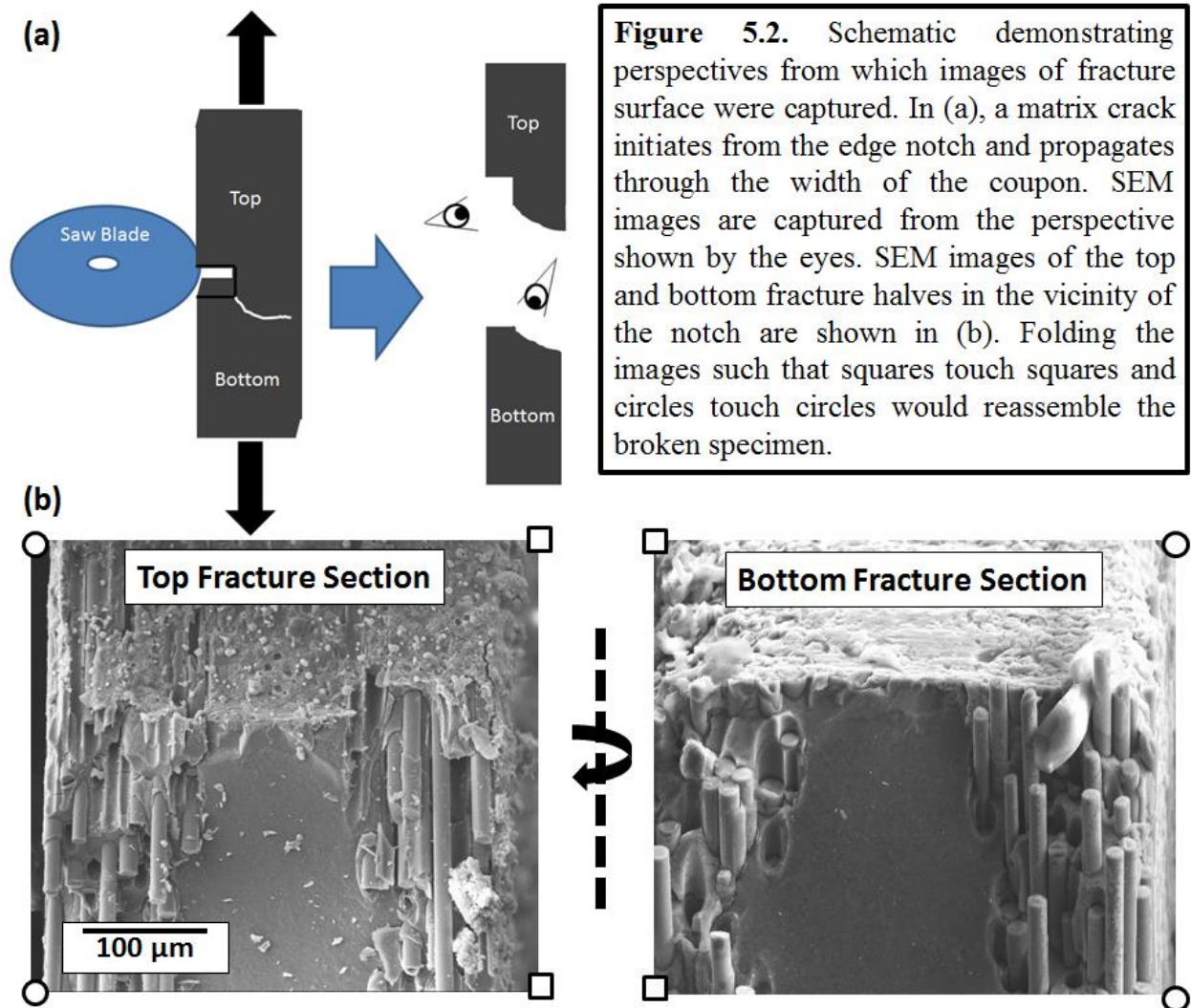


Figure 5.1 Initiation of matrix cracks from notch of longitudinal laminate tensile coupon. The bottom crack dominated at failure. Three areas of interest were probed for fractographic analysis.

Three areas of interest (AOIs) were probed along the fracture surface: (1) the notch, (2) the region where the bottom crack orients itself normal to the loading direction and (3) the region where there is a slight decrease in the magnitude of the strain field. These AOIs are depicted in

Figure 5.1. Figure 5.2 illustrates the perspective from which the notch (AOI 1) was initially imaged. Imaging at the notch tip from an angle as opposed to dead-on reduced the amount of material in the line-of-sight path of electrons from fracture surface to secondary electron detector in the SEM.



From the fracture surfaces it appears that the matrix crack that initiates at the lower fillet of the notch originates from small flaws that resemble coarse zipper cracks (see [3]). This is depicted in Figures 5.3 and 5.4. In Figure 5.3, dashed arrows point to possible zipper cracks. Coarse hackle emanates from the flaws and along the crack front in the direction of crack propagation. Based on the observed hackle, the matrix crack that initiates at the notch is oriented such that the left hand side (side opposite of that imaged for DIC) of the crack front leads the right hand side (side that was painted and imaged for DIC).

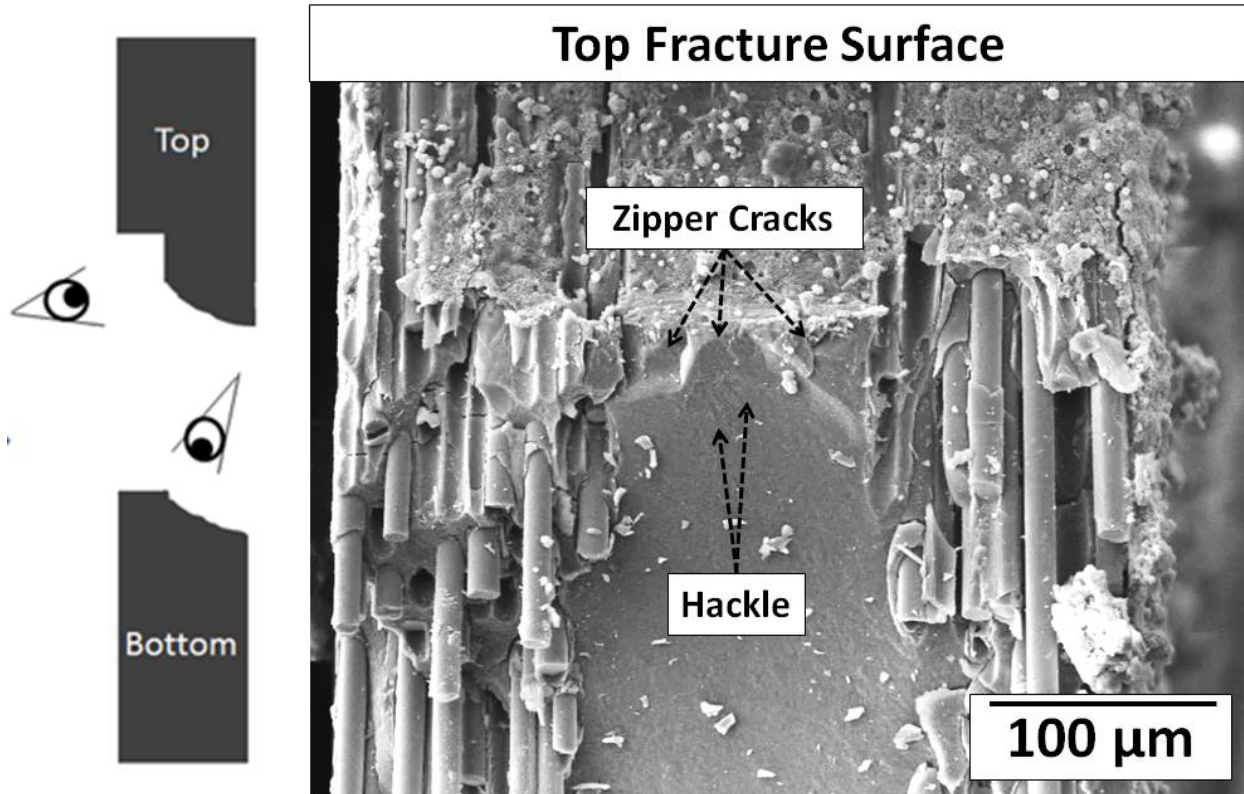


Figure 5.3 Magnified image of top fracture surface. Perspective is indicated on left hand side. Several flaws, likely zipper cracks induced by grinding the notch, emanate from the fillet. Coarse hackle emanates from the zipper cracks and along the crack front in the direction of crack propagation. The orientation of the hackle indicated that the crack front varied through the thickness of CMC, favoring left hand side (unimaged side) over the right hand side (painted and imaged side).

Figure 5.4 shows a magnified image of the flaws that appear to be zipper cracks. Semi-elliptical cracks emanate from the zipper cracks at a slightly different orientation than the zipper cracks; their surface normals are oriented in what is likely the local direction of maximum principal stress as the driving force for their formation is a complex stress field derived from a globally applied stress and proximity to the tips of the zipper cracks. A matrix crack then emanates from these semi-elliptical cracks at yet a different orientation. It is not known if the semi-elliptical cracks originated from grinding the notch or initiated upon monotonic loading. However, the process of grinding a notch with a diamond saw induces subsurface damage in the matrix and leaves in its path a microscopically rough surface (for example, the machining groove in Figure 5.4). The top fracture surface was imaged as-fractured; hence the surface is littered with debris.

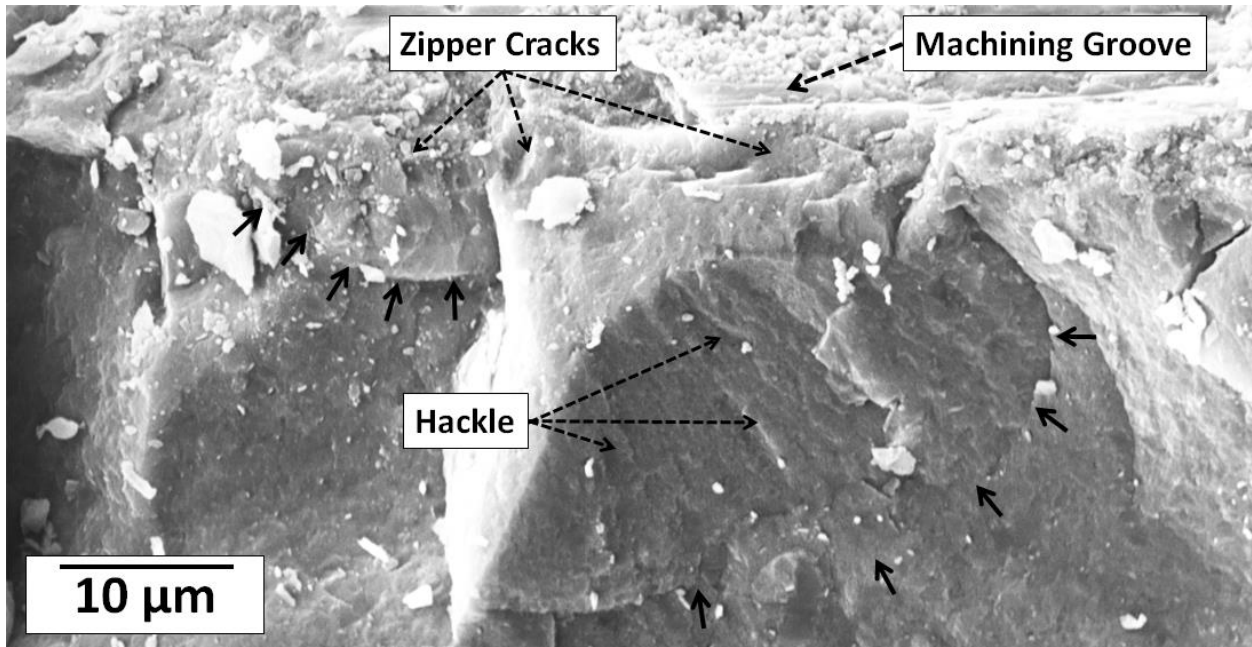


Figure 5.4 Features resembling zipper cracks located beneath a machining groove that resulted from grinding. Solid black arrows depict semi-elliptical cracks that initiate from the zipper-crack like features. Coarse hackle is present all the way up to the zipper cracks. Bright white features are fracture debris. Note the presence of one of several machining grooves that result from grinding a notch with a diamond saw.

The mating half from the bottom surface is shown in Figure 5.5. It has identical fracture features as the top half (i.e. zipper cracks, elliptical flaws and hackle indicating local direction of crack propagation), indicating that fracture patterns on the top half were not artifacts of spalls.

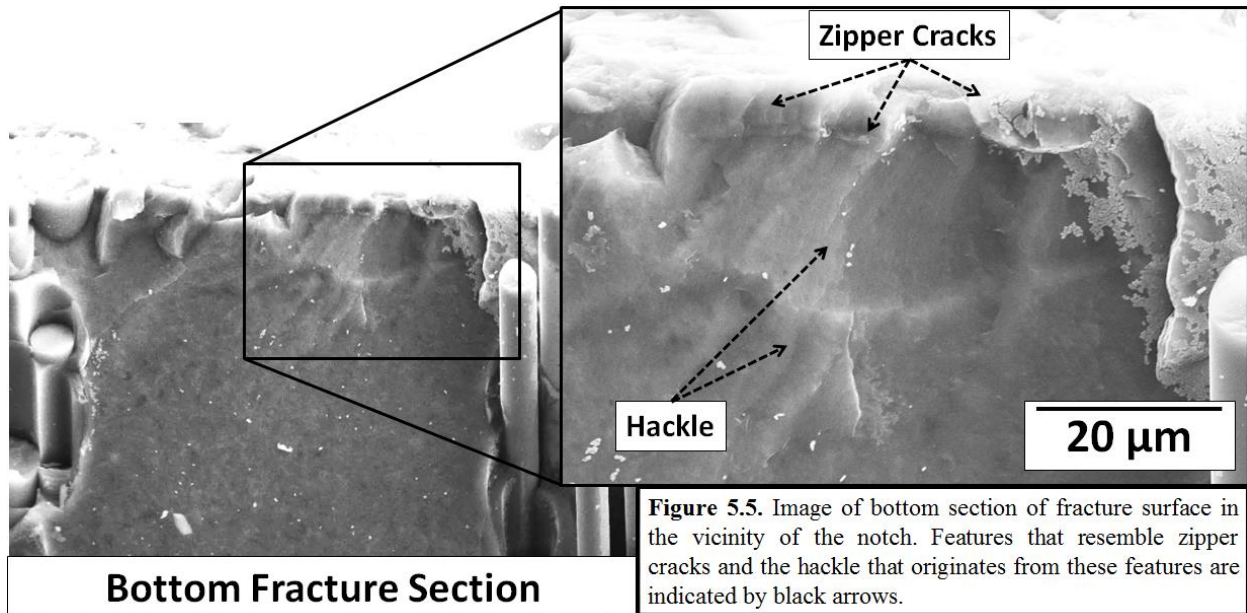


Figure 5.5. Image of bottom section of fracture surface in the vicinity of the notch. Features that resemble zipper cracks and the hackle that originates from these features are indicated by black arrows.

AOI 2 (Figure 5.1) covers a region of the crack front where the crack orientation transitions from angled to normal to the loading direction. The fracture surface is not smooth and continuous in this transition region; rather, the crack orientation transitions in distinct steps. When the crack angle changes, it often leaves a mark that spans the width of the crack front. These marks are indicative of arrest lines. This is illustrated in Figure 5.6.

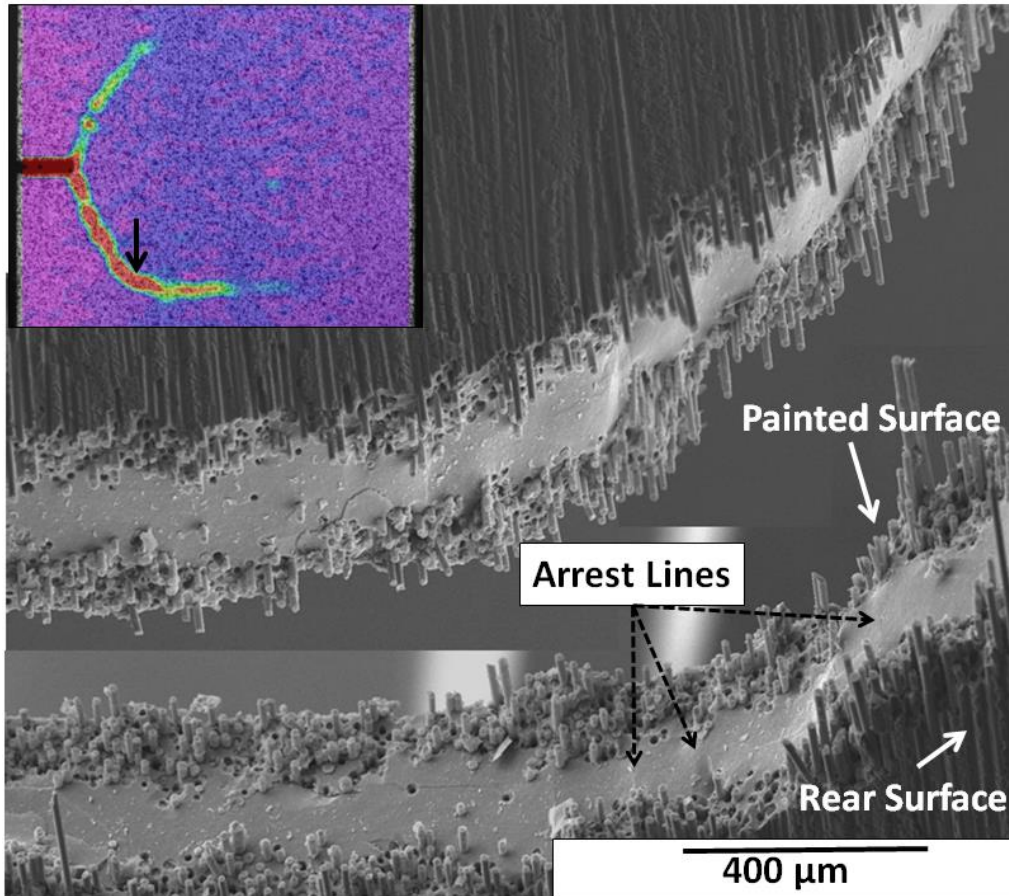


Figure 5.6 Stepped surface of region where crack path transitions to an orientation normal to the loading direction. Inset at the top-left is a longitudinal strain field with a black arrow indicating the transition region. Features that resemble arrest lines are depicted with black dotted arrows. Note: this micrograph depicts the surface opposite of that on which the DIC deformation field (inset) was captured; the crack propagates from right to left.

AOI 3 (Figure 5.1) covers an area of the crack front where the DIC-measured longitudinal strains are lower in magnitude than the strains immediately behind and ahead of it. Figure 5.7 shows the strain field and a micrograph corresponding to the equivalent position along the crack front. A large deviation in the crack path resembling a semi-circular divot is located at the patch of smaller strain. Recall from Figure 5.3 that hackle marks indicated the crack

originally propagated from the notch with the crack front oriented towards the thicker, painted side. Features of the fracture surface (the arrest line to the right and fiber tails to the left of the divot) in Figure 5.7 indicate that both before and after reaching the divot, the crack front was oriented towards the thicker lamina. However, the crack behaved differently within the divot; a new arrest line formed that favored no lamina.

Here we present two possibilities for this patch of small strain:

- 1) The local concentrations of fibers in the two lamina are not equivalent; there are more fibers in the painted lamina. Because the layup is not truly symmetric (i.e. one longitudinal lamina is thicker than the other), there is coupling between tension and bending which can influence the crack front orientation. This coupling results in complex variations in the local stress state. The crack temporarily arrests while a new crack forms ahead of the divot. The stresses redistribute at the divot, causing the local orientation of the crack front to divert from the original crack plane (thus forming the divot).
- 2) The crack front approaches a matrix-rich region (fewer fibers and more uniform distribution), cracking more symmetrically as a result of a more favorable fiber distribution. Upon traversing this region (i.e. the divot), the crack front continues to propagate along its original direction.

Although these explanations are speculative, the fact that sizeable anomalies in crack paths frequently occur is not; numerical modeling should capture this stochastic behavior.

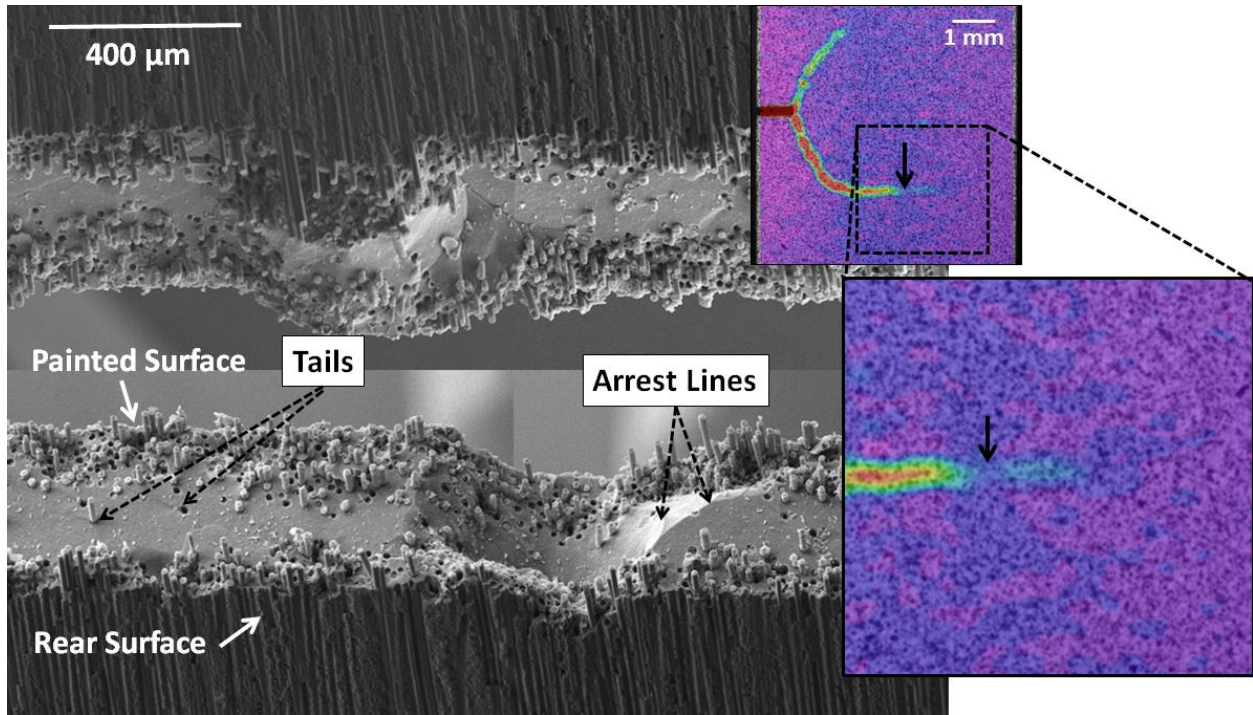


Figure 5.7 Semi-circular deviation in crack path is preceded by features that resemble arrest lines. Black arrow in longitudinal strain field (inset top-right) points to DIC data corresponding to deviation in crack path. Orientation of arrest lines suggests that crack temporarily arrested at deviation while crack front near painted (imaged for DIC) surface was allowed to catch up with rear surface. Twist hackle (‘tails’ in wake of crack path at fibers) indicate that the crack front re-orientes itself after passing the deviation.

5.4.2 Modes of Failure in Ceramic Matrix Composites

The desired failure mode in a fiber reinforced laminated CMC is saturation matrix cracking with fibers bridging the matrix cracks, followed by extensive pullout after fiber fracture. The undesirable alternative is when matrix cracks slice clear through the fibers with no toughening by fiber pullout/sliding and bridging. This situation can arise in a high temperature oxidative environment if no environmental barrier is present to protect the composite. Under these conditions, oxygen penetrates the matrix cracks to attack and weaken the fibers, causing fracture in the crack plane.

Except for the transverse unidirectional laminate, all tensile coupons tested – longitudinally oriented unidirectional laminates tested at ambient temperature, and cross-ply laminates tested at ambient temperature and at 795 °C in a vacuum – exhibited extensive fiber pullout. This is evident in Figures 5.8 and 5.9. The ambient temperature and high temperature

tensile coupons of Figure 5.8 had short pullout lengths, ranging from tens to hundreds of microns. The pullout lengths of the unidirectional samples ranged from tens of microns to tens of millimeters. The larger pullout lengths of the unidirectional CMCs were consistent with the greater toughness they exhibited (when loaded in the fiber direction) over (see Chapter 4 -- Experimental Assessment of Fracture Toughness in Ceramic Matrix Composites using the J-integral with Digital Image Correlation).

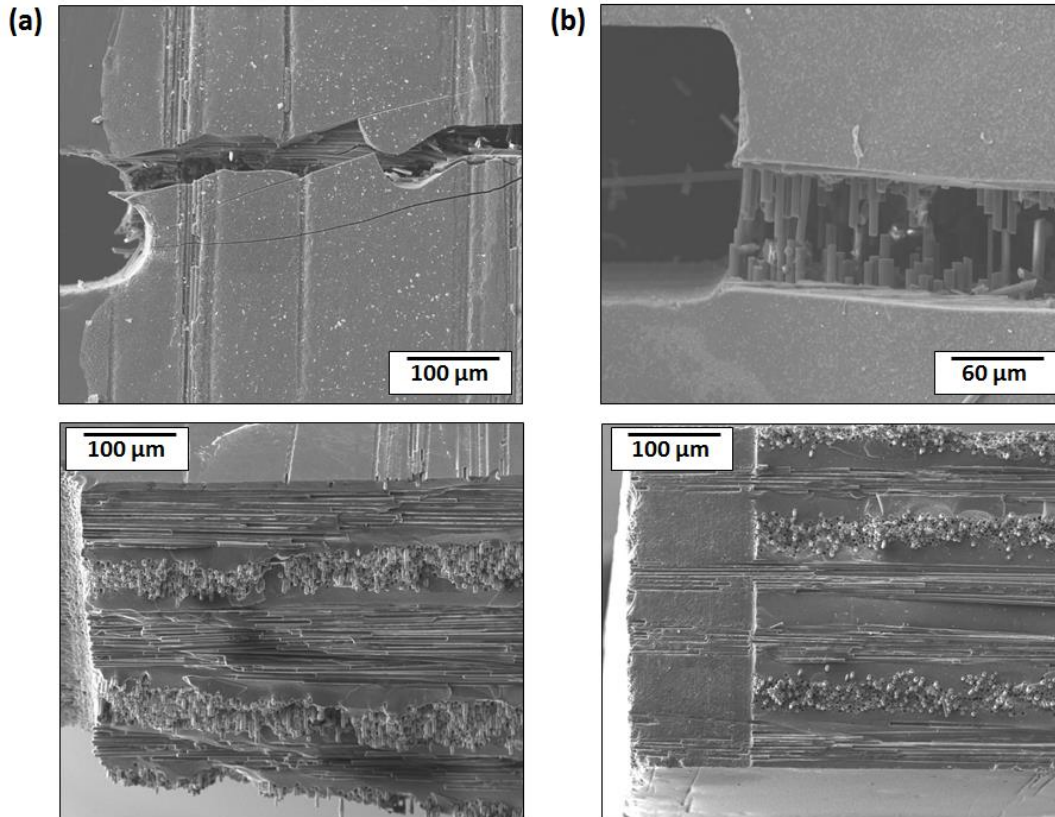


Figure 5.8 SEM micrographs of crack propagation from notch and fracture surface at notch for in-SEM testing of (a) cross-ply laminate tested at ambient temperature and (b) cross-ply laminate tested at 795 °C. Fiber pullout is evident in the longitudinal laminas with pullout lengths ranging from microns to hundreds of microns.

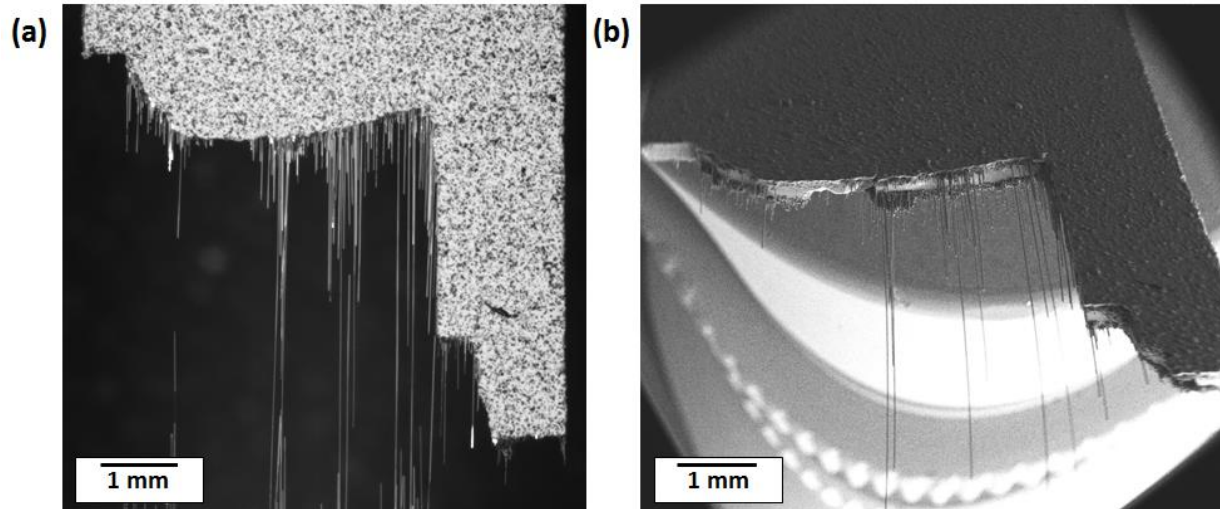


Figure 5.9 SEM micrographs of (a) crack propagation path on surface and (b) fracture surface of a cross-ply laminate tested at 795 °C in a SEM. Fiber pullout is evident in the longitudinal laminas. Pullout lengths range from several microns to several millimeters.

5.4.3 Observations from Fracture Surfaces in the Vicinity of Notch Tips

From a macroscopic perspective (commonly taken by modelers), notch tips tend to look smooth. However, as evident in Figures 5.3--5.5 and described below, machining induces subsurface damage that can trigger crack initiation. Modelers should consider incorporating these flaws in their simulations if the computed crack behavior at the notch tip does not coincide with experiment.

Figure 5.10 depicts machining cracks commonly observed at the notch tips of longitudinal unidirectional tensile coupons. Jagged features reminiscent of saw teeth emanate from the fillet of the notch and semi-elliptical features emanate from the saw teeth. Semi-elliptical and circular cracks are prevalent at the notch tip in the unidirectional laminates and are readily identifiable because of the relatively large matrix layer in these layups. Figure 5.11 shows a variety of these flaws, many likely induced by machining the notch.

Features resembling zipper cracks and semi-elliptical subsurface cracks (*Section 5.4.1*, Figures 5.4 and 5.5) may be artifacts of surface and subsurface damage induced by machining a notch with a diamond saw. These features were observed in both the longitudinal and cross-ply tensile coupons.

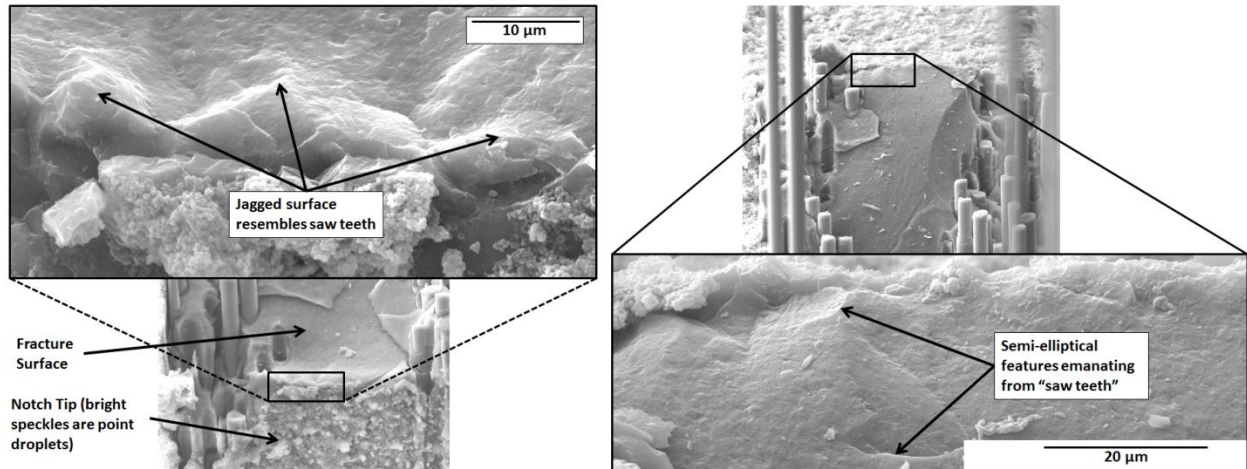


Figure 5.10 Example of subsurface damage likely induced by machining with diamond saw. On left, jagged features emanate from fillet of edge notch in a unidirectional laminate. On right, mating surface shows semi-elliptical cracks emanating from those same jagged features.

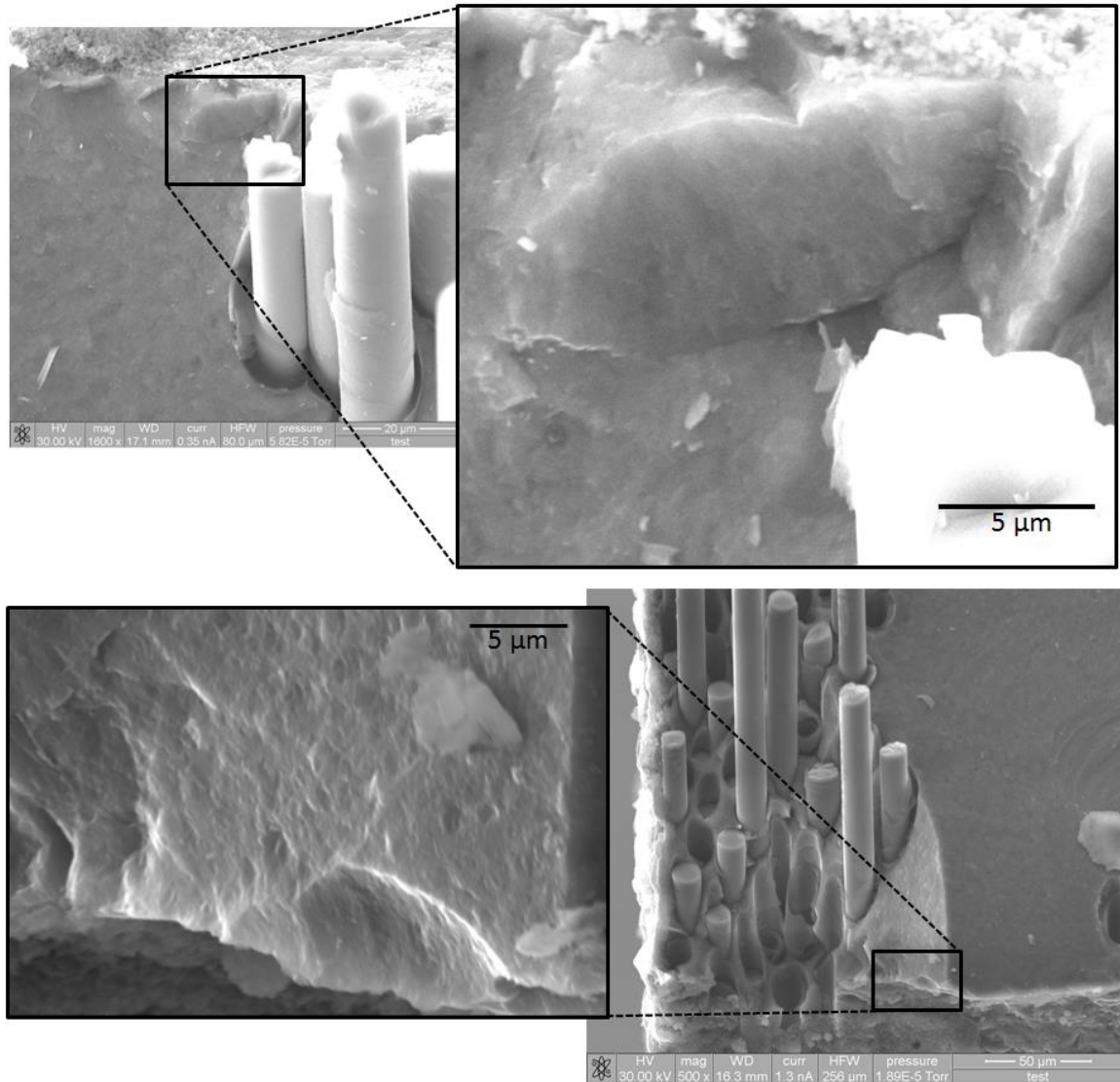


Figure 5.11 Additional examples of elliptical and circular cracks at notch tip (fillet) of longitudinal unidirectional tensile coupons.

Similar subsurface features were observed in cross-ply laminates; semi-elliptical and circular cracks were prevalent. This is shown in Figure 5.12, where circular and elliptical features emanate from the notch into the material. In Figure 5.12(a), the laminate was tested at ambient temperature while 5.12(b) was tested at 795 ° C. Note that in both cases, the features lie directly beneath grooves induced by a diamond saw blade.

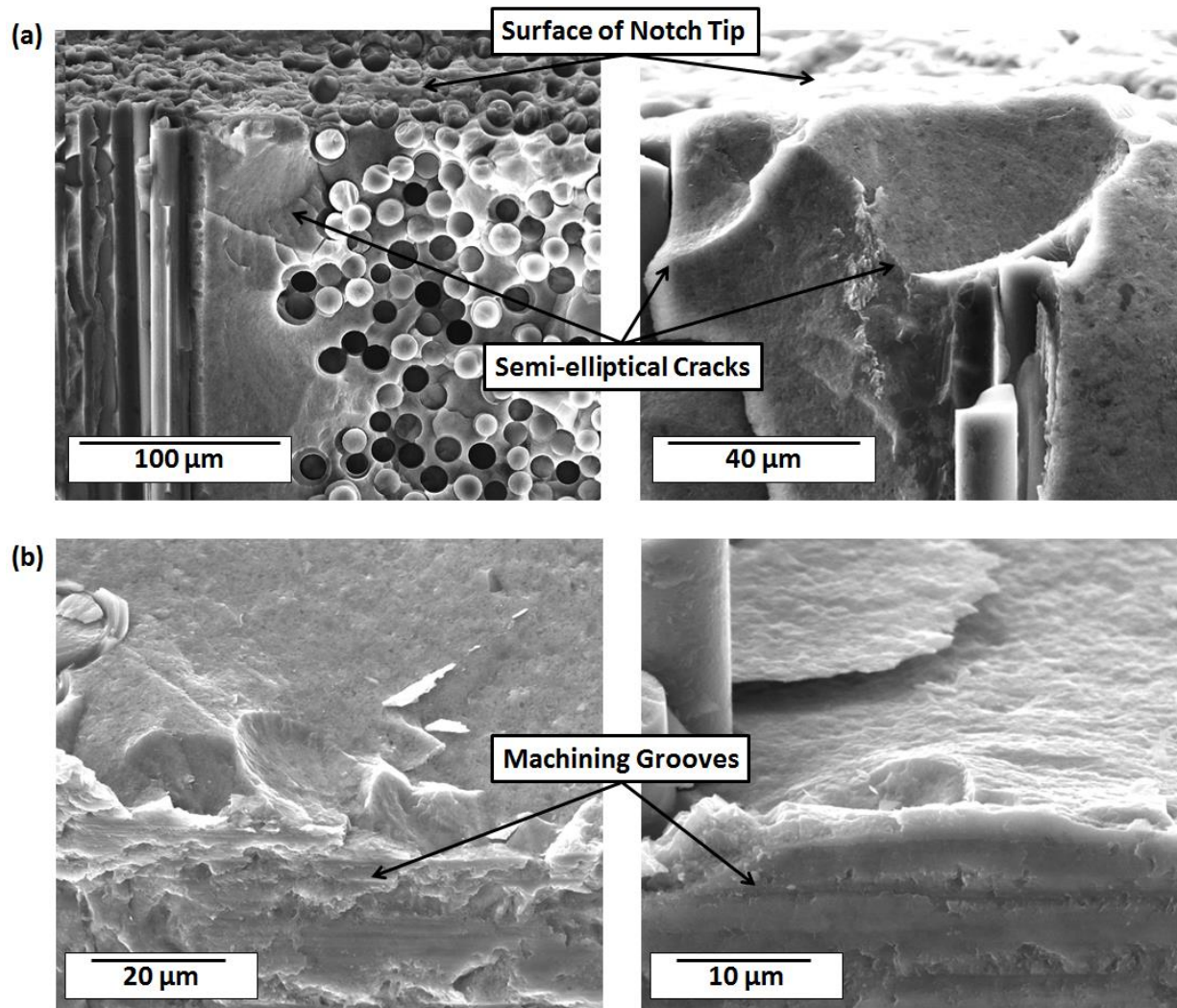


Figure 5.12 Semi-elliptical and circular cracks emanating from notch tips in cross-ply laminates loaded in tension in an SEM at (a) ambient temperature and (b) 795° C. In both (a) and (b), the cracks lie beneath machining grooves induced by cutting the notch with a diamond saw blade.

5.4.4 Subsurface Behavior of Propagating Cracks

The sub-surface deformation of CMCs is extraordinarily complex, and DIC-obtained measurements capture damage evolution only on the specimen surface. As illustrated in Figures 5.13 and 5.14, measurements of a crack on the surface do not necessarily depict processes occurring beneath the surface. In Figure 5.13 a surface crack is tracked by digital image correlation propagating up and to the right. However, the fractograph shows that on the opposite surface, the crack propagated down and to the right (one sees both the DIC observed surface and the back edge of the opposite surface on the top half of the specimen in the fractograph.)

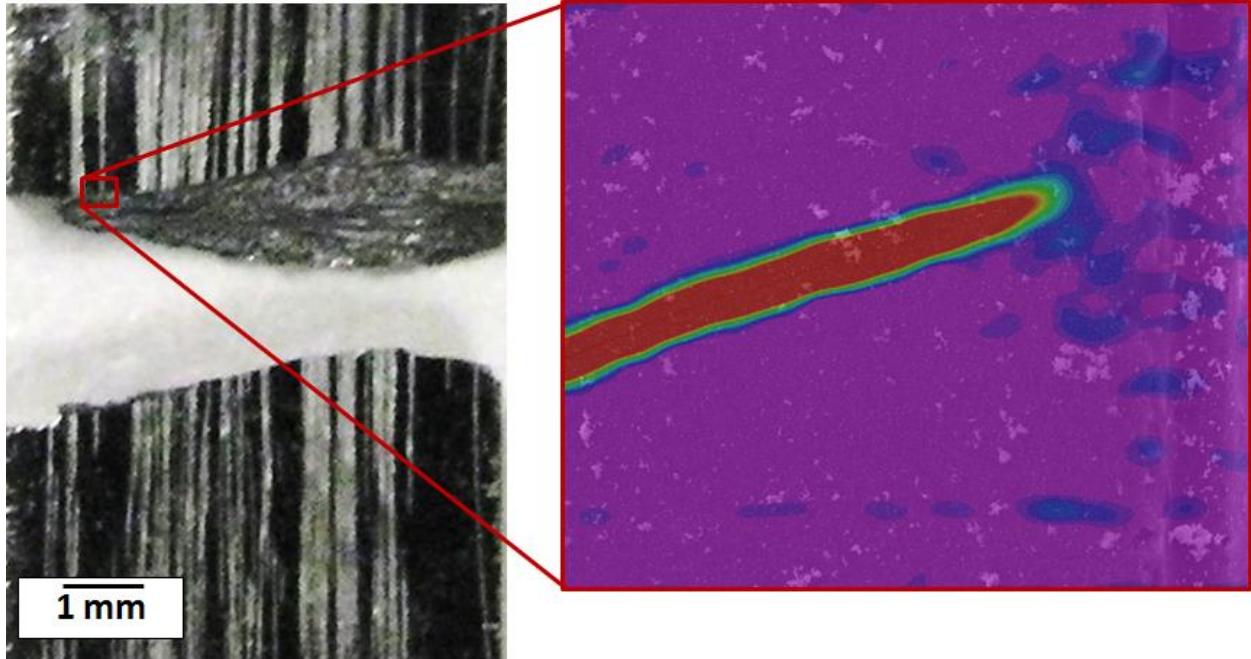


Figure 5.13 Fractograph of final fracture in single edge notched cross-ply laminate loaded in uniaxial tension. Inset is a longitudinal strain field measured with DIC. Cracks on the front and rear surfaces of the tensile coupon propagated at opposite angles with respect to the loading axis. Fracture observations from DIC must be interpreted with caution as they do not necessarily reflect subsurface behavior. Note that the front face of the fracture slopes upward while the back face slopes downward.

In Figure 5.14, the subsurface crack path temporarily deviates from the surface crack path. In addition to the through-thickness crack, there are two sub-surface cracks propagating in the longitudinal direction.

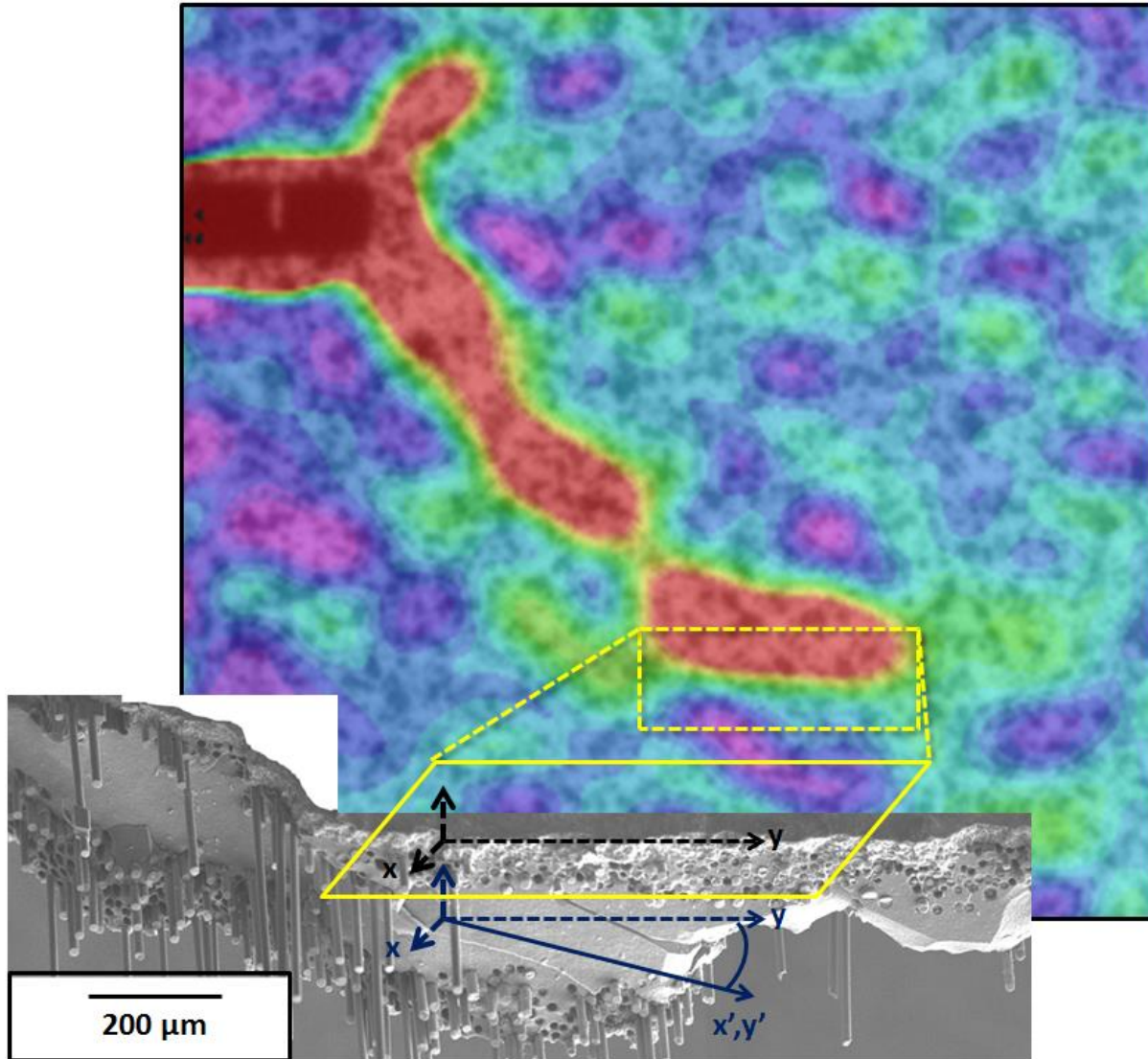


Figure 5.14 Fractograph of crack propagation in longitudinal unidirectional laminate and corresponding longitudinal strain field measured with DIC. Direction of crack propagation below the surface deviates locally from that at the surface. Additionally, matrix cracks propagate in the loading direction.

The tortuous topography of fracture surfaces is not solely attributable to a single matrix crack meandering about the laminate in multiple directions. Fracture surfaces in CMCs are often comprised of multiple cracks, each propagating on different planes and intersecting at the fracture surface. Figure 5.15 shows examples of crack propagation on multiple planes. In Figure 5.15a, cracks propagate on planes originating from flaws at the notch tip and from fibers in the longitudinal plies. In the Figure 5.15b, a fracture plane originates at the notch then deviates along a new plane that forms in a large pool of free silicon.

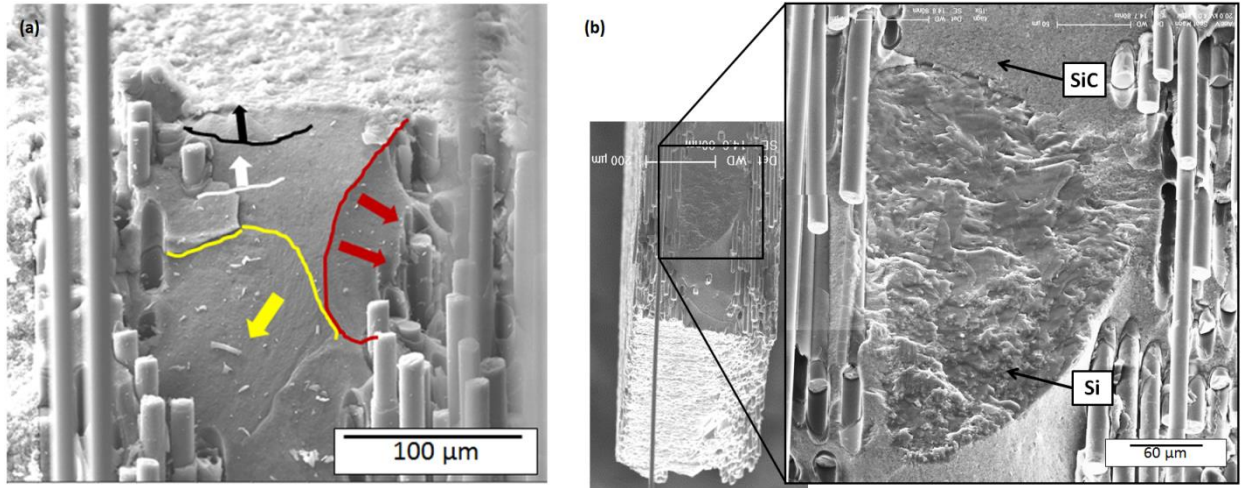


Figure 5.15 Examples of crack propagation along multiple planes in longitudinal unidirectional tensile specimens. In (a), fractures propagate along planes that originate at or near the notch tip and within each of the longitudinal plies. Arrows point towards source of crack initiation as indicated by the observed hackle/mist patterns. In (b) a matrix crack propagates along a plane that originates at the notch tip as well as along another plane within a large pool of free silicon. Full-field deformation measurements at the surface cannot detect the subsurface deviations from the initial propagation path.

5.4.5 Crack Propagation in Longitudinal Lamina

Conventional theories of damage evolution in CMCs assume that when a crack propagates through a fiber containing lamina, the crack front is deflected around individual longitudinal fibers if the matrix and fiber have a weak interface bond. These fibers then bridge the crack, debonding along the fiber/matrix interface for some distance on either side of the fracture plane. In the laminated CMCs tested in this work, there was a distinct layer of matrix-only material between laminas. It is often assumed that crack initiation originates in these layers and in transverse lamina, then propagates through the entire laminate. Fractographs can only be collected post-test, and therefore cannot always provide the sequence in which individual crack fronts initiated; however, they do suggest that initiation does not only occur in the transverse and matrix-rich layers. Figures 5.16 and 5.17 show examples of cracks that appear to have initiated in longitudinal plies in unidirectional and cross-ply laminates. In Figure 5.16, a matrix crack deflected vertically along longitudinal fibers. A new crack then originated in the longitudinal lamina as evidenced by the presence of hackle directed toward the fiber layer.

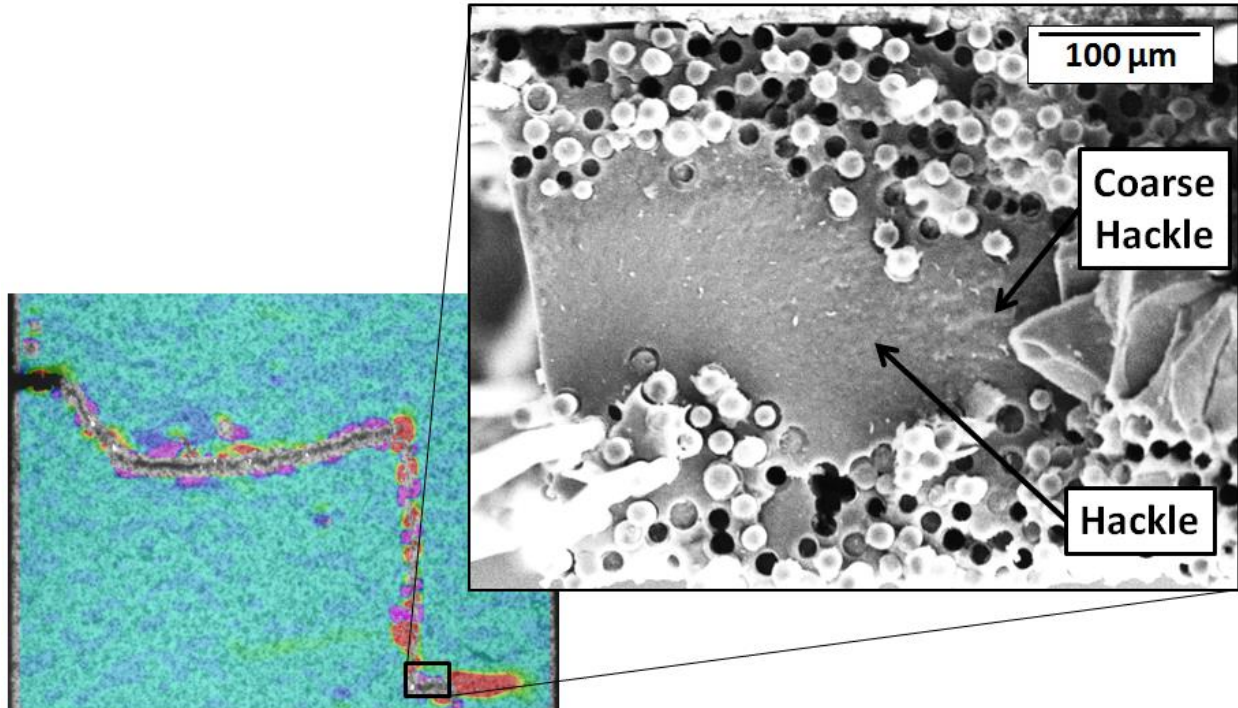


Figure 5.16 Hackle markings in the SiC matrix of a longitudinal unidirectional CMC indicate a new fracture surface originated in the longitudinal lamina.

Figure 5.17 shows examples of cracks that appear to have initiated in longitudinal laminas within a cross-ply laminate that was loaded to failure at 795° C in an SEM. In Figure 5.17 (a), hackle indicates a circular crack emanated from the longitudinal ply on a different crack plane than the neighboring transverse ply. Likewise, in Figure 5.17 (b) hackle markings run from fibers in a longitudinal ply to the adjoining matrix ply. It is possible that the primary crack that generated the fracture surface propagated through the matrix layer, but because fibers in the adjacent longitudinal ply were compressing the matrix material, the primary crack arrested laterally. At some point, stresses in the fiber layer became larger enough to initiate a crack in the fiber layer, which inevitably joined up with the primary matrix crack.

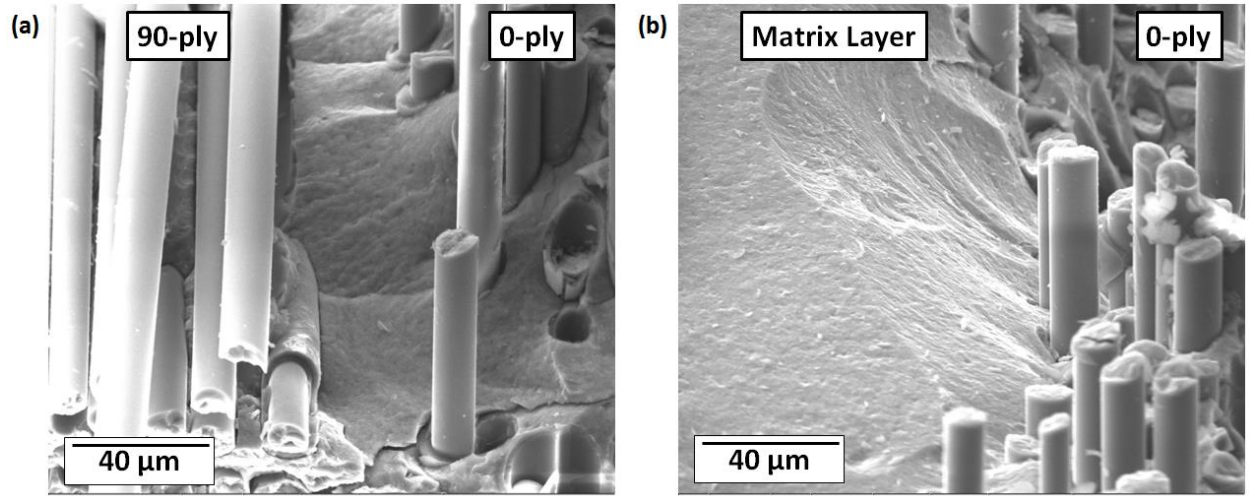


Figure 5.17 Apparent crack initiation in longitudinal laminas of a cross-ply $[(0/90/0/90)_s]$ CMC loaded in uniaxial tension at 795°C . In (a), a hackle emanates from longitudinal fibers adjacent to a transverse lamina. In (b), hackle emanates from longitudinal fibers adjacent to matrix-rich region.

5.4.6 Wallner Lines in Transverse Unidirectional Laminates

Wallner lines were not readily identifiable in longitudinal and cross-ply laminates. This may be due in part to the complex stress state induced by the fiber reinforcements. Fibers in transverse unidirectional laminates provide little reinforcement under a longitudinally applied tensile force. The SiC matrix supports the brunt of the load; consequently, the transverse laminate exhibits brittle behavior similar to a monolithic ceramic. It is perhaps for this reason that Wallner lines were readily identifiable only in a transverse unidirectional laminate loaded in tension. Figure 5.18 shows the Wallner lines that accompanied fracture in a transverse laminate. The source of fracture appears to be a flaw at the fiber-coating-matrix interface. Hackle points toward the flaw. Beyond the hackle, Wallner lines are observed. They may have formed as elastic pulses ahead of the crack front intersect flaws along the coatings in fibers that bound the matrix.

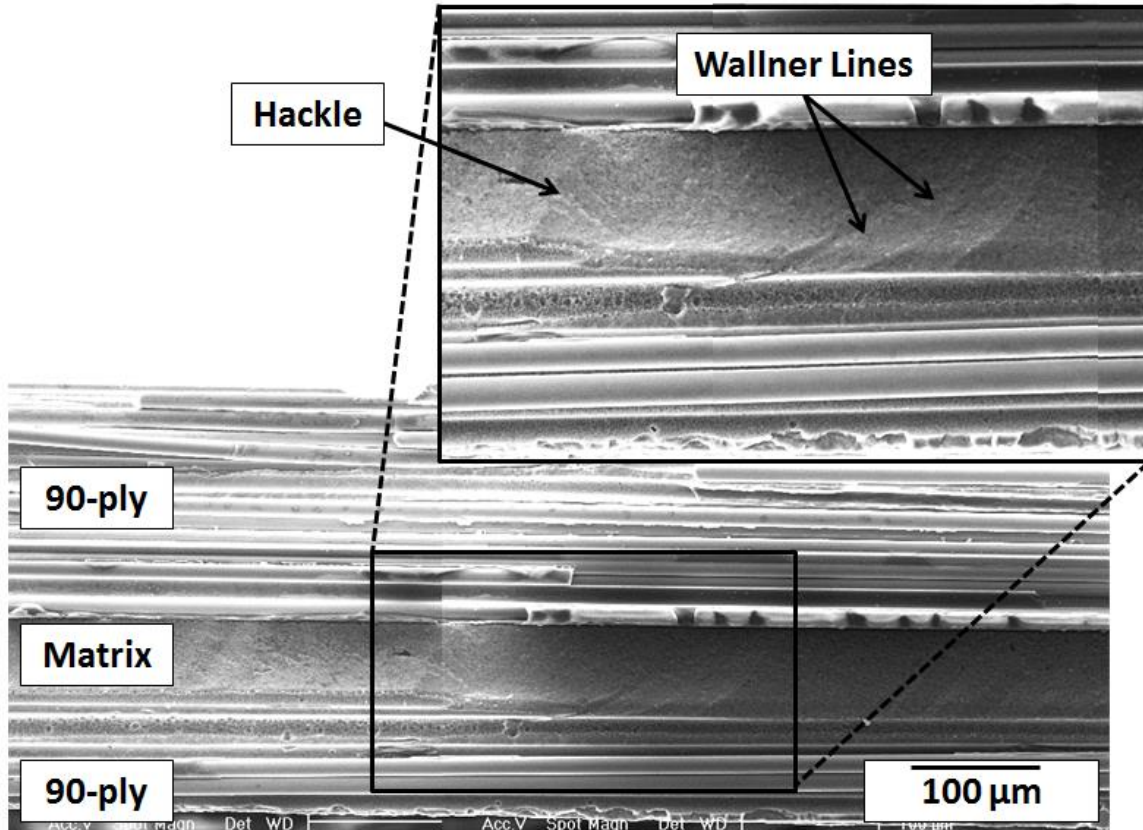


Figure 5.18 Micrograph of fracture surface in transverse unidirectional laminate loaded in tension in longitudinal direction. Hackle points towards potential source of crack initiation, which is flaw at matrix-coating interface. Wallner lines can be observed beyond hackle and coincide with regions of spalling in coatings of fibers that bound the matrix.

5.4.7 Influence of Fibers on Crack Propagation

The complex residual stresses introduced by thermal mismatch between the constituents (fiber, coating and matrix) of a CMC are not well understood. These stresses likely influence crack propagation and the resulting tortuous fracture surfaces. It has been reported that residual stresses in the vicinity of fibers are influenced by the fiber distribution, with radial compressive stresses exhibiting the most sensitivity to fiber distribution [4]. Specifically, it was noted that the variability in stress increased in the vicinity of fibers in contact with one another. This suggests that cracks emanating from fiber/coating/matrix interfaces may favor high-stress regions of clustered fibers. It has also been reported that the fiber arrangement and distribution of matrix cracks both influence the local stress state in CMCs [5-6].

The matrix of the SiC/SiC CMCs tested was fabricated through melt infiltration, leading to variations in microstructure particularly near the matrix-coating interface. Nanoindentation

was used to examine variations in matrix modulus as such variations can affect the local stress state. Figure 5.19 (a) shows nanoindent locations in the matrix of a cross-ply CMC. The average elastic modulus from the six indents was 330 GPa. The lowest measured modulus came from the indent located nearest a fiber (290 GPa). Indentations were also made in the matrix region around a single fiber as shown in Figure 5.19(b). The average modulus was 355 GPa and again the lowest modulus was in the region of matrix nearest the fiber (301 GPa). The significance of these measurements is that sharp variations in elastic modulus may alter the local stress state and influence crack propagation behavior around fibers. More measurements would be needed to definitively conclude that the local matrix modulus is reduced near fiber coatings.

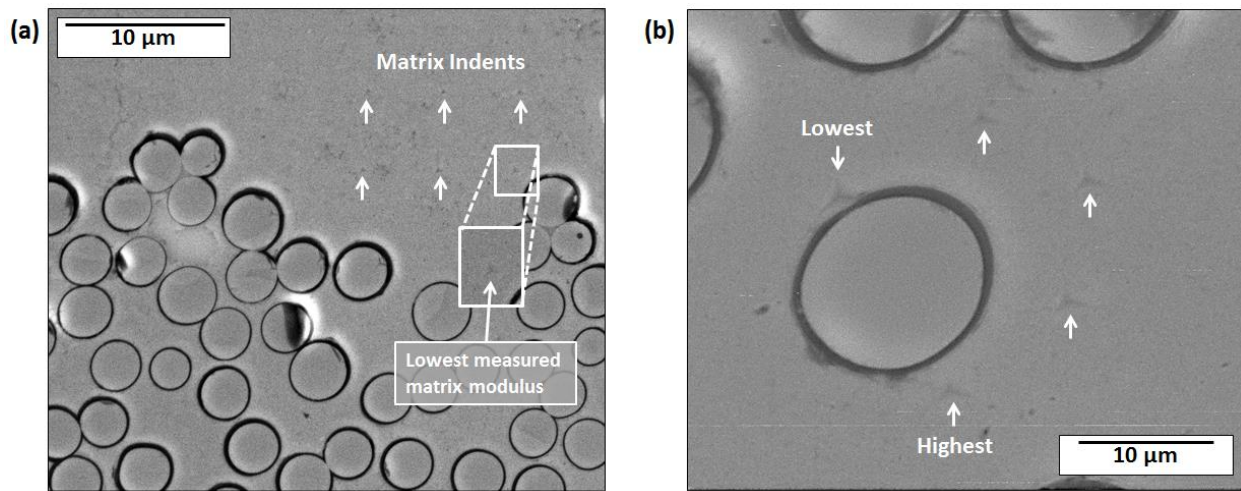


Figure 5.19 Nanoindent location in a cross-ply CMC matrix. In (a), the average elastic modulus measured from six indents was 330 GPa with the lowest modulus (290 GPa) at the indent nearest a fiber. In (b), moduli were measured in the matrix region along the perimeter of a fiber. The average modulus was 355 GPa with the lowest measurement (300 GPa) again located nearest the fiber.

Longitudinal fibers may alter the stress field in adjacent matrix regions enough to influence the trajectory of a propagating crack. This is illustrated in Figure 5.20, which depicts a portion of the fracture surface of a longitudinal unidirectional laminate that failed in tension. Characteristic tails of wake hackle are present, indicating the local direction of crack propagation and suggesting that the orientation of the crack front was guided by fibers. Additional evidence of the impact of longitudinal fibers on the local stress field is evident in the tail orientations, which mimic the undulating distribution of the longitudinal fibers.

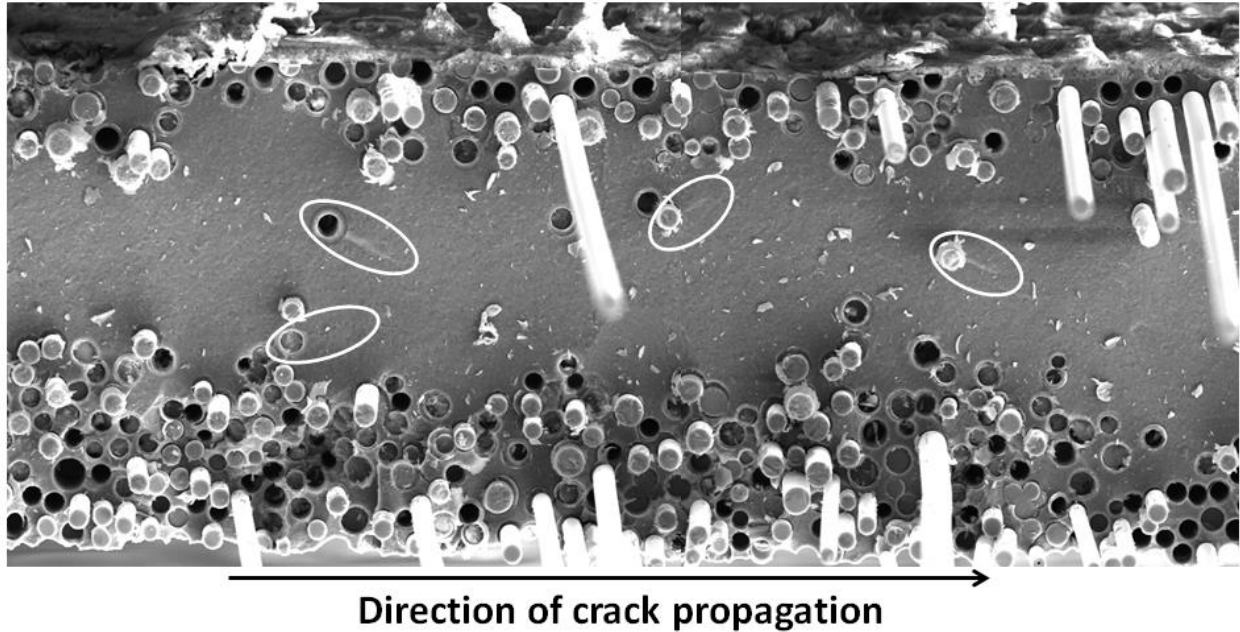


Figure 5.20 Wake hackle on the fracture surface of a longitudinal unidirectional laminate that failed in tension. The orientation of the tails of several hackle markings (circled in white) mimic the undulations in the distribution of longitudinal fibers. This suggests that the arrangement of fibers may influence the orientation of the crack front during propagation.

5.5 Conclusions

Fractography and full-field surface deformation analyses were combined to acquire a pseudo-3D perspective of crack initiation and propagation in CMCs. Cross-ply and unidirectional laminated composites were simultaneously imaged and mechanically loaded to failure. Conventional ceramic fractography was adapted to CMCs to obtain an understanding of crack evolution sub-surface while DIC provided a qualitative image of crack propagation on the surface. Hackle and rivermarks on fracture surfaces suggested that:

- machining with coarse tools (such as diamond saw blades) induces sub-surface cracking which can be sources of local initiation
- crack initiation can occur in longitudinal lamina in cross-ply laminates
- uneven distribution of fibers between opposite lamina in unidirectional laminates may influence the local direction of crack propagation.

Nanoindentation indicated that the matrix elastic modulus was lower near fiber coatings. A larger sample size is needed to establish a definitive correlation between matrix modulus and proximity to fiber coatings.

References

1. “Standard Practice for Fractography and Characterization of Fracture Origins in Advanced Ceramics,” ASTM C1322 (2010).
2. J. Dusza and M. Steen, “Fractography and Fracture Mechanics Property Assessment of Advanced Structural Ceramics,” *Int. Mater. Rev.*, **44** [5] 165-216 (1999).
3. G.D. Quinn, *Fractography of Ceramics and Glass Composites*, U.S. Government Printing Office, Washington, 2006.
4. B Sorenson and R. Talreja, “Effects of Non-uniformity of Fiber Distribution on Thermally-Induced Residual Stresses and Cracking in Ceramic Matrix Composites,” *Mech. Mater.*, **16** 351-363 (1993).
5. V. Calard and J. Lamon, “Probabilistic-Statistical Approach to Matrix Cracking in Ceramic Matrix Composites — Part I: Experimental Investigation of 2D Woven SiC/SiC Composites,” *Compos. Sci. Technol.*, **62** 395-399 (2002).
6. V. Calard and J. Lamon, “Probabilistic-Statistical Approach to Matrix Cracking in Ceramic Matrix Composites — Part II: Macroscopic Model,” *Compos. Sci. Technol.*, **62** 385-393 (2002).

Chapter VI

On the Association between Microscopic and Macroscopic Damage Evolution in Ceramic Matrix Composites

6.1 Introduction

Ceramic matrix composites (CMC) have traits that are desirable for structural, high-temperature engineering applications. The light weight, low thermal expansion coefficient, high thermal conductivity, large tensile strength and reputable toughness of a fiber reinforced silicon carbide-silicon carbide (SiC/SiC) composite, for example, makes it a prime candidate for gas turbine engine components. The SiC/SiC CMC belongs to a class of ceramic composites that can be characterized as having continuous fibers which are coated with a low-modulus material to provide a weak fiber-matrix interface. It is because of the weak interface that cracks propagate around fibers rather than through them, which allows the fibers to impart bridging tractions that make crack growth stable. The goal of this chapter is to convey the significance of incorporating multiple length scales in investigations of damage evolution in CMCs. Although several classes of CMC exist (short fiber, particle reinforced, porous matrix to name a few), the term “CMC” in this work refers to a continuous fiber ceramic composite with weakly bonded fiber-matrix interfaces.

Early investigations of damage in continuous fiber CMCs initially focused on the simple case of crack initiation and propagation in a unidirectional laminate in tension. Aveston et. al. [1] developed an analytical model (ACK) that correlated matrix crack spacing with (a) first matrix cracking stress and (b) interfacial shear stress. If provided with empirical crack spacing data, the

model can predict composite properties (e.g. interfacial shear strength). This model assumed that the fiber-matrix interface was not bonded, but under a constant frictional shear stress [1-2]. The model was later updated to include bonded interfaces [3] and subsequent models were developed to account for weakly bonded interfaces that partially debond in the presence of a crack tip [2, 4-5]. Solti [5] adopted a different modeling approach than Avetson, et. al. [1, 3] and Budiansky et. al. [4] by using shear-lag micromechanics to predict mechanical behavior. The ACK model assumed cracks in longitudinal unidirectional laminates form only if matrix flaws exceed a critical length [6]. Citing analytical investigations of the influence of flaw size on crack initiation [7-9], Beyerle et. al. concluded that appreciable cracking occurs only for flaws that exceed the critical length [6].

A shortfall of the ACK and similar models is that they do not account for all mechanisms of toughening in propagating matrix cracks that permit the CMC to fail in a non-catastrophic manner. Properties of the fiber-matrix interface dictate how cracks propagate in longitudinal unidirectional CMCs. A weakly bonded interface causes propagating cracks to deflect around fibers, leaving in their wakes partially debonded fiber-matrix interfaces [2]. Debonding at the interface initiates due to the region of high stress intensity at the crack tip. If the bond is too strong, debonding will not occur and the crack will cut through the fiber. It is of enough significance that some damage models are concerned solely with the mechanics of debonding at the fiber-matrix interface [10-11]. Crack deflection is partially responsible for the reputable toughness of continuous fiber CMCs, and several studies have analytically characterized this toughening effect [12-13]. Fibers that fracture at a distance remote from the plane of a matrix crack experience interfacial frictional shear along debonded regions of their fiber-matrix interfaces [2]. This is referred to as fiber pullout and is also partially responsible for graceful failure in CMCs. As with debonding, a fair amount of research has been devoted to the pullout process [14-17]

The utility of the previously discussed damage models is in predicting material properties (e.g. matrix cracking stress, tensile strength and matrix crack density) of simple composite layups. Most require empirical data inputs and, as noted by Beyerle [6], the simplifying assumptions used to develop these models can result in unreliable predictions when applied to real materials. Alternative approaches have been taken that are broader in scope; they

characterize damage, from crack initiation to failure, by correlating experimental measurements of cracks with global stress-strain behavior [18-19].

Using acrylic replica and acoustic emission techniques to investigate damage in a CAS/SiC longitudinal laminate, Sorenson [18] concluded that damage occurs in four progressive stages, each corresponding to unique behavior in stress-strain curves: (1) linear-elastic deformation (i.e. below the proportional limit (PL)), (2) initiation and accumulation of matrix cracks (at and above the PL), (3) interfacial sliding at debonded fibers (well beyond the PL) and (4) additional matrix cracks and fiber fracture (well above the PL and through failure). Although evidence of damage was observed near the upper limit of the first stage, matrix cracking did not occur until the second stage. Matrix cracking was most abundant in the second stage, approaching crack saturation at the upper limit. By the third stage, deformation was linear but with a reduced loading modulus. No cracking events were observed, load retention was attributed to debonding and frictional sliding. Additional matrix cracking, fracture of bridging fibers and final failure characterized the fourth stage. The behavior observed by Sorenson in CAS/SiC composites doesn't necessarily reflect behavior in SiC/SiC CMCs of similar layup. The CAS/SiC composites have a much larger ratio of fiber stiffness to matrix stiffness than that of SiC/SiC and other non-oxide CMCs. In this case, the SiC fibers not only toughen the glass composite, but increase its elastic modulus. However, the work of Sorenson provides valuable insight into damage behavior in stiff, fibrous composites.

The Sorenson model provided illustrative insight into damage evolution in continuous fiber CMCs, but only considered the case of a unidirectional laminate. Investigating damage accumulation in cross-ply CAS/SiC (calcium aluminosilicate/silicon carbide) CMCs with optical microscopy, Daniel et. al. noted that damage initiated in transverse plies in the form of microcracks that extend radially from the fiber-matrix interface [20]. This event marked the first deviation from proportional loading in the laminate. With further loading, cracks developed along the fiber-matrix interfaces; this was accompanied by a drop in modulus. Eventually the radial and interfacial cracks merged, forming macroscopic matrix cracks. Matrix cracks accumulated in the transverse plies until they reached saturation spacing on the order of the lamina thickness. Matrix cracks did not develop in the longitudinal plies until after crack

saturation in the transverse plies. In short, their findings imply damage does not initiate until the PL.

Using acoustic emission to monitor matrix crack initiation in woven SiC/SiC CMCs, Morscher found that matrix cracks develop during linear-elastic loading [21]. The discrepancy between the findings of Daniels and Morscher could be a result of differences in composite architecture. On the other hand, optical microscopy may have lacked the spatial resolution to detect damage in early stages of loading. This chapter discusses techniques to more reliably detect the onset of damage. The implication of early-stage cracking in CMCs is that it could provide a pathway for aggressive environmental attack of the fibers [2], which could be a major concern in hot sections of a gas turbine engine.

This chapter adopts a different approach for investigating damage in CMCs. Rather than establishing discrete damage stages with respect to the stress-strain response like Sorenson did, damage is characterized with respect to three distinct length scales defined below. Combining high-magnification imaging with digital image correlation enabled damage detection at stresses well below the proportional limit. There were two primary objectives:

- (1) identify the capabilities and limitations at each length scale with regard to identifying damage in SiC/SiC CMCs
- (2) determine the implications, if any, that damage observed at microscopic length scales has on damage observed at the macroscopic length scale.

It was found that fine cracks initiated in localized regions of fiber coatings at low stresses. Some of these cracks evolved into matrix cracks. Matrix crack propagation was dependent on the state of stress near the crack tip and the local microstructure. Some of these matrix cracks morphed into larger cracks. The density of large matrix cracks increased with load, reaching saturation prior to failure.

6.2 Experimental Methods

Cross-ply ($[0/90/0/90]_s$) and longitudinal ($[0/m/0]$) SiC/SiC CMCs were mechanically loaded in a miniature load frame (Kammrath & Weiss GmbH) capable of operating in a scanning electron microscope (SEM) and micrographs were captured under load. Imaging was

conducted at three distinct length scales: (1) constituent length scale ($FOV \leq 100 \mu\text{m}$), (2) lamina length scale (FOV several hundred microns wide) and (3) laminate length scale ($FOV > 1 \text{ mm}$). The constituent and lamina level tests were conducted in an FEI Quanta 3d (SEM). Laminate level tests were imaged outside of the SEM with digital cameras (most experiments used a 5 megapixel Grasshopper GRAS-50S5M charge-coupled device at 15 fps; one experiment utilized Photron FASTCAM SA1 high speed cameras at frame rates ranging from 50 to 1500 fps). Surface deformations were subsequently measured using Vic-2D DIC software. Figure 6.1 depicts the set-up for in-situ tensile testing in the SEM. In Figure 6.1a, a CMC tensile coupon is mounted in the grips of a miniature load frame; it is configured such that the SEM images the edge of the coupon rather than the surface. The miniature load frame sits on a stage that is attached to the SEM door. The entire load frame then slides into the chamber of the SEM (shown in Figure 6.1b) upon shutting the door.

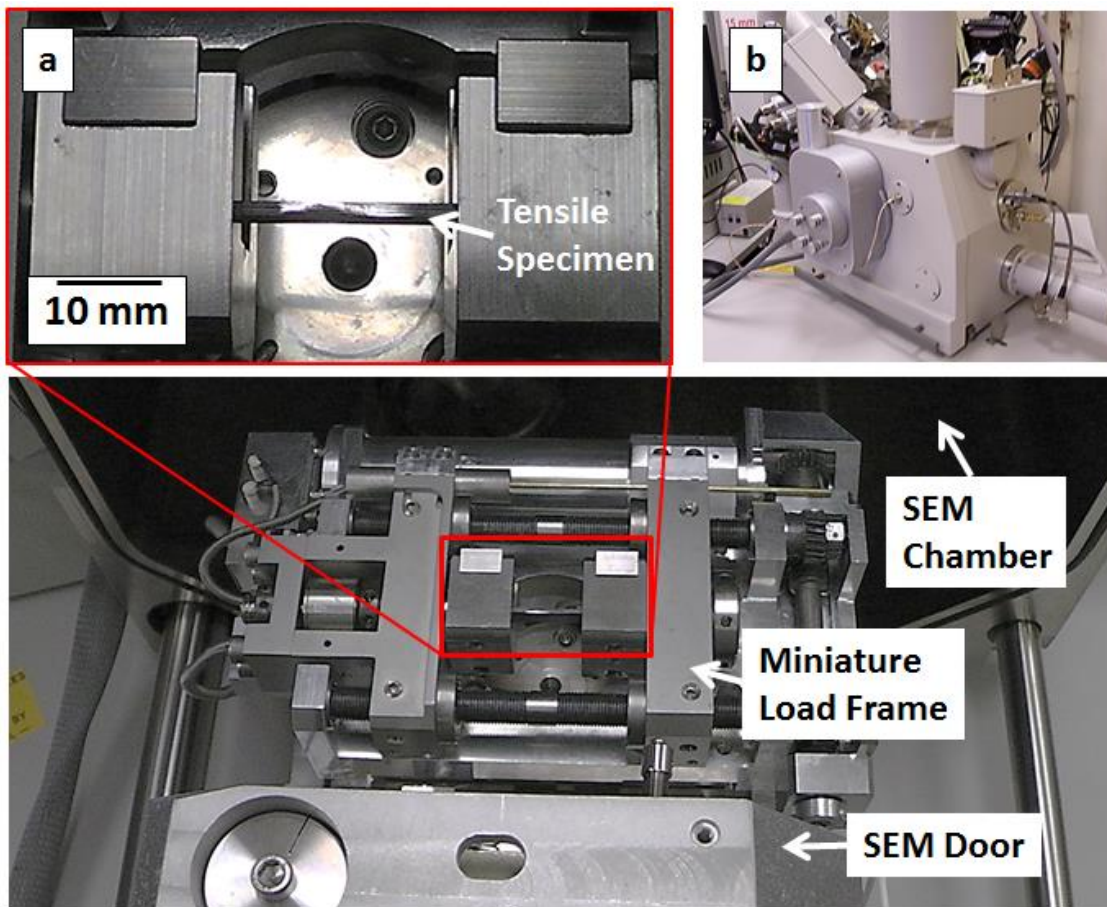


Figure 6.1 Experimental set-up for in-situ testing in the SEM. In (a), a CMC tensile coupon is mounted in the grips of a miniature load frame that is attached to a door-mounted stage. The

grips are rotated 90 degrees to image the edge of the test coupon. In (b), the entire load frame is enclosed in the SEM.

Digital image correlation requires that a high-contrast and uniformly dispersed speckle pattern be applied to the surface of the tensile coupon. For the constituent and lamina level tests this was accomplished using gold nanoparticles (NPs) with individual particle diameters ranging from 30 to 150 nm. Many tests were concerned only with imaging a localized field of view (such as fracture at the tip of notch). For these tests, 150 nm Au nanoparticles suspended in isopropyl alcohol were drop cast onto the surface. Most constituent-level tests, however, required imaging at several locations spread far apart along the gage section. This required quality patterns over a large swath of the coupon. Immersing silanized tensile coupons in a 30 nm Au colloidal suspension ensured this happened (please refer to Chapter 2 for patterning details). Patterns for the laminate level tests were applied with paint using an airbrush (Iwata Micron-b). This method produced speckles of a few microns in diameter. Figure 6.2 provides examples of nanoparticle speckle patterns applied to the edge of a tensile coupon. The NP patterns facilitate imaging at FOVs small enough to resolve deformation at the fiber-coating-matrix interface.

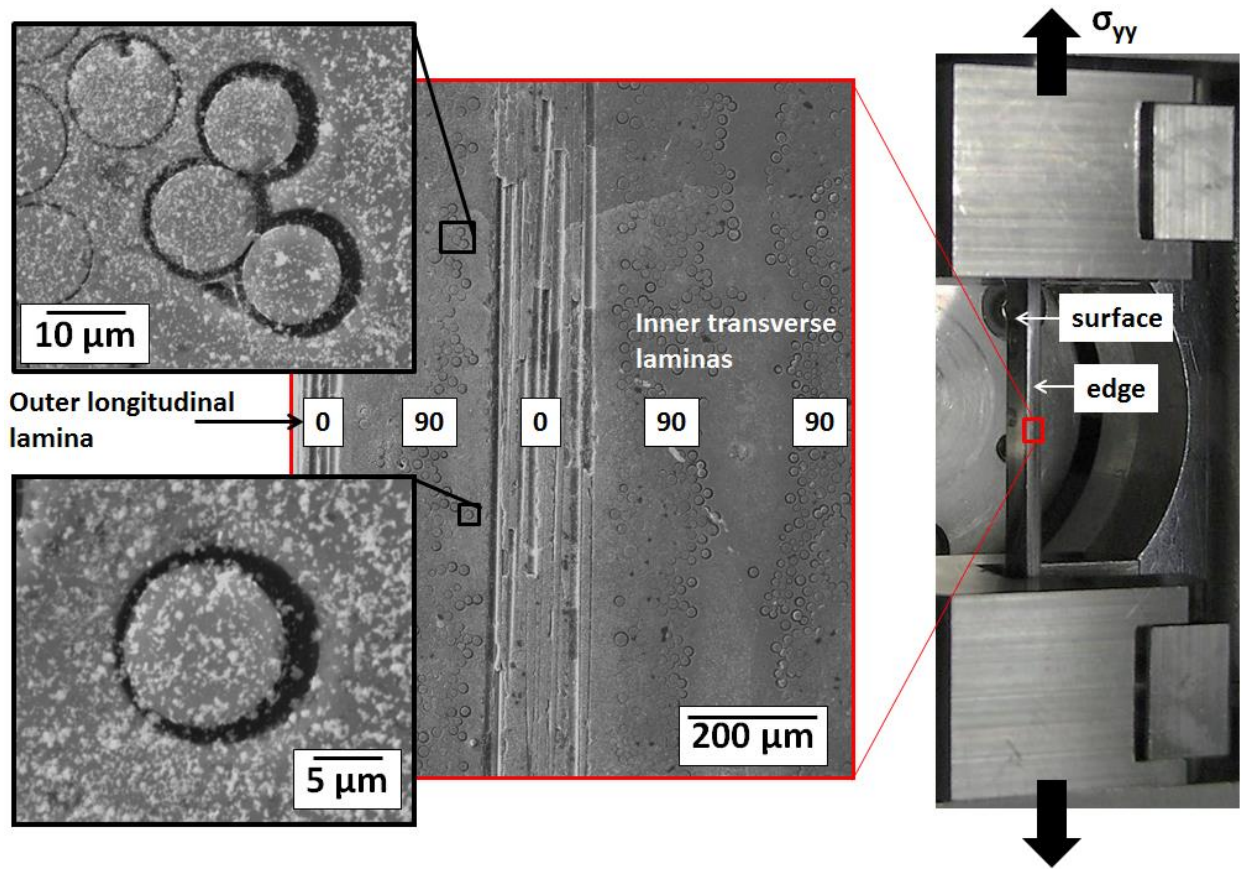


Figure 6.2 SEM micrographs of transverse fibers captured along the edge of a $[0/90/0/90]_s$ SiC/SiC CMC loaded in tension. Gold NP agglomerates covering the fibers permit measurement of full-field deformations using DIC. A larger scale micrograph of the cross-ply CMC depicts several longitudinal (0) and transverse (90) lamina.

The term “proportional limit” is used extensively in this work. The proportional limit represents the first point in the stress-strain relation where loading is no longer proportional (i.e. a permanent deviation from linearity occurs). In most of the tensile tests conducted, a distinct deviation from linearity was not evident in load-displacement curves. To normalize findings from each test, damage states are reported relative to a pre-established, single-valued proportional limit stress. Per the manufacturer, the PL stress for the SiC/SiC CMCs represents the intersection of the stress-strain curve with a line drawn parallel to the linear-elastic portion and with 0.05% strain offset.

6.3 Evolution of Damage in CMCs at Multiple Length Scales

The subsections that follow examine damage (i.e. cracking) in the SiC/SiC CMCs at multiple length scales under monotonic and cyclic loading. Localizations in the full-field strain maps are indicative of cracking, as linear elastic deformation in the ceramic constituents was smaller than the spatial resolution of the DIC data. It is shown that observations from a single length scale are insufficient to characterize damage evolution. Therefore, deformation data was collected at both the microscale (constituent and lamina) and the macroscale (laminate). Damage, specifically crack initiation and propagation, was examined on the surface and edges of CMC laminates to gain multidimensional perspectives. *Section 6.3.1* discusses crack initiation in microstructural constituents. *Section 6.3.2* addresses crack propagation within individual lamina. *Section 6.3.3* extends findings from the microscale to the accrual of damage at the macroscale. *Section 6.3.4* discusses the mutual dependence of the micro and macro length scales in understanding damage evolution in the composite.

6.3.1 Damage Evolution at the Constituent Length Scale

Damage assessment at the constituent length scale was focused on determining where (with respect to microstructural features) and when (with respect to the global state of stress) cracks initiate. Indications of cracking (characterized by localized concentrations of high-magnitude maximum principal strain) in the thicker regions of transverse fiber coatings in un-notched tensile coupons were observed in DIC data well below the proportional limit. This is illustrated in the deformation maps of Figure 6.3, where apparent cracking is contained to small, localized areas (primarily tops and bottoms) of fiber coatings. Strain localization occurs in areas of the fiber coating that are oriented perpendicular to the loading axis (tops and bottoms of fibers).

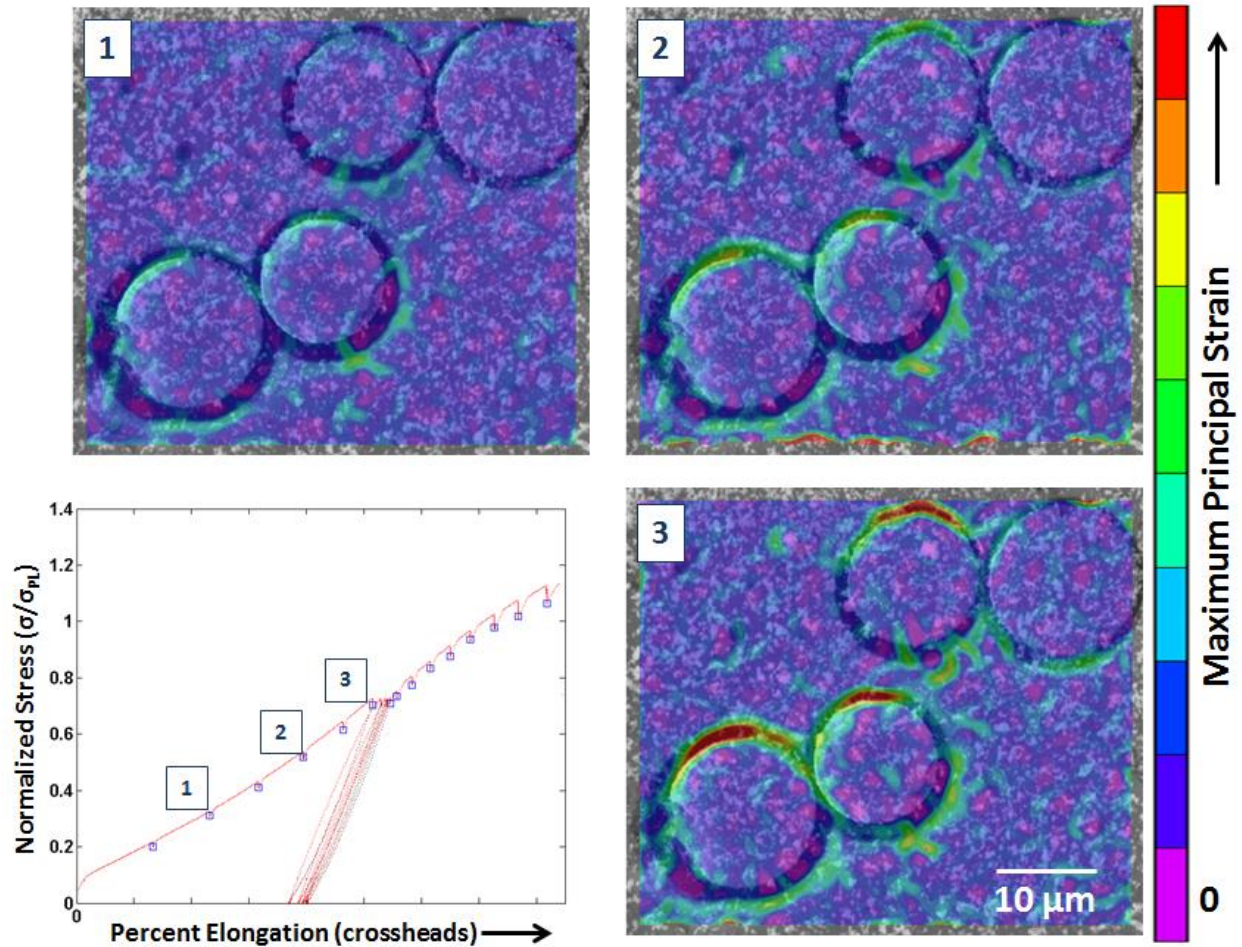


Figure 6.3 Full-field maximum principal strains overlaid on SEM images of transverse fibers at three load increments for a CMC loaded in tension. Frames (1) through (3) are below the proportional limit. Strains localize in regions of fiber coatings oriented along the loading axis, which is vertical in the plane of the page.

Although strain localizations that appeared below the proportional limit were confined to the coating, some may serve as initiation sites for cracks that later developed in the matrix. Morscher [21] measured crack densities in woven-fiber SiC/SiC CMCs using acoustic emission and reported the appearance of low crack densities (<0.1 cracks per mm) at stresses just above 50 MPa. Here, we detected strain localizations in coatings at lower stresses; the disparity between our findings and Morscher's is small and could be due to: (1) the difference in composite architectures (Morscher's woven versus our cross-ply) or (2) that damage in coatings did not register as acoustic events indicative of cracking in Morscher's work.

The localized strain magnitudes intensified and became more widespread as the PL stress was approached. Again, strain localizations were prevalent in portions of coating that lay along the loading axis. This is apparent in the third frame of Figure 6.3, where every fiber coating (rather than a few) contains strain localizations and those that existed in earlier frames have intensified. Figure 6.4 shows strain localization in transverse fiber coatings for a separate tensile coupon for which SEM images were captured at a FOV that sampled many more fibers. The deformation behavior in the first three frames of Figure 6.4 mimic the behavior observed in Figure 6.3; that is, strain localizations appear in the coatings of nearly every fiber and, within each coating, are distributed primarily along the loading axis. By the fourth frame of Figure 6.4, that is above the proportional limit stress, strain localization in several adjacent fibers merge into a band that is indicative of a tunneling crack in the matrix.

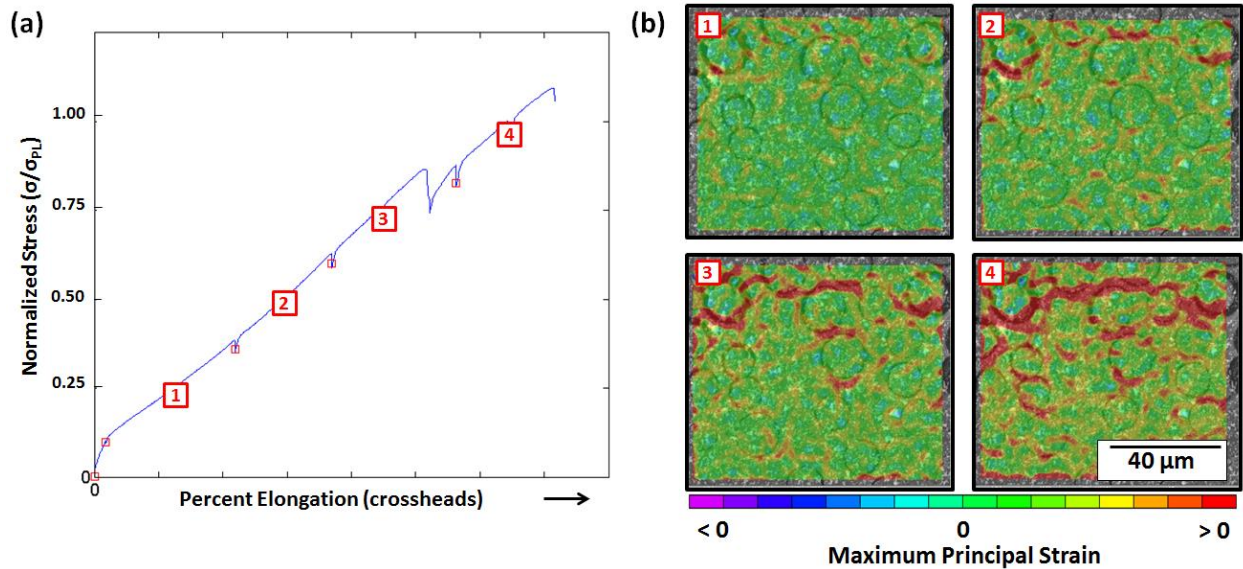


Figure 6.4 Full-field maximum principal strains overlaid on SEM images of transverse fibers at four load increments for a CMC loaded in tension. Frames (1) through (3) are below the proportional limit. Strains localize in regions of fiber coatings oriented along the loading axis. Frame (4) is captured after an unexpected drop in load that was likely due to cracking remote from the FOV. Localized strains in several adjacent fibers converge into a band of localized strain that is likely a tunneling crack. The applied stress has been normalized to the PL stress.

For reasons that will not be addressed herein, the CMCs tested were in a state of residual stress, compressive in the matrix and tensile in the fibers. The magnitude of the residual stress relaxed if the material was held at elevated temperatures for extended periods of time. To assess the effect of residual stress on strain localization in transverse fibers, constituent scale

experiments were conducted on a CMC that was annealed to a state of minimum residual stress. As shown in Figure 6.5, the strain accumulation in the annealed material was not distinctly different from the as-received sample. One may expect the annealed material to exhibit disperse cracking at early stages of loading because of the relaxed compressive matrix stresses, but this was not observed. The annealed samples did not exhibit cracking (more disperse than the as-received sample) until the later stages of loading. However, the DIC data for the annealed sample was noisier due to oxidation on the surface, which caused more pronounced charging (versus the as-received sample) after extensive imaging in the SEM. The appearance of widespread cracking may be an artifact of image noise.

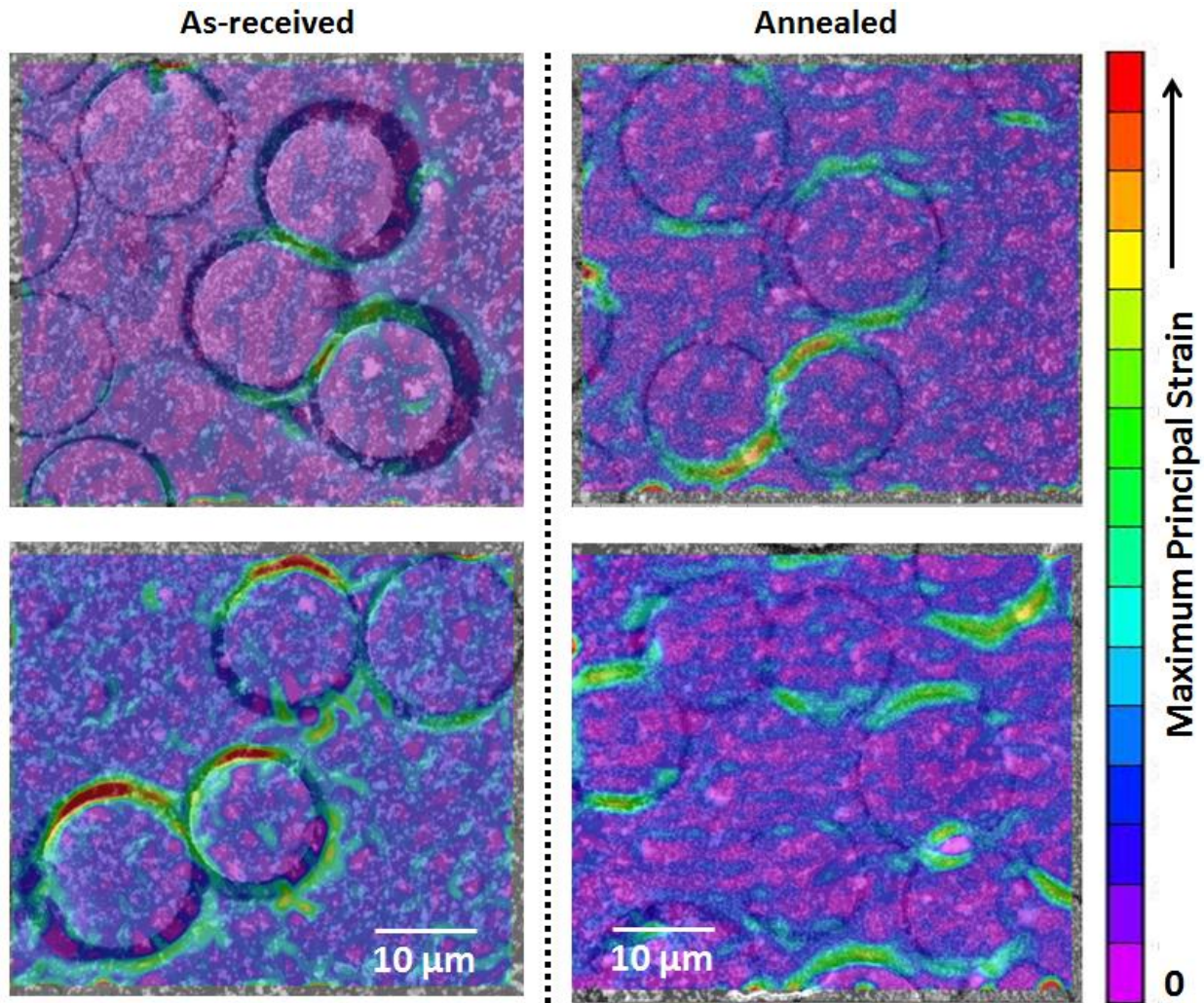


Figure 6.5 Comparison of full-field strains in transverse lamina of as-received and annealed CMCs loaded in tension at. Both examples exhibit widespread (several fibers) strain localization in the fiber coatings. Strain localization is prominent in regions of the coatings aligned with the loading axis as well as in fibers in contact.

An interesting finding from the constituent scale deformation monitoring is that, as applied load increased, the cracks at the fiber-coating-matrix interface grew to openings on the order of tens of nanometers. Using DIC displacement data, post-test virtual extensometers were placed across the coatings of selected fibers and their length was measured at each load increment as illustrated in Figure 6.6. In Figure 6.6 (a) it is shown that crack openings are larger in the direction of loading (vertical). In Figure 6.6 (b), it is shown that crack openings are larger for extensometers oriented in the loading direction as well as for extensometers between fibers in contact. These measurements of crack opening displacement at the fiber-coating-matrix interface

can be used in developing models of oxidation at cracks that propagate along the coating. Oxidation could be a significant concern if the environmental barrier coating that surrounds a CMC component were to become compromised in the hot section of a gas turbine; oxygen could travel through these channels and potentially degrade the fibers.

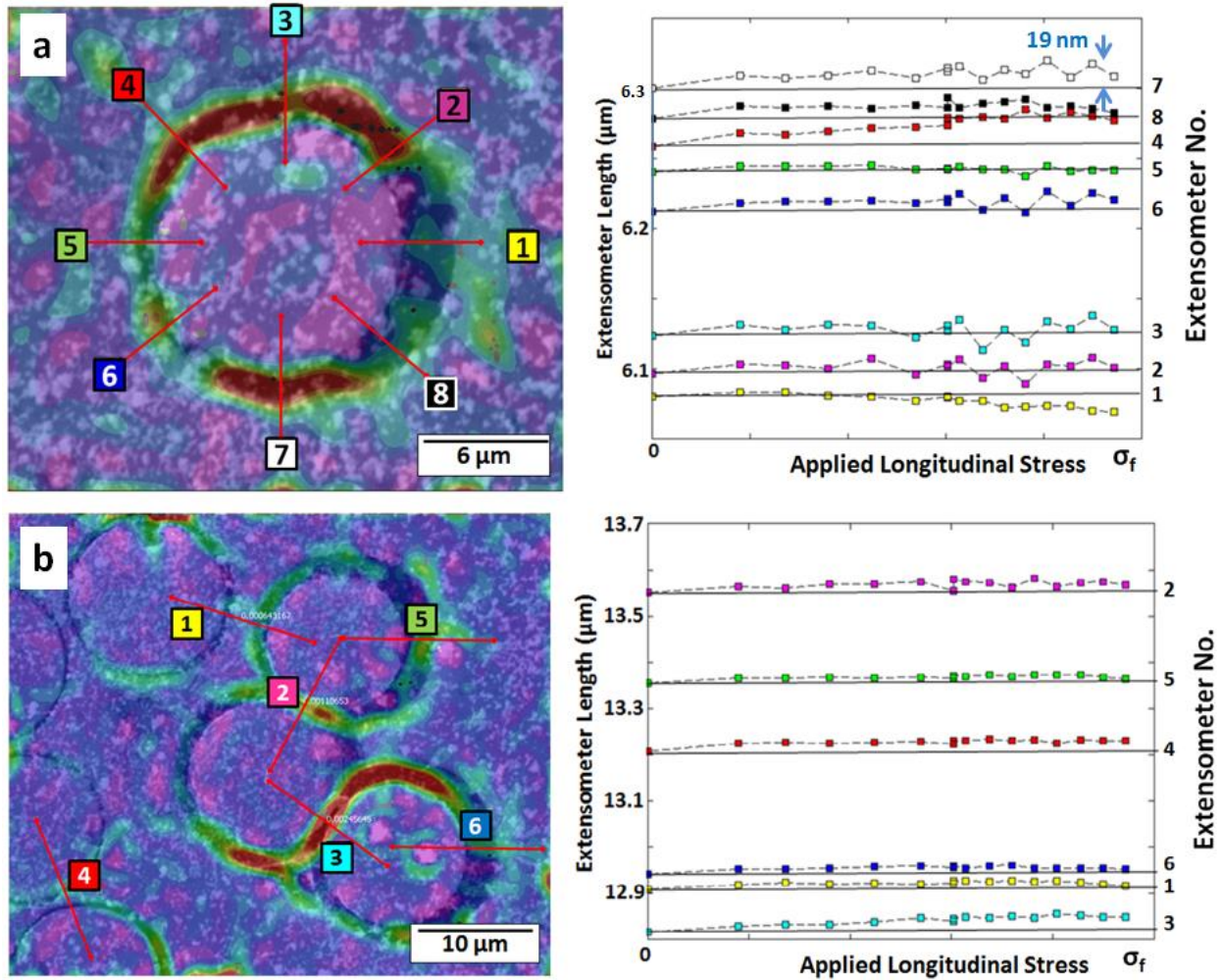


Figure 6.6 Crack openings (as measured using virtual extensometers and DIC data) across the fiber-coating-matrix interface for SiC/SiC CMC loaded to failure in tension. In (a), crack openings are larger for extensometers oriented in the loading direction (vertical in the plane of the page). In (b), crack openings are largest for extensometers bridging fibers in contact and for extensometers oriented nearest the loading direction. At their greatest, crack openings are on the order of tens of nanometers.

Up to this point, the discussion of damage evolution has considered only the case of monotonic loading. In service, however, CMCs experience cyclic loading (e.g. mechanical and thermal fatigue); hence, we investigated damage evolution in several CMCs under tensile dwell

fatigue (two minute dwells at $\sim 75\%$ of the PL stress). During the initial loading cycle, strain localizations developed and grew in the transverse fiber coatings in the same manner as discussed for monotonic loading. During cyclic loading, the intensity and dispersion of the strain localization grew with each fatigue cycle, ultimately approaching a steady state. The evolution of damage is illustrated qualitatively through full-field strain maps (Figure 6.7) and quantitatively in plots of crack opening across the fiber-matrix interface (Figure AppA1-AppA3). Steady state was reached between 10 and 20 fatigue cycles at the dwell stress. Upon unloading after ten fatigue cycles, there was residual damage at the fiber-coating interface.

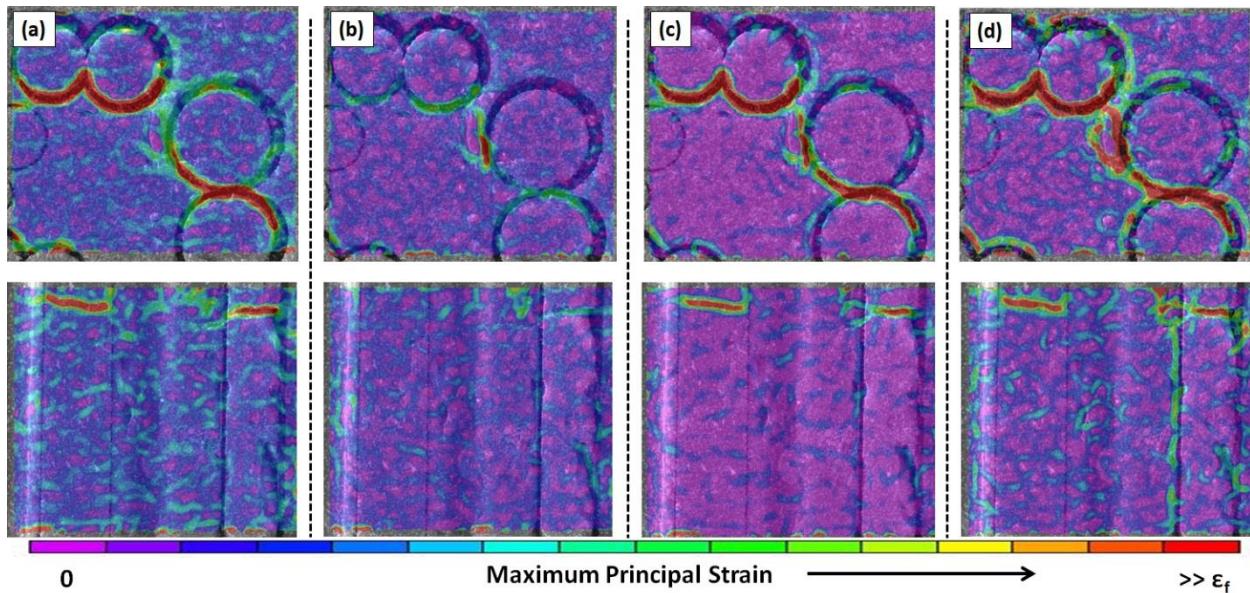


Figure 6.7 Strain maps are plotted on micrographs for two-minute tensile dwell fatigue cycles above proportional limit (PL). Above: fibers are sampled from a transverse ply; below: fibers are sampled from a longitudinal ply after (a) 10 cycles, (b) 10 cycles unloaded, (c) 20 cycles and (d) 50 cycles. After 20 cycles, there is no apparent increase in the intensity and dispersion of the strain localization. Upon unloading after 10 cycles, there was residual damage at the fiber-coating interface.

For purposes of comparison, dwell fatigue results from the previously discussed annealed sample were compared with the as-received sample. As shown in Figure 6.8, there was no distinct difference in damage behavior between the two samples. Widespread cracking would be expected in the annealed sample because the compressive residual stress in the matrix that works to impede matrix crack propagation was reduced. Strain localization appeared more widespread in the annealed sample (i.e. strains localized in multiple regions of the fiber coatings); however, the image data from which strains were measured was noisier than the as-received image data,

likely due to charging that resulted from the electrically resistive oxide coating on the surface of the sample.

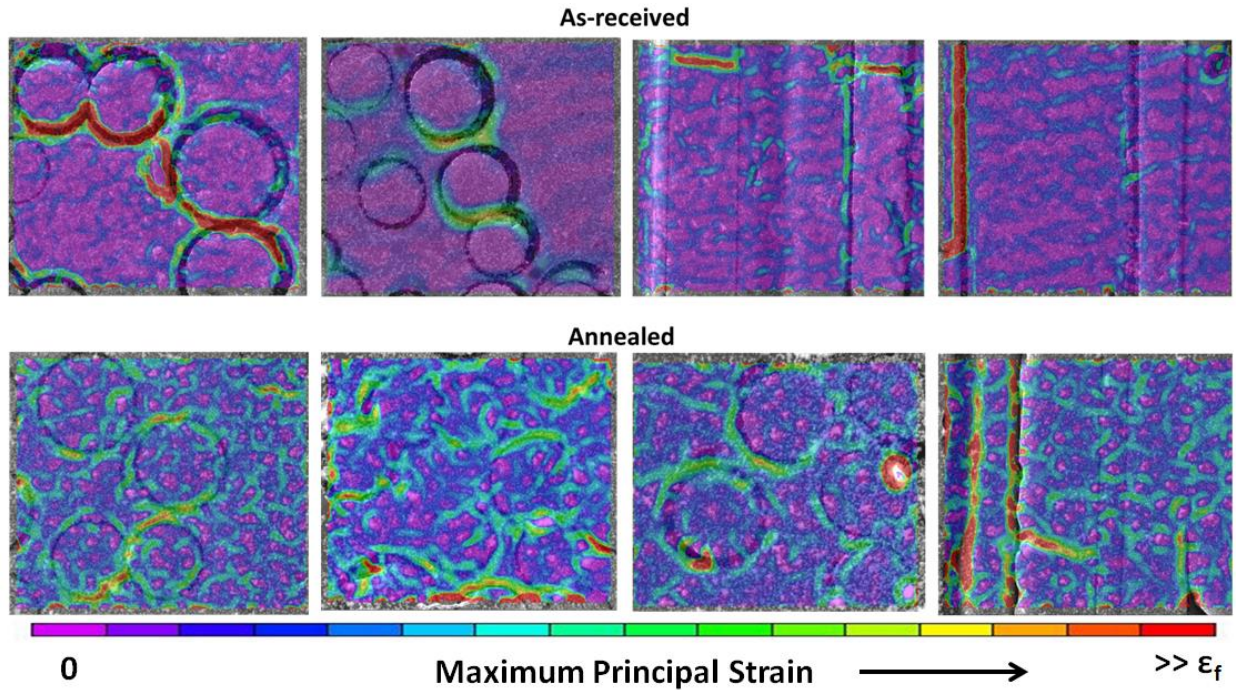


Figure 6.8 Full-field strains collected from various areas of interests along the edges of tensile coupons during dwell fatigue for an as-received (top) and annealed (bottom) CMC. Images captured after 40 two-minute dwell cycles at a stress level below the proportional limit. Damage, as indicated by strain localizations, appears more widespread in the annealed sample than in the as-received sample; however, this may be noise in the DIC data that manifested as an artifact of charging in the SEM for the heavily-oxidized annealed coupon.

During each dwell fatigue cycle, the samples were loaded to 75% of the PL stress, then the grip displacement was fixed, allowing load to relax over the course of the two-minute dwell. Figure 6.9 shows plots of the load-drop during each dwell cycle for the two samples. Again, the annealed sample exhibited the same behavior as the as-received sample; the load drops approach a bottom limit after 30 dwell cycles.

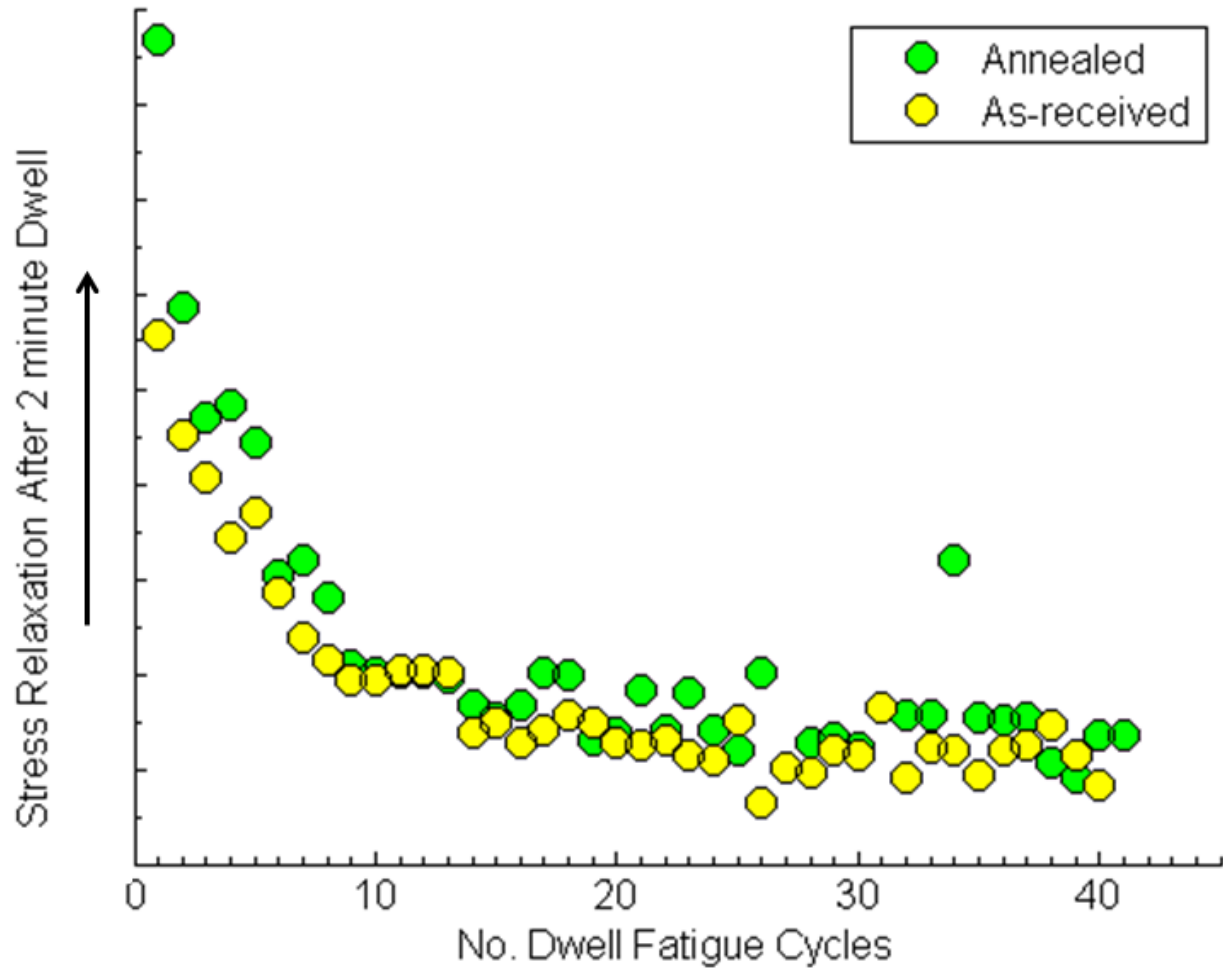


Figure 6.9 Load-drop during dwell cycles for as-received and annealed CMCs. Samples exhibit similar behavior: load drop approaches a minimum value after 30 cycles of tensile dwell fatigue.

6.3.2 Damage Evolution at the Lamina Length Scale

The transition from constituent to lamina marks a distinct difference in the information captured from deformation fields, and the applicability of this information to understanding damage evolution in CMCs. While the constituent scale informed when and where cracks initiated in transverse and longitudinal fiber coatings, the lamina scale introduces more fibers into each FOV and thus facilitates analyses of crack propagation between fibers. This is illustrated in Figure 6.10, where matrix cracks evolve along the edge of a notched tensile coupon (the edge opposite of the notch is depicted in the strain fields). Between the second and third frames, the matrix crack at the bottom of the micrographs relaxes (despite an increase in the global applied force) as a neighboring crack (top-right in the fourth frame) develops; the

neighboring cracks influence each other. The larger FOV permitted observation of multiple matrix cracks but reduced the spatial resolution of deformation measurements. At this FOV, fine cracks in fiber coatings that were readily apparent at the constituent scale may go undetected. However, the increased number of experimental fiber observations is important because the focus of effort shifts primarily to understanding how coating morphology and fiber distribution influence crack propagation.

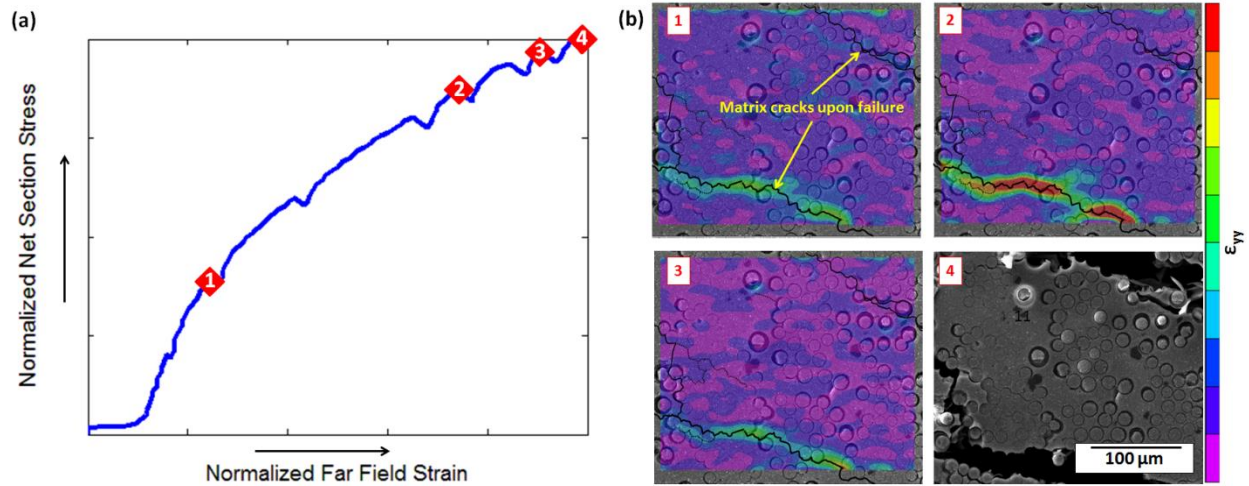


Figure 6.10 Damage evolution as depicted in longitudinal strain fields sampled along the edge of a notched tensile coupon. Micrographs depict the edge opposite of the notched edge. Numbered locations in stress-strain space of (a) correspond to frames in (b). Despite an increase in global applied stress between the second and third frame, the matrix crack at the lower-left of each from relaxes as the matrix crack at the upper-right evolves.

Beyond being useful for conducting statistical analyses, the intermediate-sized lamina scale is large enough to encircle a notch-tip; this permits high-magnification analyses beginning with crack initiation at a notch and continuing with crack propagation through the rest of the gage section. Longitudinal strain fields of a cross-ply CMC loaded in tension at 800 °C are depicted in Figure 6.11. In (a), the strains have been filtered to remove noise, but this also reduced the spatial resolution of the strain fields. In (b), minimal strain filtering has been applied so that the strain fields would reveal fine matrix cracks. It is clear that the lobes of localized strain in (a) are actually comprised of several neighboring cracks, some of which originate at the notch. These cracks would go undetected at larger length scales, which demonstrates the significance of analyzing deformation in CMCs at multiple length scales. For further information regarding high-temperature, small-scale deformation mapping, refer to Chapter 3.

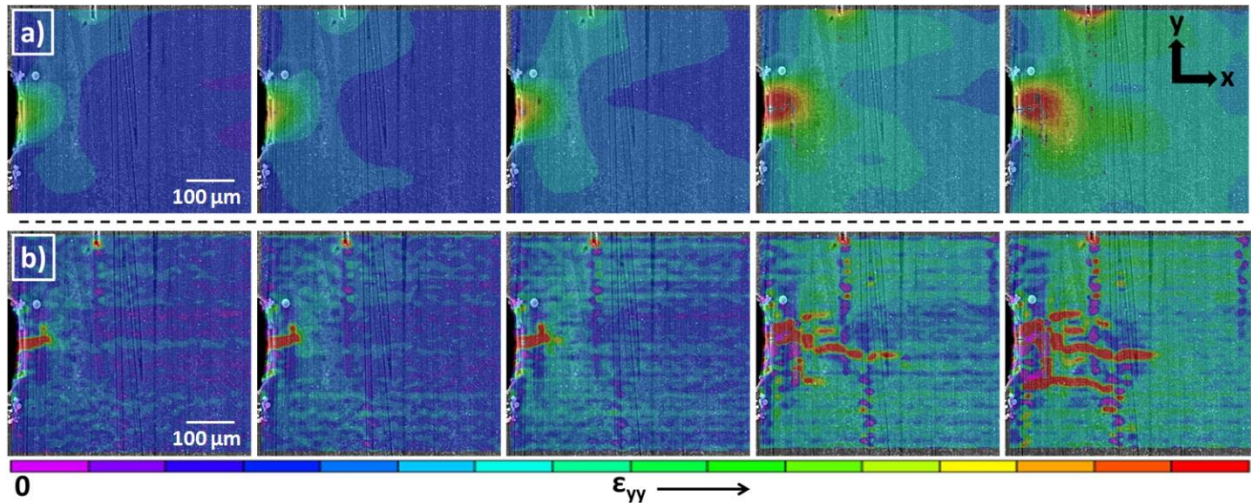


Figure 6.11 Longitudinal strain fields emphasizing the significance of scale in analyses of damage evolution in CMCs. Panels sequence indicates crack growth from left to right. The strains in (a) have been filtered more aggressively ($> 4\times$) than those in (b) at the expense of spatial resolution. As a result of the effectively smaller length scale in (b), fine cracks originating at the notch are detectable.

Figure 6.12 depicts the usefulness of lamina-scale deformation fields in understanding how matrix cracks propagate through longitudinal lamina in a CMC. In Figure 6.12 (a), a matrix crack (imaged on the surface ply of a $[0/90/0/90]_s$ CMC) deflects along longitudinal fibers as it traverses the matrix. The deflection lengths in this FOV are on the order of tens of micrometers. It should be noted that the fibers on the surface have been partially lapped, which may influence the position and length of crack deflections along each fiber. A neighboring matrix crack is shown in Figure 6.12 (b). Inset is a magnified image of the lower crack, which is emerging at the tensile coupon surface. The crack, detected by DIC, is visually undetectable in the enlarged micrograph. At macroscopic length scales, DIC would not be able to detect this crack at the early stage of loading from which the SEM image was collected. The second crack likely originated as a subsurface crack in a transverse ply. A shortfall of 2D DIC is that it is strictly a surface technique which does not inform us of the sub-surface history of a crack.

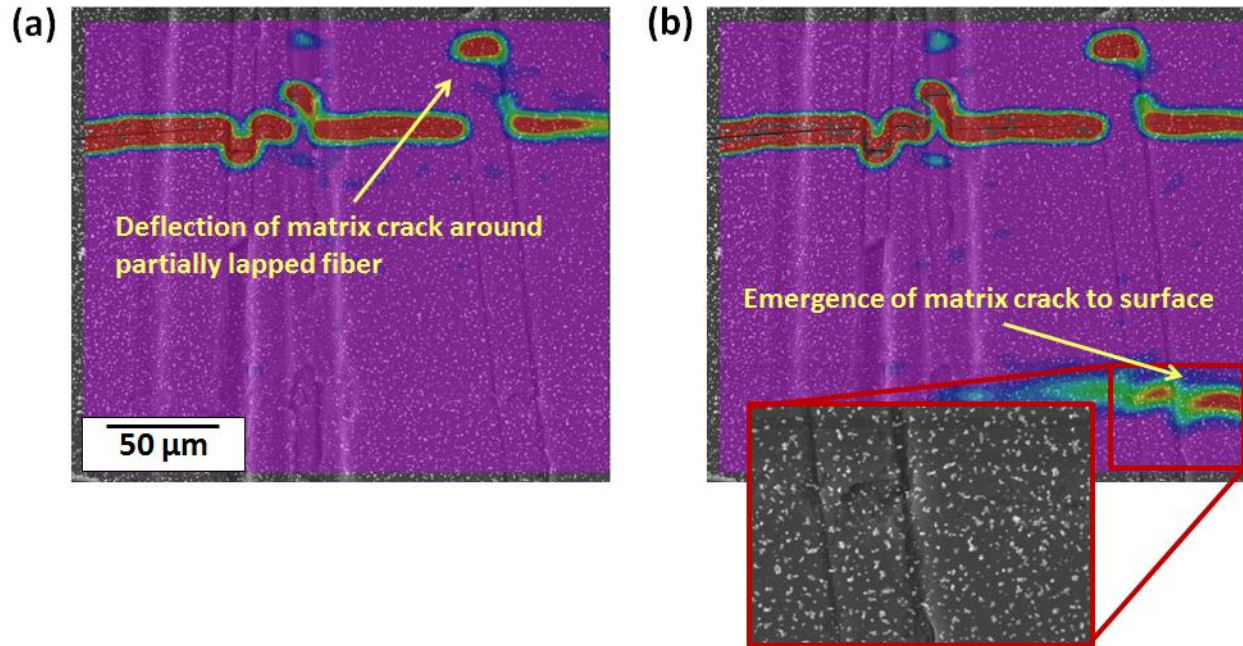


Figure 6.12 Longitudinal strain fields of matrix cracks propagating through the outer longitudinal lamina of cross-ply CMC. In (a) the matrix crack deflects along longitudinal fibers as it traverses the lamina. In (b), a second matrix cracks emerges at the surface of the longitudinal lamina. An advantage of lamina-scale experimentation is that it can detect fine matrix cracks in the early stages of their evolution.

6.3.3 Damage Evolution at the Laminate Length Scale

In transitioning from the lamina scale to the laminate scale, spatial resolution is again reduced. However, effort shifts from understanding crack behavior with respect to microstructural features to macroscopically investigating damage accumulation in CMC structures. Consequently, this is the length scale at which damage in structural components is often analyzed. Macroscale deformation fields were used to qualitatively assess crack accumulation in CMC coupons as well as quantitatively characterize toughness and establish a fiber bridging law.

The primary objective of laminate level tests was to observe the matrix crack population under mechanical loading. The behavior of propagating cracks was examined by subsequent analysis of DIC deformation fields. Figure 6.13 shows longitudinal strain fields for three separate tensile coupons loaded vertically in the plane of the page; (a) and (b) were imaged macroscopically while (c) was imaged microscopically. The three samples were of equivalent

layup ($[0/90/0/90]_s$), but (b) and (c) had machined edge-notches. The longitudinal strain fields correspond to the stress state just prior to failure. In the un-notched tensile coupon of Figure 6.13 (a), the matrix cracks accumulate at a slight angle (as much as 8° from the axis normal to the loading direction). Angled crack accumulation was not observed in the notched coupons. Although cracks often propagated from notches at angles that deviated from horizontal, they usually reoriented themselves to a direction normal to the loading axis. Although there was no characteristic distance from the notch at which reorientation occurred, it typically occurred before the crack propagated half way across the tensile coupon.

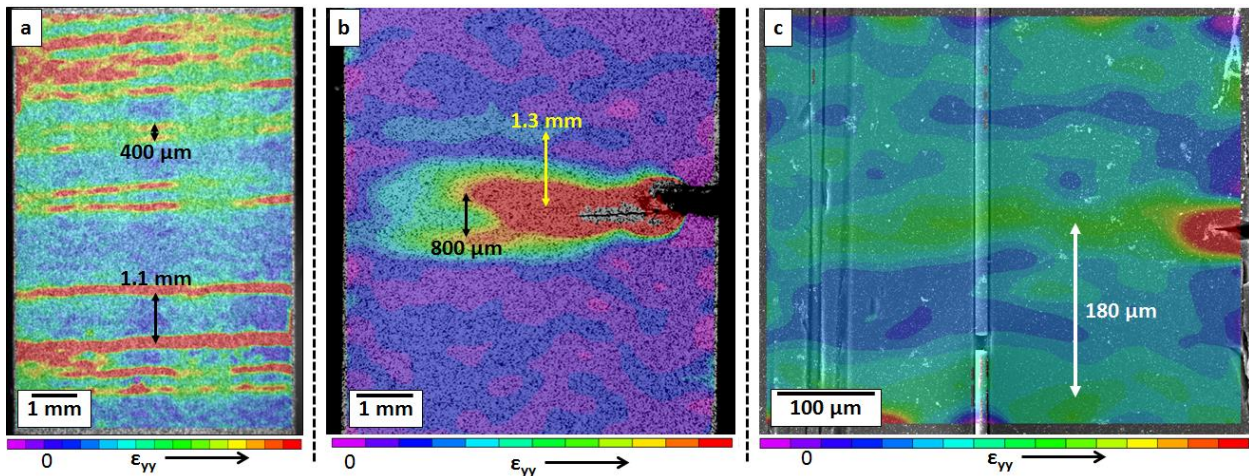


Figure 6.13 Longitudinal strain fields at multiple length scales at applied stresses near the tensile strength. Loading is vertical in the plane of the page. Frames (a) and (b) depict crack accumulation at the laminate length scale in a finite width coupon (a) and an edge-notched coupon (b). The smallest resolvable crack spacing at the macroscale was 400 microns (a). The finite width coupon had a greater crack density than the notched coupon. The higher resolution deformation field of (c) shows that crack spacing can be as small as 180 microns.

Macroscale DIC allows for measurements over a large region of the gage section but may not detect fine matrix cracks, which can lead to inaccuracies in analytical models that incorporate crack separation spacing in predictions of, for example, the ultimate stress [22] of the composite or shear stress at the fiber-matrix interface [22]. Most macroscopically observable crack separation distances were on the order of millimeters. The smallest measureable crack separations at the macroscale were 400 μm versus 200 μm on the microscale. Recall from Figure 6.12, crack spacings as low as 100 μm have been detected in longitudinal lamina of cross-ply tensile coupons. Although the green, banded strain localizations in Figure 6.13 (c) are not as distinct as those in Figure 12 (b), they are indicative of cracks and not bias. Gaussian noise

would manifest as randomly dispersed strain peaks while interpolation bias and aliasing would resemble higher frequency, periodic bands. Additionally, the notched macroscopic tensile coupon (b) revealed fewer cracks at saturation than the un-notched coupon (a).

It was found that the speed of a matrix crack varied along its propagation path. Crack velocity was measured at 1000 frames per second using high speed cameras and DIC to time and track matrix cracks in a cross-ply CMC. Variation in crack speed is shown in Figure 6.14, where a matrix crack initiates at an edge-notch and propagates normal to the loading direction at 0.007 m/s. There is a brief pause in propagation for ~0.5 seconds, followed by the crack quickly shifting left along the loading axis. After this shift, the crack resumes propagation normal to the loading axis at 0.001 m/s. After another brief interruption, the crack propagates to final fracture at an immeasurable speed. Inset in the figure is a longitudinal strain field corresponding to the stress state just prior to final fracture. The matrix crack that started at the notch has fully traversed the gage section and several small cracks have initiated along the edge opposite the notch.

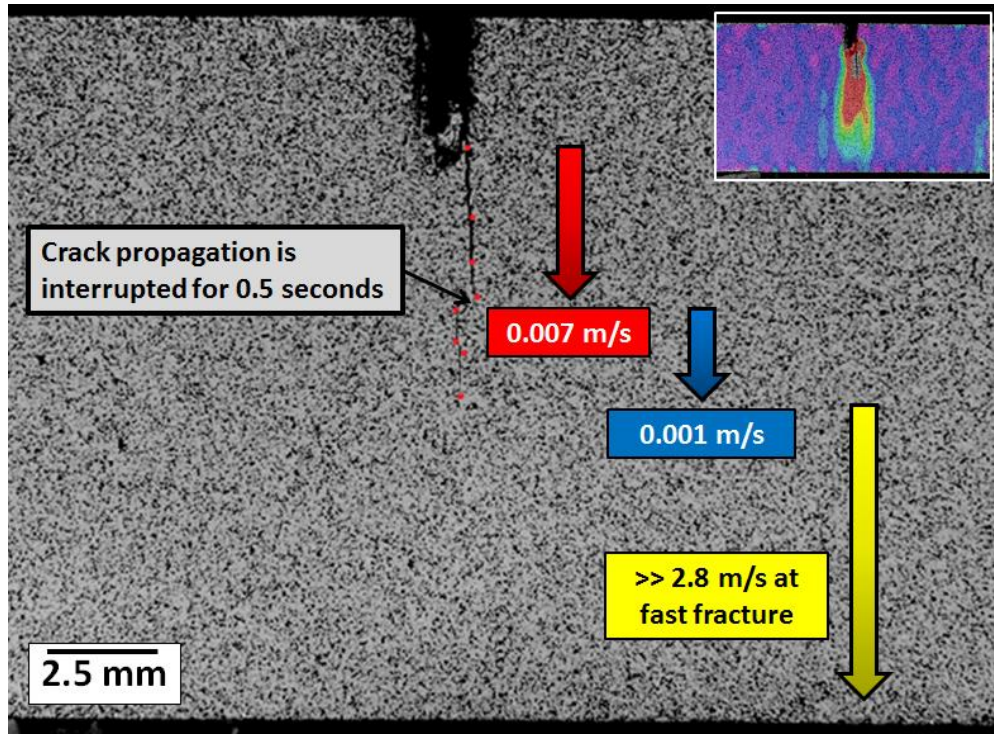


Figure 6.14 Velocity of a matrix crack that initiates from a notch in a cross-ply CMC. Inset at upper-right is a longitudinal strain field captured just prior to final fracture. Crack speed varies during propagation. Initial propagation is slow (0.007 m/s). The crack then pauses and shifts left before continuing slow propagation (0.001 m/s). Velocity increases by several orders of magnitude at final fracture.

A key advantage of macroscale full-field deformation fields is that they graphically depict the evolution of large cracks over broad fields of view. This is evident in Figure 6.15, which illustrates full-field maximum principal strains over the course of a single, fully reversed fatigue cycle, then continuing to final fracture. The sample had previously undergone 40 cycles of tensile dwell fatigue. Frames (1) and (3) of Figure 6.15 show macroscopic strain fields at compressive and tensile stresses equivalent in magnitude to the stress that was used during dwell fatigue. At this length scale, there appears to be no damage (cracks) in either the compressive or tensile strain maps. Recall from Figure 6.7, however, the strain localizations were present in transverse fiber coatings as well as in longitudinal fibers after 40 cycles of tensile dwell fatigue at this stress level. The macroscopic FOV does not capture this. Cracking is not apparent until Frame 4, which corresponds to an applied stress nearly twice as large as the dwell stress. By Frame 5, which was captured just prior to final fracture, the CMC was fully saturated with matrix cracks.

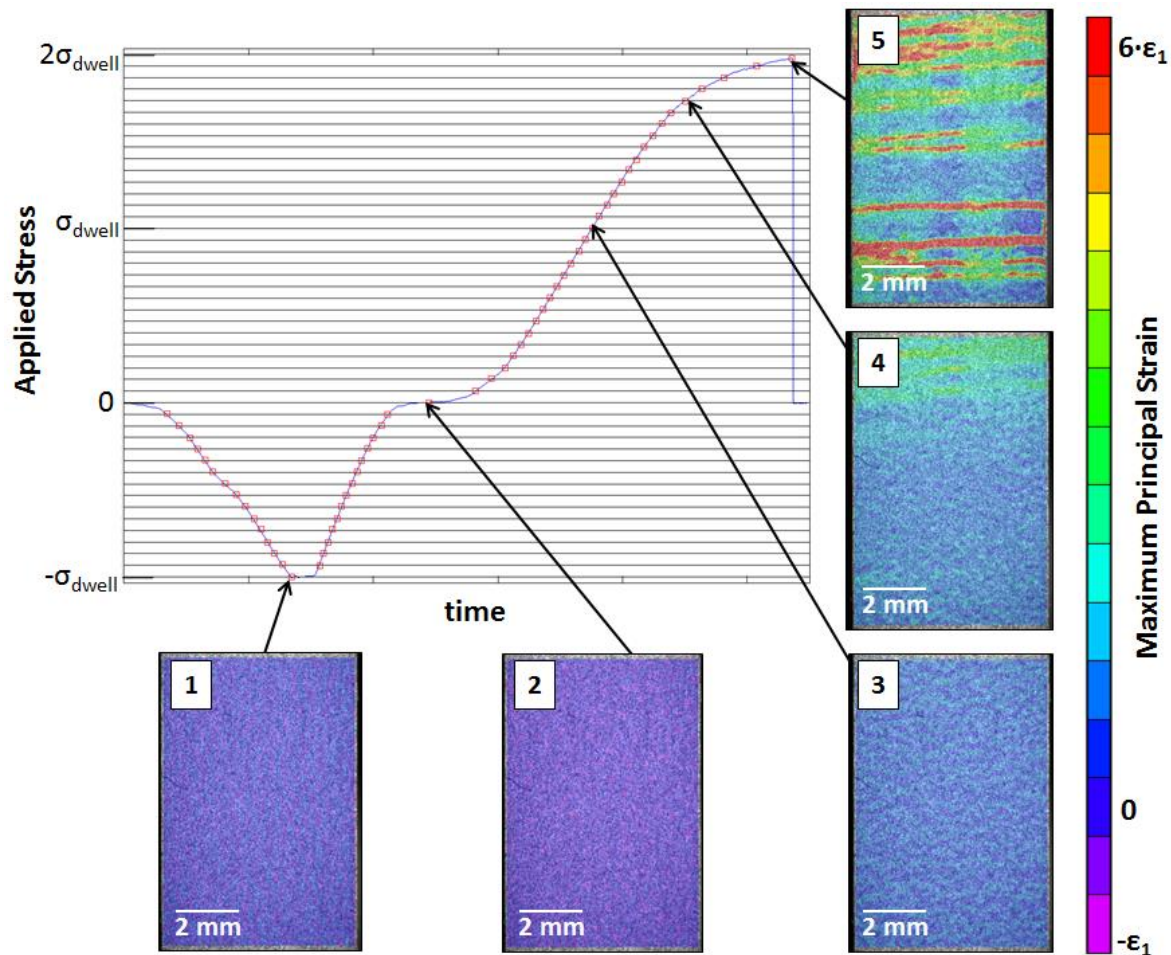


Figure 6.15 Evolution of damage in cross-ply CMC under fully reversed cycle. Sample had previously undergone 40 cycles of tensile dwell fatigue at an applied stress that near the upper bound of PL stress range. Macroscale detection of matrix cracks does not occur until well above the dwell stress.

Matrix cracks in un-notched samples do not always evolve as continuous cracks that span the gage section, leaving fully bridged fibers in their wake. Figure 6.16 shows maximum principal strains at increasingly larger applied stresses, where black arrows point to bands of localized strain indicative of a matrix crack. The severity of localized strain increases more in the three σ regions along the crack indicated by the black arrows. The three strain locations merge into a continuous band only after the applied stress has reached 97% of the failure stress. An adjacent crack develops in a similar manner just below it. At the point of crack saturation (Figure 6.15, frame 5), several matrix cracks have evolved into bands of contiguous but not continuous strain localizations. This fracture behavior is unique to this particular CMC test coupon. It may be an

artifact of damage at the fiber-coating-matrix interface as a result of the compressive cycle or from the prior dwell cycling; however, a decisive explanation warrants further investigation.

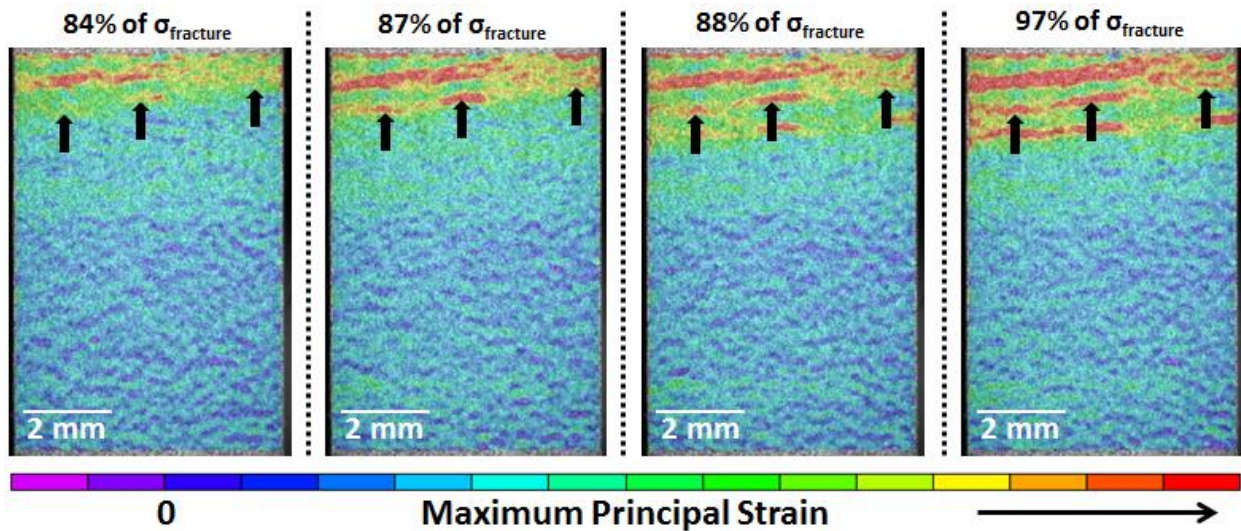


Figure 6.16 Matrix cracks in smooth bar samples do not always evolve as continuous cracks that span the gage section, leaving fully bridged fibers in their wake. For example, damage evolution is shown as applied stress approaches fracture stress. Sample had previously undergone 40 cycles of tensile dwell fatigue as well as a fully reversed compression-tension cycle. Matrix cracks manifest at the surface of the coupon at three distinct locations (indicated by black arrows). The strain localizations at each arrow broaden with applied stress, ultimately forming a band of localized strain.

Experimental measurements of crack angles in unidirectional composites are valuable for numerical modelers looking to validate simulations. In addition to cross-ply laminates, damage accrual in longitudinal unidirectional layups ([0/m/0]) was investigated at the laminate scale. Chapters 4 and 5 presented macroscopic strain fields for several unidirectional laminates loaded to failure in tension. In each test, two cracks initiated from the notch tip as illustrated for three unidirectional tensile specimens in Figure 6.17. The angle between cracks (measured from the top crack to the bottom crack in the direction of crack propagation) varied from one sample to another, but all fell within the range of 100 to 136 degrees.

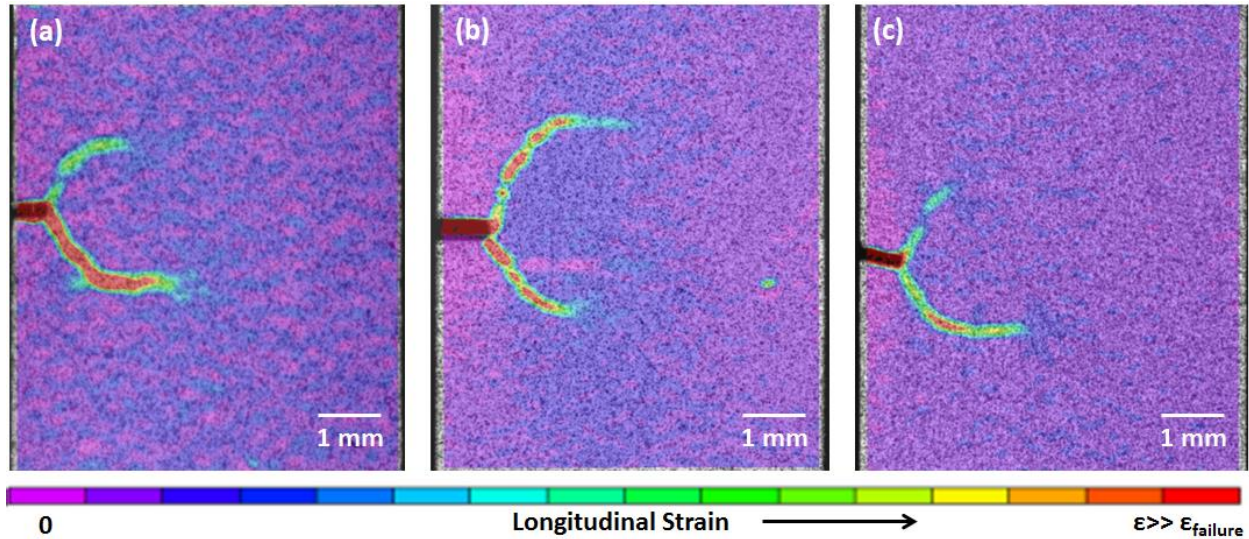


Figure 6.17 Initiation of angled cracks from notch tips of three different samples. The notches in (a) and (b) were cut perpendicular to the loading axis (which is vertical in the plane of the page). The former was shorter than the latter. The notch in (c) was cut at angle 15° clockwise from horizontal.

6.3.4 Connecting Microscopic Damage to Macroscopic Damage

The previously discussed constituent and lamina scales comprise the microscopic length scale, examined in the SEM. It is from these microscale experiments that we determined:

1. Damage initiates in transverse fiber coatings prior to the applied stress reaching the proportional limit; it manifests as strain localizations which generate fine crack openings at the fiber-coating-matrix interface on the order of tens of nanometers. Strain localizations were observed primarily in fibers with thick coatings; however, we did not sample enough fibers at the constituent scale to establish a statistically significant trend. Strain localizations were also observed in partially lapped longitudinal fiber coatings; they were oriented in the loading direction. Fibers were sampled from interior and exterior lamina near the centers of the gage lengths of each CMC so that we could verify the assumption that damage was widespread within regions of the sample experiencing the largest net section stress.
2. Matrix cracks have spacing as small as several hundred microns. These cracks are often too fine to be resolved at the macroscopic scale.

Extending the microscale findings to macroscopic analyses of damage accumulation showed that:

1. Of the numerous fine matrix cracks that manifest stochastically at the microscopic scale, some develop into large matrix cracks that traverse the full width of the CMC structure (e.g. the gage width of tensile coupons). Future work could quantify this through: (a) simultaneous data collection at the microscopic and macroscopic scales or (b) microscopic imaging of large amounts of gage section.
2. Notches in tensile coupons introduce a complex stress state in the region surrounding the notch tips. Several cracks may initiate at the tip, as shown at the microscale; but often just a single crack (as in cross-ply laminates) or two cracks (as in unidirectional laminates) are detected at the macroscale. Those that go undetected are likely fine matrix cracks that have relaxed due to close proximity to the larger, detectable cracks. Their presence may still be significant, however, as they introduce a pathway for oxygen to intercept and degrade fibers.

The significance of each length scale is summarized in Figures 6.19 and 6.20, where deformation fields for the annealed CMC are plotted at both the constituent (micro) and laminate (macro) length scales. On the left side of Figure 6.18, four solid black boxes are plotted on top of full-field maximum principle strains captured under load after 40 cycles of tensile dwell fatigue. On the right, maximum principle strains at positions corresponding to the four black boxes are plotted; they also were captured under load after 40 cycles of dwell fatigue, but in the SEM. The microstructures for these AOIs are encircled in black squares on an optical micrograph of the edge of the CMC tensile coupon. The applied stress during dwell fatigue cycles was 75% of the proportional limit stress. At this stress, the macroscopic strain field on the left side of Figure 6.18 shows no clear evidence of damage. The microscopic strain fields on the right side, however, show substantial strain localization in both the transverse and longitudinal fiber coatings. Note that the microscopic and macroscopic strain fields were not captured simultaneously.

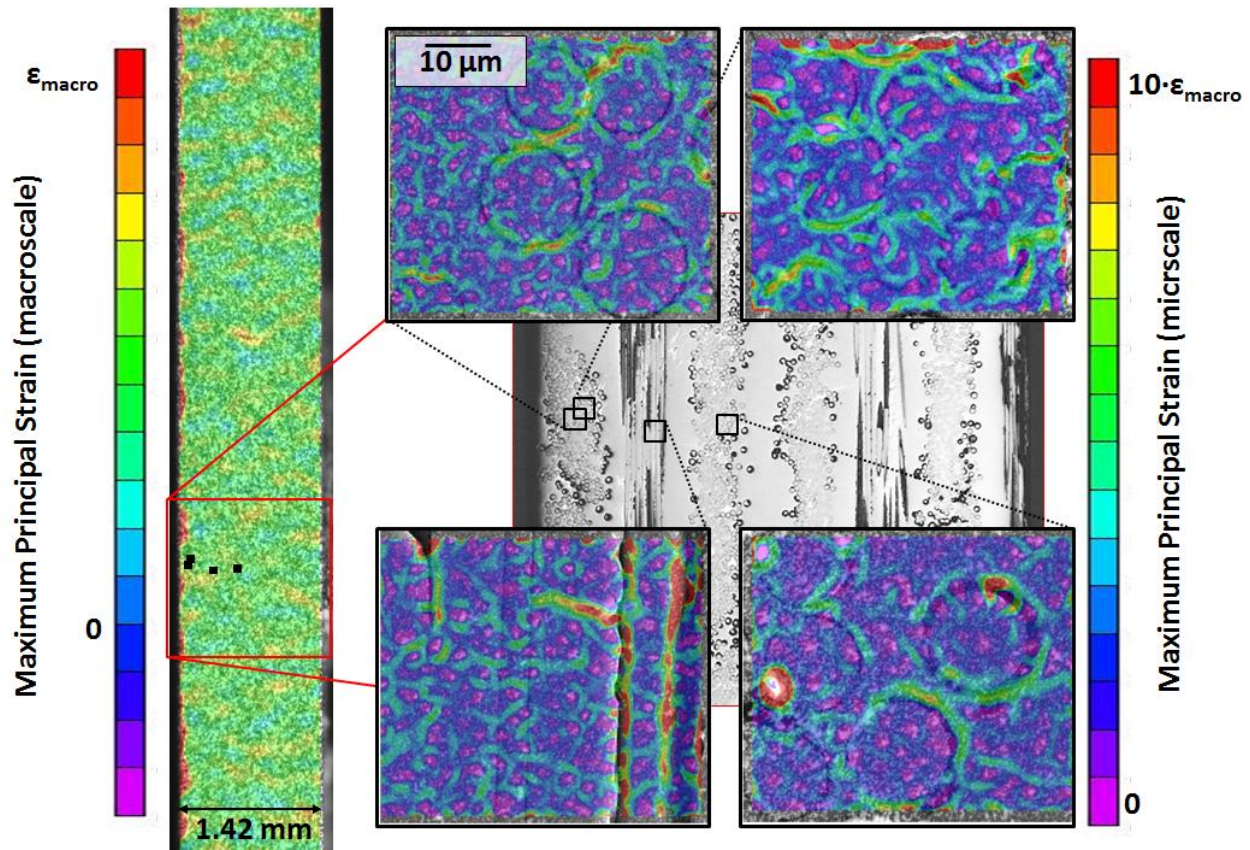


Figure 6.18 Comparison of damage evolution as-observed at microscopic and macroscopic length scales at the dwell stress. On the left is a macroscale deformation field along the edge of a cross-ply tensile. On the right are four microscale deformation fields corresponding to the positions (solid black boxes) on the macroscale field. The underlying structure of the laminate is indicated in the micrograph on the right. Macroscale measurements do not capture damage in the microstructural constituents.

Damage is not clearly evident in the macroscopic strain fields at applied stresses below the proportional limit; certain strain localizations look like noise at these stresses, but may be indicative of cracking. Figure 6.19 shows the evolution of damage in enlarged images of the edge of the annealed (and previously fatigued) CMC tensile coupon. The FOV is located at the center of the gage section. Figure 6.19 (a) shows the underlying microstructure under no applied load. Figure 6.19 (b) shows maximum principal strain fields at the same location (the edge is coated with paint for DIC) at the dwell stress. Figure 6.19(c) shows the strain fields just before failure. As applied stress approaches the failure stress, maximum principal strain fields show that a majority of the matrix cracks manifest in the right half of the laminate and propagate (through the thickness) towards the left half. The four microscale images in Figure 6.18 were sampled

from the left half of the laminate and, in Figure 6.18, correspond to locations where damage accumulated in the coatings below the proportional limit. But based on the progression of damage in Figure 6.19, damage in those coatings did not evolve into cracks with openings large enough to be detected at the macroscale; of the four microscale FOVs, only two were located on a band of high strain.

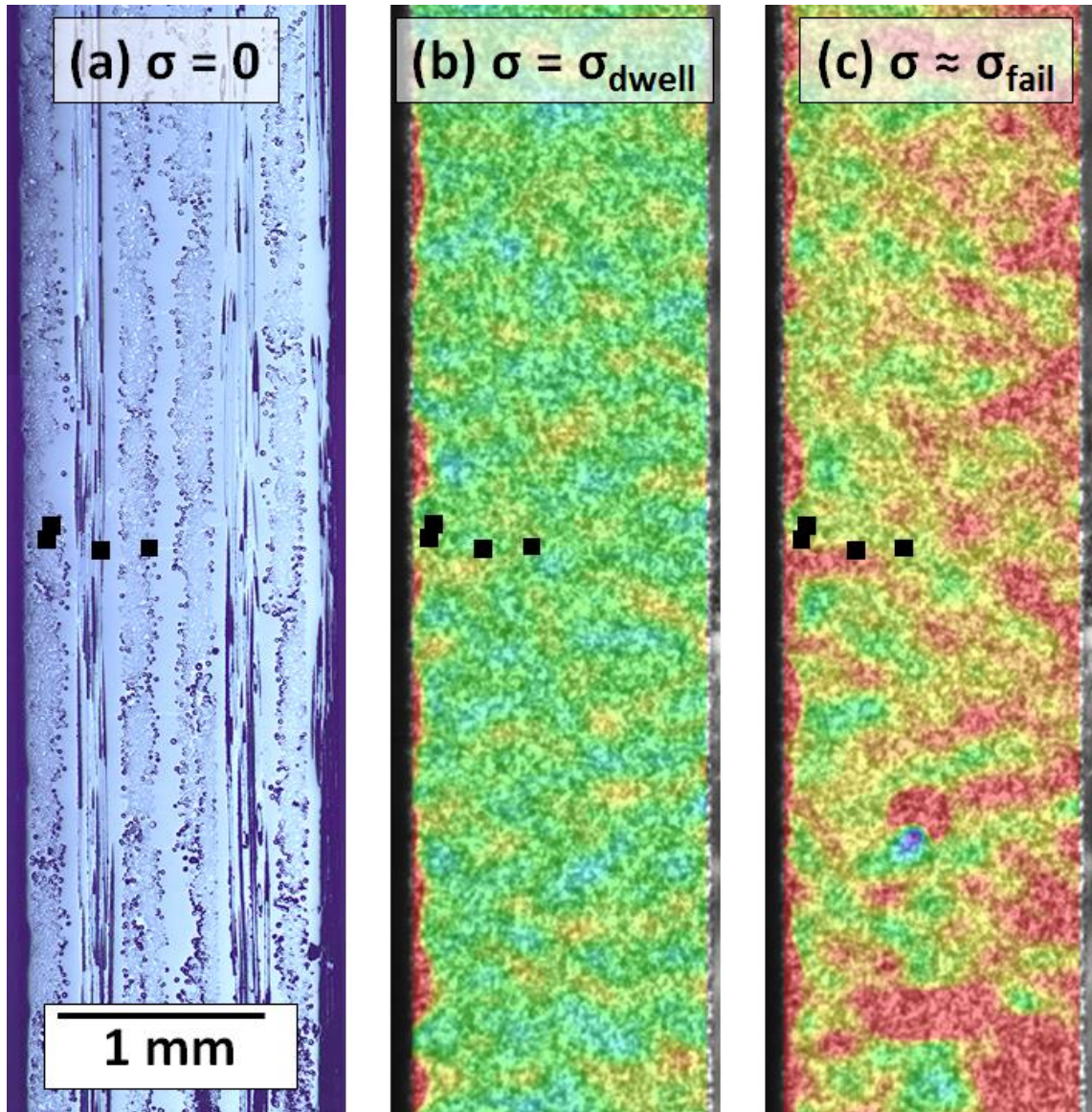


Figure 6.19 Macroscale view of damage progression along the edge of the annealed CMC tensile coupon. CMC previously underwent 40 cycles of dwell fatigue at σ_{dwell} . The solid black boxes correspond to locations where microscale the fields of view in Figure 6.18 . From the macroscale perspective, cracks initiate in right half of the laminate and propagate towards the left half. Of the four microscale FOVs, only two reside near a macroscale crack. This implies damage in coatings detected at the microscale at low stress does not always evolve into large matrix cracks detectable at the macroscale.

6.4 Conclusions

Microscale investigations showed that damage in transverse fiber coatings occurred below the proportional limit. It was contained to small, localized areas of fiber coatings and

mostly situated along the loading axis. Strain localization magnitudes intensified and became more widespread as the PL stress was approached. Above the PL, strain localizations in several adjacent fibers merged into bands that were indicative of matrix cracks. Crack openings across the fiber-matrix interface were on the order of tens of nanometers and were largest in the loading direction. Similar experimentation was conducted on a sample that was annealed to relieve residual matrix stress. The annealed material showed no distinct difference in damage behavior from the as-received sample.

Constituent level damage investigations during cyclic loading showed that the intensity and dispersion of strain localizations in fiber coatings grew with each fatigue cycle, ultimately approaching a steady state between 10 and 20 cycles. After only 10 fatigue cycles, residual damage was present in the fiber-coating interfaces. As with monotonic loading, there was no difference in damage behavior between annealed and un-annealed CMCs. At the lamina scale, it was shown that patches of localized strain that appear continuous at that macroscopic length scale, such as strain lobes extending from notch tips, were actually comprised of several neighboring cracks.

At the macroscale, it was shown that accumulation of matrix cracks is not readily apparent until well above the PL stress. Crack separation spacings measured at the macroscale were larger than at the microscale (400 μm versus 200 μm). High speed imaging of a notched sample showed that crack speed varied for a single matrix crack along its crack path. During stable growth, the crack speed was as low as 0.001 m/s. Tensile tests of notched, unidirectional laminates showed that two distinct matrix cracks initiate from notch tips. The angle between cracks ranged from 100 to 136 deg. Combining observations of damage in dwell fatigue from microscopic and macroscopic length scales, it was shown that strain localizations that appear below the PL at the microscale are not apparent at all at the macroscale, hence the need for multi-scale analyses.

There are several ways to improve the quality of data from multi-scale experimentation. In our analyses, only surface damage was analyzed because 3D imaging resources were not available. Real composite laminates may experience significant amounts of out-of-plane deformation on free edges [2], which may impact damage behavior on the surface. Damage behavior on the surfaces is not necessarily indicative of damage behavior in the interior. This

issue could be resolved through the use of 3D deformation mapping of x-ray or CT scans. Spatial resolution and high cost are challenges that must be addressed for this approach to be feasible. Volumetric digital image correlation exists (Correlated Solutions, Inc). The spatial resolution of x-ray may be too low to resolve the fine coating damage detected in SEM images; however, it is sufficient for detecting large matrix cracks and characterizing their accumulation. 2D damage measurements could be improved by simultaneously collecting data at microscopic and macroscopic length scales. An example would be rigging an SEM with ports that permit SEM imaging and optical imaging simultaneously.

References

1. J. Aveston, A. Cooper and A. Kelly, "Single and Multiple Fracture: The Properties of Fiber Composites," *IPC Science and Technology Press*, 15-26 (1971). [Conference Proceedings]
2. K. Chawla, *Ceramic Matrix Composites*, Chapman and Hall, London (1993).
3. J. Aveston and A. Kelly, "Theory of Multiple Fracture of Fibrous Composites," *J. Mater. Sci.*, **8** 352-362 (1973).
4. B. Budiansky, J. Hutchinson and A. Evans, "Matrix Fracture in Fiber Reinforced Ceramics," *J. Mech. Phys. Solids*, **34** [2] 167-189 (1986).
5. J. Solti, S. Mall and D. Robertson, "Modeling Damage in Unidirectional Ceramic Matrix Composites", *Comp. Sci. Tech.*, **54** 55-56 (1995).
6. D. Beyerle, S. Spearing, F. Zok and A. Evans, "Damage and Failure in Unidirectional Ceramic-Matrix Composites," *J. Am. Ceram. Soc.*, **75** [10] 19-25 (1992).
7. D. Marshall, B. Cox and A. Evans, "The Mechanics of Matrix Cracking in Brittle Matrix Fiber Composites," *Acta Metall.*, **33** [11] 2013-2021 (1985).
8. W. Curtin, "The Tough to Brittle Transition in Brittle Matrix Composites," *J. Mech. Physics of Solids*, **41** 217-245 (1993).
9. S. Spearing, F. Zok and A. Evans, "Stress Corrosion Cracking in a Unidirectional Ceramic Matrix Composite," *J. Am. Ceram. Soc.*, **77** [2] 562-570 (1994).

10. J. Hutchinson and H. Jensen, "Models of Fiber Debonding and Pullout in Brittle Composites with Friction," *Mech. Mater.*, **9** 139-163 (1990).
11. V. Gupta, J. Yuan and D. Martinez, "Calculation, Measurement, and Control of Interface Strength in Composites," *J. Am. Ceram. Soc.*, **76** [2] 305-15 (1993).
12. A. Evans, "Perspective on the Development of High Toughness Ceramics," *J. Am. Ceram. Soc.*, **73** [2] 187-206 (1990).
13. A. Evans and D. Marshall, "The mechanical Behavior of Ceramic Matrix Composites," *Eng. Fract. Mech.*, **38** [2-3] 185-185 (1989).
14. B. Cox, "Interfacial Sliding Near a Free Surface in a Fibrous or Layered Composite During Thermal Cycling," *Acta Metall. Mater.*, **38** [12] 2411-24 (1990).
15. M. Thouless and A. Evans, "Effects of Pull-out on the Mechanical Properties of Ceramic-Matrix Composites," *Acta Metall.*, **36** [3] 517-522 (1988).
16. M. Thouless, O. Sbaizero, L. Sigl and A. Evans, "Effect of Interface Mechanical Properties on Pullout in a SiC-Fiber-Reinforced Lithium Aluminum Silicate Glass-Ceramic," *J. Am. Ceram. Soc.*, **72** [4] 525-532 (1989).
17. J. Kerans and T. Parthasarathy, "Theoretical Analysis of the Fiber Pullout and Pushout Tests," *J. Am. Ceram. Soc.*, **74** [7] 1585-96 (1991).
18. B. Sorenson and R. Evans, "Analysis of Damage in a Ceramic Matrix Composite," *Int. Journ. Dam. Mech.*, **2**, 246-271 (1993).
19. M. Walter and G. Ravichandran, "An Experimental Investigation of Damage Evolution in a Ceramic Matrix Composite," *J. Engin. Mater. Technol.*, **117**, 101-108 (1995).
20. J. Daniel and G. Anastassopoulos, "Failure Mechanisms and Damage Evolution in Crossply Ceramic Matrix Composites," *Int. J. Solids Structures*, **32** [3] 341-355 (1995).
21. G. Morscher, "Modal Acoustic Emission of Damage Accumulation in a Woven SiC/SiC Composite," *Composites Science and Technology*, **59** 687-697 (1999).

22. J. Wachtman, W. Cannon and M. Matthewson, *Mechanical Properties of Ceramics*, Wiley, 2009, pp. 268.

Appendix A

Figures 6.A1-6.A2 are plots of crack opening across the fiber-coating-matrix interface for a CMC loaded in tensile dwell fatigue (refer to *Section 6.3.1* for further details). Virtual extensometers (encircled in yellow on the maps of principal strain in the left micrographs in each figure) are plotted as a function of applied stress and number of dwell fatigue cycles.

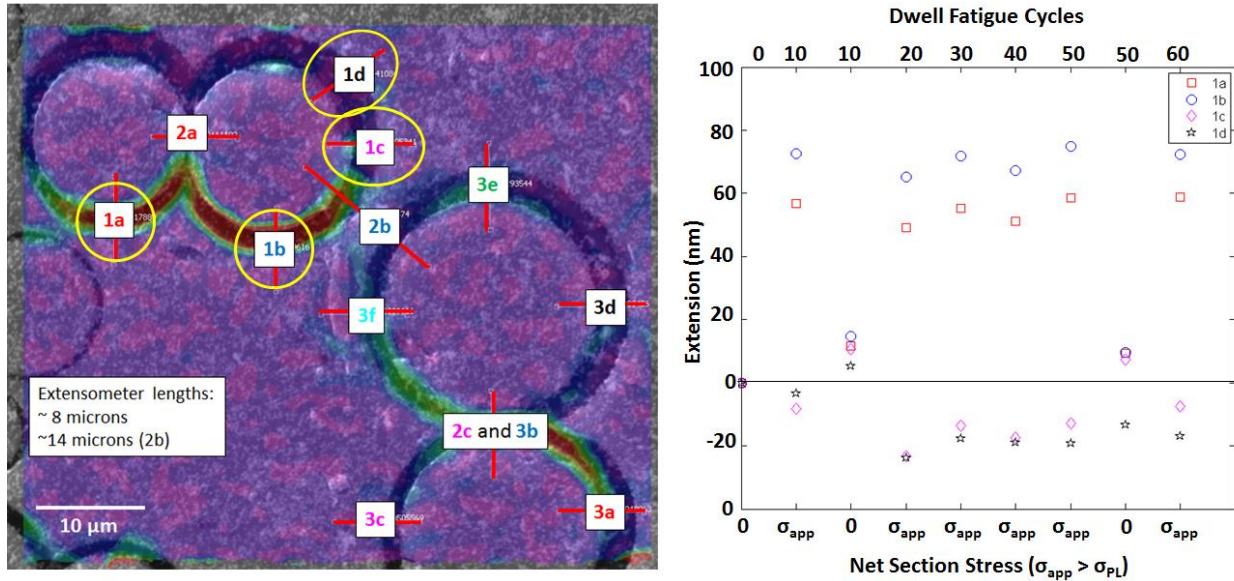


Figure 6.A1 Crack openings (as measured using virtual extensometers and DIC data) across the fiber-coating-matrix interface for SiC/SiC CMC loaded to failure in tension. Extension is plotted as a function of applied stress for the extensometers highlighted in yellow. Extensometers oriented along the loading axis (1a and 1b) exhibit positive extensions; those oriented along or nearly along the transverse axis (1c and 1d) experience compressive extension.

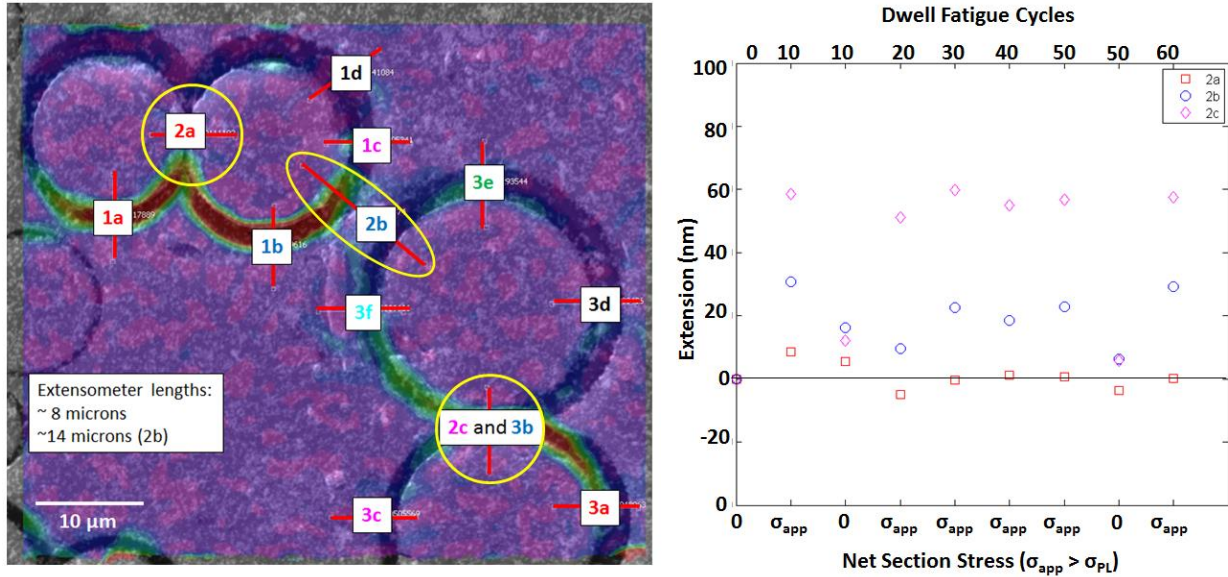


Figure 6.A2 Crack openings (as measured using virtual extensometers and DIC data) across the fiber-coating-matrix interface for SiC/SiC CMC loaded to failure in tension. Extension is positive for extensometers oriented along or nearly along the loading axis (2b and 2c). Extension is negligible for the extensometer oriented in the transverse direction (2a).

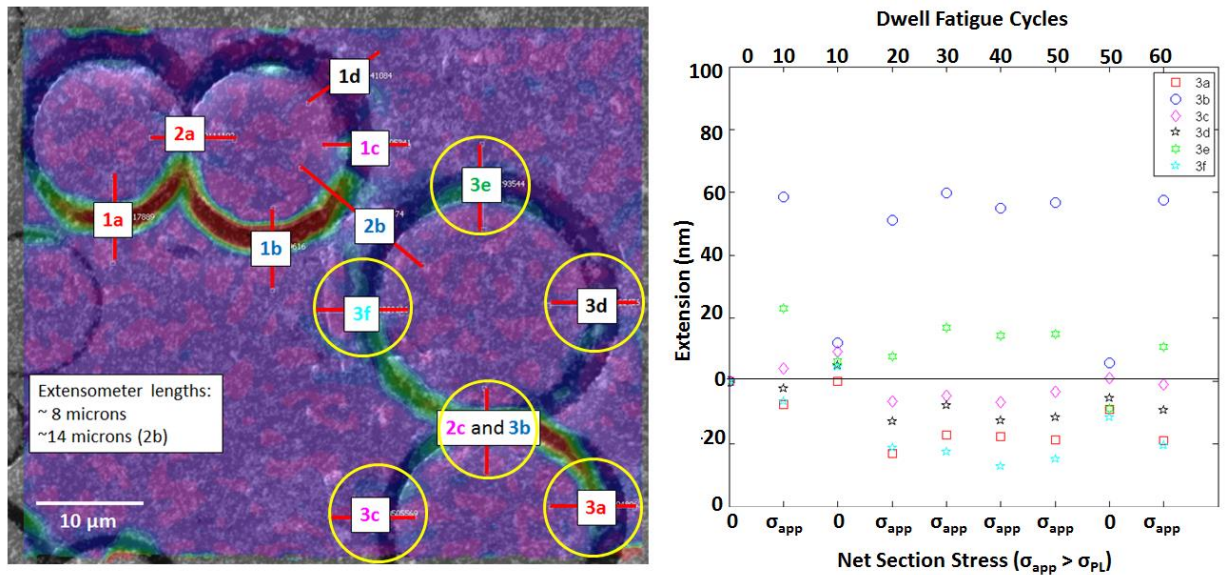


Figure 6.A3 Crack openings (as measured using virtual extensometers and DIC data) across the fiber-coating-matrix interface for SiC/SiC CMC loaded to failure in tension. Extension is positive for extensometers oriented along the loading axis (3b and 3e). Extension is compressive for extensometers oriented in the transverse direction (3a, 3c, 3d and 3f).

CHAPTER VII

Summary and Future Work

7.1 Summary

A multi-scale approach to characterize damage in continuous fiber SiC/SiC CMCs was presented. It began with a small-scale investigation of toughening mechanisms in notched, cross-ply CMCs loaded in tension at 795°C. Toughening mechanisms such as crack deflection, multiple matrix cracking and fiber pullout were evident in longitudinal strain fields. Qualitative and quantitative analyses showed that caution must be used when interpreting DIC data in CMCs. Process zones at notch tips and crack tips appeared as continuous flutes of localized strain. However, filtering the strain data in the process zones showed that the apparently smooth, continuous flutes of localized strain consisted of several distinct matrix cracks emanating from the notch at different angles. Mean strains in longitudinal fibers were computed at each load increment using DIC data. The DIC-measured mean strains increased with load, then dropped at fiber fracture, indicating that SEM-DIC was able to resolve elastic deformation in individual fibers. Accuracy of the mean strain magnitudes was questionable as the noise and bias in the data resulted in large standard deviation ranges. Standard deviations were smallest where the noise-to-signal ratio was lowest. Elastic strains in SiC matrix fell below the noise threshold and could not be accurately resolved.

Toughness in unidirectional and cross-ply CMCs was characterized using two adaptations of the J-integral: (1) numerical integration of a line contour and (2) Gaussian integration of an

area contour. Each method was validated analytically and experimentally using an isotropic, homogeneous material. The analytical validation confirmed that both methods were path independent and accurate; small systematic error (up to 0.0011% error) was introduced due to truncation of the contour about the crack flange. However, experimental DIC data introduced error in the calculation due to noise and bias. Accuracy of the J measurements was improved by filtering the DIC strain and displacement data. Both integrals (line and area) were used to calculate fracture toughness of PMMA validation samples to within the range of published values; the area integral routinely predicted slightly larger values than the line integral. The discrepancy between predictions of the two algorithms was attributed to the way data is filtered. The line integral used filtered strain and displacement data while the area integral used only filtered displacement data.

Next, the validated algorithms were applied to SiC/SiC CMCs for two different layups: (1) cross-ply single edge notched tensile coupons loaded in uniaxial tension under vacuum in an SEM at 795 °C and (2) single edge notched unidirectional (i.e. fibers oriented along the loading axis) tensile coupons loaded in tension outside of the SEM at ambient temperature and pressure. The J-integral derived stress intensity factors were larger than those computed from closed form analytical expressions (which use stress and crack length as input). The analytical expression does not account for multiple matrix cracks; it assumes a single crack with a definitive length. The J-integral is computed over a domain that encompasses multiple matrix cracks; hence the difference in measurement. Resistance curves for both the cross-ply and unidirectional laminates revealed toughening behavior. As crack opening displacement increased, K increased but the rate of increase grew smaller, indicating stable crack growth.

Plane stress fracture toughness could not be quantified with certainty because noise masked the onset of crack initiation at the notch tip. It was estimated that for cross-ply coupons tested at 795 °C in the SEM, fracture toughness was within or below the range 0.9K to 1.1K, where K is an arbitrarily chosen reference value similar in magnitude to that of reaction bonded SiC. For unidirectional laminates tested at 25 °C outside of the SEM, fracture toughness was within or below the range 0.9 to 1.5K. Bridging laws – derived from resistance curves -- for the cross ply and unidirectional laminates indicated that bridging tractions were larger in the cross ply layup than in the unidirectional layup.

Post-test fractography, analyzed in concert with full-field surface deformations, provided a subsurface perspective of crack evolution. Crack propagation on the surface did not always coincide with crack propagation sub-surface. This must be taken into consideration when analyzing damage behavior using DIC. Fractographs indicated that machining (e.g. cutting notches with a diamond saw) introduced flaws that initiated matrix cracks, and that fiber distribution may influence the local direction of crack propagation. Nanoindentation indicated the elastic modulus of the matrix near fiber coatings was smaller than the modulus in matrix-rich areas.

Multi-scale investigations revealed characteristics of damage progression from crack initiation in fiber coatings through final failure. Damage initiated in transverse fiber coatings at stresses well below the proportional limit; it manifested as strain localizations in microscale full-field strain data, which increased in magnitude and became more widespread as the PL was approached. Above the PL, localized strains merged into bands of strain indicative of matrix cracks. Macroscale analyses showed that matrix cracks accumulate until the matrix is saturated, at which point the smallest resolvable spacing between cracks was approximately 400 μm (nearly twice as large as the smallest resolvable crack spacings measured at the microscale). The velocity of a propagating crack (initiated from an edge notch) was measured with aid of DIC and high-speed macroscopic photography. The crack speed varied as it traversed the matrix, becoming unmeasurably large as it approached the far edge of the sample. Crack speeds were as low as 0.001 m/s under continuous loading in displacement control, which is remarkably low for a ceramic material, but expected for a tough CMC.

Microscale damage investigations during cyclic loading (tensile dwell fatigue below the PL at ambient temperature) of un-modified and annealed crossply CMCs showed that the intensity and dispersion of damage in fiber coatings grew with each fatigue cycle. Damage approached a steady state between 10 and 20 cycles. Although residual stresses in the matrix of the annealed samples were presumably lower than the un-modified sample, there was no discernable difference in damage behavior (under monotonic and cyclic loading). Coating damage went undetected when these experiments were repeated at the macroscale. This demonstrated the importance of investigating damage at several length scales.

7.2 Future Work

Currently, DIC is constrained to measuring deformations only on the surface of a material. This presents two major problems when analyzing damage: (1) DIC data does not reveal sub-surface deformation and (2) conclusions drawn from DIC data must make simplifying assumptions about edge and free-surface effects. Chapters VI and VII addressed these problems through two techniques -- measuring deformation on orthogonal surfaces and comparing in-situ DIC measurements with post-test fractography. A better solution to this problem is volumetric DIC. Software now exists that uses x-ray and CT imagery (collected in-situ during mechanical loading) to measure 3D full-field deformations throughout the volume of a material (Correlated Solutions, Inc.). For CMCs, the challenge of volumetric DIC is in acquiring image data at spatial resolutions sufficient to identify matrix cracks. Although x-ray and CT scanners may not have sufficient spatial resolution to measure the fine matrix cracks characteristic of crack initiation, they could possibly resolve cracks above the proportional limit.

A shortcoming of SEM-DIC is that it is too time consuming and resource intensive to analyze an entire gage section. A solution would be to automate the SEM-DIC process in such a way that a contiguous patchwork of small-scale images is collected over a large area. This would be particularly useful for a CMC since damage accumulates throughout the gage section. There are several challenges to automating SEM-DIC. Silicon carbide charges over time. The charging is not severe; however, contrast, brightness and focus have to be periodically adjusted in order to match speckle pattern attributes from test images to those of the reference image. An automated routine would have to account for this. If the working distance between the sample and the pole-piece is not uniform over the entire gage section, images may lose focus. Utilizing automatic focus may resolve this issue. With the SEM (Quanta 3D) used in this work, auto focus was inconsistent and introduced noise in DIC results. Tensile coupons, especially stiff CMCs, relax in the grips slightly upon loading. An automated system would have to incorporate a delay to prevent imaging during relaxation.

The high-temperature testing discussed in Chapter III was permissible only in a vacuum since humidity would corrode components in the heating element. Thermo-mechanical testing in a humid atmosphere (e.g. environmental mode in an SEM) would more closely simulate the service conditions of a SiC/SiC CMC. It could reveal important information about oxidation in

fine matrix cracks and in the coating, which are important in the event that an environmental protective coating is compromised in service. Environmental high-temperature testing would require a heating system that is resistant to corrosion. An auxiliary cooling system would be needed to ensure the stage and components in the SEM chamber do not overheat.

A shortfall of spot heating with (e.g. with a button resistance heater or a laser) is that thermal gradients exist throughout the gage section. A better approach may be to encapsulate the tensile coupon in a resistance heating element material. For example, platinum could be evaporated on the outer surface of the gage section. Leads can be attached to the platinum so that it can be used as a heating element. If chemical reactions between the heating material and the CMC is a concern (e.g. platinum may react with SiC high temperatures), then alumina could be evaporated over the CMC first, followed by the platinum. Prior to evaporation, FOVs for DIC can be covered with a mask (such as PMMA). The mask can then be dissolved after evaporation.

This thesis discussed the strengths and weaknesses of damage analyses at microscopic and macroscopic length scales. Future testing should take advantage of the strengths of each length scale to further the understanding of damage evolution under thermomechanical loads that replicate (as much as possible) the most extreme conditions in which CMCs may be utilized. It's been shown that damage initiates in coatings at stresses well below the proportional limit at ambient temperature. It's unknown whether the presence of fine coating cracks affect mechanical performance in an oxidizing environment; however, it is reasonable to assume that fine crack openings in the coating may expedite environmental attack of the fibers. Constituent scale SEM-DIC in a humid atmosphere, at elevated temperature, under cyclic loading could be used to assess the significance of coating damage at stresses well below the proportional limit.

Lamina scale SEM-DIC should investigate the effect of oxidation on fine matrix cracks that develop at stresses above coating crack initiation but below the proportional limit. The outer surfaces of the CMCs tested in this thesis were composed of partially lapped longitudinal plies. Experimental observations of damage and oxidation in exposed longitudinal fibers, however, may not accurately reflect the damage state in fibers fully immersed in matrix. Accurately characterizing damage in longitudinal fibers is critical as they contribute significantly to toughening. More meaningful data could be obtained from deformation data collected on the surfaces of cross-ply CMCs that have thin layers of matrix material covering the outer

longitudinal lamina. After thermomechanical testing, the thin matrix layer could be lapped to reveal the underlying microstructure. DIC data could be superposed on the microstructure for damage analyses and EDAX could be used for oxidation analyses.

Macroscopic damage investigations should focus on damage accrual in the vicinity of the proportional limit since, by then, matrix cracks are large enough to be detected. Macroscale tests are less time and resource intensive than microscale tests, so a larger volume of test data can be analyzed (large sample sizes are critical for CMCs due to their stochastic nature of failure). Dwell fatigue in this thesis was executed below the proportional limit. These tests should be repeated, but similar tests should be run at the proportional limit to capture damage behavior under the most severe conditions that a SiC/SiC CMC may experience in service. Resources permitting, macroscale testing in a hot and humid environment would best simulate extreme service conditions.